3-21-2019

Creep of Nextel 720/Alumina Ceramic Matrix Composite with Diamond-Drilled Effusion Holes at 1200°C in Air and in Steam

Megan L. Harkins

CREEP OF NEXTEL 720/ALUMINA CERAMIC MATRIX COMPOSITE WITH DIAMOND-DRILLED EFFUSION HOLES AT 1200°C IN AIR AND IN STEAM

THESIS

Megan L. Harkins, Major, USAF

AFIT-ENY-MS-19-M-218

DEPARTMENT OF THE AIR FORCE
AIR UNIVERSITY

AIR FORCE INSTITUTE OF TECHNOLOGY

Wright-Patterson Air Force Base, Ohio

AFIT-ENY-MS-19-M-218

CREEP OF NEXTEL 720/ALUMINA CERAMIC MATRIX COMPOSITE WITH DIAMOND-DRILLED EFFUSION HOLES AT 1200°C IN AIR AND IN STEAM

THESIS

Presented to the Faculty

Department of Aeronautics and Astronautics

Graduate School of Engineering and Management

Air Force Institute of Technology

Air University

Air Education and Training Command

In Partial Fulfillment of the Requirements for the

Degree of Master of Science in Materials Science

Megan L. Harkins, BS

Major, USAF

March 2019

AFIT-ENY-MS-19-M-218

CREEP OF NEXTEL 720/ALUMINA CERAMIC MATRIX COMPOSITE WITH DIAMOND-DRILLED EFFUSION HOLES AT 1200°C IN AIR AND IN STEAM

Megan L. Harkins, BS

Major, USAF

Committee Membership:

Dr. Marina B. Ruggles-Wrenn
Chair

Dr. Eric L. Jones
Member

Dr. Thomas G. Eason
Member

Abstract

A recent study evaluated tensile stress-strain and tensile creep behavior of an oxide-oxide composite (Nextel™720/alumina) with laser-drilled effusion holes at 1200°C. It was determined that the presence of laser-drilled holes degraded the mechanical properties and performance of the CMC as a result of damage caused to the composite microstructure by the laser drilling process. Based on these results, the present effort sought to assess the effects of diamond-drilled holes on the mechanical behavior of this CMC. Tensile properties of the N720/A composite at 1200°C in laboratory air were unaffected by the presence of an array of 17 diamond-drilled effusion holes. Notably, examination of the composite microstructure did not reveal any damage caused by the drilling process. The diamond-drilled specimens exhibited similar degradation to creep lifetimes as laser-drilled specimens for creep tests between 46-150 MPa in air, but contrary to unnotched and laser-drilled specimens, saw minimal degradation to creep lifetimes due to steam. These results were attributed to a change in dominant damage mechanism that caused minimum creep rates in air to exceed those in steam. Further experiments and analysis are needed to explore the damage mechanism at play in specimens with diamond-drilled effusion holes.

Acknowledgments

My time at AFIT has been extremely challenging, and I owe any/all of my successes to my team of faculty, friends and family that supported me along the way. I feel privileged to have been able to work so closely with Dr. Ruggles-Wrenn, and truly appreciate her patience, guidance and expertise throughout this whole experience. I'd also like to thank my lab technicians, Mike Ranft and Jamie Smith. I'm sure I required a little more assistance than usual due to my overly cautious and somewhat inquisitive personality, but they were always ready and willing to support. I know my time in the lab would not have gone as smoothly if it wasn't for them. Thank you also to my family at home for being a constant reminder of what matters most. You kept my spirits high when times were tough, and that was exactly what I needed to get through this.

Megan L. Harkins

Table of Contents

Page

List of Figures

List of Tables

Chapter 1: Introduction

1.1 Motivation

As technology and designs of air vehicles continue to advance and push the limits in terms of speed, temperature or pressure requirements, so too does the demand for structural materials that exhibit long-term mechanical properties and retained properties under these extreme conditions. Ceramic-matrix composites (CMCs) are prime candidates for such applications since they are capable of maintaining excellent strength and fracture toughness at high temperatures. Furthermore, since many of these applications also require exposure to oxidizing environments, current research efforts have focused on evaluating properties of CMCs constructed from environmentally stable oxide constituents. These oxide/oxide CMCs exhibit both damage tolerance and inherent oxidation resistance and have also displayed excellent high-temperature mechanical properties.

In addition to studying the basic mechanical properties of these oxide/oxide CMCs, it's also important to understand how this material will respond to geometric discontinuities in the likely event that notches are needed for cooling or attachment points [1]. While fiber-reinforced CMCs do possess the ability to undergo inelastic deformation and therefore relieve stress concentrations around geometric discontinuities, studies have yet to confirm just how sensitive these materials are to notches when operating at high temperatures in both air and steam environments.

1.2 Problem Statement

This effort aims to characterize the creep behavior of an oxide/oxide CMC with an array of effusion holes at elevated temperature (1200°C). The selected composite material (N720/A) is fabricated by ATK-COIC (San Diego, CA), and consists of a porous alumina matrix reinforced with woven alumina-mullite Nextel 720 fibers. The test specimens contain an array of 17 diamond-drilled effusion holes of 0.5 mm diameter in the gage section. Monotonic tension and creep loading tests are performed at the materials maximum use temperature in air and steam environments [2]. While many studies have investigated the mechanical performance of this material under various loading conditions at elevated temperatures in air and steam, only recently has the effect of effusion holes been considered. For this same material, with the same array of laser-drilled holes, Minor reported significant notch sensitivity of N720/A under monotonic and sustained tensile loading at 1200°C [3, 4]. The present effort will leverage the results of Minor's research, as well as previous studies performed on unnotched specimens, to investigate how the method of hole fabrication affects the mechanical response of the material.

1.3 Methodology

This study follows a systematic plan. A baseline tensile test is performed to establish the at-temperature basic tensile properties. Creep resistance is evaluated in tensile creep-rupture tests performed at 1200°C at various stress levels. Strain is measured throughout each test. Thus, steady-state creep rates can be evaluated and the associated creep mechanisms can be identified. In order to examine combined effects of

temperature and moisture exposure on creep resistance of specimens with effusion holes, creep-rupture tests are conducted at elevated temperature in air and in steam environments. All specimens that achieve creep run-out of 100 h are tested in tension to failure in order to determine the retained tensile strength and stiffness. In order to assess damage and failure mechanisms in the selected CMC, the composite microstructure and fracture surface are examined before and after testing using optical microscopy, scanning electron microscope (SEM) and computed tomography (CT).

1.4 Summary

The objective of this effort is to better understand the notch sensitivity of N720/A at its maximum use temperature of 1200°C under monotonic tension and creep loading conditions. Comparing results obtained in steam to those obtained in air will help assess the impact that the presence of steam has on the creep performance of N720/A specimens with diamond-drilled holes. This impact of steam will be compared to similar results previously reported for unnotched and laser-drilled specimens to assess whether varying configurations of this CMC respond differently to the presence of steam. Furthermore, comparing results obtained in air for unnotched, laser-drilled and diamond-drilled specimens will identify how the presence and type of hole affects the tensile and creep performance of this CMC. These same comparisons will be made for results obtained in steam to assess how the impact differs between environments. Ultimately, this insight will help establish boundaries of the mechanical behavior of this CMC, which is critical for determining its suitability as well as limitations for potential applications.

Chapter 2: Background

2.1 Ceramic Matrix Composites

Ceramic matrix composites CMCs evolved from the desire to leverage the favorable characteristics of monolithic high-performance ceramics in structural applications. The inorganic ceramic materials include oxides, carbides, sulfides, nitrides and intermetallic compounds that are joined by a strong ionic or covalent bond that inherently resists dislocation motion in the lattice. The strong bonds dictate many of the favorable characteristics of the ceramic materials, such as high strength and hardness, high resistance to heat, chemical inertness, wear resistance and low density, but also create a very brittle material. Unlike metals, ceramics do not show any plasticity and are therefore prone to catastrophic failure under mechanical or thermal loading [2]. Despite this significant drawback, the quality that makes ceramics most attractive is their ability to survive and perform at significantly higher temperatures than other materials. Figure 1 captures the differences in service temperature limits between monolithic ceramics, polymers and metals. Considering that future applications will likely require materials to operate at temperatures in excess of 2000°C, it's clear that ceramics are the prime candidates. However, the fracture toughness and damage tolerance of the monolithic ceramics needed to be improved before they could reliably be used in structural applications.

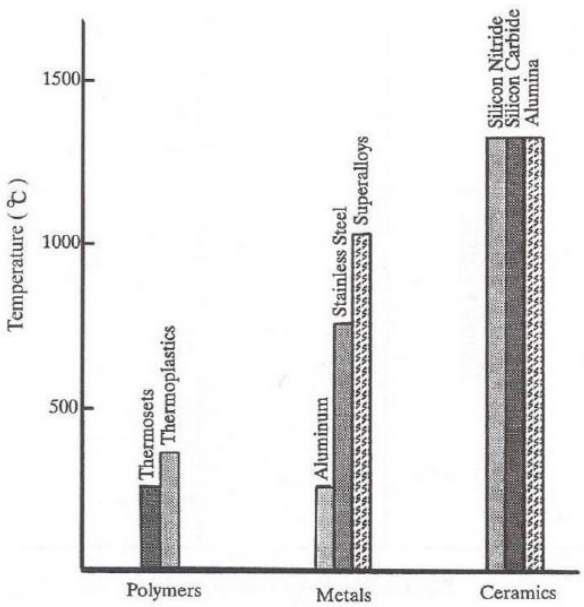

Figure 1: Service temperature limit (indicative) of polymers, metals and ceramics [2]

Multi-phase ceramics, or ceramic composites, combine single phase monolithic ceramics as a means to improve the fracture toughness of the overall material. The two constituents, the matrix and the reinforcement, are individually both brittle in nature; however, as a result of processing techniques, are able to combine and create a quasi-ductile material. This quasi-ductility not only permits a more graceful failure, but also improves the material's ability to endure cracks. The "incorporation of reinforcements (fiber, whisker or particle) introduces energy-dissipating phenomena such as debonding at the fiber/matrix interface, crack deflection, fiber bridging and fiber pullout, etc." [2]. For the purposes of this report, since the N720/A material that is being studied is a fiber-reinforced composite, all future references of the reinforcement will use the fiber terminology. With the addition of the fiber being the key contributor to the improved fracture toughness, it is clear that the fiber/matrix interface plays a significant role in determining the ultimate properties of a composite.

2.2 Fiber Matrix Interface

2.2.1 Interface Bond

Chawla defines this interface as “a surface across which a discontinuity occurs in one or more material parameters or properties, such as atomic lattice, density, elastic modulus, thermal expansion coefficient, strength, fracture toughness, etc.” [2]. Depending on the properties of each of the constituents, they will either adhere together via a strong chemical bond, which involves a diffusional process at the atomic or molecular level, or a weaker mechanical bond that relies on friction. For CMCs, a weaker bond is desirable as it enables the energy-absorbing phenomena previously mentioned. Monolithic ceramics fail in a brittle manner, which equates to a low energy fracture process. Similarly, a composite with a strong interfacial bond will be unable to deflect a propagating crack, thus also failing in a brittle manner. Crack deflection is an important aspect of this toughening mechanism because it increases the surface area of the crack, which in turn, increases the fracture energy required to propagate a crack [5]. **Error! Reference source not found.** depicts the dependence of the fracture energy (ω_f) on the surface energy (γ_s) and true crack area.

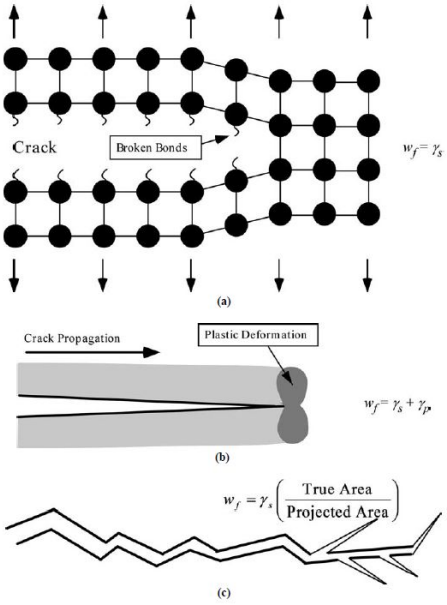

Figure 2: Crack propagation in various types of materials, with the corresponding fracture energy. (a) ideally brittle material, (b) quasi-brittle elastic-plastic material and, (c) brittle material with crack meandering and branching [5].

If the fracture energy of the interface is low, the fiber and matrix will actually debond as a crack progresses, thus permitting the matrix crack to bypass the fiber. **Error! Reference source not found.** displays the difference in crack propagation in composites with strong and weak interfacial bonds.

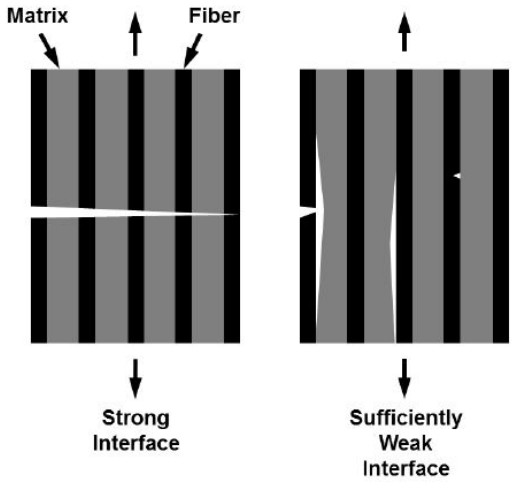

Figure 3: Failure of a CMC as a function of interfacial bond strength: (a) strong interfacial bond; (b) weak interfacial bond [2]

As the interface continues to debond and therefore deflect a propagating crack back into the matrix, the matrix will naturally reach ultimate failure first, but will gradually transfer the load to the fibers as the crack progresses. This phenomenon is referred to as fiber bridging, and is ultimately what produces the quasi-ductile material response seen in Figure 4 [5]. The damage in the composite accumulates gradually until final failure occurs. As a result, the material now displays improved fracture toughness and damage tolerance via a non-catastrophic failure mode.

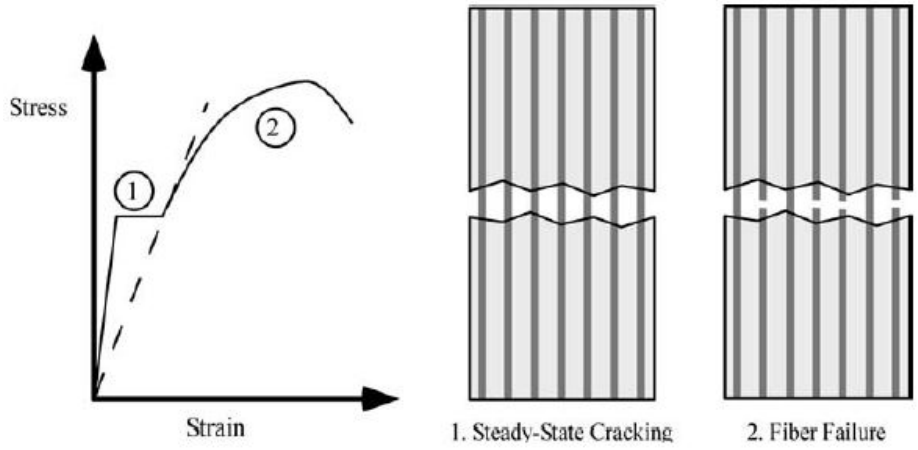

Figure 4: Stress-strain behavior of fiber-reinforced ceramic composites [5]

2.2.2 Crack Deflection Mechanisms

Two microstructural design philosophies are currently utilized in order to achieve the desired crack deflection at the fiber/matrix interface. The first method aims to engineer a weak interface bond by applying a fiber coating prior to combining the constituents into a composite. This coating is designed to minimize any chemical reactions between the fibers and matrix, thus creating a weaker mechanical bond. This has been the traditional method for enabling tough behavior in SiC/SiC CMCs; however, it is less applicable for oxide/oxide CMCs. Few coatings have been found that satisfy all

of the requisite properties needed for use with oxide/oxide CMCs, such as "thermochemical compatibility with the fibers, oxidation resistance at elevated temperature, low toughness, and moderate processing temperature" [6]. Monazite is one promising coating material [7]. However, due to challenges encountered in being able to uniformly coat the fiber surfaces, this coating material currently cannot be implemented in a large-scale production environment.

Alternatively, the second crack deflection method accepts that oxide/oxide CMCs possess a strong, chemically bonded fiber/matrix interface, and forces the crack to grow through the matrix by making the matrix porous and exceptionally weak. In this manner, the cracks connect pores, and propagate through the matrix, leaving the fibers intact [8]. If leveraging this technique, it's important to ensure that the constituents are thermodynamically stable with each other, and that the porosity does not change at the intended use temperature. It's not uncommon for additional matrix sintering to occur at high temperatures, at which point the material would densify and lose its ability to deflect a propagating crack. According to previous studies, a minimum matrix porosity (p_m) of approximately 30% is needed for crack deflection within a porous matrix [8]; based on Equation 1, this equates to roughly 16.8% total composite porosity (p_c) for a CMC with a 44% fiber volume fraction (V_f). Note, the total composite porosity is less than the matrix porosity due to the assumption that fibers are fully dense. Current composites that leverage the porous matrix approach have a matrix porosity between 35-50%, and total composite porosity between 25-40% (reference Table 2 below**Error! Reference source not found.**) [8]. The material being studied in this effort has a 38% fiber volume fraction

and 23.1% total composite porosity; however, all results will be normalized to a 44% fiber volume for comparison to previous research.

$$p_c = p_m(1 - V_f) \quad (1)$$

Error! Reference source not found. shows the sequence of damage events leading to fracture for composites with a) the conventional weak interface, and b) the porous matrix.

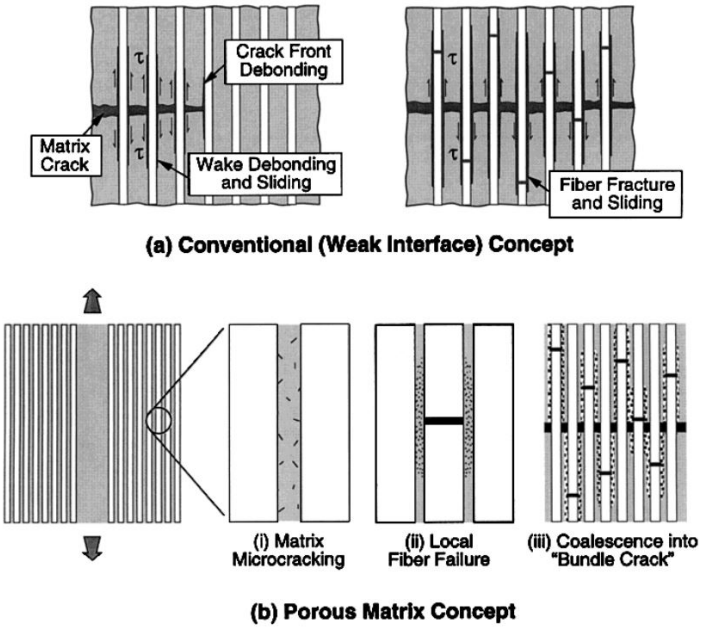

Figure 5: Schematic of the damage processes that enable damage tolerance in a) conventional dense-matrix weak interface CFCCs and b) porous matrix CFCCs without fiber coatings [6]

2.3 Oxide/Oxide CMCs

Ceramic matrix composites comprised of oxide matrices and oxide fibers were introduced as a means to address the life limiting oxidation susceptibility that traditional non-oxide CMCs experienced in aggressive high temperature environments. The finely distributed porous matrix approach to improving damage tolerance is used with oxide/oxide CMCs as the constituents tend to be thermodynamically stable, and therefore

possess a strong chemical bond. There are many advantages to this porous matrix composite system, most notably being the superior environmental stability at high temperatures. Additionally, the use of lower cost oxide fibers that do not require coating make the fabrication process more economical. These advantages come at the cost of reduced strength and elastic modulus, as well as larger thermal strain compared to the properties of SiC/SiC CMCs [8]. A brief overview of the properties of the oxide constituents are presented below.

2.3.1 Fibers

The most commonly used oxide fibers are the fine-diameter Nextel 312, 440, 550, 610 and 720 fibers made by 3M Corporation (St. Paul, MN). However, only Nextel 610 and Nextel 720 fibers are used for high temperature applications (> 1000°C). The Nextel 610 fiber is comprised almost entirely of alumina (Al_2O_3), whereas the Nextel 720 fiber consists of approximately 85% Al_2O_3 and 15% silica (SiO_2) in the form of crystalline mullite. These compositions give the Nextel 610 fiber the higher tensile strength, and the Nextel 720 fiber the superior creep resistance at higher temperatures [8]. Provided that creep resistance "is the life limiting property in many high temperature applications" [8], the Nextel 720 fiber is more commonly used when temperature is the limiting factor in design considerations.

The fine diameter of the Nextel fibers allows for a woven architecture to be used, which improves the handleability. Multiple weave patterns are possible, but the most commonly used form is the 8 harness satin-weave (8HSW) [8]. Furthermore, the 0°/90°

woven ply orientation has been proven to be the most favorable in terms of mechanical performance, and all other orientations are referred to as “off-axis” [8, 9].

2.3.2 Matrix

Common matrix materials used in porous matrix oxide/oxide CMCs include aluminosilicate, alumina-mullite and alumina. Aluminosilicate is made of alumina particles, held together by a silica binder. However, silica is known to densify when exposed to high temperature environments, thus reducing the porosity of the matrix as well as the overall toughness of the composite. Alumina-mullite matrices were intended to address this issue as mullite does not sinter as quickly at higher temperatures. The alumina powders sinter around the mullite, providing strength to the porous matrix structure. While this matrix material did improve the long-term thermal stability of the CMC, relative to the aluminosilicate matrix, the silica in the mullite still posed a concern for high temperature water and fuel rich environments. This consideration drove the effort to develop a silica-free all-alumina matrix. “ATK-COIC has utilized the bimodal concept to increase the thermal stability of an all alumina matrix by using a colloidal alumina (nanometer size) as the filler for the larger alumina powder” [8].

Table 1 lists properties of the oxide constituents, and Table 2 presents physical properties of selected woven cloth oxide/oxide CMCs.

Table 1: Constituent Properties [8]

	Composition, wt%			Tow Strength MPa	Modulus GPA	Density g/cc	Thermal Limits, °C		Expansion ppm/°C
	Al_2O_3	SiO_2	Other				Creep	Strength	
Nextel 312	63	25	B_2O_3	-	150	2.7	600	850	3.0
Nextel 610	>99	<0.3	Fe_2O_3	1600	380	3.9	1000	1225	8.0
Nextel 720	85	15	-	800	260	3.4	1200	1350	6.0
Sapphire	100	0	-	2250	435	3.8	-	-	-
Alumina	100	0	0	-	380	3.96	-	-	8.1

Mullite	75.5	24	<0.5	-	220	3.16	-	-	5.0

Table 2: Physical Properties of Selected Woven Cloth CMC Laminates [8]

Designation	Fiber	Matrix	Fiber Volume, %	Matrix Porosity, %	Composite Porosity, %	Density g/cc
COI-312/AS	Nextel 312	Aluminosilicate	48	42	22	2.30
COI-610/AS	Nextel 610	Aluminosilicate	51	51	25	2.82
GE-610/GEN-IV	Nextel 610	Aluminosilicate	30	35	25	2.90
UCBS-610/M	Nextel 610	Mullite-alumina	40	40	24	-
UCSB-720/M	Nextel 720	Mullite-alumina	40	29-35	7-2	-
COI-720/AS	Nextel 720	Aluminosilicate	48	48	25	2.60
COI-720/A	Nextel 720	Alumina	46	46	25	2.71

2.4 Previous Research

2.4.1 Mechanical Behavior and Environmental Effects

The mechanical behavior of unnotched N720/A (with 0°/90° fiber orientation) at room and elevated temperatures have been studied for quite some time now, and the properties are relatively well understood. Table 3 summarizes the average tensile properties obtained prior to 2011 at various temperatures in laboratory air. This data consolidates published data from the most current handbook on CMCs [10], as well as several journal articles [11–14]. Note that strength and modulus data in Table 3 are adjusted for a fiber volume of 44%. The UTS recently reported by Minor [3, 4] for unnotched N720/A at 1200°C was 203 MPa, slightly higher than the published value of 189 MPa at 1200°C. This small variation in ultimate strength (< 6% difference) is well within the expected data scatter, especially given the improvements to manufacturing processes that occur over time. This current effort will leverage Minor's results for comparison purposes as the data is more recent and likely more representative of current

batch properties. Additionally, this effort will focus on the mechanical behavior under sustained tensile loading as previous studies have concluded that creep loading is more detrimental to porous matrix oxide/oxide CMCs than cyclic fatigue [12, 15]. As can be seen from Table 3, the tensile properties of N720/A are significantly degraded at temperatures above 1200°C. This is consistent with other studies that have reported 1200°C to be the maximum use temperature for this material [2].

Table 3: Average Unnotched N720/A Tensile Properties in Laboratory Air [10–14]. Strength and modulus data are adjusted for V_f=44%.

	23°C[a]	900°C	1000°C	1100°C	1200°C	1330°C[a]
UTS (MPa)	169	190	188	190	189	120
E (GPa)	60	70.1	73.5	69.6	74.7	42
Failure Strain (%)	0.35	0.33	0.32	0.33	0.38	1.7
[a] Data at room temperature (23°C) and 1330°C from Ruggles-Wrenn et al. [11]						

All data reported in Table 3 was produced from tensile tests conducted at a constant displacement rate of 0.05 mm/s. These stress-strain plots all behave similarly, and are fairly independent of temperature until 1330°C. The initial modulus of the CMC is stiffer than that of the fibers alone, but decreases when the matrix cracking begins. This results in a stress-strain curve that is nearly linear to failure, which is typical for a fiber-dominated composite. Additionally, it has been shown that tensile properties of N720/A (as well as other oxide/oxide CMCs) are significantly degraded at faster loading rates in both air and steam environments [13]. As is frequently the case for monolithic ceramics at elevated temperatures, the rate dependence of tensile strength suggests that environmentally assisted subcritical crack growth in the N720 fibers is the dominant failure mechanism for this CMC [10].

Creep performance of N720/A is more sensitive to temperature and environment. Experimental investigations revealed that the stress at which N720/A survived 100 h of creep without failure dropped from 160 MPa to 80 MPa as the temperature increased from 1000°C to 1200°C. The effect of steam on the creep lifetime was not noticeable at 1000°C, but became significant at higher temperatures. At 1100°C in steam, the material achieved creep run-out of 100 h at 100 MPa, and was unable to achieve run-out at 1200°C. For stresses ≥ 100 MPa at 1200°C, steam caused a reduction in creep lifetime of at least 90%. Creep strains accrued prior to failure also increased with both temperature and environment. At 1000°C, creep strains in steam were larger than those in air, but both were below the failure strains obtained in tensile tests. As the temperature increased to 1200°C, the creep strain produced in steam reached as high as five times the strain produced in air at a given test duration. However, for all tests that failed before run-out in both air and steam for a given creep stress, the final strain at failure for all air tests exceeded that of steam tests. This result was due to a difference in creep strain rate which was determined to be highly influenced by applied stress, temperature and environment. As the temperature increased from 1000°C to 1200°C, the effects of steam went from negligible (relative to creep rates in air) to an order of magnitude larger. At 1200°C, the presence of steam accelerated minimum creep strain rates, and therefore reduced creep lifetimes. Furthermore, it was determined that both steam and higher temperatures can accelerate the sintering of the alumina matrix, causing a loss of matrix porosity via matrix densification. As a result, the N720/A CMC becomes less damage tolerant [10].

2.4.2 Notch Sensitivity

The mechanical behavior of notched N720/A at room and elevated temperatures in air and steam environments is less understood. The results that have been produced thus far suggest that there are many factors that can affect the performance of a notched oxide/oxide CMC, to include composite constituents, environmental conditions and notch size/fabrication method. Since we're focused on high-temperature applications, the constituents researched as part of this effort include a variation of the Nextel 610 and Nextel 720 fibers, with the aluminosilicate or pure alumina matrices. Furthermore, most studies evaluated the mechanical performance of these oxide/oxide CMCs at elevated temperature in laboratory air. The effects of steam were not considered. However, as discussed above, steam has been demonstrated to dramatically degrade the mechanical performance of these materials [10]. Minor did consider this environmental condition in her research, and those results will be discussed below. Finally, the notch size and fabrication method have also varied between studies. In general, a notch size is deemed large if its length exceeds that of an average tow size (~1 mm). Note that the effusion holes considered in the present research are significantly smaller, with a diameter of 0.5 mm. Hole (or notch) fabrication methods and orientations that have been considered thus far include twist-drilled, machined and laser-drilled at 90° and 20° to the specimen plane. The results of these studies are discussed below.

2.4.2.1 Large Notches

This area was first studied back in 1999, where Kramb et al [1, 16] investigated the fracture behavior of a single edge notched Nextel 610/aluminosilicate (N610/AS) composite in tension at room temperature and 950°C. Notch dimensions were 0.4 mm

(height) and 3.8 mm (length). Kramb et al reported that the presence of the notch decreased the UTS by approximately 35% at 23°C and by 65% at 950°C. Additionally, the net section failure stress decreased by 50% when the temperature was increased from 23°C to 950°C. These tests concluded that the material was highly notch sensitive. In 2000, John et al [17–19] investigated the fracture behavior of the Nextel 720/aluminosilicate (N720/AS) composite under varying loading and temperature conditions. The test specimens had semi-circular [DEH(T)] and sharp [DE(T)] double-edge notches with notch lengths in excess of 1 mm. The results showed that the material was only slightly notch sensitive under monotonic and sustained tensile loading at temperatures below 1000°C. However, notch sensitivity increased significantly at higher temperatures (≥ 1100°C) for the same loading conditions. John et al also determined that the increase in notch sensitivity was independent of the initial stress concentration at the notch tip as the creep-rupture behavior of the specimens with a semi-circular notch was similar to that of the specimens with a sharp notch. Conversely, Mall and Sullivan [20] reported in 2011 that the N720/A composite, with a machined single center circular hole of 4.0 mm in diameter, was notch insensitive under monotonic tension, tensile creep and tension-tension fatigue loading conditions at 1200°C. They reported that the presence of the hole only reduced the UTS by 5%, and had no effect on the fatigue life/strength when cycled at 1.0 Hz with a stress ratio of 0.05. They attributed this notch insensitivity to the development of localized damage at the minimum cross section of the notched specimen. Optical and SEM images revealed that the specimens fractured as expected, with matrix cracks growing along the weak fiber/matrix interface prior to fracturing in a typical brushy manner.

2.4.2.2 Effusion Holes

Potential applications may require various patterns of smaller effusion holes (0.5 mm in diameter), thus driving the need to better understand the mechanical behavior and damage mechanisms of specimens containing an array of small holes at elevated temperature. Buchanan et al [21] initiated this investigation in 2001, where N720/AS specimens with one, two and five effusion holes oriented perpendicular to the loading axis were subjected to sustained loading conditions at 1100°C in air. The results showed that the presence of the effusion holes had no detrimental effect on the creep behavior of the material. Subsequent studies in 2002 [22] investigated the creep behavior of N720/AS specimens with a different pattern of effusion holes at 982°C and 1200°C in laboratory air. This study compared the results of prior unnotched and large notched studies, with a pattern of 17 twist-drilled or laser-drilled effusion holes, oriented 90° or 20° to the specimen plane. As was the case for specimens with large notches, the tensile strength was relatively insensitive to the presence of effusion holes at 1100°C. Based on the results of creep tests at 1100°C, the authors concluded that the response of the specimens with twist-drilled 90° effusion holes was similar to that of unnotched specimens, whereas the specimens with laser-drilled 20° effusion holes showed significant reduction in creep life (~90%), even at lower stress levels. Considering the similarity between the data obtained for specimens with laser-drilled holes and those containing large notches, the authors speculated that the laser drilling process was generating an “affected” zone close to or larger than the tow size, and recommended that further investigations be made into the technique for drilling effusion holes in these advanced CMCs.

However, no further studies considered the effect of the effusion hole drilling technique until 2018 when Ruggles-Wrenn and Minor [3, 4] investigated the creep behavior of a N720/A composite containing an array of 17 laser-drilled effusion holes at 1200°C in air and in steam. The effusion holes were 0.5 mm in diameter and were oriented 90° to the specimen surface. Monotonic tension tests at 1200°C revealed a 19% reduction in tensile strength and 23% reduction in modulus of elasticity due to the presence of holes. Considering that the composite is designed to rely on a porous matrix for its damage tolerant behavior, the authors did not expect such a dramatic degradation in tensile properties. They suspected that the laser-drilled holes were likely the cause for the degraded properties. Furthermore, the specimens with the effusion holes displayed a significant reduction in creep resistance for creep stresses in the 27-141 MPa range. Creep run-out of 100 h was reached at 38 MPa in air and at 27 MPa in steam, compared to 80 MPa and ~70 MPa, respectively, for the unnotched specimens (a reduction in creep run-out stress of over 50%). Following 100 h of creep at 38 MPa in air, the specimen retained ~90% of its tensile strength and 93% of its modulus. These results are similar to those obtained for the unnotched specimens that retained 90% of their strength and 85% of their modulus after 100 h of creep at 80 MPa in air. These observations further support the assumption that the laser-drilled holes caused the reduction in tensile properties, not the prior creep. Following 100 h of creep at 27 MPa in steam, the specimen tested retained 65% of its tensile strength, and 91% of its modulus, confirming that steam is a more damaging environment. Additionally, for creep stresses > 75 MPa, creep lifetimes were reduced by over 90% in both air and steam environments due to the laser-drilled effusion holes. A closer look at the composite microstructure with an optical

microscope and SEM showed that a glassy phase had formed around the holes. The presence of a glassy phase indicated that silicon had been leached from the mullite in the N720 fibers, and had fused the fibers and matrix together in the vicinity of the holes. This mullite depletion in the N720 fibers and associated loss of matrix porosity were determined to be the primary cause for the reduced tensile properties and degraded creep resistance. The microstructural damage was attributed to the intense localized heat that occurred during the laser drilling process. A different method of fabricating holes had to be considered.

The present effort investigates the behavior of N720/A containing an array of 17 small diamond-drilled effusion holes, oriented 90° to the specimen surface, under monotonic tension and creep loading conditions at 1200°C in air and steam.

Chapter 3: Experimental Setup

3.1 Specimen Preparation

The material evaluated in this research effort was Nextel 720/Alumina (N720/A) ceramic composite. This oxide/oxide CMC was fabricated by ATK-COIC (San Diego, CA) and consists of a porous alumina matrix reinforced with Nextel 720 fibers woven in an eight-harness satin weave (8HSW) pattern. The panel provided was comprised of 12 0/90 woven plies, and had an average thickness of 2.88 mm. The AFIT machine shop utilized a water-cooled diamond saw to cut the panels into standard dog-bone shaped specimens according to the dimensions shown in Figure 6**.**

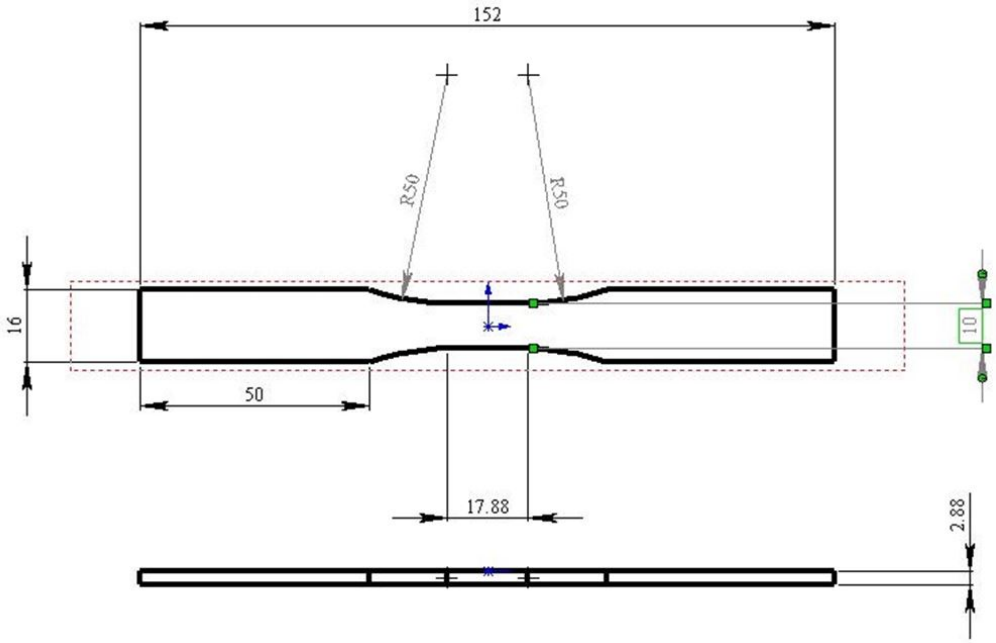

Figure 6: Drawing of test specimen geometry (dimensions in mm)

Furthermore, in order to assess the effect of an array of effusion holes on the creep response of the N720/A composite, the AFIT machine shop also diamond-drilled 17

holes in the gage section of each specimen, per the defined pattern shown in Figure 7. The holes were 0.5 mm in diameter, and were oriented 90° to the specimen surface.

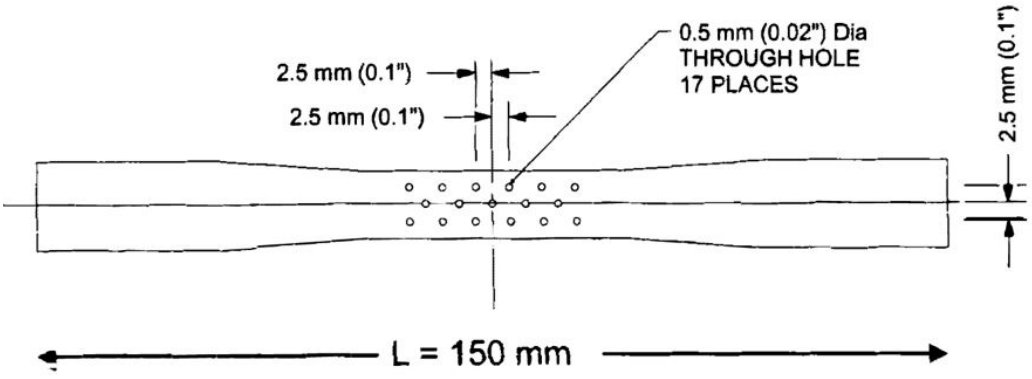

Figure 7: Drawing of effusion hole geometry

Upon receipt of the dog-bone shaped test specimens with an array of 17 diamond-drilled effusion holes, each specimen was measured with Mitutoyo Corporation Digital Calipers. Width and thickness dimensions were averaged over five measurements, and a cross-sectional area was calculated. In order to account for the material lost due to the presence of the holes, an "effective" cross-sectional area was calculated. This was accomplished by multiplying the previously calculated cross-sectional area by a specified gage length (i.e., calculating the volume without holes), subtracting the volume of 17, 0.5 mm diameter holes (i.e., calculating the effective volume), then dividing by the same gage length (i.e., calculating the effective cross-sectional area). These values are summarized in Table 4.

Table 4: Specimen Dimensions and Area Calculations

Specimen ID	Width (mm)	Thickness (mm)	Cross-Sectional Area without holes (mm^2)	Effective Cross-Sectional Area (mm^2)
1	10.138	2.81	28.488	27.963
2	10.094	2.812	28.384	27.859
3	10.092	2.832	28.581	28.052
4	10.116	2.828	28.608	28.080
5	10.096	2.818	28.451	27.924
6	10.128	2.864	29.007	28.472
7	10.1	2.84	28.684	28.154
8	10.114	2.806	28.380	27.856
9	10.07	2.842	28.619	28.088
10	10.106	2.814	28.438	27.913
11	10.072	2.786	28.061	27.540
12	10.074	2.804	28.247	27.724
13	10.018	2.764	27.690	27.174
14	10.082	2.738	27.605	27.093

The final step in preparing the specimens for testing was to attach 1/16-inch thick fiberglass tabs to the gripping ends of each specimen. The tabs were bonded using M-Bond 200 adhesive, and served to protect the specimen surface from the pressure applied by the hydraulic wedge grips during testing. Figure 8 shows a specimen, ready for testing.

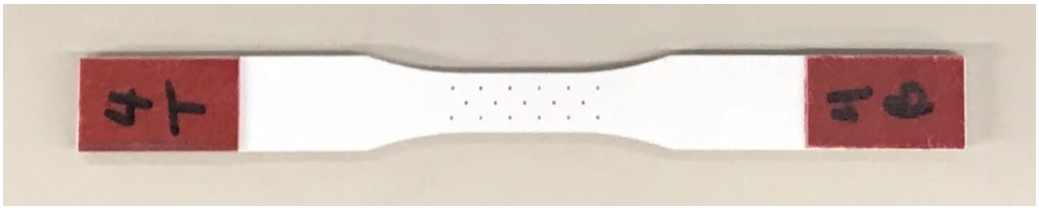

Figure 8: Specimen ready for testing

3.2 Test Equipment

3.2.1 Mechanical Testing Equipment

All experiments were performed using a vertically actuated, servo-controlled Material Test System (MTS, model 810), and an MTS Flex Test 40 digital controller.

The tests were programmed and executed in the MTS System Software (Multi-Purpose Testware/MPT), and the digital controller generated the input signals and stored the test data. The MTS machine had a load capacity of 25 kN (5.5-kip), which was measured using an MTS Force Transducer (Model 661.19E-04). An internal LVDT was used to measure displacement changes, and a high temperature, low contact force extensometer (Model 632.53E-14) was used to measure strain. The specimen was mounted in the MTS machine with hydraulic wedge grips (series 647) at a grip pressure of 8 MPa. The grip wedges were coated with Surfalloy and were water-cooled using a NESLAB RTE 7 chiller that continually circulated water at a temperature of 15°C.

3.2.2 Environmental Controls

A temperature of 1200°C was maintained for all tests using a compact, dual zone AMTECO hot-rail furnace system (Figure 9) controlled by two MTS (Model 409.83) Temperature Controllers (Figure 10).

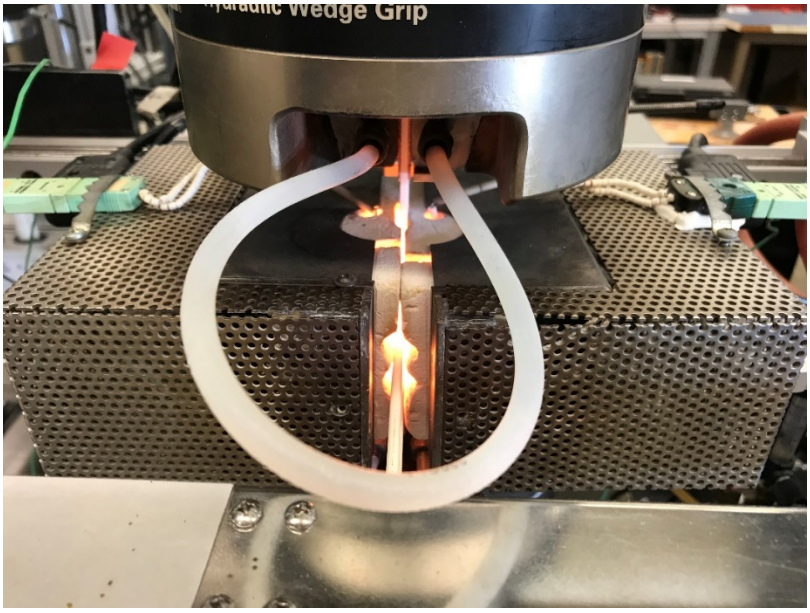

Figure 9: Dual zone AMTECO hot-rail furnace system

Figure 10: MTS Temperature Controllers

Each half of the furnace contained two heating elements and was separately insulated with alumina in order to minimize heat loss. The temperature inside the insulated chamber was measured by two R-type control thermocouples (Figure 11) which provided the necessary feedback to the Temperature Controllers.

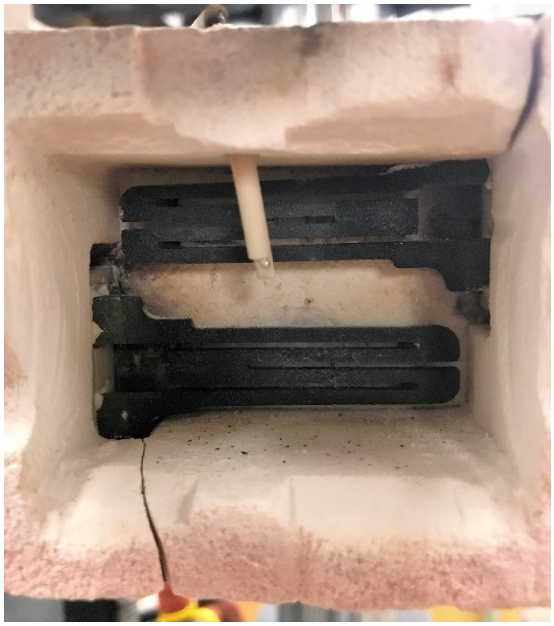

Figure 11: Interior view of insulated furnace with heating elements and control thermocouple

In order to produce a near 100% steam environment, an alumina susceptor was specifically designed to house the gage section of the specimen while providing an opening for a steam feeding tube and slots for the two extensometer extension rods (Figure 12). Steam was provided to the susceptor from an AMTECO HRFS-STMGEN steam generation system (Figure 13) in a continuous flow at a rate sufficient to displace the dry air and create a near 100% steam environment around the specimen gage section.

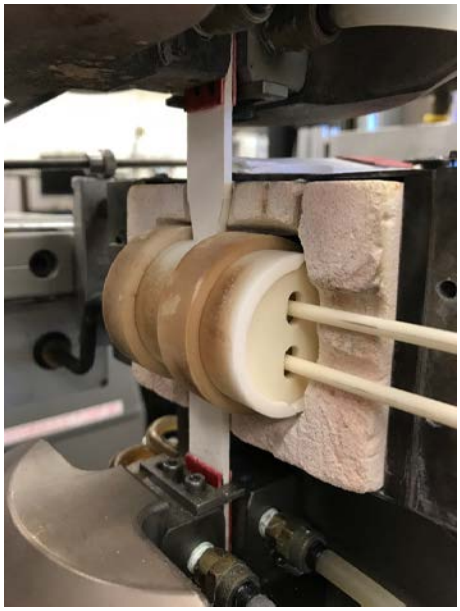

Figure 12: Alumina susceptor

Figure 13: AMTECO steam generation system

Figure 14 captures most of the fully assembled test set-up. Shown in Figure 14 are the Force Transducer, the water-cooled hydraulic wedge grips, the dual zone furnace system, the two R-type control thermocouples, and the high temperature extensometer.

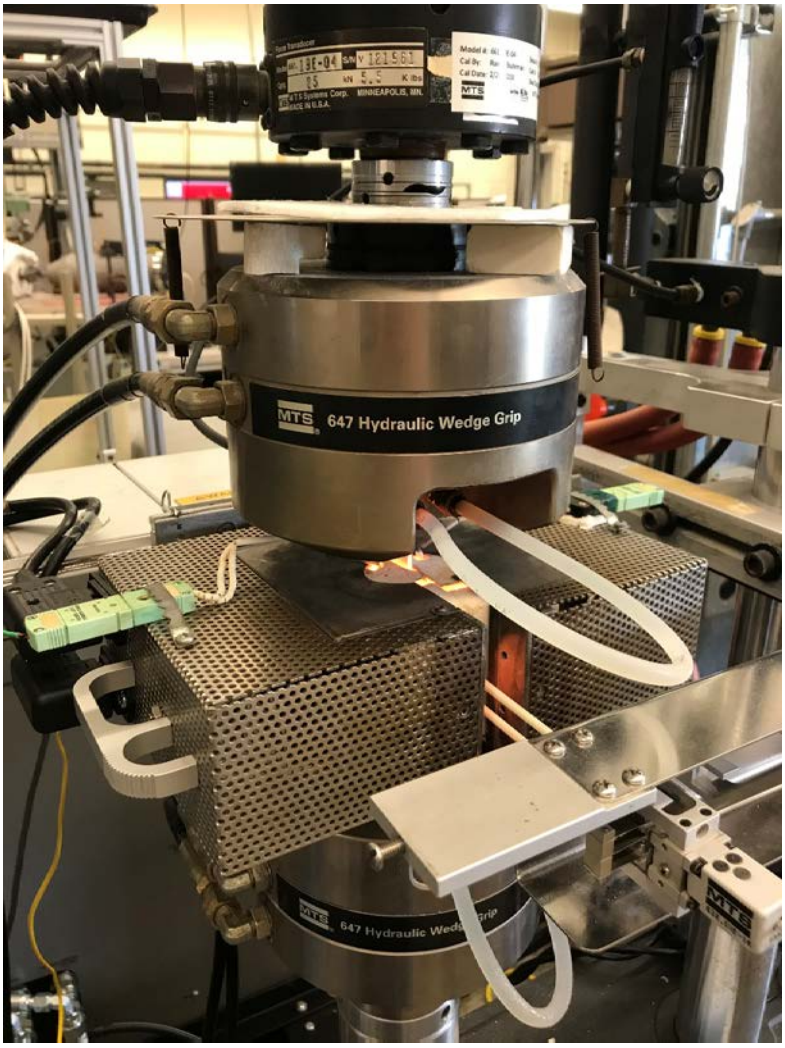

Figure 14: Fully assembled MTS set-up

3.2.3 Microstructural Characterization

A ZEISS SteREO Discovery.V12 optical microscope (Figure 15), equipped with an AxioCam HRc digital camera and AxioVision software (version 4.8) was used before and after testing to examine the microstructure surrounding a few randomly selected holes as well as the post-test fracture surfaces.

Figure 15: ZEISS optical microscope

A Nikon XT H 225 ST Computed Tomography (CT) scanner (Figure 16) was used to examine specimens after testing to provide additional insight into interior damage zone penetration that may not be captured via optical microscopy.

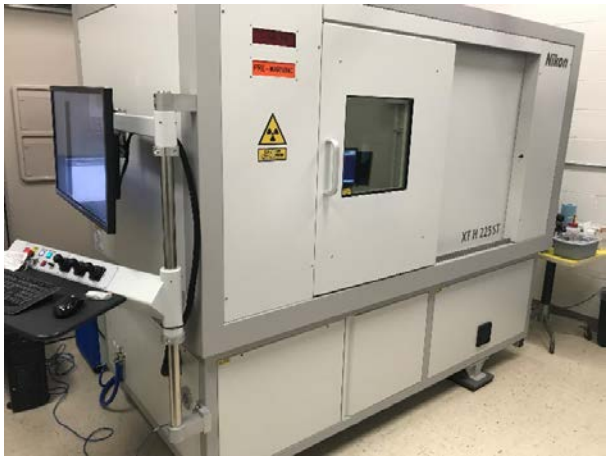

Figure 16: Nikon CT scanner

A Quanta FEG 650 (Figure 17) and MAIA3 Triglav TESCAN SEM (Figure 18) were used to further characterize the microstructure of the material by examining the fracture surfaces. Unlike the optical microscope, the SEM can achieve a resolution on

the order of nanometers; however, the specimen must have conductive properties for a clear image to be collected. Considering that the N720/A constituents are both poor conductors, an EMS Quorum sputtering machine (Figure 19) was used to coat the fracture surfaces with a gold-palladium (Au-Pd) alloy prior to SEM examination.

Figure 17: Quanta FEG SEM

Figure 18: MAIA3 TESCAN SEM

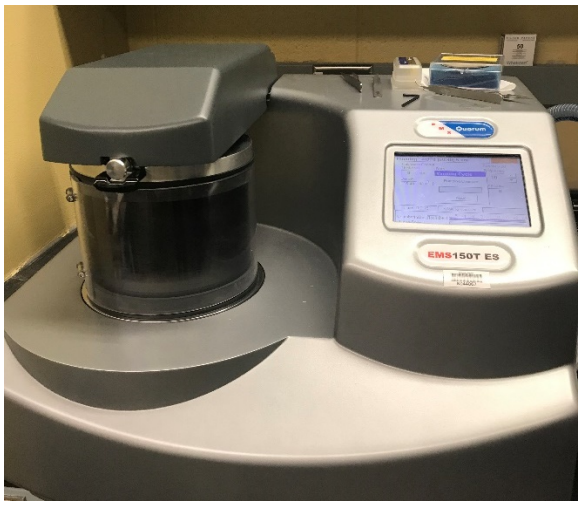

Figure 19: EMS Quorum sputtering machine

3.3 Test Procedures

3.3.1 Temperature Calibration

For this research, it was important that each specimen be tested at a temperature of 1200°C. However, considering that the design of the alumina susceptor prevented the use of thermocouples to verify this temperature during a test, a temperature calibration procedure was utilized as a means to establish set points for the MTS Temperature Controllers. This temperature calibration procedure was performed in force control under zero load, with a temperature calibration specimen instrumented with 2 R-type thermocouples that were fed through the extensometer holes in the susceptor. The thermocouples were attached to both sides of the specimen gage section by two small pieces of alumina and stripped thermocouple wire (Figure 20).

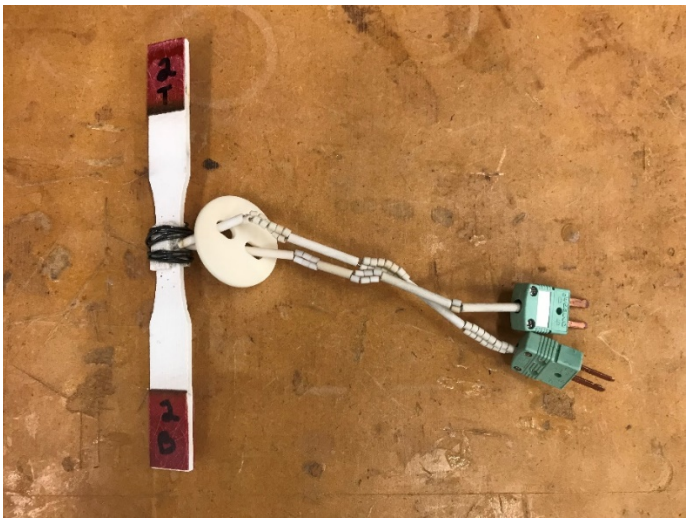

Figure 20: Temperature calibration specimen instrumented with two thermocouples

Once the temperature calibration specimen was mounted in the MTS machine, the thermocouples were connected to an Omega HH501BR handheld type R thermometer for readout. Manual commands were sent to the MTS Temperature Controllers and temperature readings were recorded. This process continued slowly until the temperature of the specimen surface reached 1200°C. The value of the commanded temperatures necessary to reach this target test temperature are called set points, and these values were programmed into the procedures used for all tests. Table 5 summarizes the MTS Temperature Controller set points obtained for testing at 1200°C in air and in steam.

Table 5: MTS Temperature Controller Set Points (°C)

	Left	Right
Air	1283	1275
Steam	1275	1269

3.3.2 Preparation of Mechanical Testing Equipment

Prior to each test, multiple steps were required in order to prepare the equipment and specimen. These steps included inspecting the equipment, warming up the MTS hydraulics, turning on the chiller and steam generation system, and assembling and

mounting the specimen. The first checks always involved a thorough inspection of the four heating elements to ensure no oxidation was present, and a scrub of the wedge grips with a wire brush to clear the surface of any residual dust from previous tests. The hydraulics were warmed up using the MTS Function Generator application, which cycled the actuator in displacement control at 0.1 Hz. Typical duration for this warm-up was 10-15 minutes, after which it was manually stopped. The water level within the chiller was checked prior to each test; the chiller was refilled with deionized water if necessary. The chiller was set to circulate water at 15°C, and took roughly 10 minutes to stabilize at this temperature after being turned on. If steam was going to be used, the steam generation system took roughly 10 minutes to warm-up after being powered on, and another 15 minutes to produce a stable steam flow after the pump was turned on. The feeding tube would be connected to the pump; however, the pump would not get turned on until just prior to each test.

Following the hydraulic warm-up, the actuator of the MTS would be raised in displacement control to the appropriate mounting height (-81 mm), such that the L-shaped guide pins on both the upper and lower grips could be used to ensure the specimen was mounted vertically and properly centered within the grips. Prior to mounting the specimen, the alumina susceptor would be assembled around the specimen gage section. This assembly would then be mounted in the top grip while still in displacement control, and fully secured with the bottom grips after switching to force control and sending a zero force command. For testing in steam, the steam feeding tube would be inserted into the opening in the rear end cap of the susceptor. The extensometer extension rods would be fed through the openings in the front end cap of the susceptor,

and placed in contact with the specimen. The pressure applied by the extensometer in conjunction with the rough surface of the test material was sufficient to ensure contact between the extensometer and the test specimen was maintained throughout each test. After the extensometer was mounted, the current strain reading was digitally zeroed in the MTS software in order to ensure data acquisition began at zero strain. For testing in steam, the strain would be zeroed prior to turning the steam pump on in order to ensure that the thermal strain data accounted for any strain accumulated during the steam ramp-up period prior to starting a test. After the furnace was closed, final checks included verifying that the chiller reached the desired temperature and was working properly, that the Temperature Controllers were not in an error state, and that the extensometer was still floating free of the mounting bracket.

Prior to initiating a test, the appropriate test procedure would be loaded in the MPT software, and the file path and specimen name for data acquisition would be verified. After the requisite adjustments were made, the procedure was locked, manual control was relinquished, and the procedure was executed. A detailed description of all the steps involved in each test are outlined in the following sections. In all tests, temperature was ramped up to test temperature at a rate of 1°C/s, followed by a 45-minute dwell to allow temperature equilibration.

3.3.3 Monotonic Tensile Test

The purpose of the monotonic tensile test was to measure tensile properties that could be compared to those obtained for unnotched specimens in order to identify the extent of the degradation caused by the diamond-drilled holes. The tension test to failure

was performed in air, and aimed to measure the ultimate tensile strength (UTS), Modulus of Elasticity (E) and failure strain. The tension test was performed in displacement control with a constant displacement rate of 0.05 mm/s. Data was recorded every 0.05 s, and included time, strain, load, displacement and both left and right furnace temperature settings. A screenshot from the MPT software of the procedure used to perform this test is shown in Figure 21.

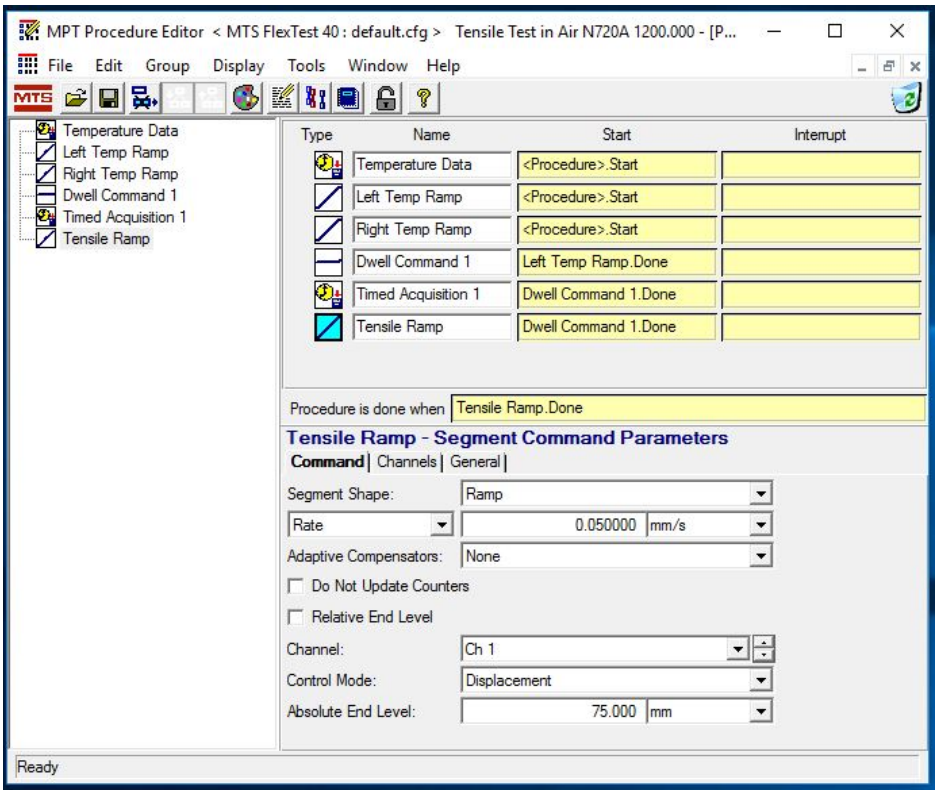

Figure 21: Monotonic tensile test procedure

3.3.4 Creep-Rupture Tests

Creep tests were performed in force control with the load-up to creep stress occurring at a rate of 20 MPa/s. Note that the effective cross-sectional area of each specimen was used to calculate the peak load and loading rate at each creep stress level according to Equations 2 and 3, respectively:

$$\sigma = \frac{P}{A_{eff}} \quad \rightarrow \quad P = \sigma \times A_{eff} \tag{2}$$

$$\dot{\sigma} = \frac{\dot{P}}{A_{eff}} \quad \rightarrow \quad \dot{P} = \dot{\sigma} \times A_{eff} \tag{3}$$

Once the peak force and loading rate were calculated, these values were updated in the "Ramp Stress Up" and "Ramp Stress Down" commands of the Creep Rupture Test procedure (Figure 22).

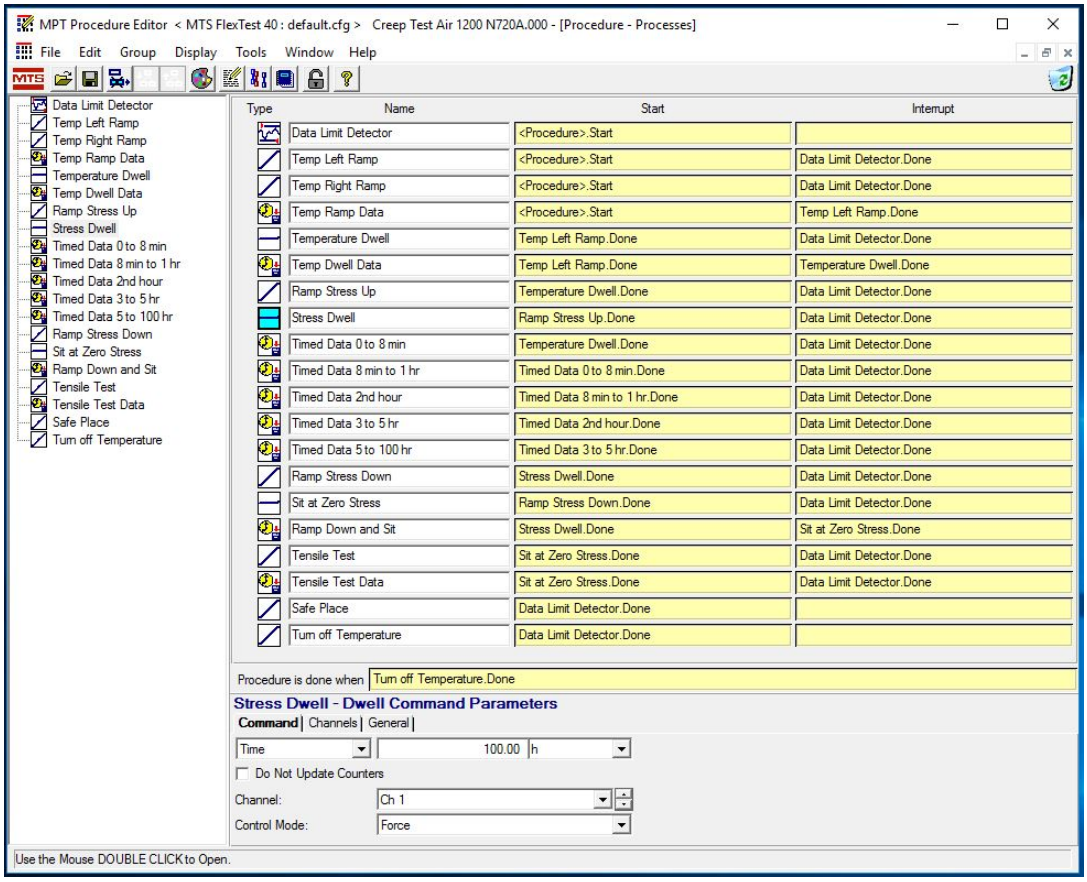

Figure 22: Creep rupture test procedure

As indicated in Figure 22, the procedure starts with a temperature ramp to the previously calculated left and right temperature set points, followed by a 45-minute temperature dwell. Then the stress is ramped up at a rate of 20 MPa/s to the desired

creep stress level. Creep run-out was defined as surviving 100 h at creep stress. If run-out was achieved, the program would automatically unload the specimen at a rate of 20 MPa/s, then perform a tensile test to failure at 0.05 mm/s in order to measure retained properties.

Multiple data acquisition commands were utilized, all of which recorded time, strain, force, displacement, and left/right temperature at varying sample rates: (i) every second during temperature ramp, (ii) every 15 s during temperature dwell, (iii) at 30 Hz during the first 8 min of creep, (iv) at 6.65 Hz during the remainder of the first hour of creep, (v) every 2 s during the second hour of creep, (vi) every 10 s during hours 3-5 of creep, and (vii) every 3 min during hours 5-100 of creep. The data limit detector was always running in the background, and would automatically shut down the testing system and turn off the furnace in the event the displacement or temperature limits were tripped.

3.3.5 Preparation for Microstructural Characterization

Microstructure examination via optical microscopy and CT scan did not require any specimen preparation. These processes are non-invasive, and could take place at any time prior to SEM examination. Steps required for preparing an SEM sample included removing the fiberglass tabs with a water-cooled saw, adding a piece of copper tape along the length of the specimen to ensure conductivity to the base, rigidly mounting the specimen to a 90-degree platform using a conductive carbon adhesive, adding a drop of conductive silver paint between the platform and copper tape as an additional means to ensure conductivity, and sputter coating the specimen with a ~5 nm thick Au-Pd alloy in the sputtering machine. Figure 23 shows a specimen ready for SEM examination.

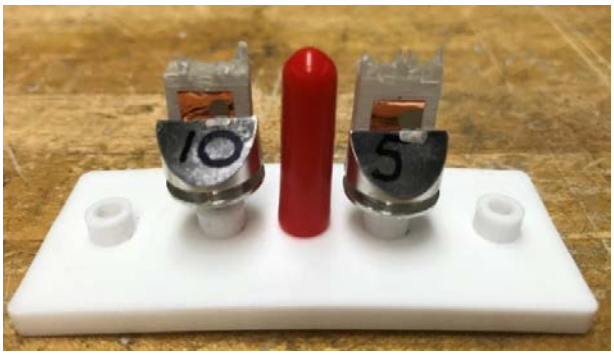

Figure 23: Coated specimen prepared for SEM examination

Chapter 4: Results and Discussion

4.1 Test Summary

The tests carried out during this research effort are summarized in Table 6. Specimens were labeled sequentially, with Specimen 1 and 2 being used for temperature calibration. All tests measured thermal strain during the initial temperature ramp to 1200°C, and those results will be discussed in the following section. Referencing Table 6, the Maximum Stress levels were pre-determined, and the Adjusted Stress levels were calculated based on normalizing the data for a CMC with 44% fiber volume (multiplied the maximum stress by $\frac{44}{38}$). This adjustment was made in order to standardize the results with previous research, therefore enabling direct comparison. The referred to stress level from this point on with be the Adjusted Stress values.

Table 6: Tests Performed on N720/A Specimens with Diamond-Drilled Effusion Holes at 1200°C in Air and in Steam

Specimen ID #	Test Type	Test Environment	Maximum Stress (MPa)	Adjusted Stress (MPa)
3	Tensile	Air	176	204
4	Creep	Air	102	118
5	Creep	Air	81	94
6	Creep	Air	60	69
7	Creep	Air	40	46
8	Creep	Air	130	150
9	Creep	Steam	100	116
10	Creep	Steam	80	93
11	Creep	Steam	130	150
12	Creep	Steam	40	46
13	Creep	Steam	60	69
14	Creep	Steam	100	116

4.2 Thermal Expansion

Thermal strain was measured during the initial temperature ramp and 45-minute dwell at 1200°C in each test. The assumption was made that thermal strain (ε_{th}) was linearly related to temperature change (ΔT) via the following equation:

$$\boldsymbol{\varepsilon_{th} = \alpha * \Delta T} \quad (4)$$

The proportionality constant, α, is the coefficient of linear thermal expansion, and can readily be calculated from measured thermal strain and a known temperature change. Taking 23°C to be the nominal room temperature, ΔT for this effort was 1177°C. Table 7 summarizes the recorded thermal strain and calculated coefficient of thermal expansion for each test specimen.

Table 7: Thermal Strain and Coefficients of Linear Thermal Expansion

Specimen ID #	Test Environment	Thermal Strain (%)	Coefficient of Thermal Expansion (x10-6/°C)
3	Air	0.75	6.372
4	Air	0.7	5.947
5	Air	0.74	6.287
6	Air	0.8	6.797
7	Air	0.775	6.585
8	Air	0.775	6.585
9	Steam	0.7	5.947
10	Steam	0.74	6.287
11	Steam	0.73	6.202
12	Steam	0.75	6.372
13	Steam	0.68	5.777
14	Steam	0.65	5.523
		Average	6.223

While the average coefficient of thermal expansion in Table 7 is lower than the average values previously reported for unnotched specimens [23–25], it is consistent with both the average value of 5.885 x10^{-6} 1/°C recently reported by Minor for specimens

containing an array of laser-drilled holes [3], and with the value of 6.0 $x10^{-6}$ 1/°C currently reported by the N720/A manufacturer [26]. Harlan [23], Mehrman [24] and Hetrick [25] reported thermal expansion coefficients for unnotched N720/A specimens as 7.2 $x10^{-6}$, 7.66 $x10^{-6}$ and 7.57 $x10^{-6}$ 1/°C. Notably, these unnotched specimens were all cut from the same batch of panels manufactured in 2005. With ~10 years separating the work carried out by Harlan, Mehrman and Hetrick from the research effort carried out by Minor in 2018 and the current work, it is likely that basic material properties have changed slightly as processing techniques have been refined.

4.3 Monotonic Tensile Test

A tensile test to failure was performed at 1200°C in laboratory air in order to assess the effect of an array of diamond-drilled effusion holes on the tensile properties of N720/A. For comparison purposes, Table 8 shows tensile properties for unnotched N720/A specimens at 1200°C, reported by Harlan in 2005 [23], Mehrman et al. in 2007 [12], Minor et al. in 2018 [4] and ATK-COIC [26]. As can be seen from this data, there is a known variation between properties as a result of improvements in manufacturing brought on by scale up, automation, and experience over the past decade. Due to the recent nature of the research performed by Minor et al. [4], these data will be referenced for comparing with current results.

Table 8: Tensile Properties for Unnotched N720/A Specimens at 1200°C in Air

Data Source	UTS (MPa)	E (GPa)	ε_f (%)
Harlan [23]	192	75	0.38
Mehrman et al. [12]	190	76	0.38
Minor et al. [4]	203	67	0.40
ATK-COIC [26]	224	69	0.44

Tensile properties obtained for N720/A specimens containing an array of 17 effusion holes are summarized in Table 9.

Table 9: Notched Tensile Properties for N720/A at 1200°C

Data Source	Hole Fabrication Method	UTS (MPa)	E (GPa)	ε_f (%)
Minor et al. [4]	Laser Drilling	165	51.9	0.38
Current effort	Diamond Drilling	204	70.9	0.42

Minor et al. [4] reported that the presence of laser-drilled holes reduced the UTS by ~19% and elastic modulus by ~23%. Conversely, the presence of 17 diamond-drilled holes has little effect on the tensile properties of N720/A. Assuming that diamond drilling does not negatively affect the composite microstructure in the vicinity of the holes, this result was not unexpected as this oxide-oxide CMC gains its damage tolerance from its porous matrix. If adding the holes simply increased the overall porosity of the specimen, the damage tolerance of the CMC should remain relatively unaffected. In the case of the laser-drilled holes, however, it was determined that the heat from the lasers did affect the microstructure by both decomposing the mullite in the N720 fibers and increasing the sintering of the alumina matrix in the vicinity of the holes. The deterioration of tensile properties of the N720/A specimens with laser-drilled holes was attributed to these microstructural changes caused by the laser drilling. A review of the composite microstructure of the diamond-drilled specimens via optical microscopy and SEM will be discussed in a later section.

4.4 Creep-Rupture Tests at 1200°C

Creep tests were performed at stress levels of 46, 69, 93, 116 and 150 MPa in both air and steam (adjusted for a V_f of 0.44% from 40, 60, 80, 100 and 130 MPa stress levels

at a V_f of 0.38%). It should be noted that results obtained from the 150 MPa creep tests in both air and steam environments have been omitted from the consolidated data below and will be addressed separately in section 4.4.3 when discussing creep strain rates.

4.4.1 Creep Strain vs Time Curves

Results of the creep-rupture tests in air and steam environments for N720/A specimens containing an array of diamond-drilled (DD) holes are presented in Figure 24 and Table 10.

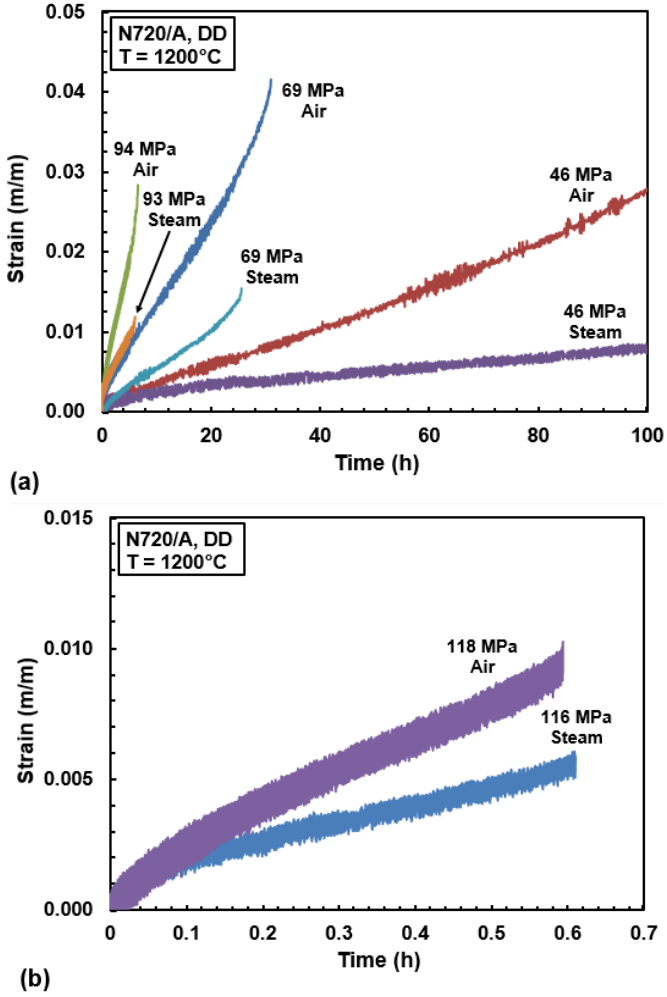

Figure 24: Creep strain vs time curves obtained for N720/A specimens with an array of diamond-drilled holes in air and steam at 1200°C: (a) time scale selected to show results obtained at 46-94 MPa, and (b) time scale selected to show creep curves obtained at higher creep stresses

Table 10: Rupture Time and Strain at Failure Results

	Time to Rupture (h)				Creep Strain at Failure (%)		
Creep Stress (MPa)	Air	Steam	Air/Steam	Life Reduction (%) Due to Steam	Air	Steam	Air/Steam
46	100	100			2.78	0.78	
69	30.95	25.55	1.21	-17.45	4.1	1.5	2.73
93	6.55	6.05	1.08	-7.63	2.8	1.15	2.43
116	0.59	0.61	0.97	3.39	0.95	0.55	1.73
116	0.59	0.48	1.23	-18.64	0.95	0.94	1.01

Notable observations include similar creep lifetimes for all air and steam tests at a given stress level, as well as consistently larger creep strains at failure for all air tests, relative to steam tests at the same stress level. In calculating the percentage of life reduction and air to steam ratios for both rupture time and creep strain at failure, data points were not included for the two tests that reached run-out as final rupture time and creep strain values are unknown. These ratios would not provide the most accurate information when assessing the materials performance in air versus steam. That said, the average reduction in creep lifetime due to steam, for N720/A specimens with DD holes, is approximately 10%. Moreover, specimens tested in air accrued on average 1.98 times more strain at failure than specimens tested in steam. Compared to data reported by RW et al. in 2006 [11], Mehrmen et al. in 2007 [12], and RW et al. in 2008 [14], steam reduced unnotched N720/A lifetimes by an average of ~92%, and final strain for those specimens that reached failure was an average of 1.32 times more in air than steam. For specimens with laser-drilled (LD) holes, data reported by Minor et al. [4] indicate that steam reduced lifetimes by an average of 85%, with air tests accruing an average of 2.18 times more strain at failure than tests performed in steam. Furthermore, it should be noted that for all stress levels below 70% of each configurations UTS, data confirms that

all specimens accrued more creep strain at failure in both air and steam tests than that seen in each of their respective tensile tests. These results suggest that steam is least degrading to the DD configuration in terms of creep lifetimes, and that all tests that reach failure, regardless of configuration, will accrue more strain in an air environment.

At this point, it's also important to recognize that both steam as well as the presence of holes are degrading to the creep resistance of N720/A. Unnotched results attributed the reduced damage tolerance in steam to the increase in matrix sintering, whereas the LD results attributed both matrix sintering and microstructural damage caused by the laser drilling as contributing factors. Initial observations from the DD results suggest that the presence of holes is more degrading to the creep resistance of this CMC than the presence of steam.

Additional observations can be made by comparing DD and LD creep curves in both air and steam environments (Figure 25 and 26, respectively). Considering the differences in creep stress levels employed in the two research efforts, direct comparisons cannot be made; however, trends can be noted. Referencing Figure 25 for all air tests, it can be seen that DD specimens accumulate more creep strain and produce longer creep lifetimes than LD specimens at similar creep stresses. The figure also suggests that creep strain increases with decreasing stress (until run-out is achieved) for both LD and DD specimens. Furthermore, it appears that all creep curves display primary and secondary regimes, with the transition to secondary creep occurring within the first two hours of each test. For the DD specimens, tertiary creep is seen at creep levels below 94 MPa (~46% UTS). For the LD specimens, tertiary creep is observed at creep levels below 75-84 MPa (~45-50% UTS). This transition to tertiary creep marks the initiation of the

failure process, which for this oxide-oxide CMC, represents the beginning of crack and void formations.

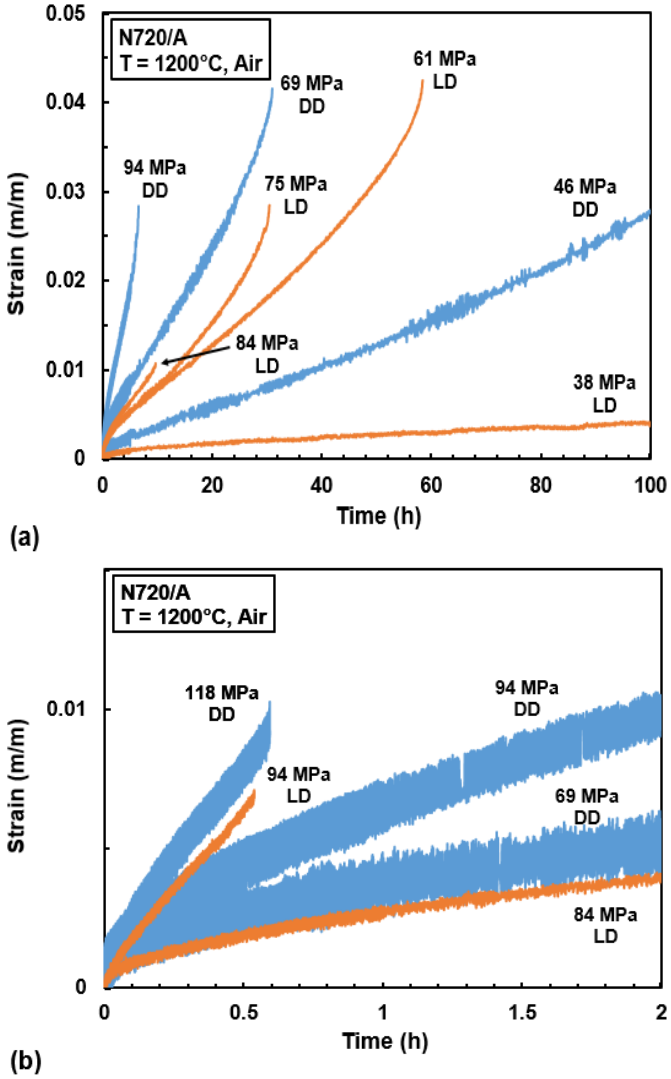

Figure 25: Creep strain vs time curves obtained for N720/A specimens with diamond-drilled and laser-drilled holes in air at 1200°C: (a) time scale selected to show creep curves obtained at 38-94 MPa, and (b) time scale selected to show creep curves obtained at higher creep stresses

Similarly, referencing Figure 26 for all steam tests, it can be seen that DD specimens produce longer creep lifetimes and accumulate more creep strain than LD specimens at similar stress levels. Note that steam did not change the appearance of the creep curves. Primary and secondary creep regimes are still observed in all tests, with the

transition from primary to secondary creep occurring early in creep lifetimes. Tertiary creep is observed in some tests.

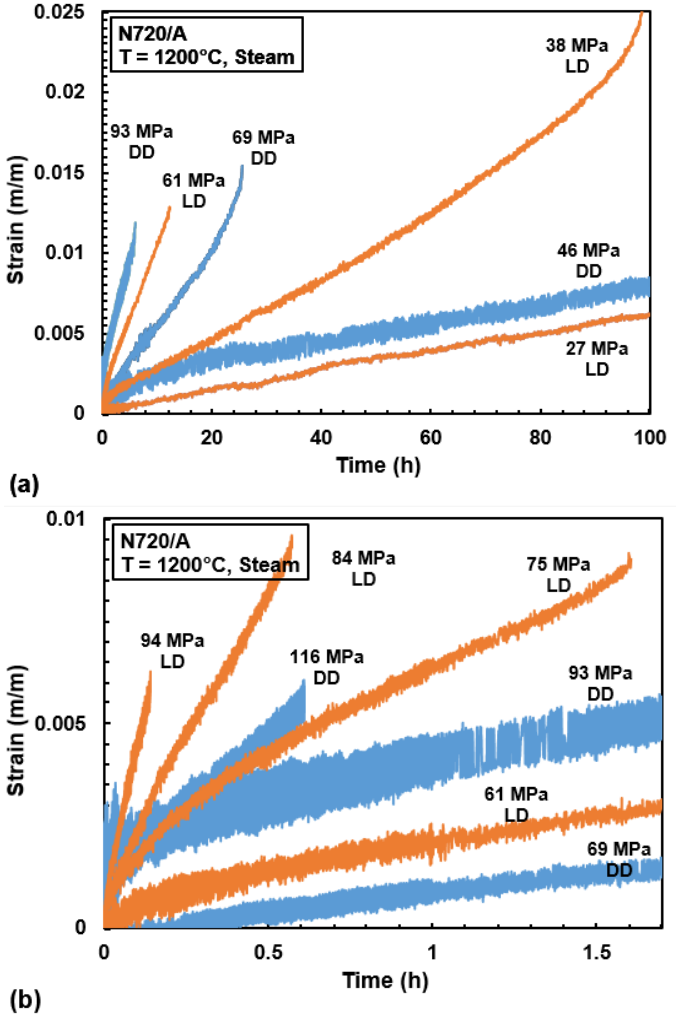

Figure 26: Creep strain vs time curves obtained for N720/A specimens with diamond-drilled and laser-drilled holes in steam at 1200°C: (a) time scale selected to show results obtained at 27-93 MPa, and (b) time scale selected to show creep curves obtained at higher creep stresses

Recognizing that the amount of strain accumulation differed significantly between the two environments for all specimen configurations, it is important to understand the various damage mechanisms that could be contributing to this phenomenon. Strain accumulated in a creep test is a result of (1) creep deformation of the intact constituents under constant load, and (2) damage accumulation as a result of fiber failures or

increased matrix cracking, leading to a redistribution of the load between the remaining intact constituents. All of these damage mechanisms play a role in the failure of N720/A, and it's difficult to know which mechanism is dominant in each environment. Similar to both the unnotched and LD results, the lower creep strains at failure for the DD specimens in steam suggests that matrix sintering is still present. A dense matrix produces sharp crack tips at any geometric discontinuity (i.e., fibers or holes), which results in a higher stress concentration than that produced by porous matrix cracks that reach the fiber surface in pores [8]. This higher stress concentration results in fiber failure instead of a crack being deflected around the fiber, ultimately producing less overall strain at failure. Optical microscopy and SEM micrographs sought to explore this assumption, and those results will be discussed in a later section.

4.4.2 Stress vs Rupture Time

Stress-rupture results obtained for the N720/A specimens with DD holes at 1200°C in air and in steam are presented in Figure 27. Considering that DD specimens produced similar creep lifetimes in air and in steam, the standalone plot in Figure 27 does not identify much degradation due to steam. This depicts the earlier finding that steam degraded creep lifetimes by only 10%, and suggests that all degraded properties, relative to unnotched specimens, are due to the presence of DD holes. Note, data points for the 150 MPa creep tests in air and steam have been included for comparison purposes, but have not been incorporated into any of the trendlines.

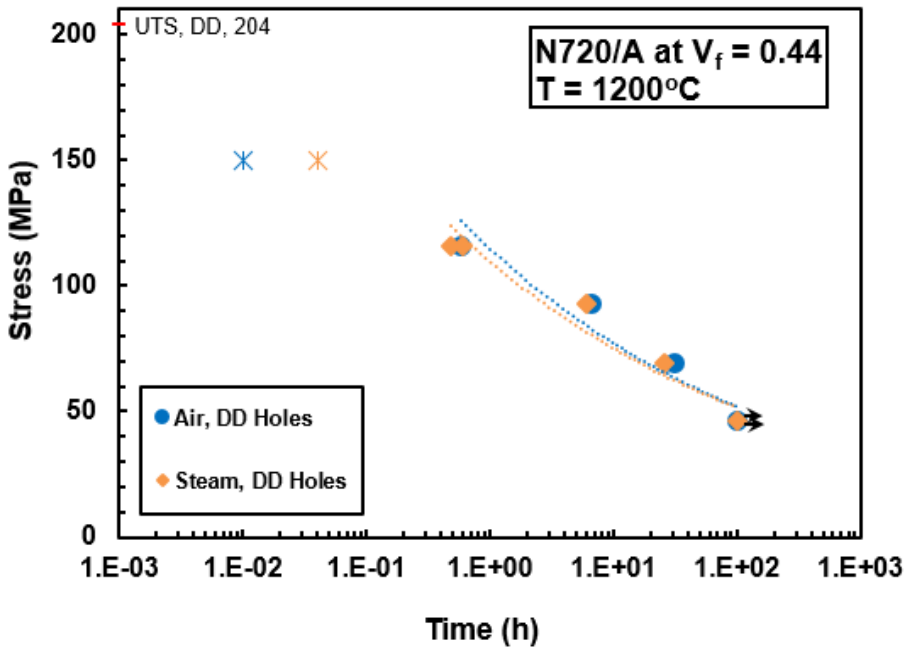

Figure 27: Creep stress vs time to rupture for N720/A specimens with diamond-drilled holes in air and steam at 1200°C

Alternatively, the DD data can be compared to both unnotched and LD results to identify trends between the different configurations. Figure 28 consolidates the stress (in both MPa and % UTS) versus rupture time for unnotched, LD and DD specimens tested in creep at 1200°C in air. Note that creep run-out of 100 h was achieved by the unnotched specimens at 80 MPa (39% UTS), by the LD specimens at 38 MPa (23% UTS) and by the DD specimens at 46 MPa (22% UTS). The creep run-out stresses for both LD and DD specimens decreased by ~50% in air relative to the unnotched specimens, suggesting that this degradation in creep resistance is purely due to the presence of holes. Additionally, the data suggests that both LD and DD holes reduce creep lifetimes in air by >90% relative to unnotched specimens.

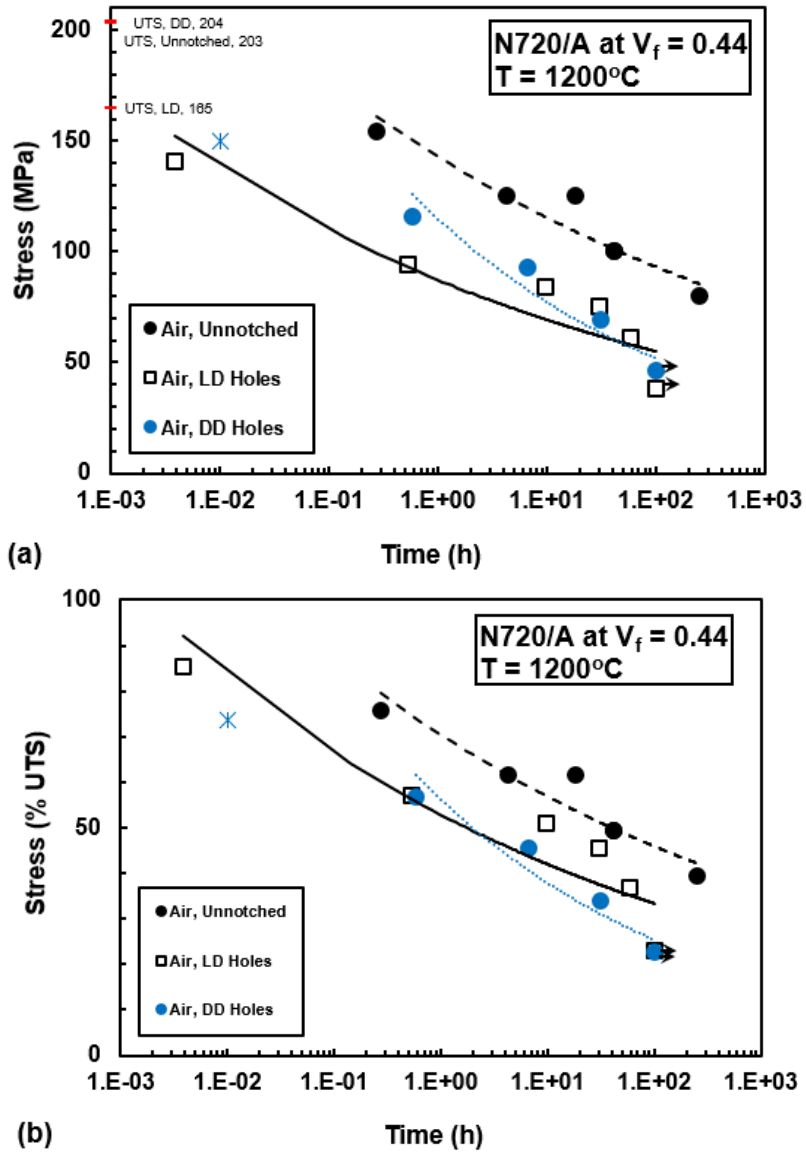

Figure 28: Creep stress vs time to rupture for unnotched, laser-drilled and diamond-drilled N720/A specimens in air at 1200ºC: (a) stress in MPa, and (b) stress in % UTS

In order to make similar comparisons for the steam data, an extrapolation was necessary to estimate the run-out stress for unnotched specimens in steam. Referencing Figure 29, it can be estimated that run-out would be achieved at ~73 MPa (36% UTS). Note that creep run-out was achieved by LD specimens at 27 MPa (16% UTS) and DD specimens at 46 MPa (22% UTS). Therefore, it appears that at 1200°C in steam, the

presence of holes decreased creep run-out stress by 63% for LD holes and by 37% for DD holes. This confirms an earlier observation that steam is least degrading to specimens with DD holes.

Within the steam environment, the data suggests that LD holes are just as degrading to creep lifetimes as they are in air (>90%); however, DD holes are less degrading. For stresses ≤ 50% UTS, the presence of DD holes reduces creep lifetimes in steam by an average of 67%; however, for stresses > 50% UTS, the presence of DD holes has little effect on creep lifetimes. In fact, when referencing the % UTS plot below, it appears that specimens with DD holes actually perform similar to unnotched specimens at stresses over 45% UTS in steam. This observation further supports the assumption that the presence of DD holes is more degrading to the creep resistance of this CMC than the presence of steam. Finally, relative to LD holes in a steam environment, DD holes significantly improve creep lifetimes; extrapolated results suggest an average ratio of DD to LD lifetimes of ~11.

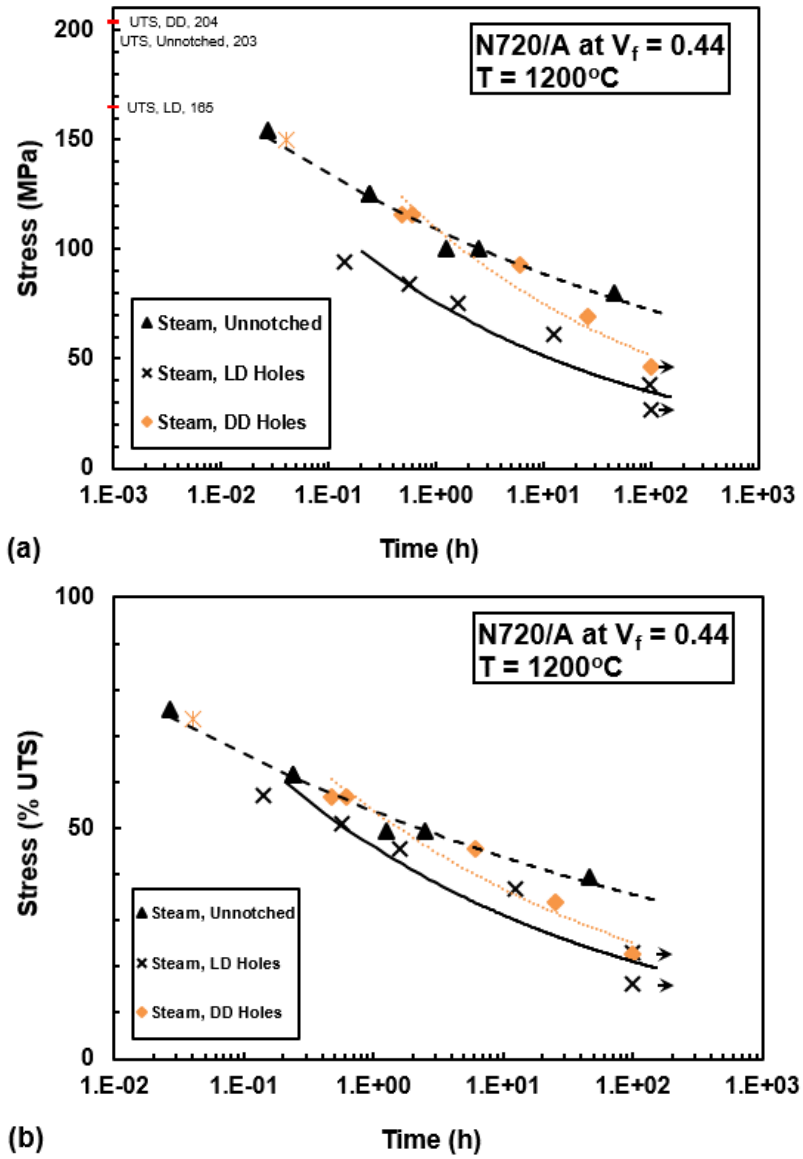

Figure 29: Creep stress vs time to rupture for unnotched, laser-drilled and diamond-drilled N720/A specimens in steam at 1200°C: (a) stress in MPa, and (b) stress in % UTS

4.4.3 Minimum Creep Strain Rates

Minimum creep rates were achieved in all tests performed on DD specimens, and are summarized in Table 11. Figure 30 plots the minimum creep rates as a function of creep stress.

Table 11: Summary of Minimum Creep Strain Rates Obtained for N720/A Specimens with Diamond-Drilled Holes at 1200ºC in Air and in Steam

Creep Stress (MPa)	Tests in Air Creep Rate (1/s)	Tests in Steam Creep Rate (1/s)	Air/Steam
46	6.564E-08	1.617E-08	0.25
69	2.79E-07	1.23E-07	0.44
93	8.47E-07	3.18E-07	0.38
116	3.34E-06	1.68E-06	0.50
116	3.34E-06	2.95E-06	0.88
150	8.83E-05	1.49E-05	0.17

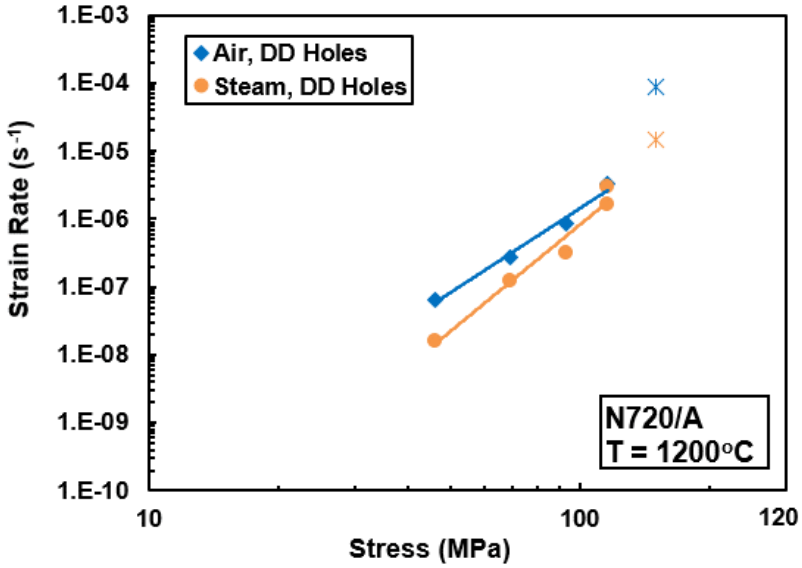

Figure 30: Minimum creep rate vs creep stress for N720/A specimens with diamond-drilled holes tested in air and in steam at 1200ºC

Notable observations include consistently faster strain rates in air, relative to steam, as well as increasing strain rates with increasing applied stress. Additionally, with the exception of the data produced in the 150 MPa creep tests, it appears that the strain rates obtained in the two environments were progressively getting closer in magnitude as the applied stress increased.

As a brief aside, note that the creep rates obtained in the 150 MPa tests in air and steam are considerably higher than that predicted by the trendline from the creep rates obtained at 46-116 MPa. This discrepancy was significant enough to warrant additional

investigation. Specifically, it was unclear whether the deformation produced in the 150 MPa tests was due to creep or progressive failures of the load-bearing fibers. Figure 31 overlays the strain vs time data from the tensile test in air, with the 150 MPa creep tests performed in air and steam. Results in this plot demonstrate that the strain rates produced during load-up to creep stress in each of the creep tests is close to the strain rate produced in the tension test. Once the target creep stress level is achieved, the strain rates observed in the creep tests decelerate. However, the strain rates from the creep data are closer in magnitude to the tensile test strain rate ($\sim 5.0x^{-4}\ s^{-1}$) than to the previously mentioned creep test strain rates. Additionally, the plot clearly shows that the strain rate in air is faster than that recorded in steam, which ultimately resulted in more accrued strain and a shorter lifetime. The short duration of the 150 MPa creep tests, as well as the high strain rates, indicate that the deformation and failure in these tests are likely caused by continuously increasing stress due to progressive failures of the individual fibers and increased matrix cracking. It is believed that progressive failures of the individual load-bearing fibers start as soon as the 150 MPa creep stress is reached. After each fiber failure, the load is redistributed to the intact fibers resulting in ever increasing stress. Deformation caused by this continual load redistribution is more representative of a tension test to failure than a creep test, which is why the decision was made to remove the 150 MPa creep test data from the consolidated creep data. .

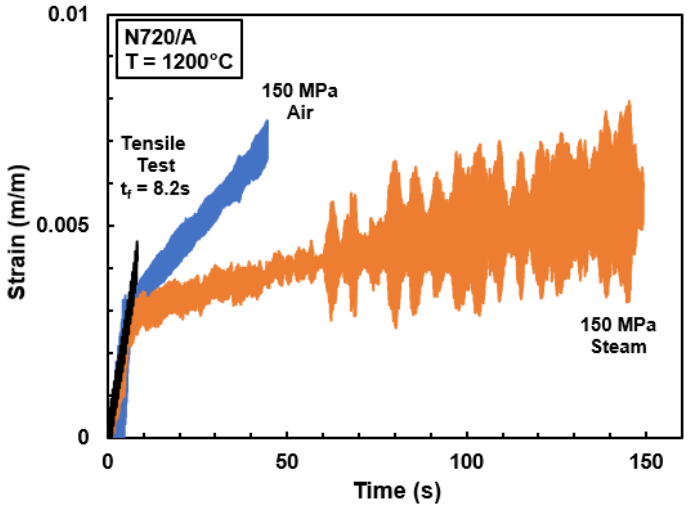

Figure 31: Strain vs time comparison between tension test in air and creep tests at 150 MPa in air and steam for N720/A specimens with diamond-drilled holes at 1200°C

Continuing the minimum creep rate discussion, Figure 32 consolidates DD, LD and unnotched specimen creep rates in air and steam at 1200°C. One obvious difference identified from this comparison is the impact that steam had on the results. For both the unnotched and LD specimens, the presence of steam accelerated the minimum creep strain rates; however, the opposite was true for the DD specimens.

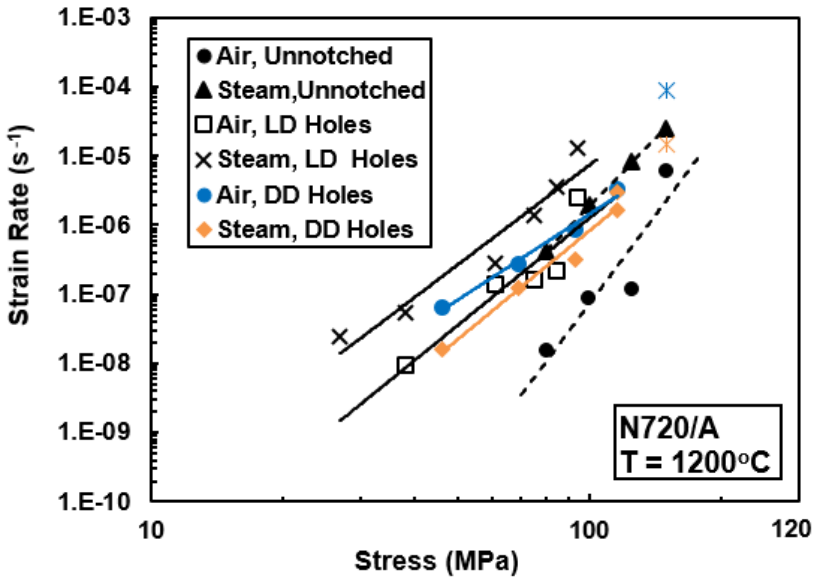

Figure 32: Minimum creep rate vs creep stress for unnotched, laser-drilled and diamond-drilled N720/A specimens tested in air and steam at 1200ºC

A closer examination of the creep rates obtained in air (Figure 33) suggest that the presence of a hole (LD or DD) does accelerate minimum creep rates, but the method of hole fabrication has little influence. However, in a steam environment (Figure 34), the creep rates produced by the DD specimens are similar to those of unnotched specimens. These observations suggest that the dominant damage mechanism at play for the DD specimens is different than the damage mechanisms operating for the unnotched and LD specimens. One possible explanation stems from considerations of matrix porosity. Recall that the N720/A composite relies on a porous matrix for its damage tolerant behavior, and that a minimum porosity is required for this concept to work. If the DD holes did not negatively affect the composite microstructure aside from making the CMC more porous, it could be that there exists an upper porosity limit beyond which the creep resistance of the material begins to degrade. This degradation manifests itself in faster creep strain rates which ultimately reduce creep lifetimes. In this case, the added matrix sintering that is present in a steam environment could potentially return the overall porosity of the DD specimens to acceptable levels. While this explanation may be debated, the data indicates that the presence of steam changes the dominant damage mechanism such that strain rates for DD specimens in steam are not only lower than the strain rates seen in air, but are also in-line with rates reported for unnotched specimens.

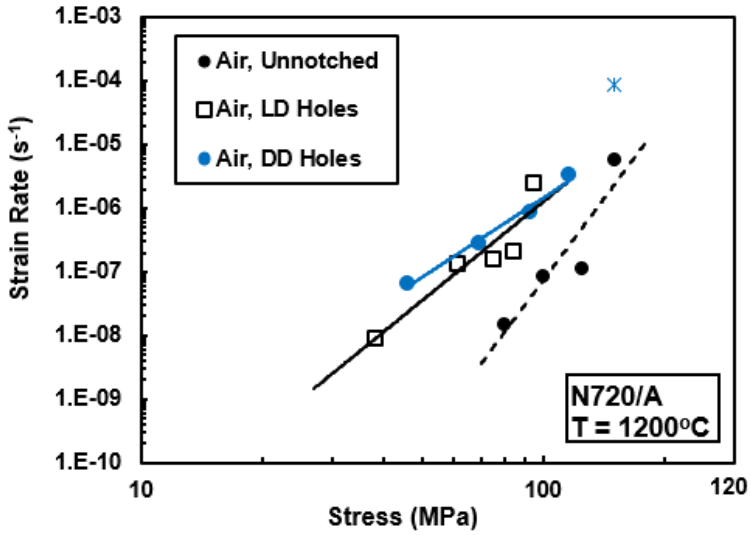

Figure 33: Minimum creep rate vs creep stress for unnotched, laser-drilled and diamond-drilled N720/A specimens tested in air at 1200ºC

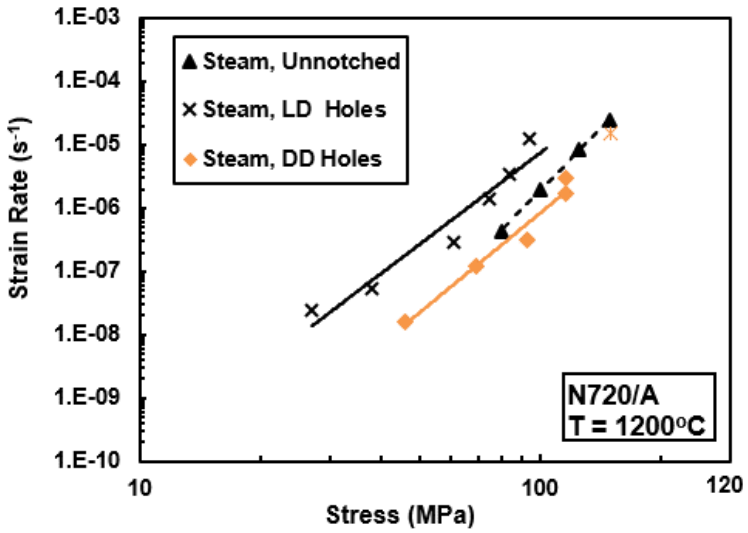

Figure 34: Minimum creep rate vs creep stress for unnotched, laser-drilled and diamond-drilled N720/A specimens tested in steam at 1200ºC

4.5 Retained Properties

A tension test to failure was performed on the two specimens that reached creep run-out in order to measure the retained tensile properties. Results are summarized in Table 12 and Figure 35.

Table 12: Retained Tensile Properties for Diamond-Drilled N720/A Specimens Following 100 hours of Creep at 1200°C and 46 MPa in Air and Steam

	Tensile Test	100 Hours of Prior Creep at 46 MPa in Air	100 Hours of Prior Creep at 46 MPa in Steam
UTS (MPa)	204	143	152
E (GPa)	70.9	61.2	50.1
Retained UTS (%)		70.2	74.5
Retained E (%)		86.4	70.8

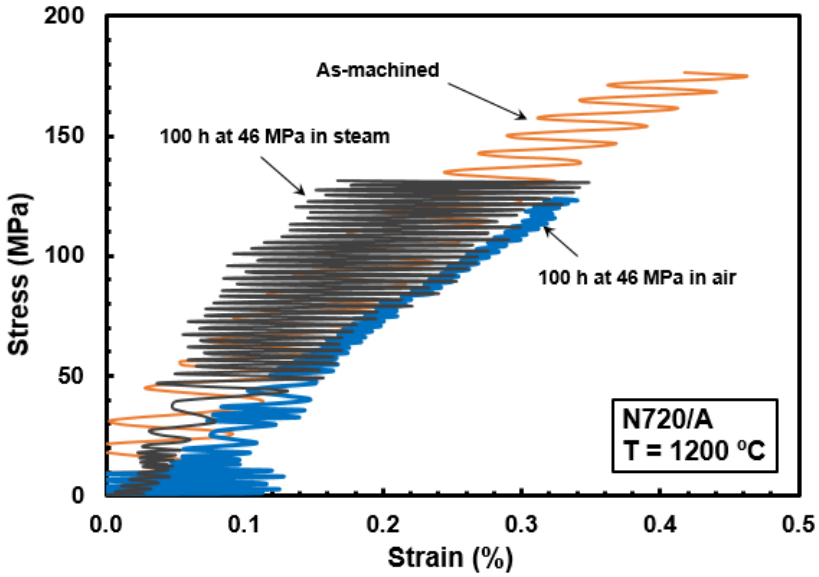

Figure 35: Stress vs strain curves obtained at 1200°C for the as-machined N720/A specimen with diamond-drilled holes and specimens with 100 hours of prior creep in air and in steam

The stress-strain behavior of pre-crept DD specimens in Figure 35 is qualitatively the same as that of the as-machined DD specimen. Note that the DD specimen pre-crept in air produced larger failure strain than the DD specimen pre-crept in steam. This observation is consistent with the results of the creep tests where larger strains were accumulated in air than in steam. Specifically, the DD specimen that achieved creep run-out at 46 MPa in air accumulated 2.78% strain during 100 h of creep, whereas the DD specimen that achieved creep run-out at 46 MPa in steam accumulated only 0.78% strain. These results once again suggest that additional matrix sintering takes places at 1200°C

in steam. The DD specimen pre-crept in air retained ~70% of its tensile strength, whereas the DD specimen pre-crept in steam retained ~75% of its UTS. This observation suggests that while the properties and performance of the CMC are degraded due to the presence of DD holes (because the composite porosity may now exceed the upper porosity limit), testing in steam may be beneficial to the DD specimens (possibly by reducing porosity and returning it to acceptable levels).

Notably, the results reported in this work for the DD specimens differ slightly from those reported previously for the LD specimens [3]. The LD specimens that achieved creep run-out in air at 38 MPa retained ~90% of its tensile strength and modulus, whereas the LD specimen that achieved creep run-out in steam at 27 MPa retained only 65% of its tensile strength and 90% of its modulus [3]. These results suggest that steam is much more degrading to the tensile properties of the LD specimens.

4.6 Composite Microstructure

4.6.1 Optical Microscopy

Optical microscopy was used to assess the composite microstructure in the vicinity of a DD hole prior to testing, as well as to capture the entire fracture surface after testing in order to assess macroscopic differences between the two environments. When examining specimens with LD holes using an optical microscope, Minor discovered the formation of a glassy phase in the area surrounding the holes (Figure 36) [3].

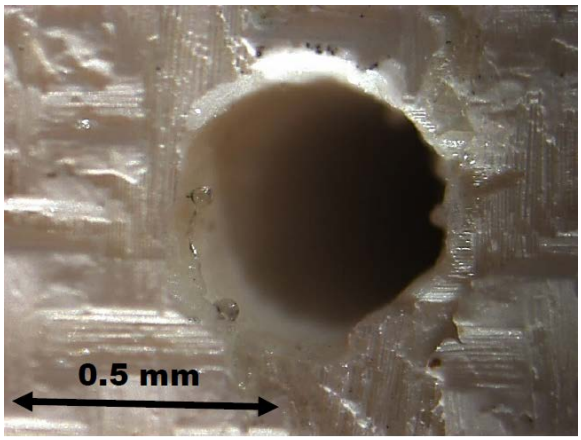

Figure 36: Pre-test optical micrographs of an N720/A specimen with laser-drilled holes showing material in the vicinity of a randomly selected hole. Reproduced from Ref. 3.

Considering the chemical and phase composition of the N720 fibers, it was concluded that the intense localized heat from the laser was causing silicon to leach from the fibers, react with oxygen and form a SiO_2 glass in the vicinity of the holes. This leaching of silicon from the mullite phase in the fibers turned out to be very detrimental to both the tensile properties and creep resistance of the material as it not only reduced the load carrying capacity of the fibers, but also fused the fibers and matrix together in the vicinity of the LD holes [3].

Similarly, this effort sought to use optical micrographs to characterize the composite microstructure in the area surrounding the DD holes. Figures 37-39 show representative optical micrographs of composite microstructure for untested DD specimens (Figure 37), and DD specimens tested in creep at 1200°C in air (Figure 38) and in steam (Figure 39). The key takeaway from this analysis is the lack of a glassy phase in the vicinity of any DD hole. Additionally, there appears to be more fiber pull-out and less fiber-matrix bonding relative to optical micrographs of LD holes (Figure 40)

[3]. These observations suggest that the diamond drilling process is less damaging to the composite microstructure than laser drilling.

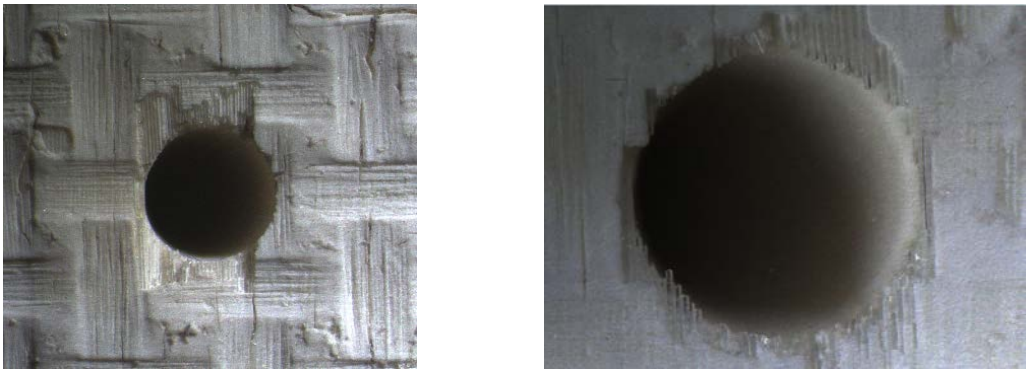

Figure 37: Pre-test optical micrographs of N720/A specimens with diamond-drilled holes showing material in the vicinity of randomly selected holes

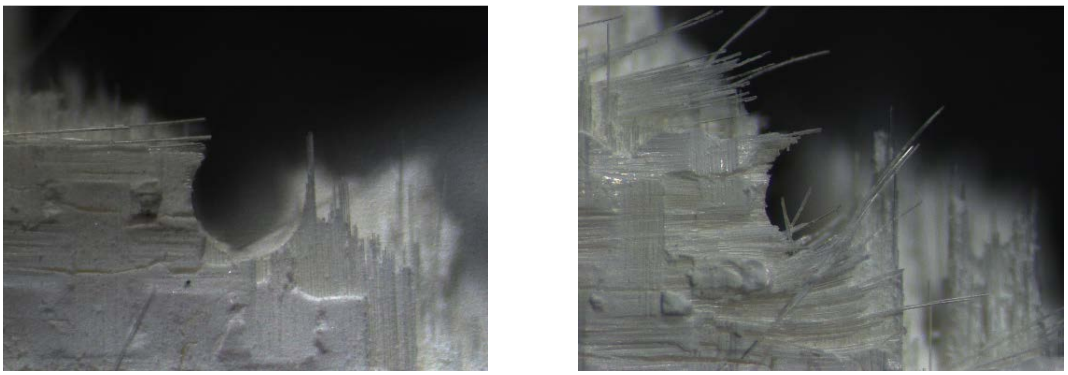

a) b)

Figure 38: Optical micrographs of N720/A specimens with diamond-drilled holes creep tested at 1200ºC in air: (a) σ_{cr} = 116 MPa, t_f = 0.59 h, and (b) tested in tension to failure following 100 h of creep at 46 MPa

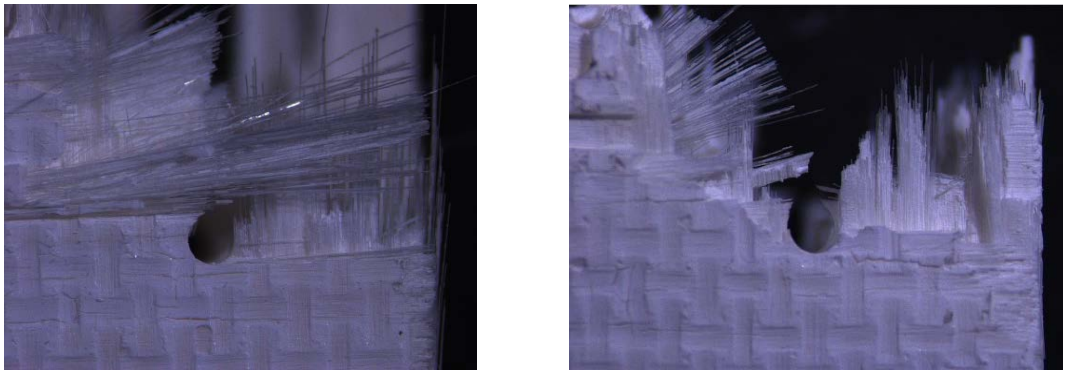

a) b)

Figure 39: Optical micrographs of N720/A specimens with diamond-drilled holes creep tested at 1200ºC in steam: a) σ_{cr} = 116 MPa, t_f = 0.61 h, and b) tested in tension to failure following 100 h of creep at 46 MPa

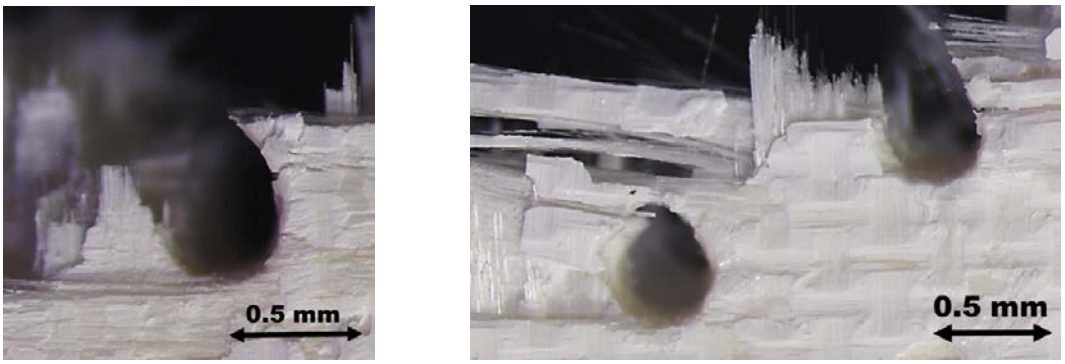

a) b)

Figure 40: Optical micrographs of N720/A specimens with laser-drilled holes creep tested at 1200ºC in air: a) σ_{cr} = 61 MPa, t_f = 58.45 h, and b) tested in tension to failure following 100 h of creep at 38 MPa. Reproduced from Ref. 3.

Examination of the fracture surfaces produced at various stress levels in each environment suggests that the size of the damage zone can be correlated with the failure strain. This observation was also made for the N720/A CMC by Ruggles-Wrenn, Radzicki et al. [27] in 2008. They reported that longer damage zones accompanied larger strain accumulations. This was true for the DD specimens as well, as can be seen in Figures 41-43. Figure 41 shows the fracture surface from the tensile test in air, and Figures 42 and 43 show the fracture surfaces produced from creep testes performed in air and steam, respectively. These images highlight two observations that were previously made from the creep data. First, for all creep stresses below 70% UTS (~140 MPa for the DD specimen), failure strains produced in both environments exceed the failure strain produced in the tension test. Second, as the applied creep stress decreases, strain at failure increases. These observations, paired with the below micrographs, support the presumed correlation between damage zone size and failure strain. However, the correlation is not as strong for all micrographs, as is true for the specimen tested in air at 69 MPa. This is merely due to the limitation of the optical microscope only being able to assess external damage. Based on visual examinations of the failed specimens, there

appeared to be a fair amount of damage penetrating the internal plies of the composite. A CT scanner was used to investigate this topic, and those results will be discussed in the next section.

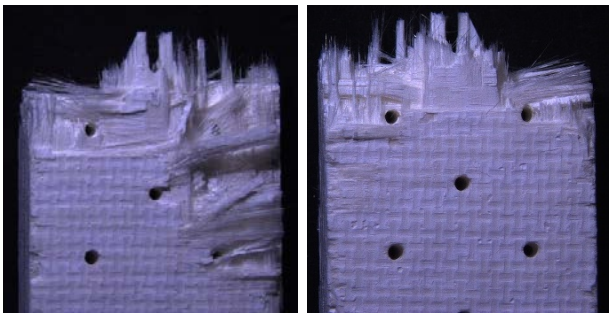

Figure 41: Fracture surfaces obtained for an N720/A specimen with diamond-drilled holes tested in tension to failure at 1200°C in air (ε_f = 0.42%)

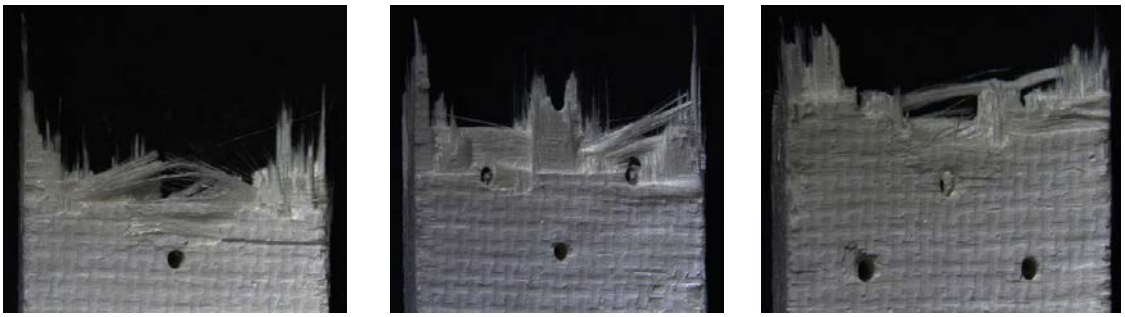

a) b) c)

Figure 42: Fracture surfaces obtained for N720/A specimens with diamond-drilled holes tested in creep at 1200°C in air: (a) σ_{cr} = 116 MPa and ε_f = 0.95%, (b) σ_{cr} = 93 MPa and ε_f = 2.8%, and (c) σ_{cr} = 69 MPa and ε_f = 4.1%

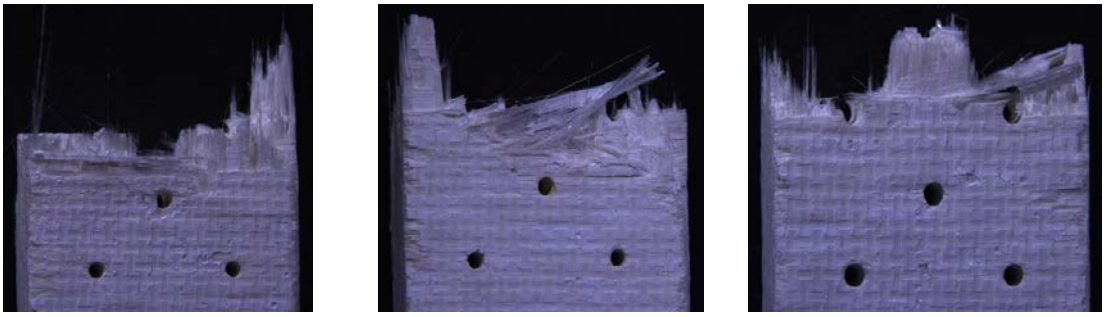

a) b) c)

Figure 43: Fracture surfaces obtained for N720/A specimens with diamond-drilled holes tested in creep at 1200°C in steam: (a) σ_{cr} = 116 MPa and ε_f = 0.55%, (b) σ_{cr} = 93 MPa and ε_f = 1.15%, and (c) σ_{cr} = 69 MPa and ε_f = 1.5%

Regarding macroscopic trends between the fracture surface topography in the two environments, both show some degree of uncorrelated fiber fracture spanning the entire width of the specimen. However, as was the case for the unnotched specimens [4], the steam fracture surfaces appear to be more planar compared to the slightly brushier fracture surfaces produced in air. This difference in topography is likely due to additional matrix sintering occurring in steam.

Conversely, Minor et al. [4] reported that all specimens with LD holes tested in creep at 1200°C exhibited near planar fracture surfaces with little fiber pull-out in both air and steam environments. They attributed this result to the damage caused to the composite microstructure by the laser drilling process.

4.6.2 Computed Tomography

Computed Tomography (CT) is a nondestructive imaging tool that has the ability to examine internal features of a sample. In this effort, a CT scanner was used to help estimate the size of a damage zone in DD specimens after testing. The objective was to determine whether optical microscopy was sufficient to make this assessment, or if CT scans offered additional information. A systematic approach was leveraged in order to identify the damage zone that penetrated the furthest into the specimen interior. Following the scan of each specimen, a three-dimensional (3D) model was built in the CT interface software (VGSTUDIO MAX 3.2). The model was set-up such that the x-axis aligned with the specimen width, the y-axis aligned with the specimen depth, and the z-axis aligned with the specimen length (i.e. the loading direction). Two-dimensional (2D) images were generated based on the location of an x-y or x-z plane; those locations were controlled by the user. The approach consisted of starting at the top of the fracture

surface and stepping the x-y plane down the length of the specimen until dark spots (signifying damage) disappeared. After orienting the x-y plane with the bottom of that crack, the x-z plane would be positioned over that same dark spot in order to display the 2D side view of the specimen at that point. This process was repeated until it was clear that the deepest portion of the damage zone had been identified. These x-z images were then compared to the optical micrographs of the same specimen. Figures 44-47 show the results of these comparisons for a few randomly selected specimens, where the red line overlaid on the optical micrographs estimates the deepest damage zone penetration identified by the CT scan.

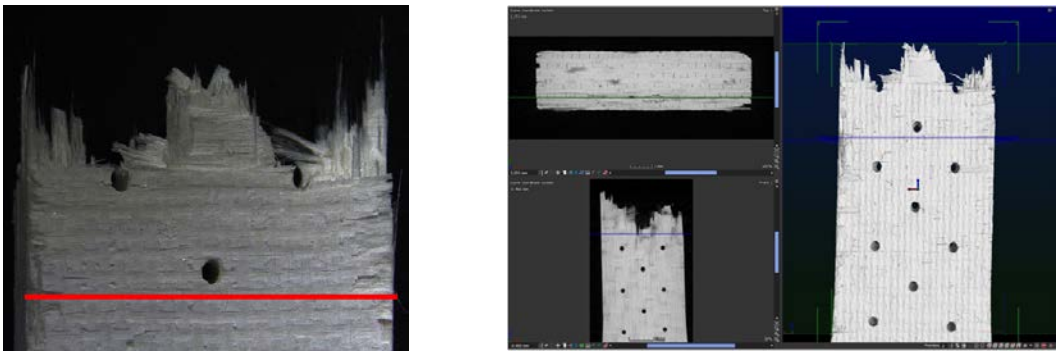

a) b)

Figure 44: Comparison of damage zone penetration for an N720/A specimen with diamond-drilled holes tested in creep at 1200°C in air (σ_{cr} = 93 MPa, t_f = 6.55 h): (a) optical micrograph, and (b) CT scan

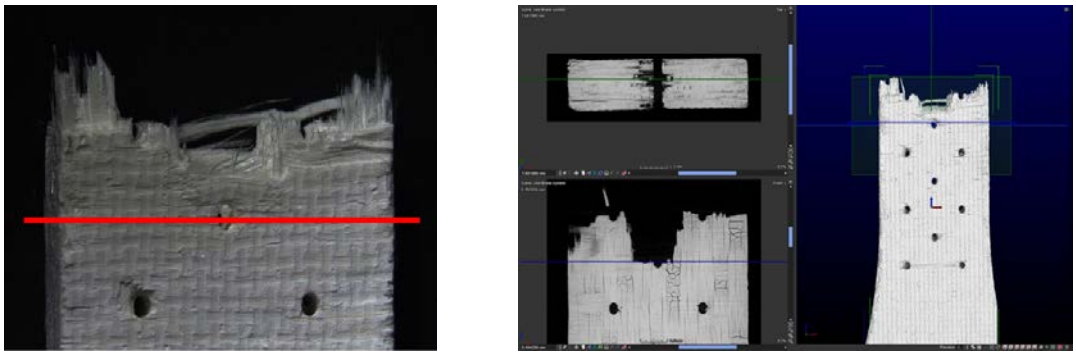

a) b)

Figure 45: Comparison of damage zone penetration for an N720/A specimen with diamond-drilled holes tested in creep at 1200°C in air (σ_{cr} = 69 MPa, t_f = 30.95 h): (a) optical micrograph, and (b) CT scan

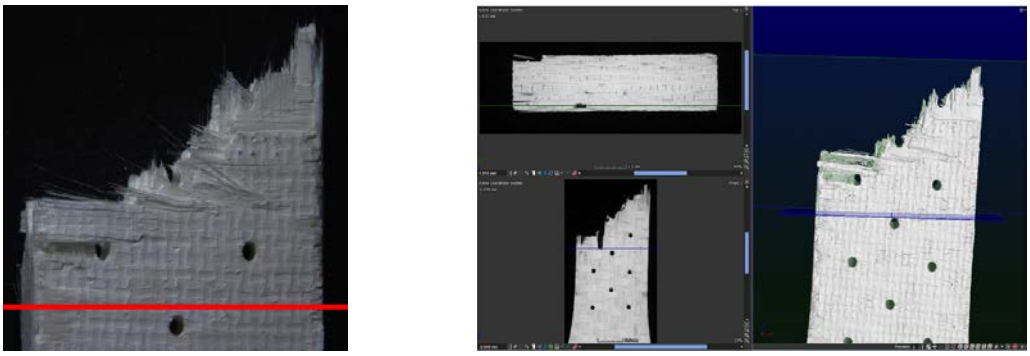

a) b)

Figure 46: Comparison of damage zone penetration for an N720/A specimen with diamond-drilled holes tested in tension to failure following 100 h of creep at 46 MPa in air at 1200°C: (a) optical micrograph, and (b) CT scan

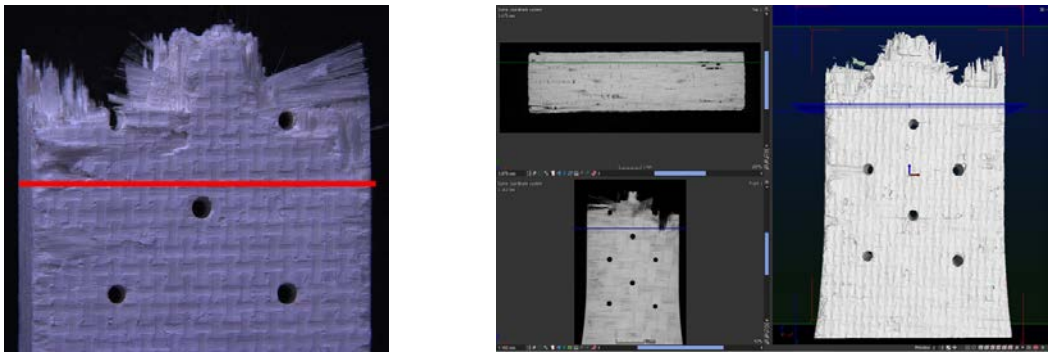

a) b)

Figure 47: Comparison of damage zone penetration for an N720/A specimen with diamond-drilled holes tested in tension to failure following 100 h of creep at 46 MPa in steam at 1200°C: (a) optical micrograph, and (b) CT scan

Based on the comparisons in Figures 44-47, it would appear that CT scans do offer additional insight into the true depth of a damage zone that may or may not be fully characterized by optical microscopy. In this work, the additional information from the CT scans helped support the claim that there is a correlation between damage zone size and strain at failure. Note, an additional observation related to the correlation claim was made when comparing this analysis to the results presented in section 4.6.1 for the specimens tested at 93 and 69 MPa in air. From the CT scans, it would appear that the damage zone from the specimen tested at 93 MPa in air penetrated deeper than that of the specimen tested at 69 MPa in air, but the accrued strain at failure is less. It is assumed

that this is a result of only assessing depth of a damage zone, not width, as visual observations of each of these fracture surfaces suggest that the specimen tested at 69 MPa in air had a much wider damage zone. However, further analysis via CT scans would be needed to validate this assumption.

4.6.3 Scanning Electron Microscope

Representative SEM micrographs obtained in this work are shown in Figures 48-53. Note that some SEM images were produced with the Quanta FEG 650 SEM and some with the MAIA3 TESCAN SEM. Figures 48-50 present typical features of a fracture surface obtained from creep tests performed at 1200°C in air, and Figures 51-53, similarly capture features from creep tests performed at 1200°C in steam.

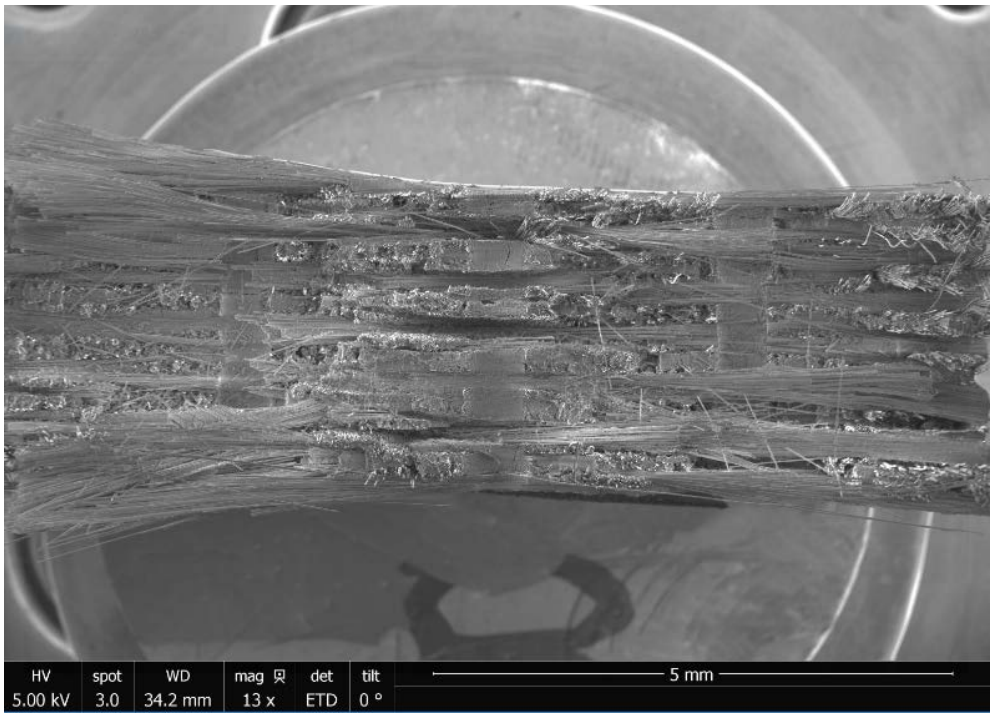

Figure 48: Fracture surface of an N720/A specimen with diamond-drilled holes tested in creep at 1200°C in air (σ_{cr} = 150 MPa, t_f = 0.01 h)

Figure 49: Fracture surface of an N720/A specimen with diamond-drilled holes tested in creep at 1200°C in air (σ_{cr} = 93 MPa, t_f = 6.55 h)

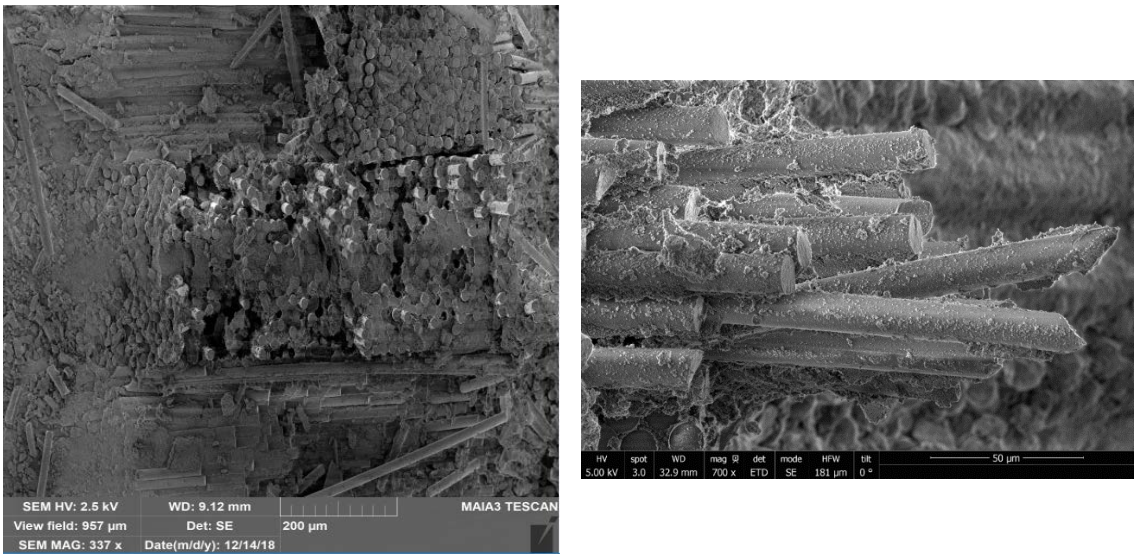

Figure 50: Fracture surface of an N720/A specimen with diamond-drilled holes tested in tension to failure following 100 h of creep at 46 MPa in air at 1200°C

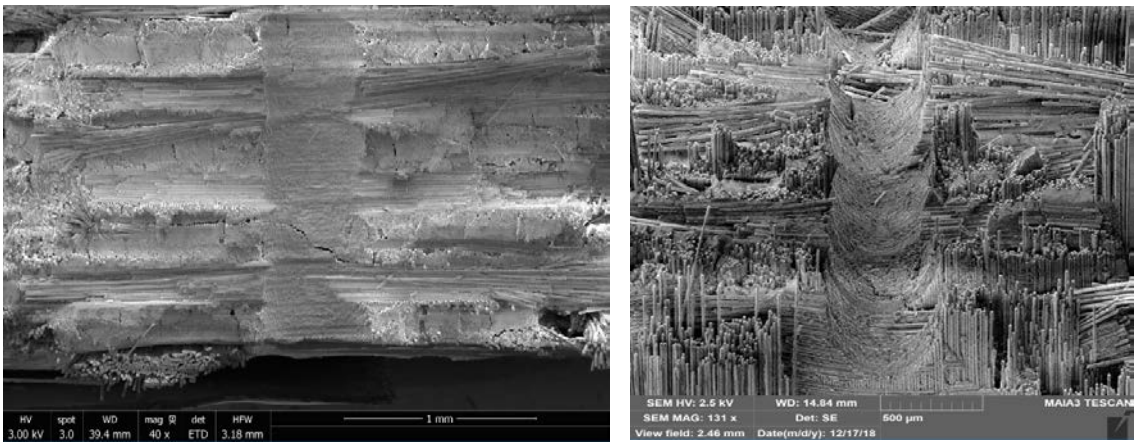

a) b)

Figure 51: Fracture surface of an N720/A specimen with diamond-drilled holes tested in creep at 1200°C in steam (σ_{cr} = 93 MPa, t_f = 6.05 h). Image obtained with (a) Quanta FEG 650 SEM, and (b) MAIA3 TESCAN SEM at a 55° tilt.

Figure 52: Fracture surface of an N720/A specimen with diamond-drilled holes tested in creep at 1200°C in steam (σ_{cr} = 93 MPa, t_f = 6.05 h)

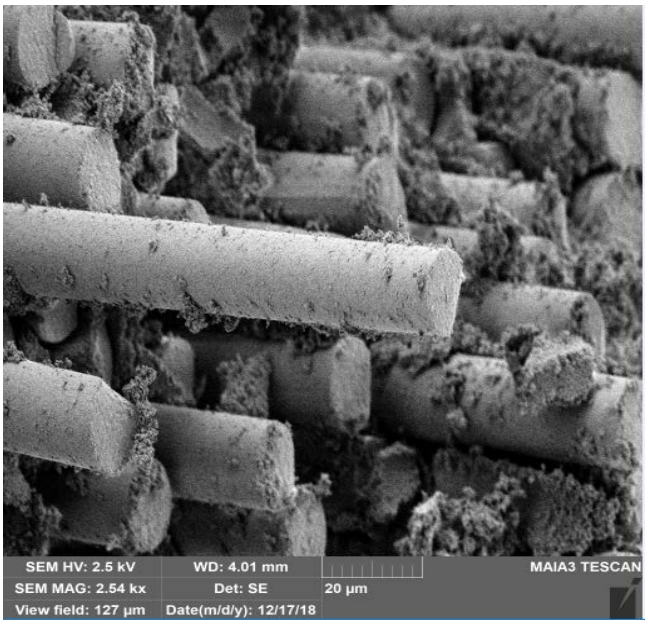

Figure 53: Fracture surface of an N720/A specimen with diamond-drilled holes tested in tension to failure following 100 h of creep at 46 MPa in steam at 1200°C

These micrographs consistently show a grainy surface on the hole interior, where both fibers and matrix are readily discernable. Additionally, both air and steam fracture surfaces show signs of fiber pull-out in the vicinity of the holes, with little matrix remaining bonded to the exposed fibers. The lower magnification micrographs also show more regions of coordinated fiber failure for specimens tested in steam, which ultimately contributes to the more planar fracture surface. While matrix sintering is not a distinct feature that can be measured via SEM, it is the presumed cause for the correlated fiber failures in steam based unnotched creep results [11, 12, 14].

The SEM micrographs obtained in this work (Figures 48-53) differ significantly from those obtained by Minor for specimens with LD holes [3]. Specifically, Minor estimated that the laser drilling process caused a damage zone close to 1 mm in diameter around each hole. As seen in Figure 54 reproduced from Minor [3], SEM micrographs of the LD specimens identified this damage as a glassy phase covering the hole interior, as

well as fused fibers and matrix in the vicinity of the hole that ultimately reduced the matrix porosity in this area and caused planar fracture.

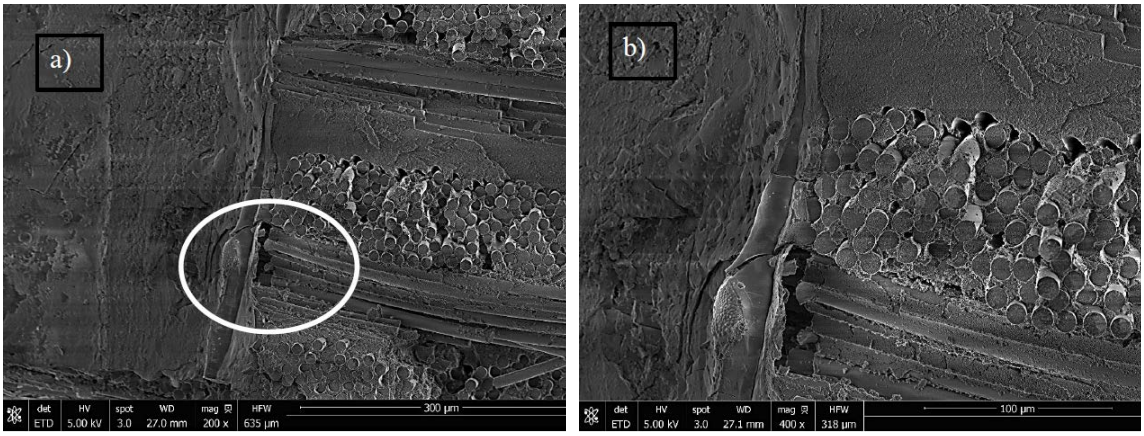

Figure 54: Fracture surface of a N720/A specimen with laser-drilled holes tested in creep in laboratory air at 1200ºC (σ_{cr} = 61 MPa, t_f = 58.4 h). a) Edge of the hole and the glassy phase found in the interior of the hole are clearly visible. (b) Higher magnification view showing edge of the hole and glassy phase in the interior of the hole. Reproduced by Ref. 3.

When comparing the results reported by Minor [3] to the results obtained in this work, it's clear that the diamond drilling process has a significantly different effect on the composites microstructure. The lack of glassy phase on the interior of the DD hole suggests that silicon in not leaching from the fibers and forming an oxide layer on the drill surface. Assuming this is true, the load carrying capacity of the intact N720 fibers in these specimens should be unaffected. Additionally, the lack of noticeable bonding between fiber and matrix near the DD holes suggests that the porosity of the matrix in this area is not influenced by the presence of holes. This observation indicates that diamond drilling does not create an additional damage zone beyond that of the hole itself. This result would suggest that the degraded creep resistance of DD specimens can simply be attributed to the removal of load-bearing fibers and matrix via the drilling process.

Without a degrading damage zone surrounding the hole, the DD specimens show improved tensile properties and creep resistance compared to LD specimens.

Chapter 5: Conclusions and Recommendations

5.1 Concluding Remarks

Mechanical tests were performed on an N720/A oxide-oxide CMC with an array of DD effusion holes in order to evaluate the tensile properties and creep resistance of this material at 1200°C in both air and steam environments. In order to assess the effects of steam and DD holes on the performance of this material, results of this effort were compared to prior research that performed similar investigations on unnotched specimens as well as specimens with the same pattern of LD holes.

The monotonic tensile test performed in air produced an ultimate tensile strength of 204 MPa, modulus of elasticity of ~71 GPa, and failure strain of 0.42%. These results are similar to those reported for unnotched specimens at 1200°C, indicating that the presence of DD holes did not negatively affect the tensile properties. Conversely, the presence of LD holes reduced the UTS and modulus of the CMC by 19% and 23%, respectively.

For creep-rupture tests at 46, 69, 93, 116 and 150 MPa at 1200°C, the DD specimens achieved run-out of 100 hours at 46 MPa in both air and steam environments. While the creep run-out stress was unaffected by steam, the results obtained in creep tests at stresses above 46 MPa revealed a 10% degradation in creep lifetime due to steam. This result differs significantly from unnotched and LD results which reported a lifetime degradation due to steam of 92% and 85%, respectively. Furthermore, steam reduced the creep run-out stress by nearly 9% for unnotched specimens, and nearly 29% for LD specimens. These data suggest that steam is least degrading to the DD configuration.

Comparing the results obtained for the specimens with holes (DD as well as LD) with those obtained for the unnotched specimens indicates that the presence of a hole has a strong detrimental effect on the creep performance of this material at 1200°C in air. Both the LD and DD specimens saw a 90% reduction in creep lifetime, and a reduction by approximately a factor of two in creep run-out stress relative to unnotched specimens.

Comparing the results obtained at 1200°C in steam suggests that the presence of LD holes is just a detrimental to the creep performance in steam as air, but the presence of DD holes is not. Relative to unnotched results in steam, the presence of LD holes caused a 90% reduction in creep lifetime and nearly 63% reduction in creep run-out stress. Conversely, the presence of DD holes caused a 67% reduction in creep lifetime for stresses below 100 MPa (~50% UTS), but had little effect on creep lifetimes for stresses > 100 MPa. Considering this result, as well as the reduction in creep run-out stress of only 37% relative to unnotched results, it appears that the presence of DD holes is less degrading to the creep performance of this material in a steam environment than they are in air.

The apparent difference in the impact of steam on the creep performance of these three configurations can be attributed to a change in damage mechanism that affected minimum creep rates. Unnotched and LD specimens both produced faster minimum creep rates in steam than in air, which resulted in significantly shorter lifetimes. Conversely, DD specimens saw slower creep rates in steam, which ultimately extended the creep lifetimes of those creep tests, and therefore reduced the detrimental impact of steam. However, despite this difference in minimum creep rate, all configurations that failed before run-out accrued 1-2 times more strain at failure in air than steam.

This difference in damage mechanism, and associated impact on creep rates, appeared to influence the retained property results as well. After 100 h of prior creep at 46 MPa (22% UTS), the DD specimen had accrued 2.78% strain in air, and 0.78% strain in steam. This difference in damage accumulation during creep is a direct result of the faster creep rates produced in air, and ultimately affected the retained tensile properties as well. When tested in tension to failure at 1200°C, the DD specimen that survived 100 h of creep in air retained a lower UTS than the specimen that survived prior creep in steam. The results for the LD specimens differed due to the dominant damage mechanism that caused accelerated creep rates in steam. After 100 h of prior creep at 38 MPa in air (23% UTS) and 27 MPa in steam (16% UTS), the LD specimen had accrued 0.4% and 0.62% strain, respectively. As expected, the LD specimen that accrued more damage during creep retained a lower UTS during the subsequent tension test to failure at 1200°C. A comparison of all the results indicates that DD holes are more detrimental to the retained tensile properties than LD holes following prior creep in air, but LD holes are more detrimental to the retained tensile properties following prior creep in steam.

An examination of the composite microstructure via optical microscopy and SEM helped assess damage and failure mechanisms operating in the DD specimens. Notably, the degraded performance of the LD specimens was attributed to damage caused to the microstructure during the laser drilling process. The intense localized heat from the laser caused a damage zone around each hole, which effectively reduced the load carrying capacity and damage tolerance of the CMC. This microstructural damage appeared in optical images as a glassy phase near the LD holes, and in SEM images as a glassy phase covering the hole interior. No such damage was observed in the composite

microstructure of DD specimens. The degraded creep performance of DD specimens is believed to be a result of the removal of load-bearing material via the drilling process which subsequently altered the dominant damage mechanisms such that creep rates were accelerated in air tests. Consistent with unnotched results, optical and SEM images of the DD specimens identified the impacts of steam on composite microstructure as additional matrix sintering which caused shorter damage zones and more regions of correlated fiber failures. This is a preliminary result based on testing and examination of a limited number of test specimens. Further experiments and analysis are needed to explore the damage mechanism at play in specimens with DD effusion holes.

5.2 Recommendations

First and foremost, it is recommended that these experiments be duplicated to confirm that the results of this work are repeatable for specimens cut from different composite panels. The noticeable difference in minimum creep strain rates obtained for the DD specimens in this effort and those obtained in prior research for unnotched and LD specimens is of primary interest. Additional testing would ensure that other panels of this CMC behave similarly, therefore ruling out manufacturing or experimental errors as a potential cause of the observed differences in behavior. Assuming that the results of this work are confirmed, subsequent efforts should aim to characterize the damage mechanism that causes accelerated minimum creep rates in air for the DD specimens.

Additionally, it would be beneficial to understand how this material would perform in an environment that is more representative of its intended use. Since this material is being considered as a thermal protection system, it is recommended that a similar

experiment be performed with one-sided heating. The temperature gradient caused by exposing one side to 1200°C and the other to ambient air would likely affect the creep performance of unnotched and DD specimens differently. This difference would be indicative of whether film cooling and the presence of holes is actually beneficial to the materials performance. Digital image correlation (DIC) could be used to investigate the strain distribution around the holes on the side open to ambient air, and identify whether there are any detrimental interactions of strain concentrations affecting the materials response.

Appendix A: Optical Micrographs

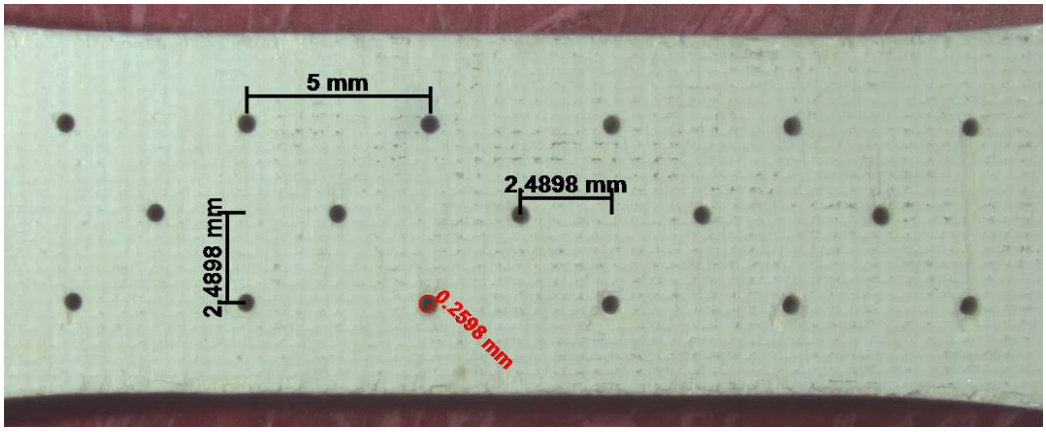

Figure A. 1: Pre-test optical image of specimen hole pattern

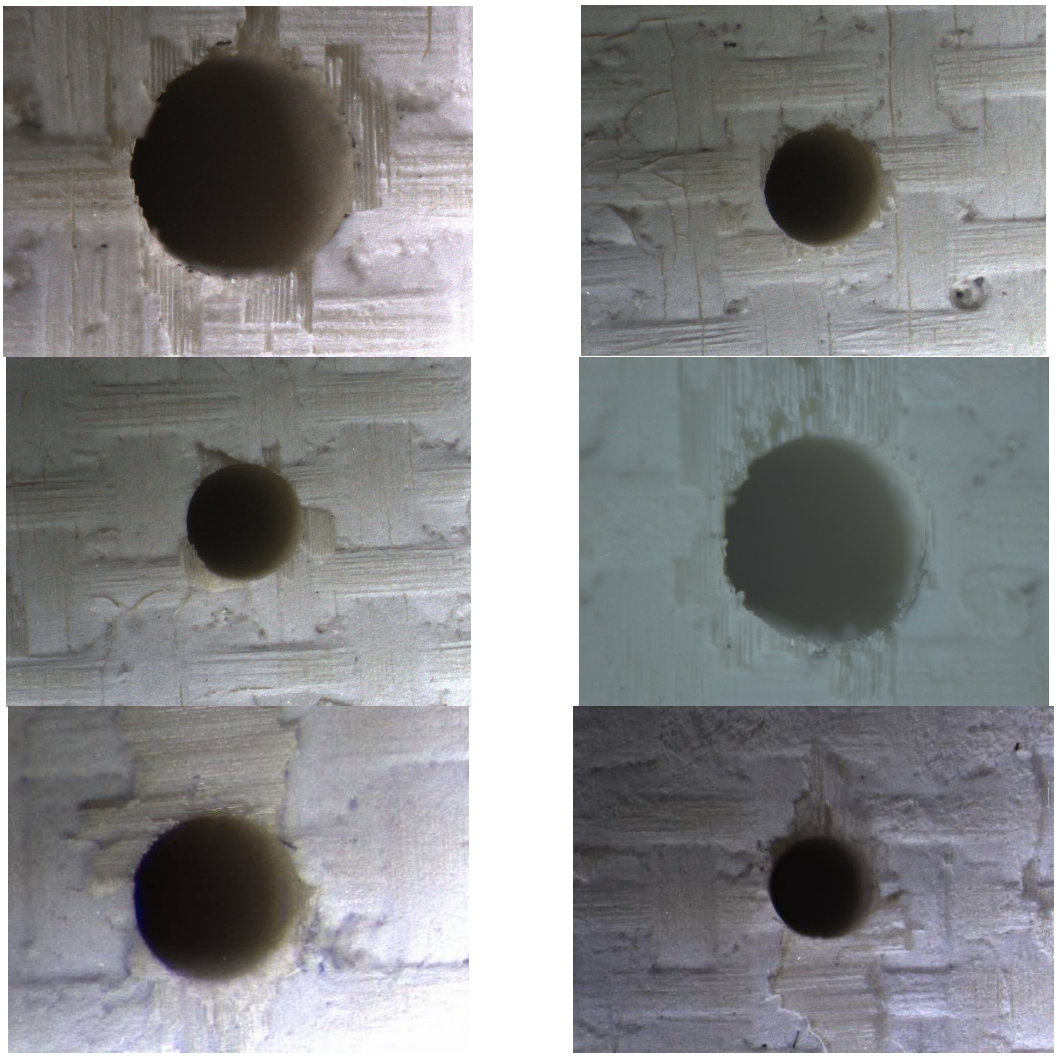

Figure A. 2: Pre-test optical images of randomly selected holes

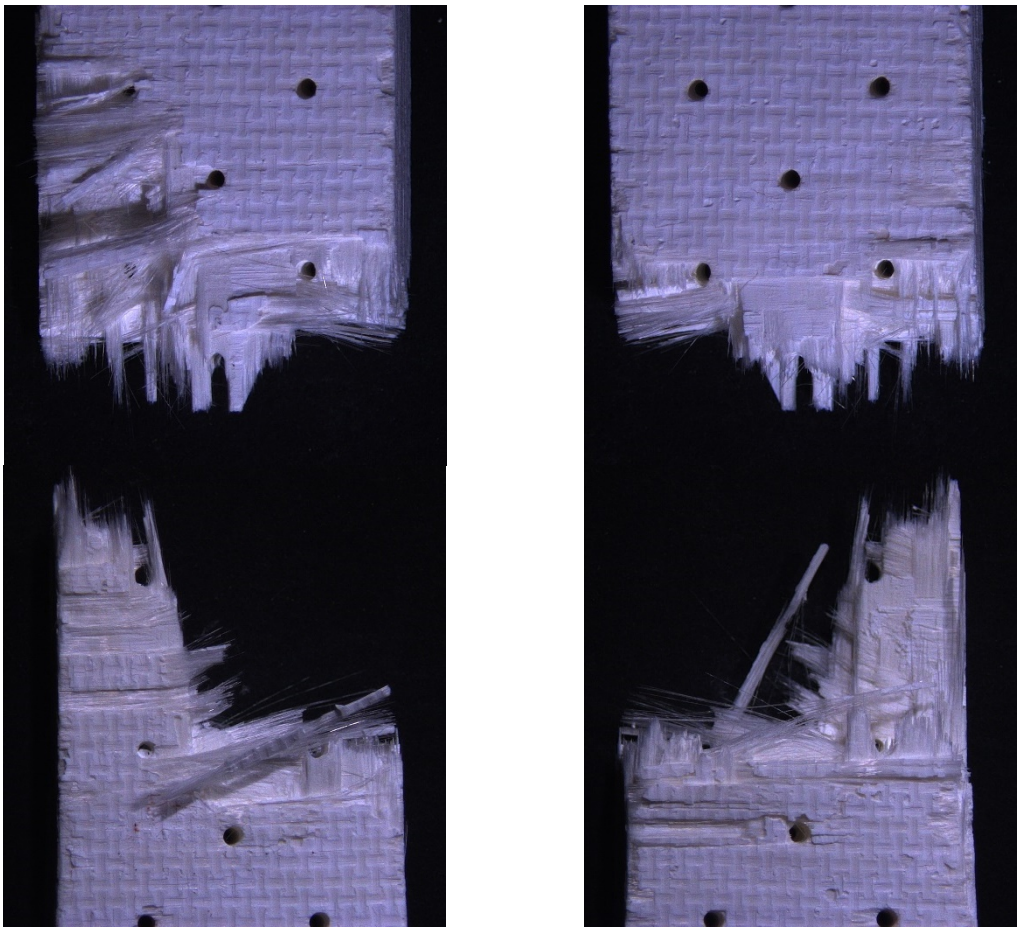

Figure A. 3: Top and bottom fracture surfaces of specimen #3, tested in tension to failure at 1200°C in air

Figure A. 4: Fracture surface of specimen #3, tested in tension to failure at 1200°C in air

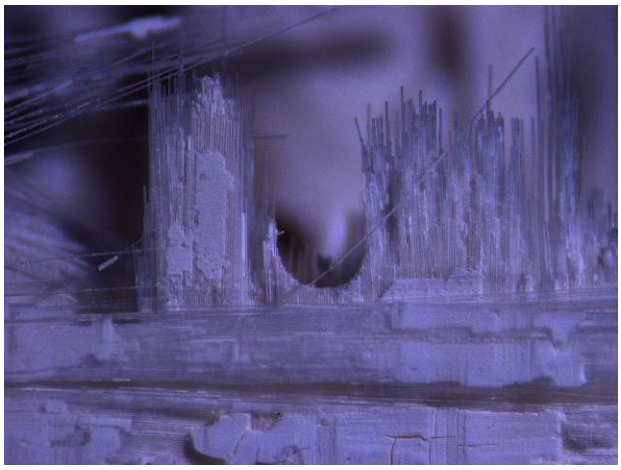

Figure A. 5: Fracture surface of specimen #3, tested in tension to failure at 1200°C in air

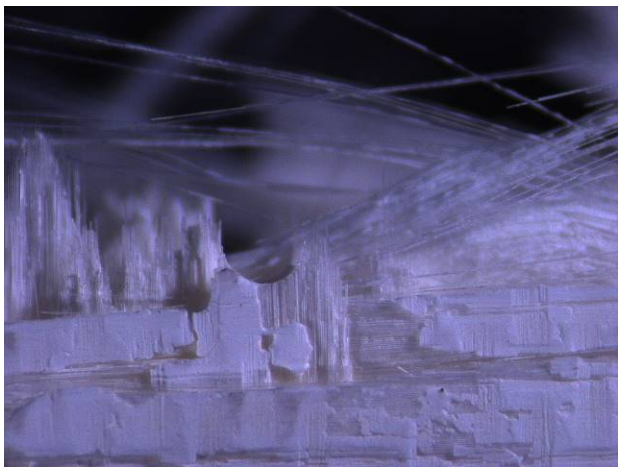

Figure A. 6: Fracture surface of specimen #3, tested in tension to failure at 1200°C in air

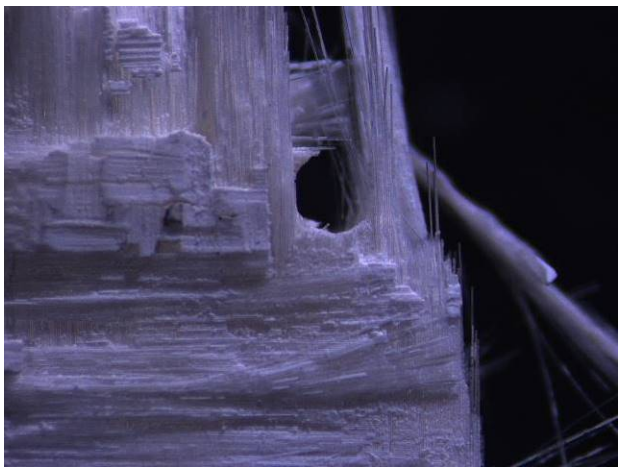

Figure A. 7: Fracture surface of specimen #3, tested in tension to failure at 1200°C in air

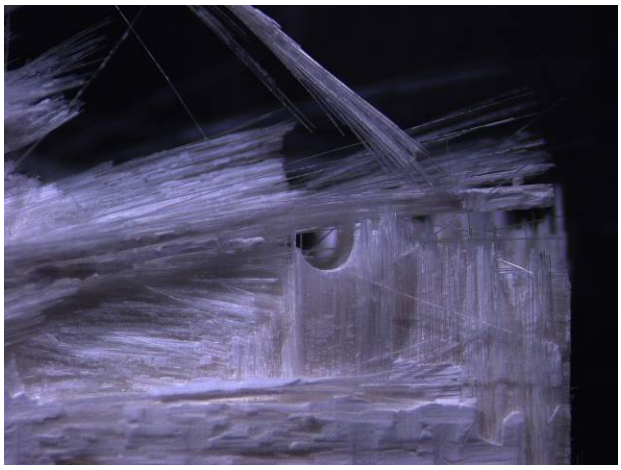

Figure A. 8: Fracture surface of specimen #3, tested in tension to failure at 1200°C in air

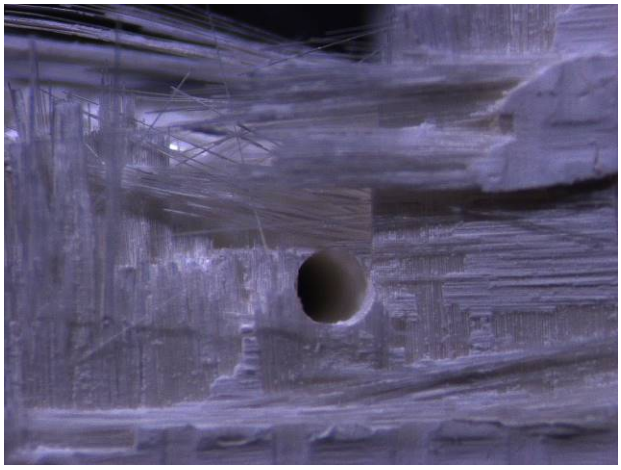

Figure A. 9: Fracture surface of specimen #3, tested in tension to failure at 1200°C in air

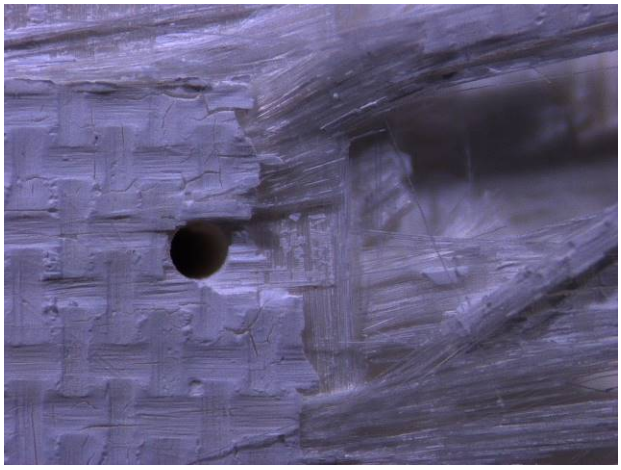

Figure A. 10: Fracture surface of specimen #3, tested in tension to failure at 1200°C in air

Figure A. 11: Fracture surface of specimen #3, tested in tension to failure at 1200°C in air

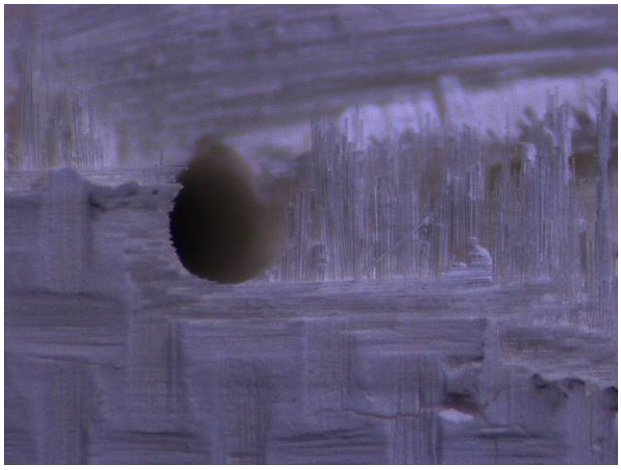

Figure A. 12: Fracture surface of specimen #3, tested in tension to failure at 1200°C in air

Figure A. 13: Fracture surface of specimen #3, tested in tension to failure at 1200°C in air

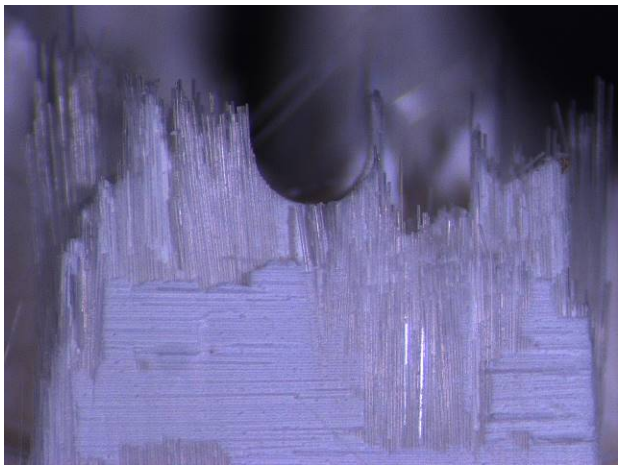

Figure A. 14: Fracture surface of specimen #3, tested in tension to failure at 1200°C in air

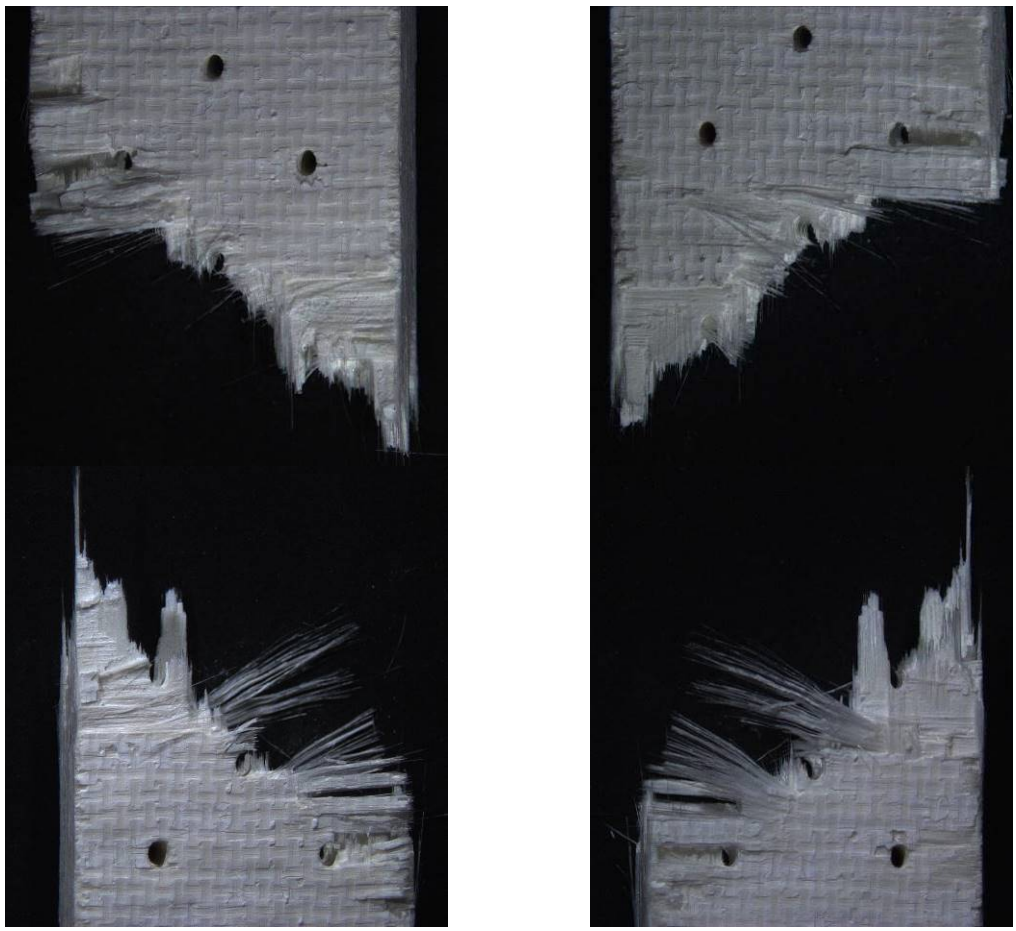

Figure A. 15: Top and bottom fracture surfaces of specimen #7, tested in tension to failure following 100 h creep at 46 MPa at 1200°C in air

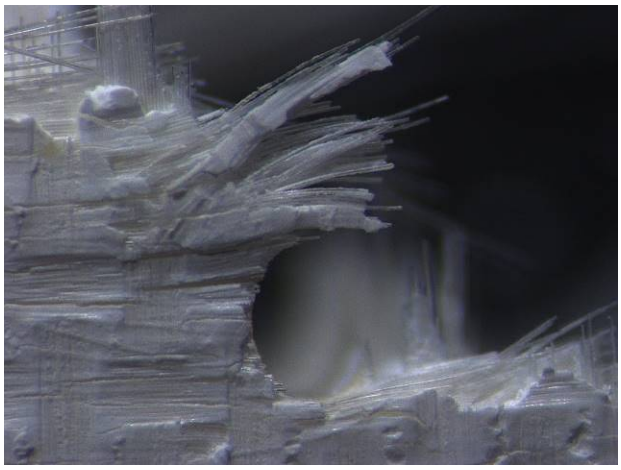

Figure A. 16: Fracture surface of specimen #7, tested in tension to failure following 100 h creep at 46 MPa at 1200°C in air

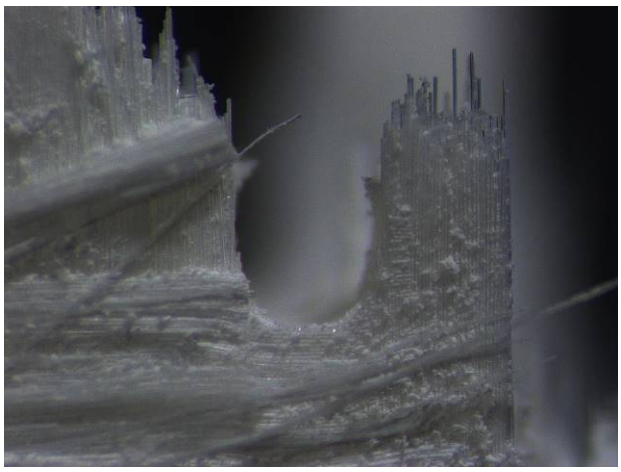

Figure A. 17: Fracture surface of specimen #7, tested in tension to failure following 100 h creep at 46 MPa at 1200°C in air

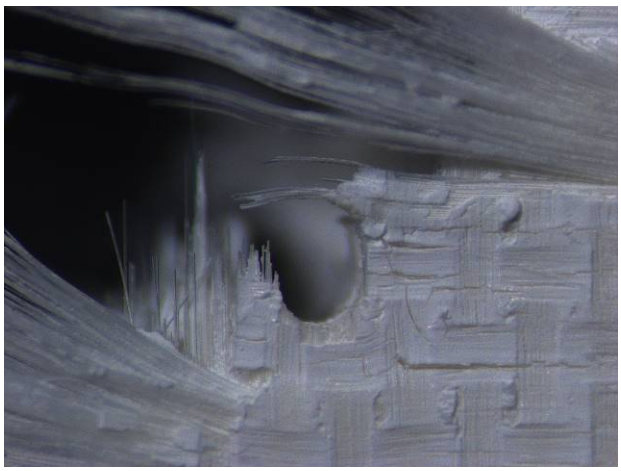

Figure A. 18: Fracture surface of specimen #7, tested in tension to failure following 100 h creep at 46 MPa at 1200°C in air

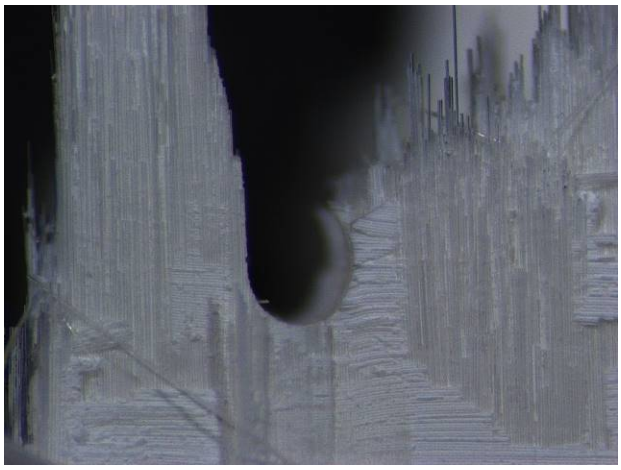

Figure A. 19: Fracture surface of specimen #7, tested in tension to failure following 100 h creep at 46 MPa at 1200°C in air

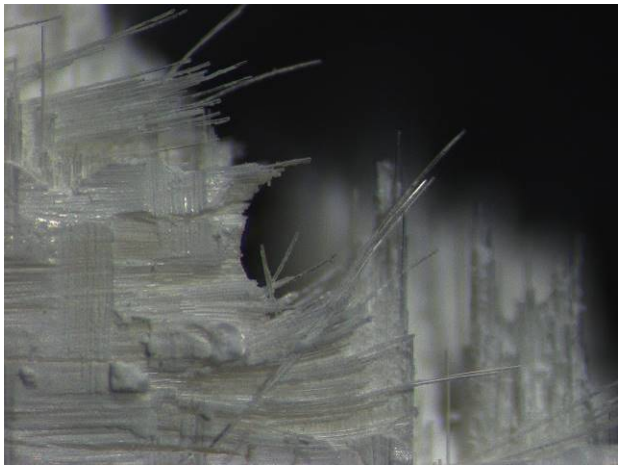

Figure A. 20: Fracture surface of specimen #7, tested in tension to failure following 100 h creep at 46 MPa at 1200°C in air

Figure A. 21: Fracture surface of specimen #7, tested in tension to failure following 100 h creep at 46 MPa at 1200°C in air

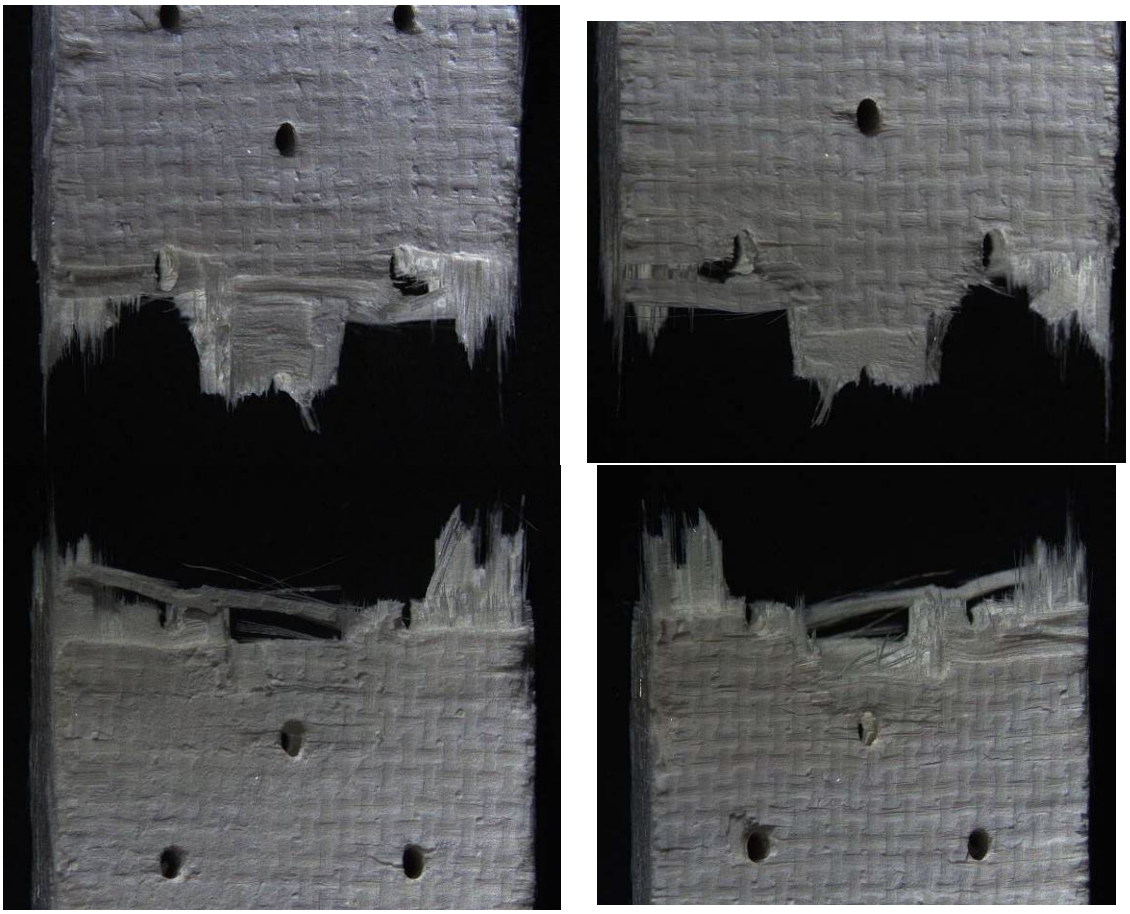

Figure A. 22: Top and bottom fracture surfaces of specimen #6, tested in creep at 1200°C in air (σ_{cr} = 69 MPa, t_f = 30.95 h)

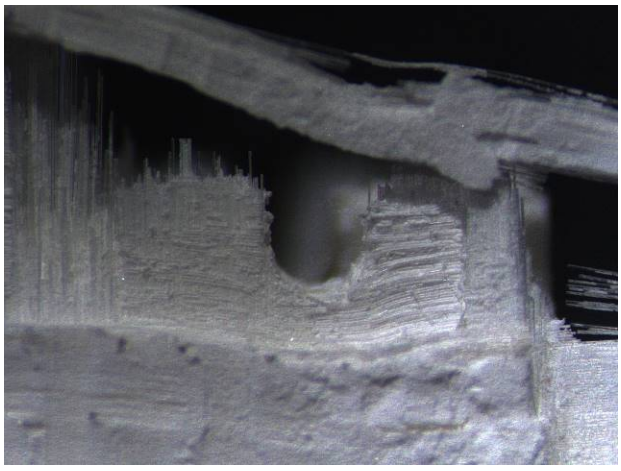

Figure A. 23: Fracture surface of specimen #6, tested in creep at 1200°C in air (σ_{cr} = 69 MPa, t_f = 30.95 h)

Figure A. 24: Fracture surface of specimen #6, tested in creep at 1200°C in air (σ_{cr} = 69 MPa, t_f = 30.95 h)

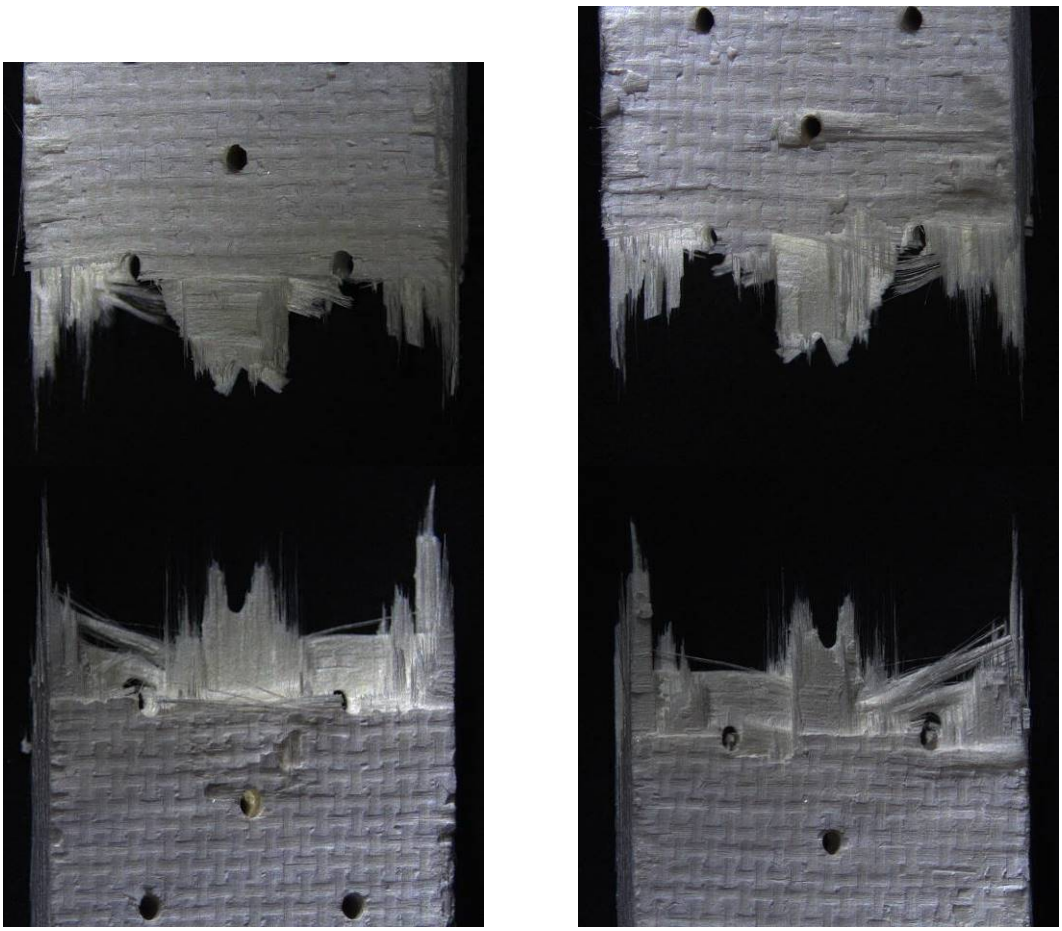

Figure A. 25: Top and bottom fracture surfaces of specimen #5, tested in creep at 1200°C in air (σ_{cr} = 94 MPa, t_f = 6.55 h)

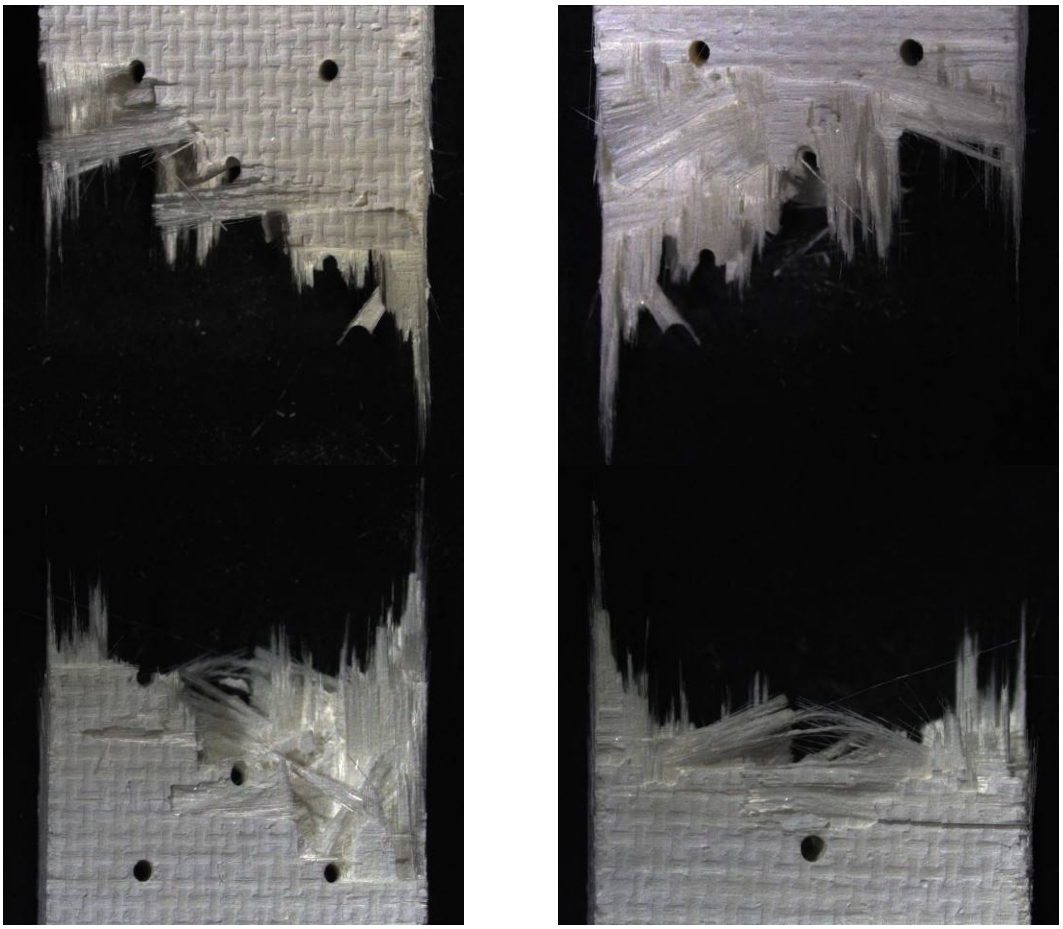

Figure A. 26: Top and bottom fracture surfaces of specimen #4, tested in creep at 1200°C in air (σ_{cr} = 118 MPa, t_f = 0.59 h)

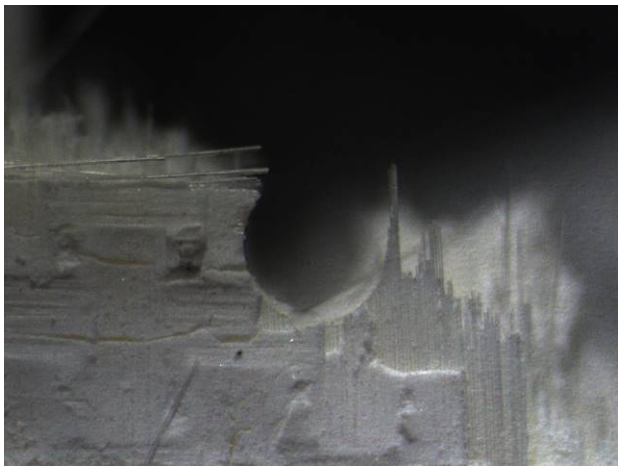

Figure A. 27: Fracture surface of specimen #4, tested in creep at 1200°C in air (σ_{cr} = 118 MPa, t_f = 0.59 h)

Figure A. 28: Fracture surface of specimen #4, tested in creep at 1200°C in air (σ_{cr} = 118 MPa, t_f = 0.59 h)

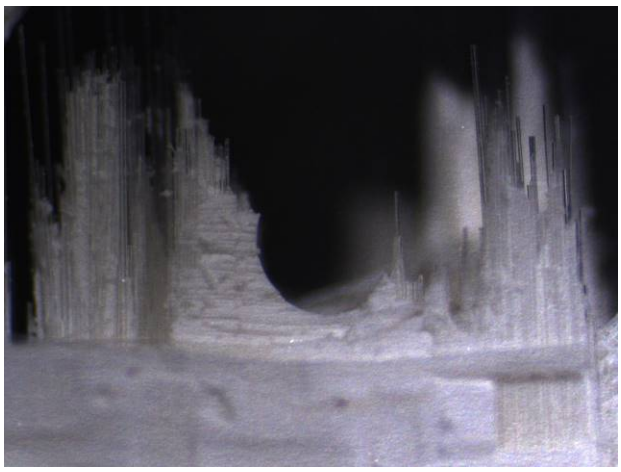

Figure A. 29: Fracture surface of specimen #4, tested in creep at 1200°C in air (σ_{cr} = 118 MPa, t_f = 0.59 h)

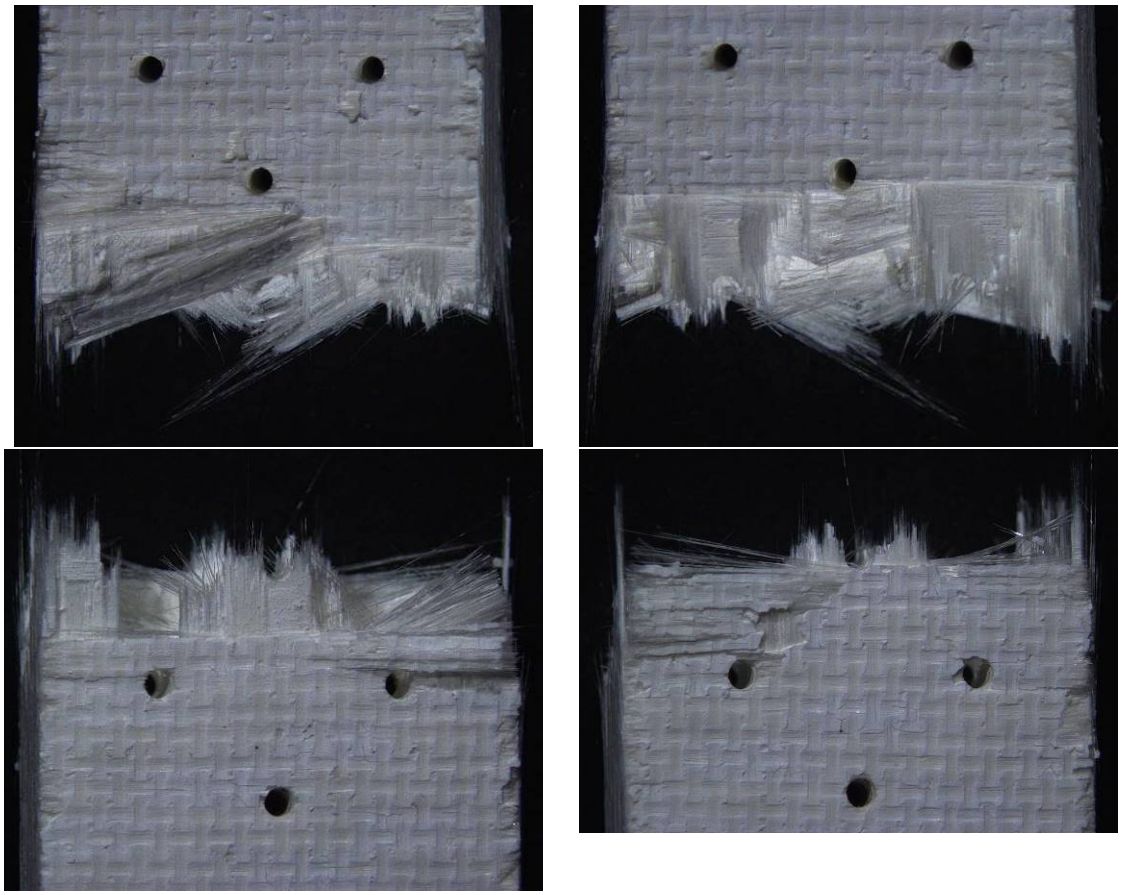

Figure A. 30: Top and bottom fracture surfaces of specimen #8, tested in creep at 1200°C in air (σ_{cr} = 150 MPa, t_f = 0.01 h)

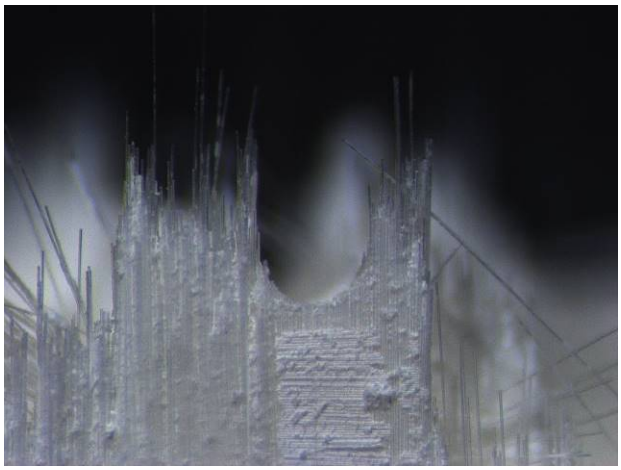

Figure A. 31: Fracture surface of specimen #8, tested in creep at 1200°C in air (σ_{cr} = 150 MPa, t_f = 0.01 h)

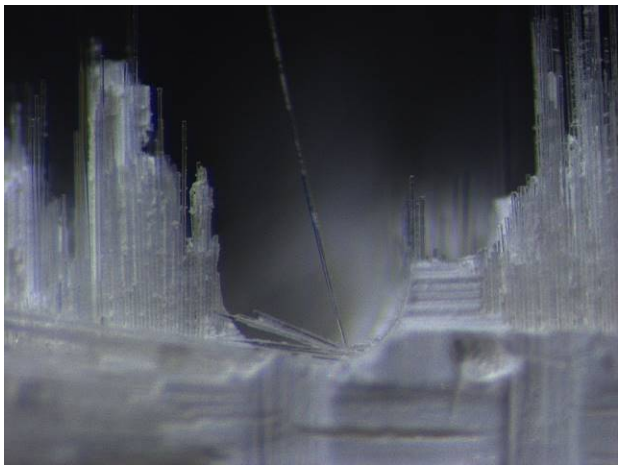

Figure A. 32: Fracture surface of specimen #8, tested in creep at 1200°C in air (σ_{cr} = 150 MPa, t_f = 0.01 h)

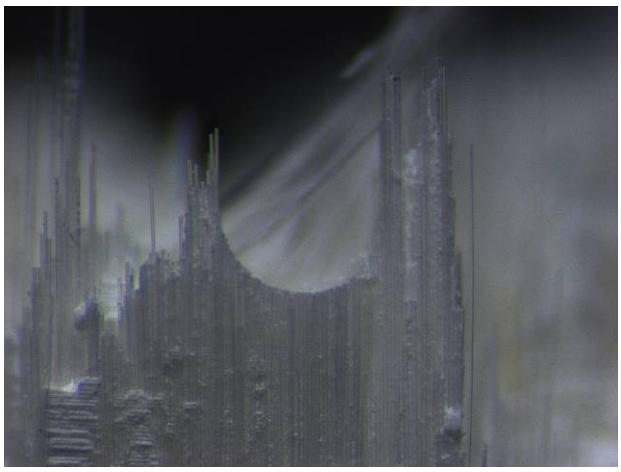

Figure A. 33: Fracture surface of specimen #8, tested in creep at 1200°C in air (σ_{cr} = 150 MPa, t_f = 0.01 h)

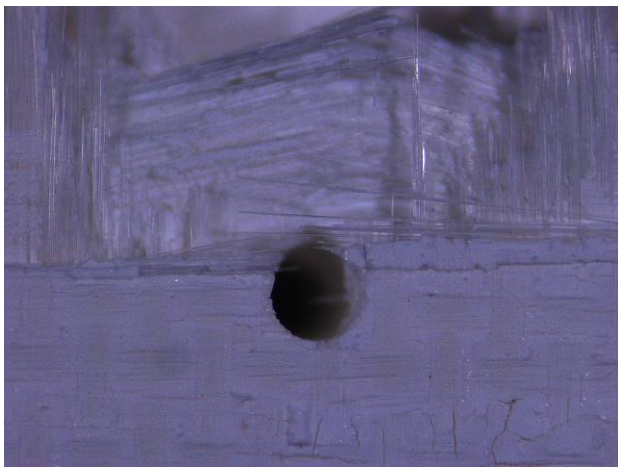

Figure A. 34: Fracture surface of specimen #8, tested in creep at 1200°C in air (σ_{cr} = 150 MPa, t_f = 0.01 h)

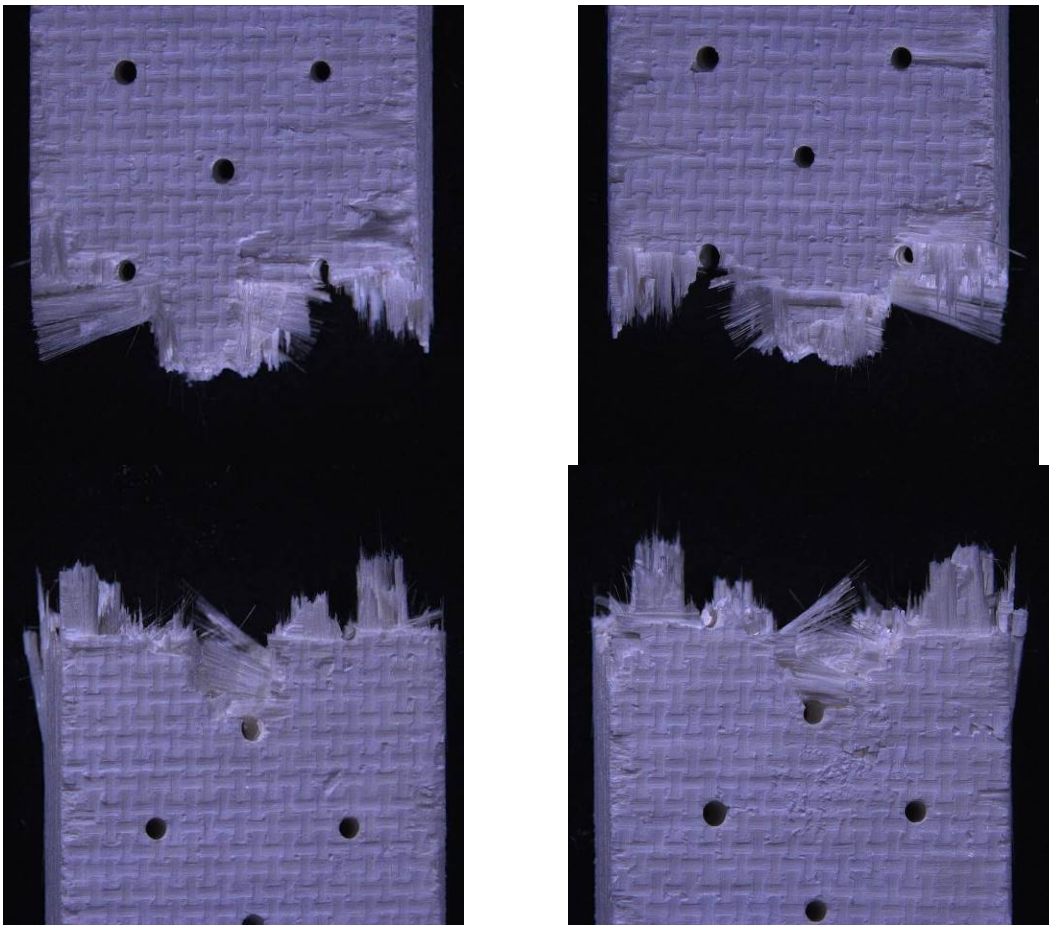

Figure A. 35: Top and bottom fracture surfaces of specimen #12, tested in tension to failure following 100 h creep at 46 MPa at 1200°C in steam

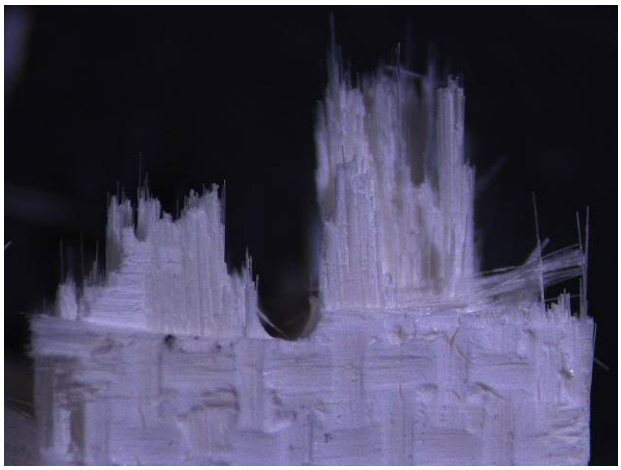

Figure A. 36: Fracture surface of specimen #12, tested in tension to failure following 100 h creep at 46 MPa at 1200°C in steam

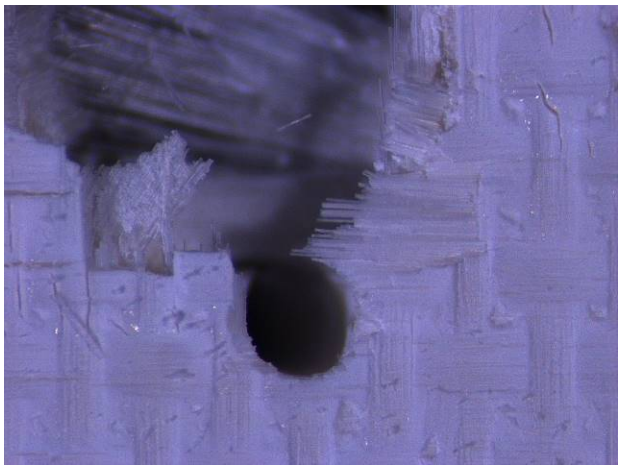

Figure A. 37: Fracture surface of specimen #12, tested in tension to failure following 100 h creep at 46 MPa at 1200°C in steam

Figure A. 38: Fracture surface of specimen #12, tested in tension to failure following 100 h creep at 46 MPa at 1200°C in steam

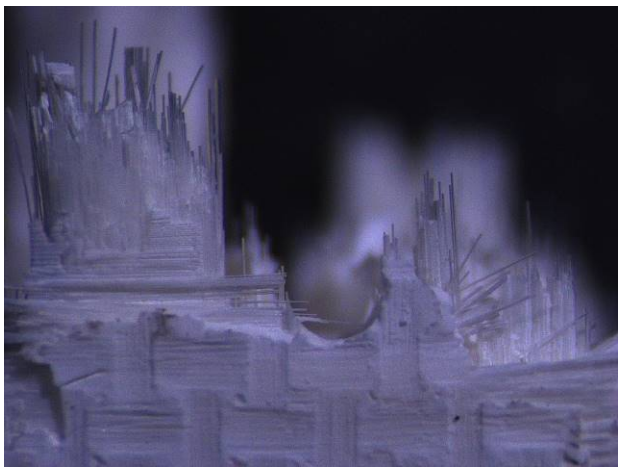

Figure A. 39: Fracture surface of specimen #12, tested in tension to failure following 100 h creep at 46 MPa at 1200°C in steam

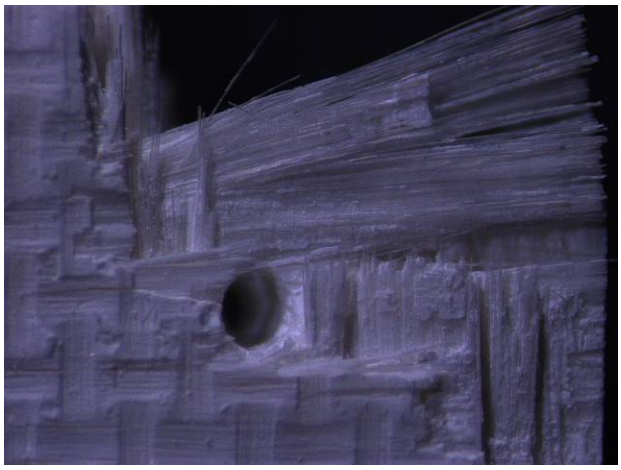

Figure A. 40: Fracture surface of specimen #12, tested in tension to failure following 100 h creep at 46 MPa at 1200°C in steam

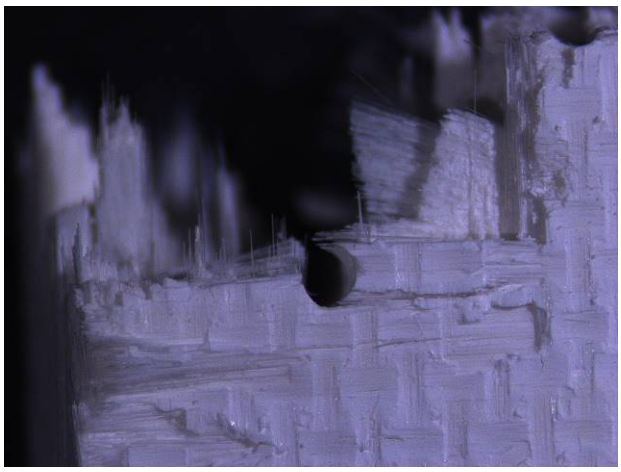

Figure A. 41: Fracture surface of specimen #12, tested in tension to failure following 100 h creep at 46 MPa at 1200°C in steam

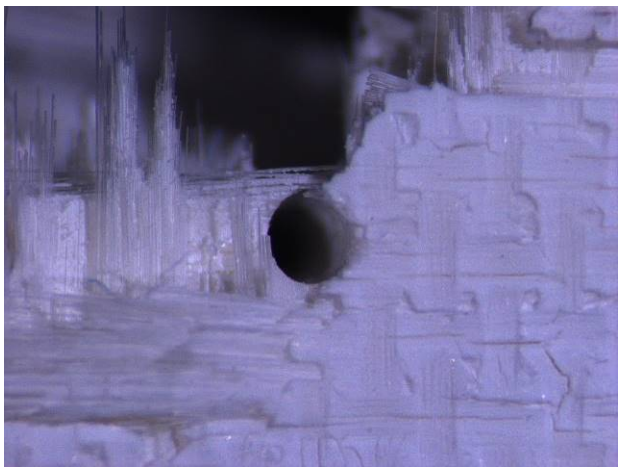

Figure A. 42: Fracture surface of specimen #12, tested in tension to failure following 100 h creep at 46 MPa at 1200°C in steam

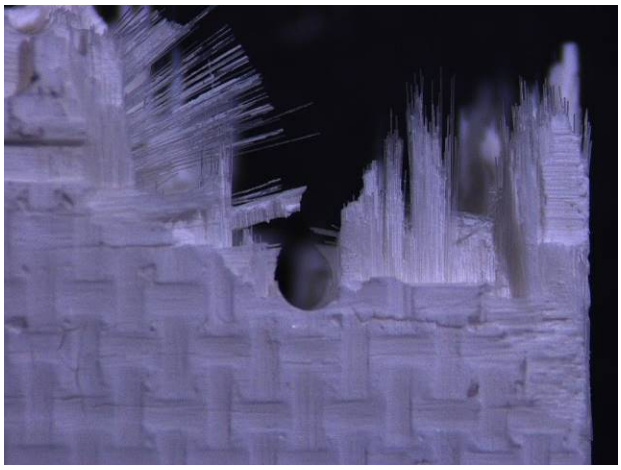

Figure A. 43: Fracture surface of specimen #12, tested in tension to failure following 100 h creep at 46 MPa at 1200°C in steam

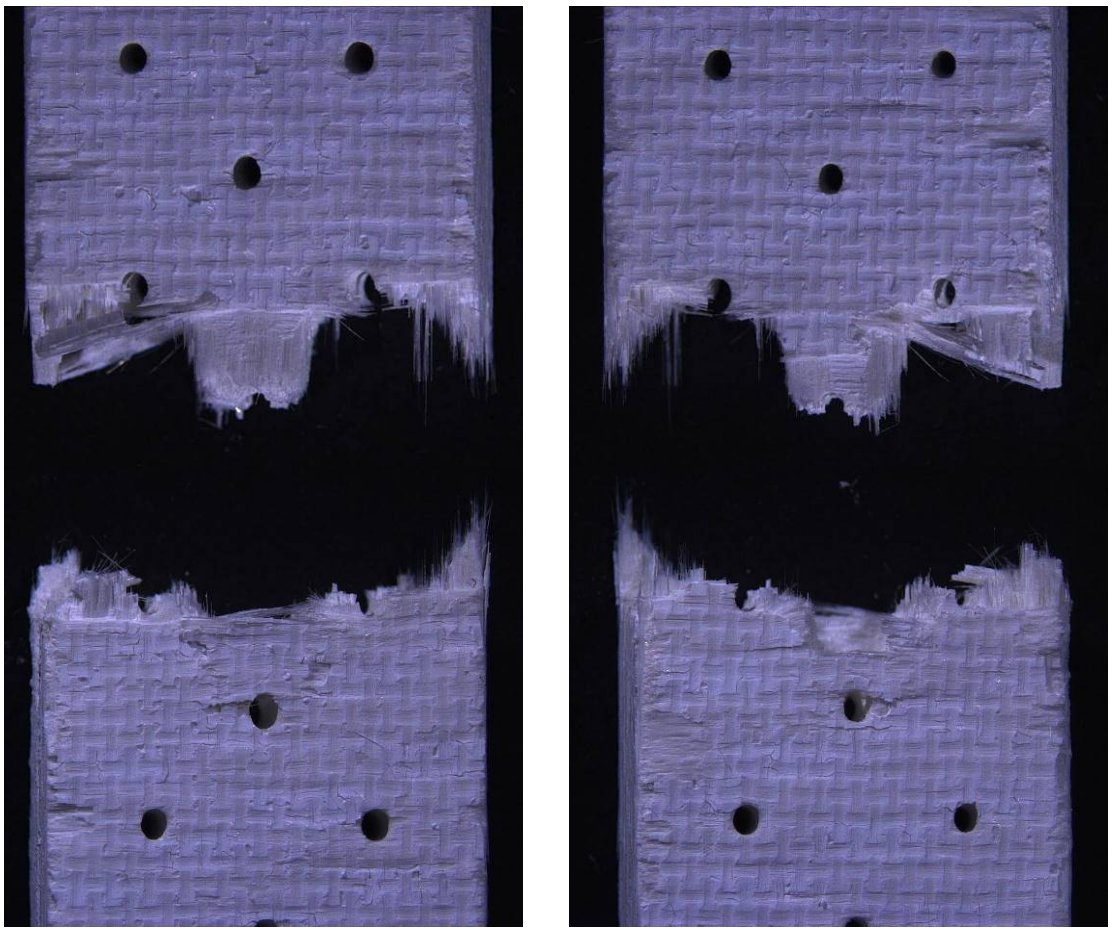

Figure A. 44: Top and bottom fracture surfaces of specimen #13, tested in creep at 1200°C in steam (σ_{cr} = 69 MPa, t_f = 25.55 h)

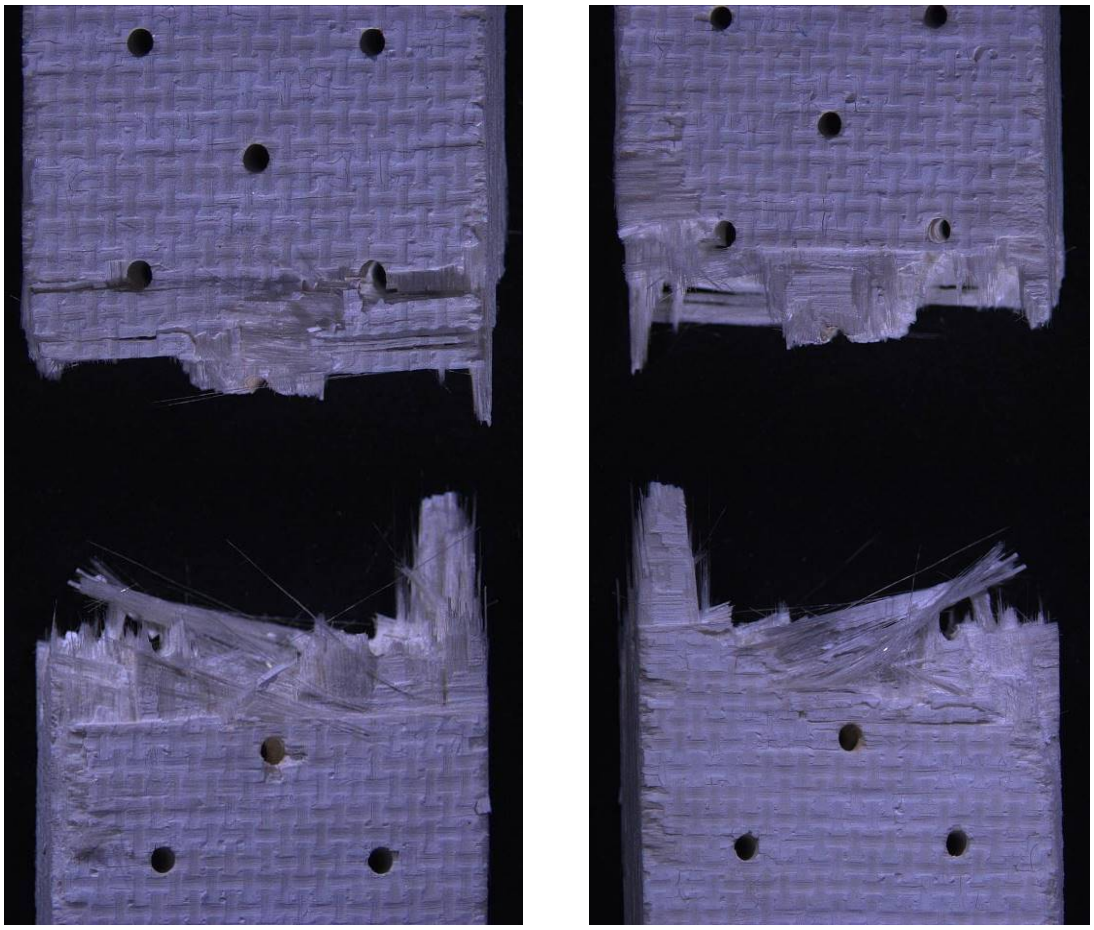

Figure A. 45: Top and bottom fracture surfaces of specimen #10, tested in creep at 1200°C in steam (σ_{cr} = 93 MPa, t_f = 6.05 h)

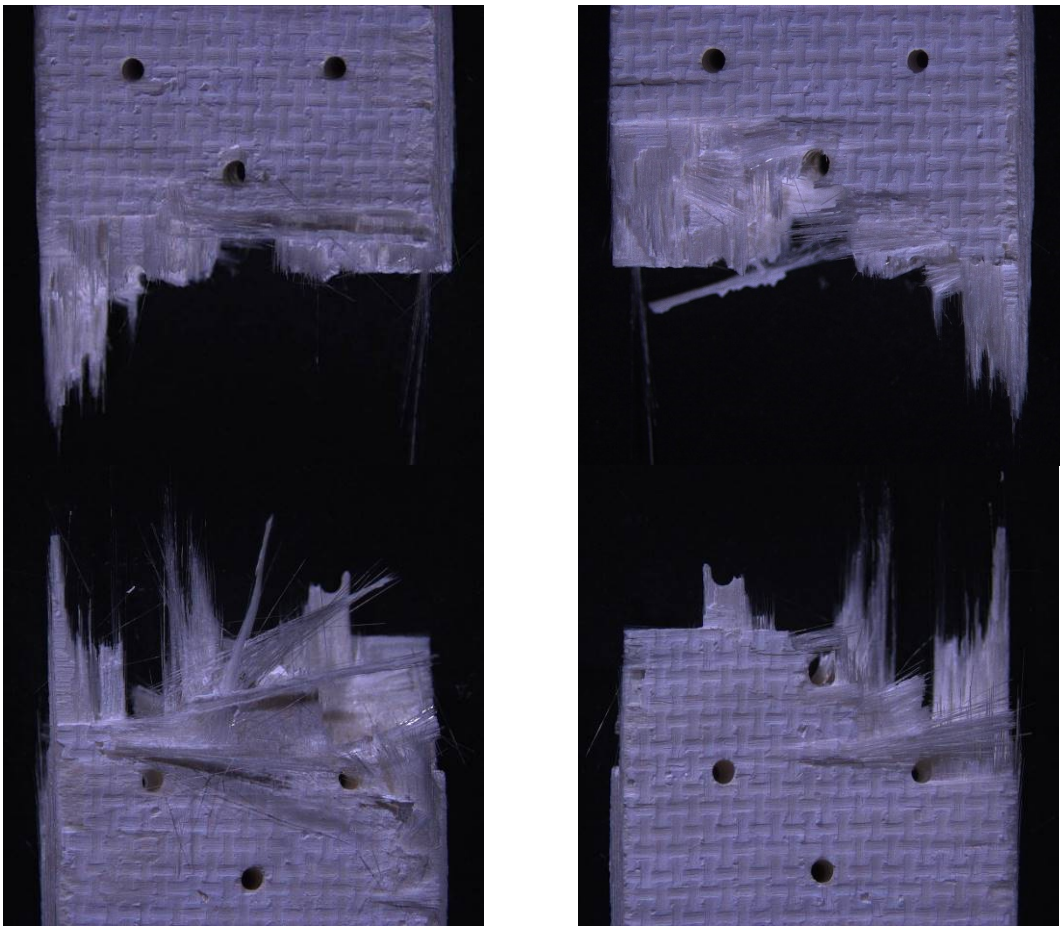

Figure A. 46: Top and bottom fracture surfaces of specimen #9, tested in creep at 1200°C in steam (σ_{cr} = 116 MPa, t_f = 0.61 h)

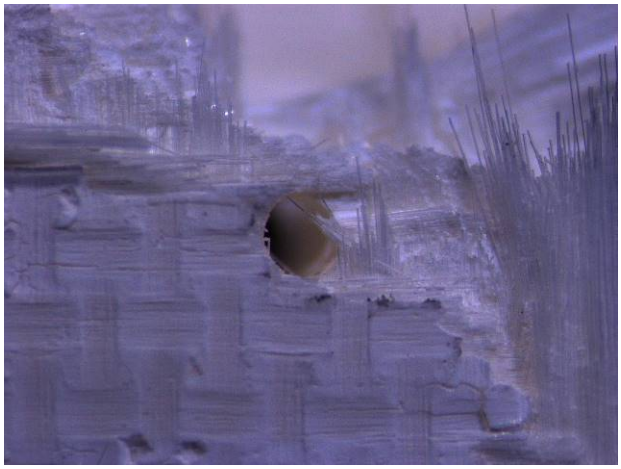

Figure A. 47: Fracture surface of specimen #9, tested in creep at 1200°C in steam (σ_{cr} = 116 MPa, t_f = 0.61 h)

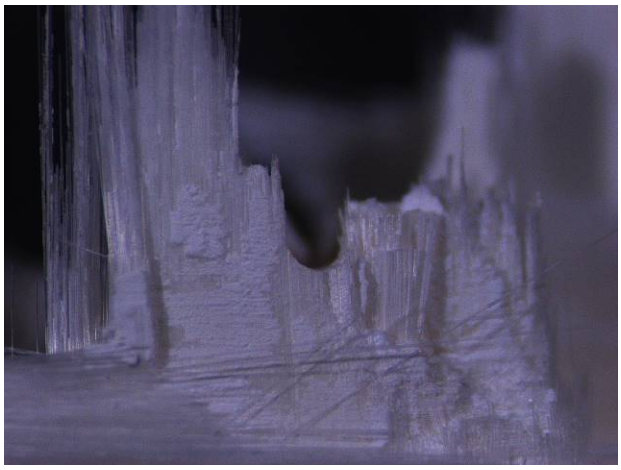

Figure A. 48: Fracture surface of specimen #9, tested in creep at 1200°C in steam (σ_{cr} = 116 MPa, t_f = 0.61 h)

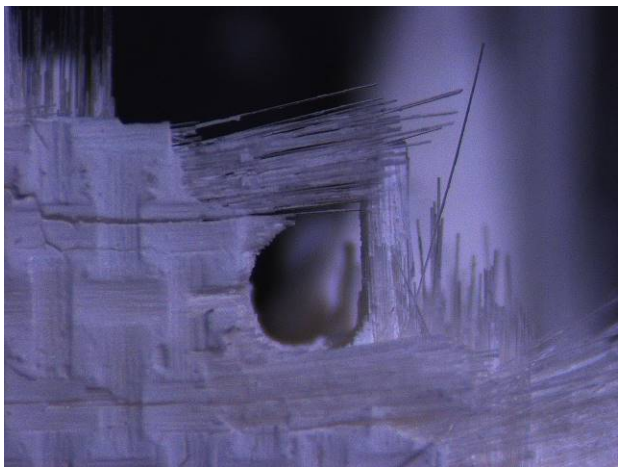

Figure A. 49: Fracture surface of specimen #9, tested in creep at 1200°C in steam (σ_{cr} = 116 MPa, t_f = 0.61 h)

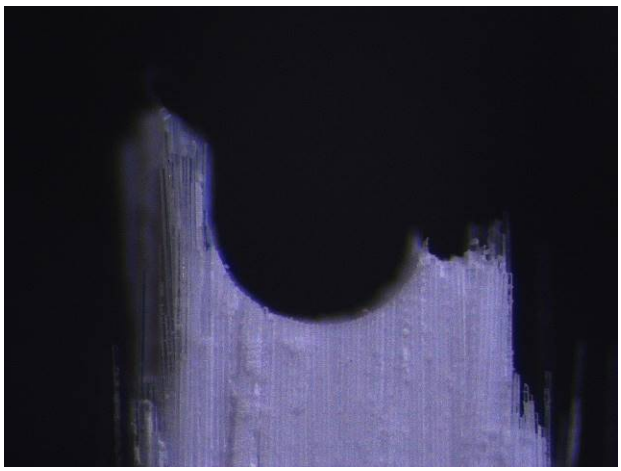

Figure A. 50: Fracture surface of specimen #9, tested in creep at 1200°C in steam (σ_{cr} = 116 MPa, t_f = 0.61 h)

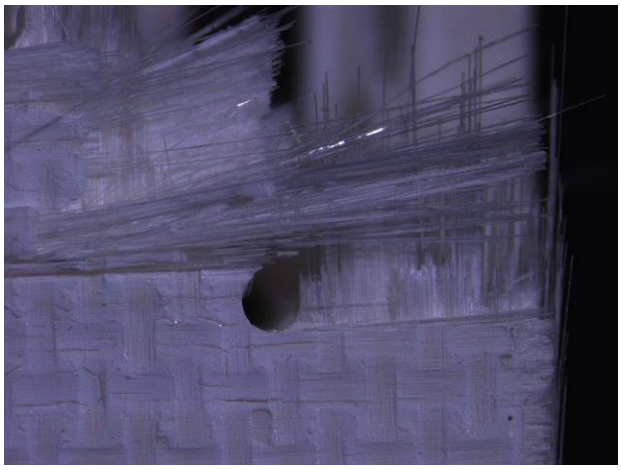

Figure A. 51: Fracture surface of specimen #9, tested in creep at 1200°C in steam (σ_{cr} = 116 MPa, t_f = 0.61 h)

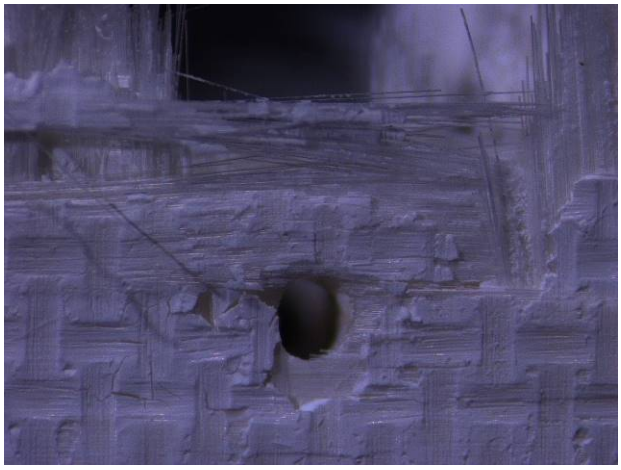

Figure A. 52: Fracture surface of specimen #9, tested in creep at 1200°C in steam (σ_{cr} = 116 MPa, t_f = 0.61 h)

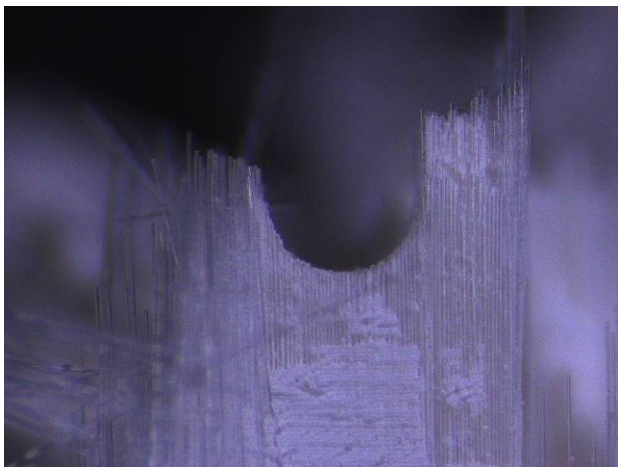

Figure A. 53: Fracture surface of specimen #9, tested in creep at 1200°C in steam (σ_{cr} = 116 MPa, t_f = 0.61 h)

Figure A. 54: Fracture surface of specimen #9, tested in creep at 1200°C in steam (σ_{cr} = 116 MPa, t_f = 0.61 h)

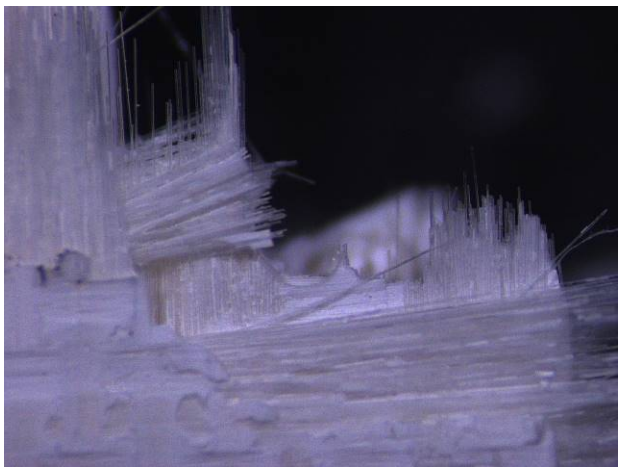

Figure A. 55: Fracture surface of specimen #9, tested in creep at 1200°C in steam (σ_{cr} = 116 MPa, t_f = 0.61 h)

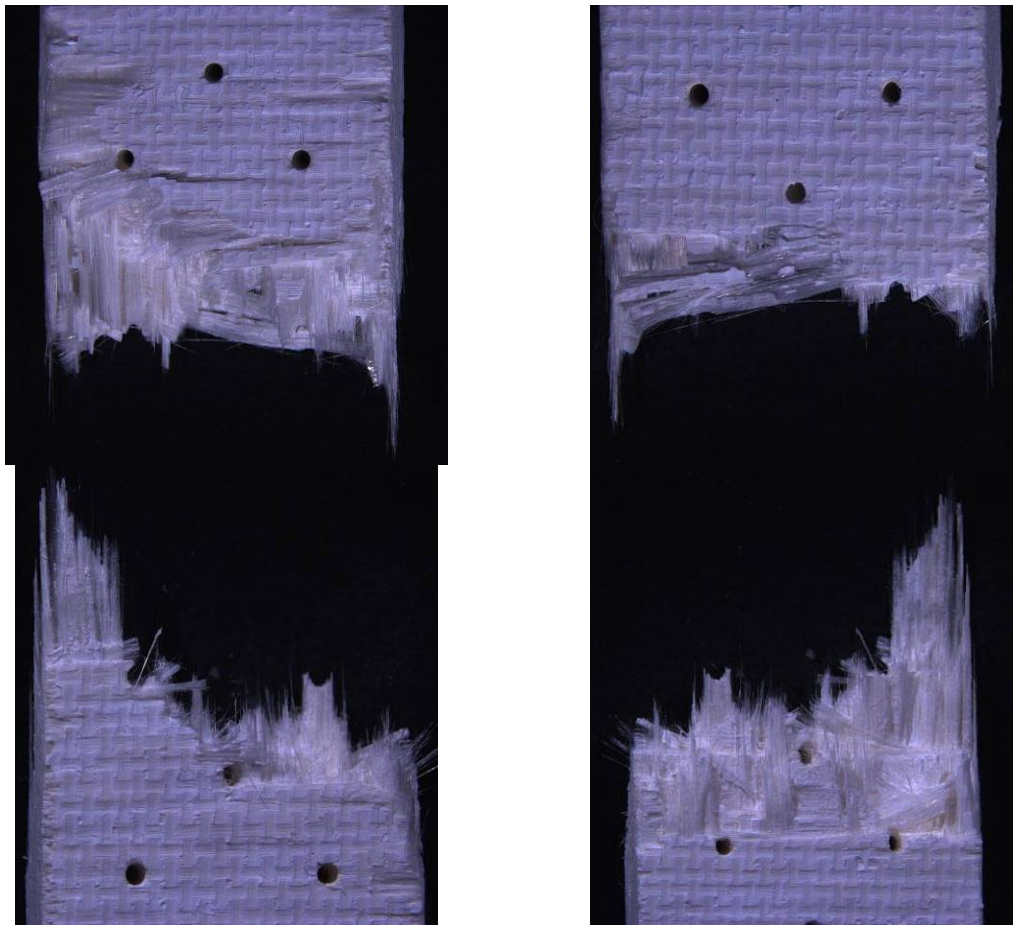

Figure A. 56: Top and bottom fracture surfaces of specimen #14, tested in creep at 1200°C in steam (σ_{cr} = 116 MPa, t_f = 0.48 h)

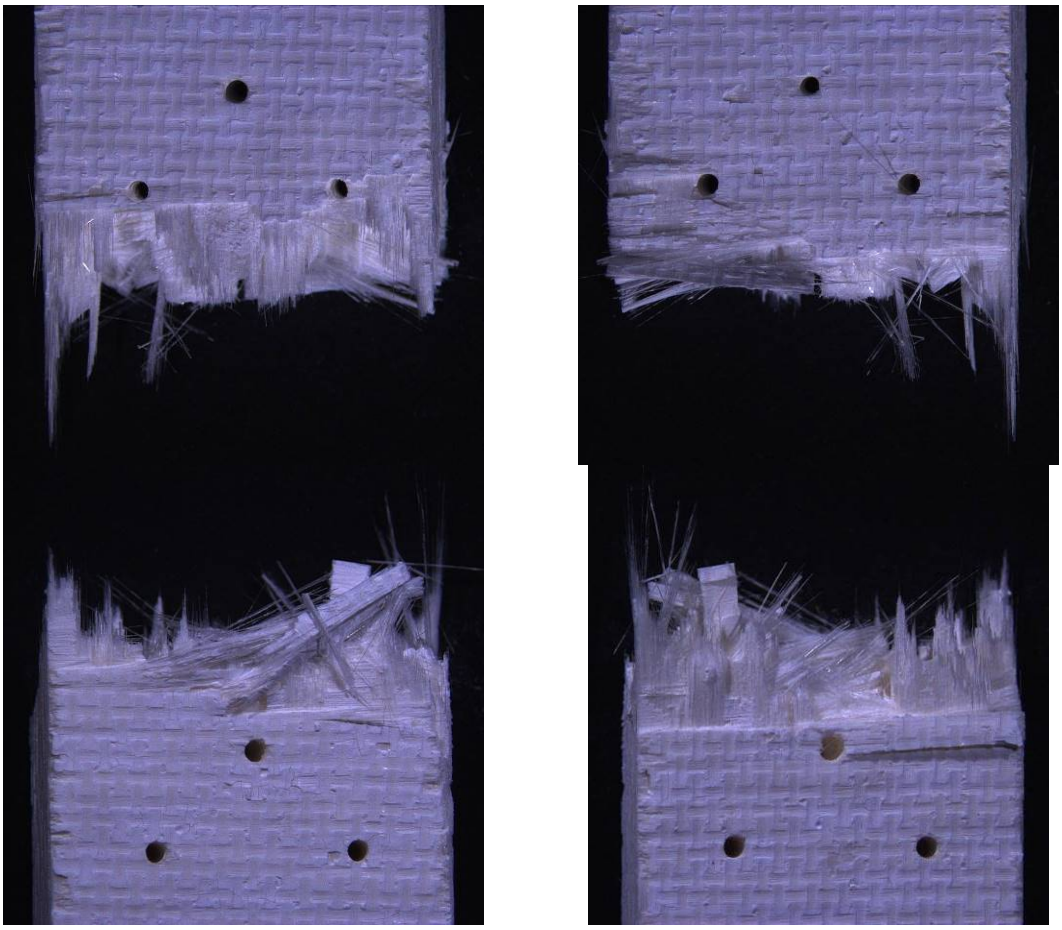

Figure A. 57: Top and bottom fracture surfaces of specimen #11, tested in creep at 1200°C in steam (σ_{cr} = 150 MPa, t_f = 0.04 h)

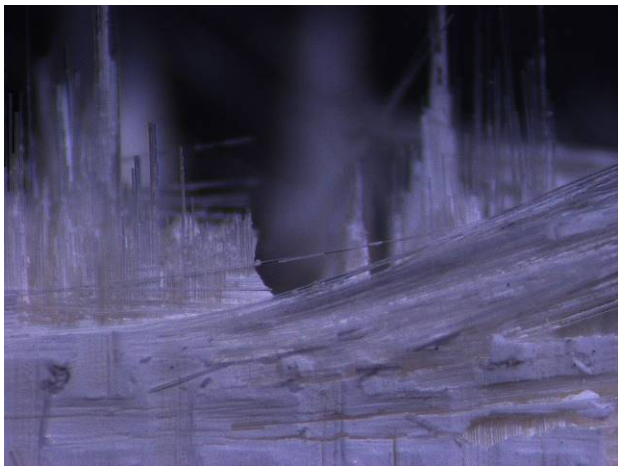

Figure A. 58: Fracture surface of specimen #11, tested in creep at 1200°C in steam (σ_{cr} = 150 MPa, t_f = 0.04 h)

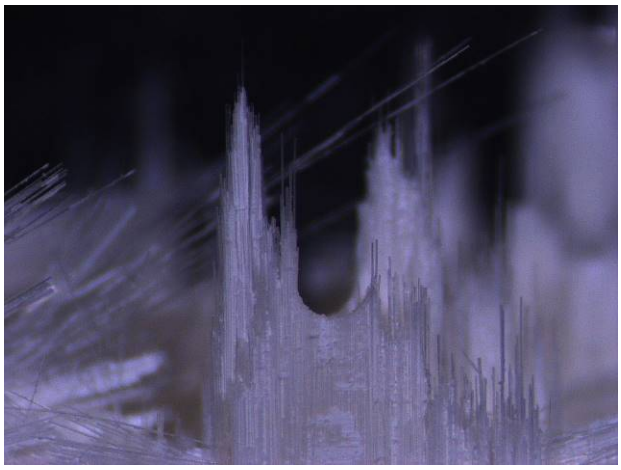

Figure A. 59: Fracture surface of specimen #11, tested in creep at 1200°C in steam (σ_{cr} = 150 MPa, t_f = 0.04 h)

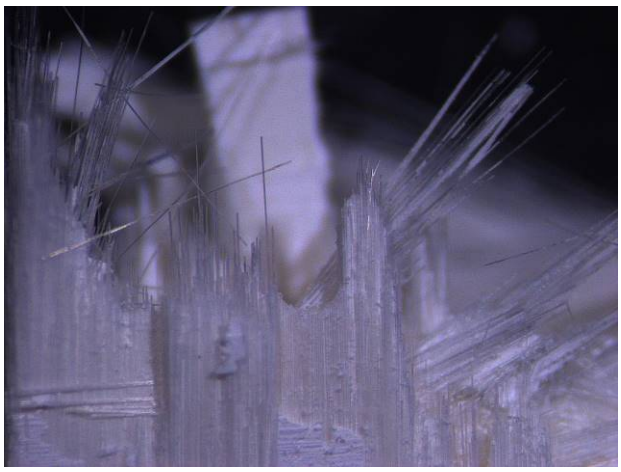

Figure A. 60: Fracture surface of specimen #11, tested in creep at 1200°C in steam (σ_{cr} = 150 MPa, t_f = 0.04 h)

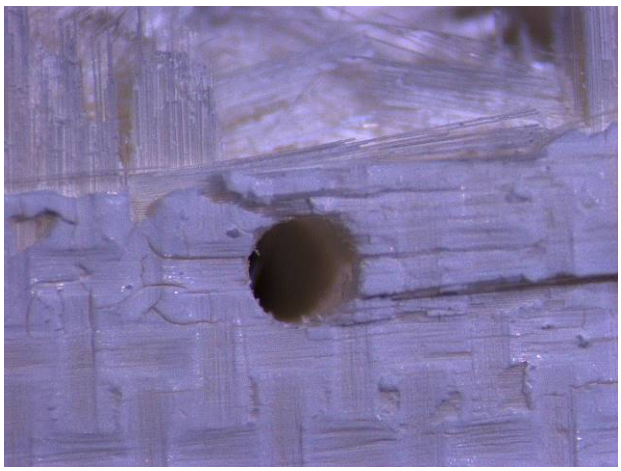

Figure A. 61: Fracture surface of specimen #11, tested in creep at 1200°C in steam (σ_{cr} = 150 MPa, t_f = 0.04 h)

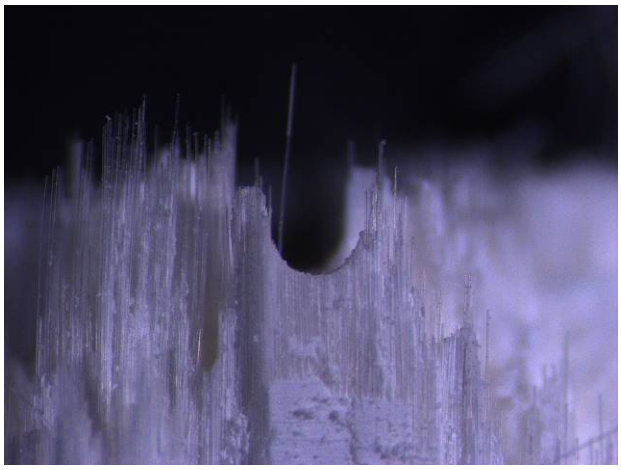

Figure A. 62: Fracture surface of specimen #11, tested in creep at 1200°C in steam (σ_{cr} = 150 MPa, t_f = 0.04 h)

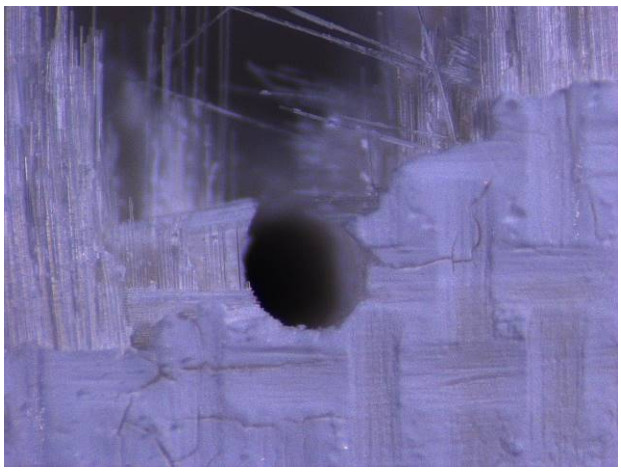

Figure A. 63: Fracture surface of specimen #11, tested in creep at 1200°C in steam (σ_{cr} = 150 MPa, t_f = 0.04 h)

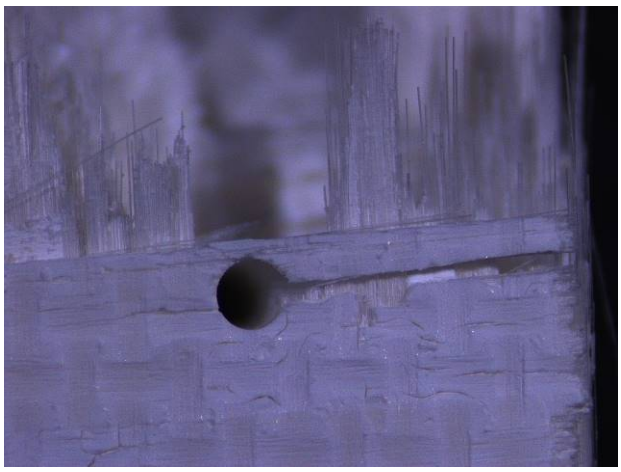

Figure A. 64: Fracture surface of specimen #11, tested in creep at 1200°C in steam (σ_{cr} = 150 MPa, t_f = 0.04 h)

Appendix B: Computed Tomography Images

As discussed in section 4.6.2, a systematic approached was used to identify the damage zone that penetrated the deepest in each specimen. The following CT images show the same progression for each specimen, starting with a 3D image of one half of a fracture surface (top or bottom), then capturing 2D (x-y plane) images while stepping down the specimen gage section. 2D (x-z plane) images were taken periodically to view the bottom of a penetrating damage zone. Note, the blue line/plane in the 3D image denotes the location of the x-y plane, and the green line in the 2D x-y image denotes the location of the x-z plane.

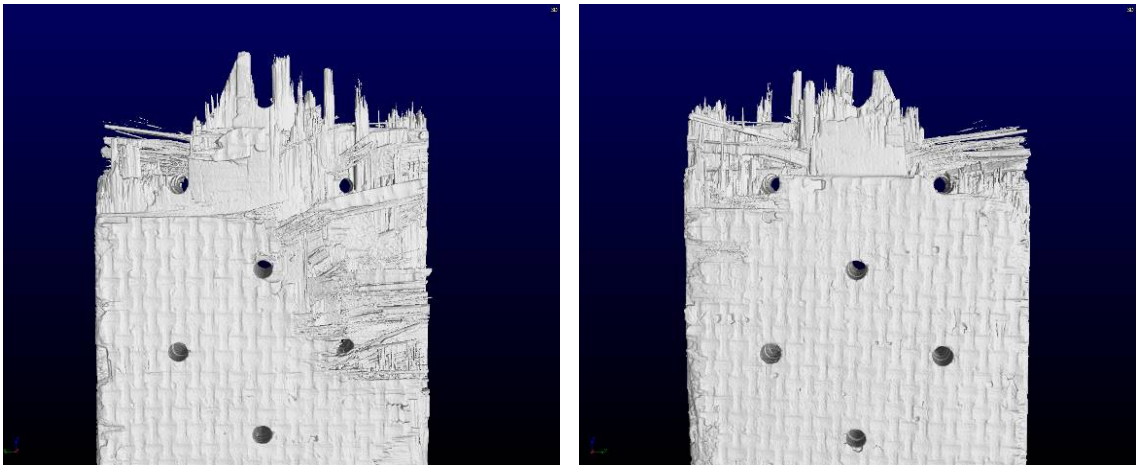

Figure B. 1: 3D image of the top fracture surface of specimen #3, tested in tension to failure at 1200°C in air

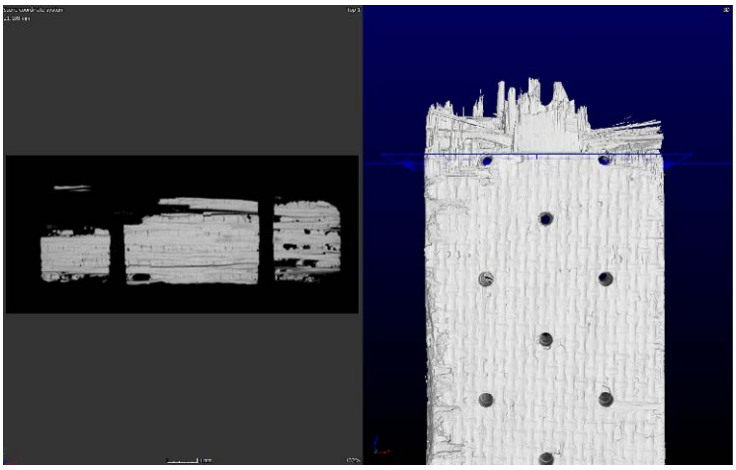

Figure B. 2: Step 1 – 2D (x-y plane) vs 3D location for specimen #3, tested in tension to failure at 1200°C in air

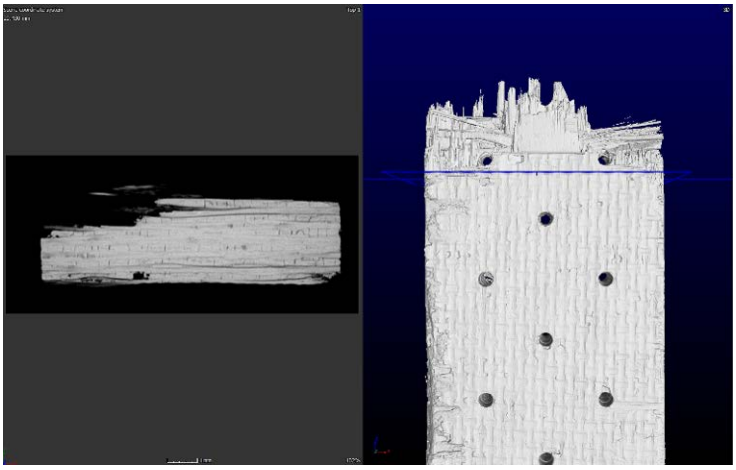

Figure B. 3: Step 2 – 2D (x-y plane) vs 3D location for specimen #3, tested in tension to failure at 1200°C in air

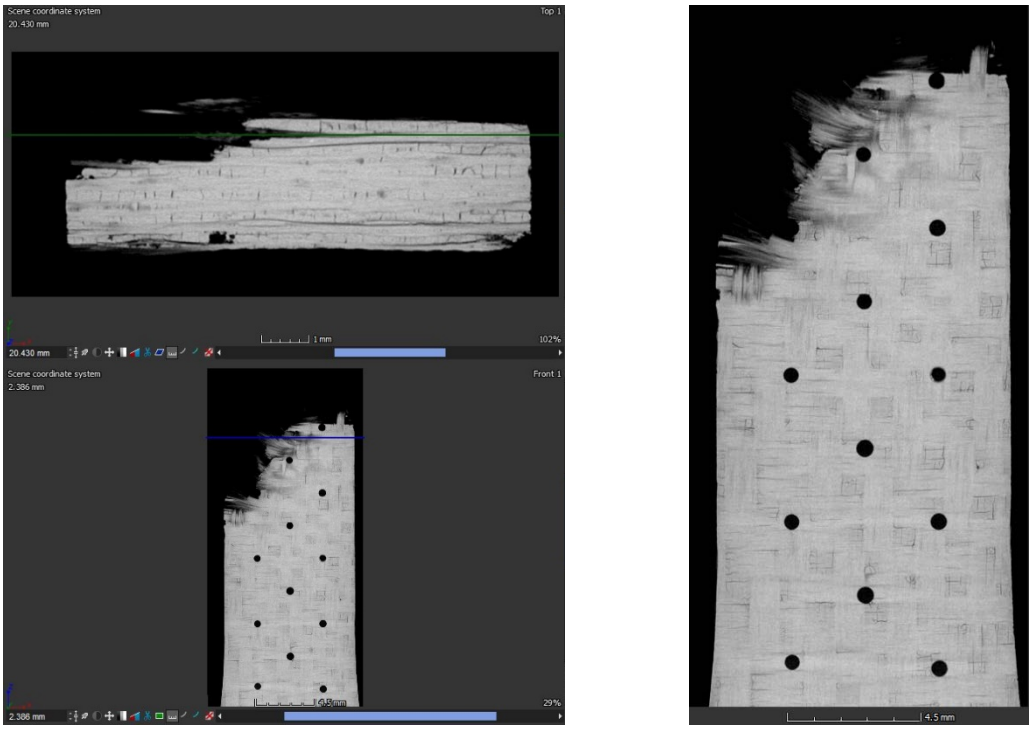

Figure B. 4: 2D (x-z plane) vs 2D (x-y plane) location showing damage zone at Step 2 for specimen #3, tested in tension to failure at 1200°C in air

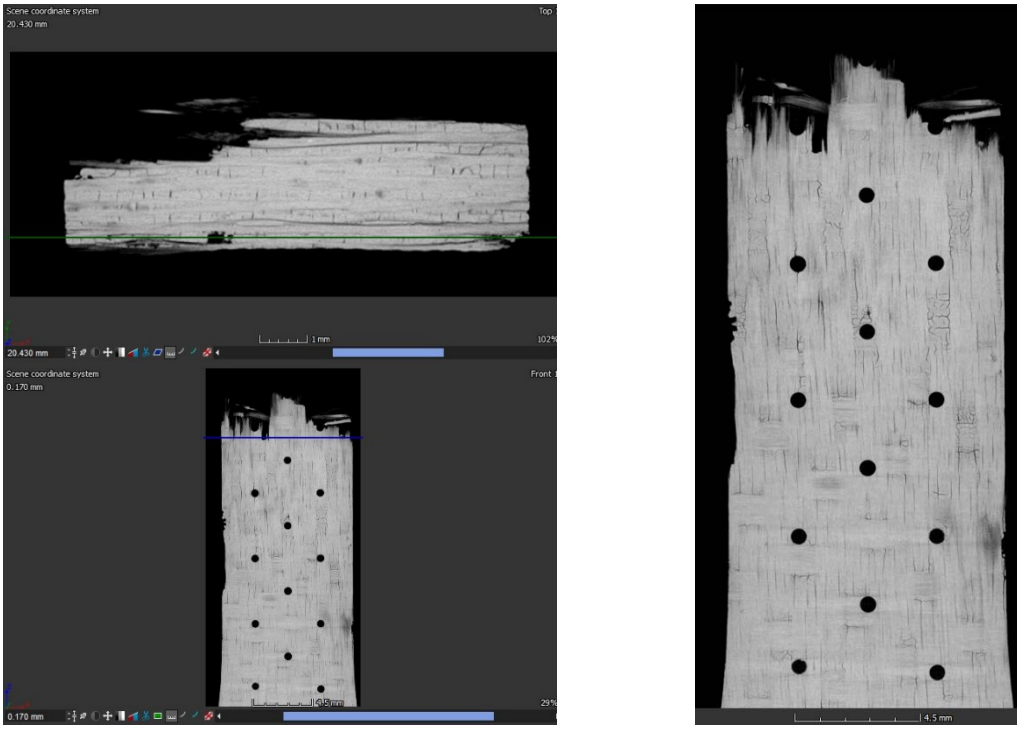

Figure B. 5: 2D (x-z plane) vs 2D (x-y plane) location showing damage zone at Step 2 for specimen #3, tested in tension to failure at 1200°C in air

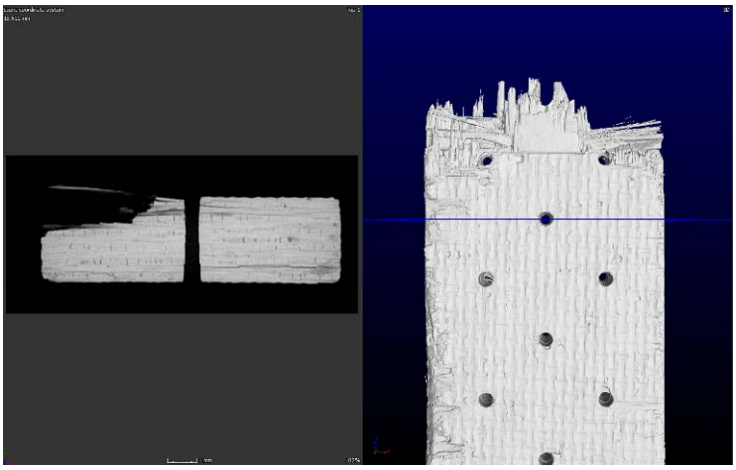

Figure B. 6: Step 3 – 2D (x-y plane) vs 3D location for specimen #3, tested in tension to failure at 1200°C in air

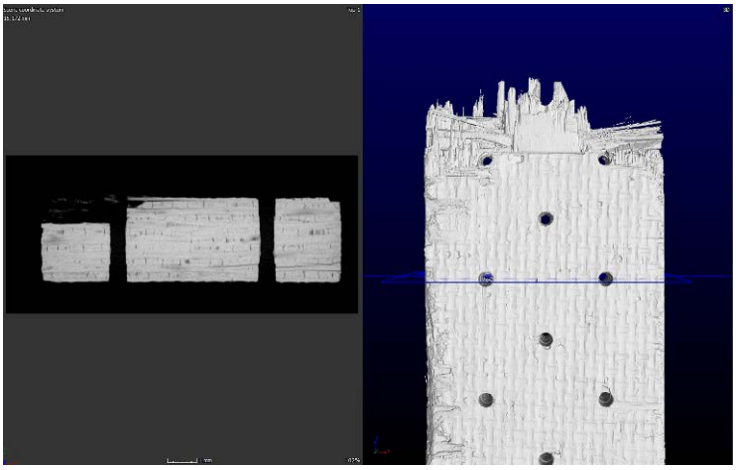

Figure B. 7: Step 4 – 2D (x-y plane) vs 3D location for specimen #3, tested in tension to failure at 1200°C in air

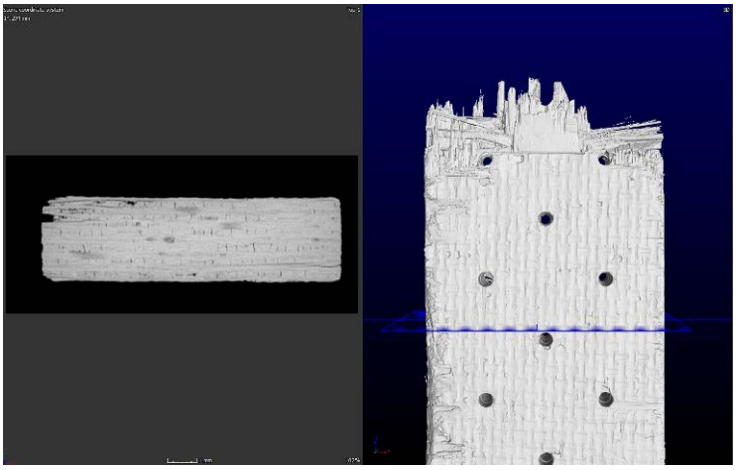

Figure B. 8: Step 5 – 2D (x-y plane) vs 3D location for specimen #3, tested in tension to failure at 1200°C in air

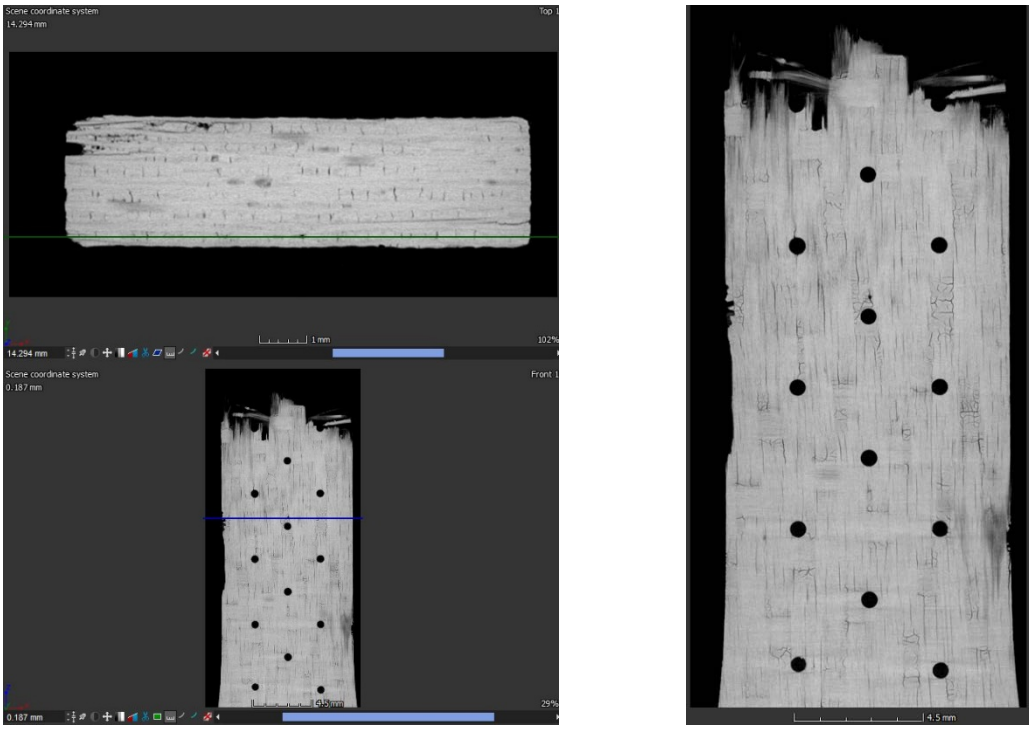

Figure B. 9: 2D (x-z plane) vs 2D (x-y plane) location showing damage zone at Step 5 for specimen #3, tested in tension to failure at 1200°C in air

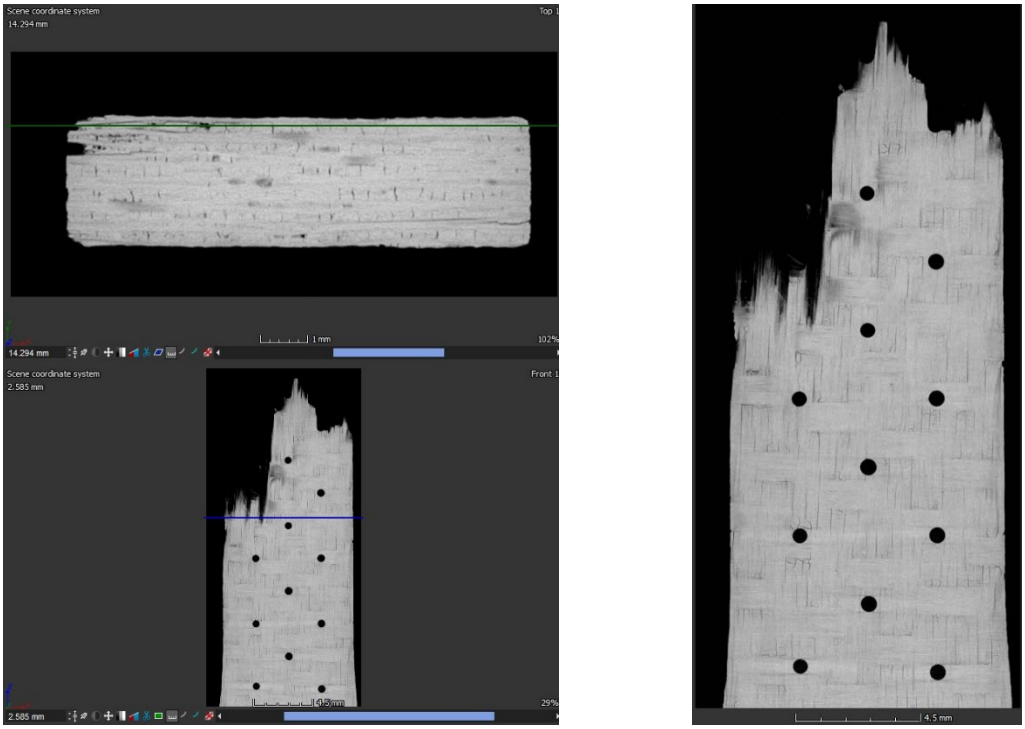

Figure B. 10: 2D (x-z plane) vs 2D (x-y plane) location showing damage zone at Step 5 for specimen #3, tested in tension to failure at 1200°C in air

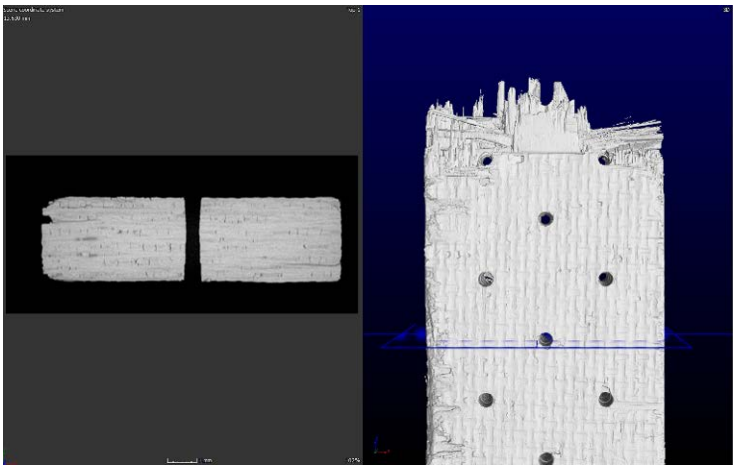

Figure B. 11: Step 6 – 2D (x-y plane) vs 3D location for specimen #3, tested in tension to failure at 1200°C in air

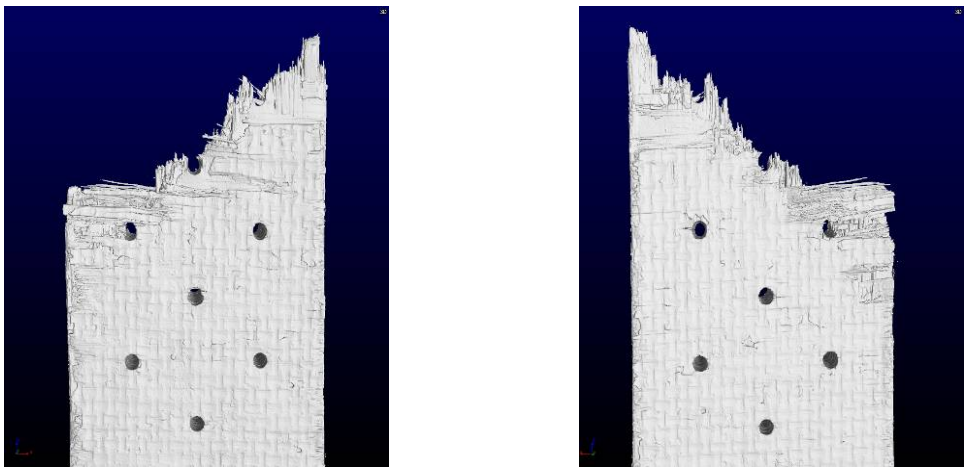

Figure B. 12: 3D image of the top fracture surface of specimen #7, tested in tension to failure following 100 h creep at 46 MPa at 1200°C in air

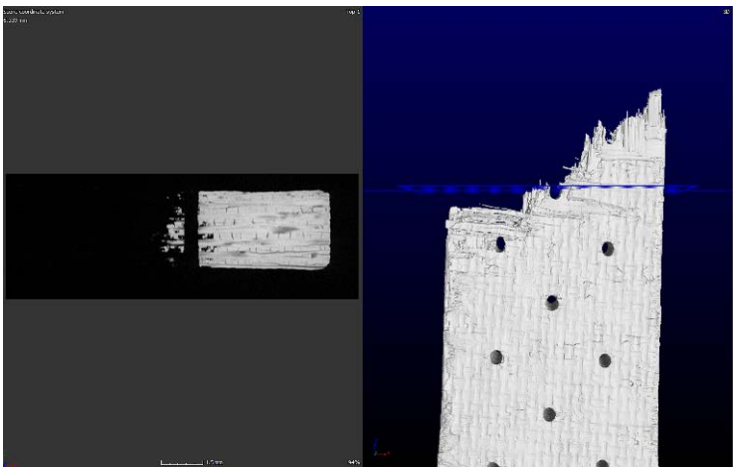

Figure B. 13: Step 1 – 2D (x-y plane) vs 3D location for specimen #7, tested in tension to failure following 100 h creep at 46 MPa at 1200°C in air

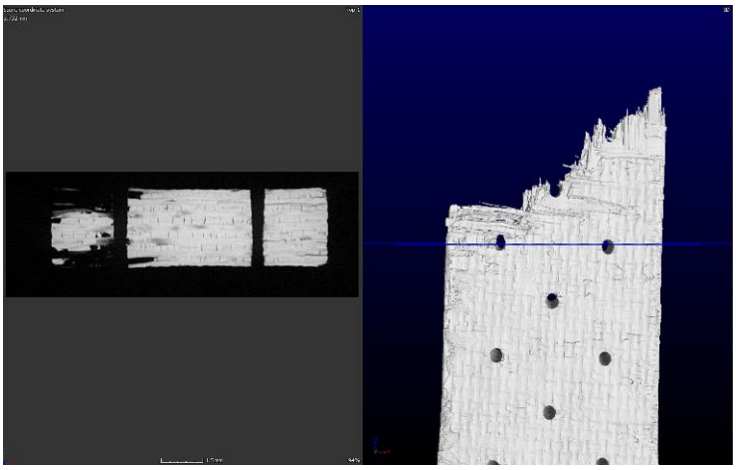

Figure B. 14: Step 2 – 2D (x-y plane) vs 3D location for specimen #7, tested in tension to failure following 100 h creep at 46 MPa at 1200°C in air

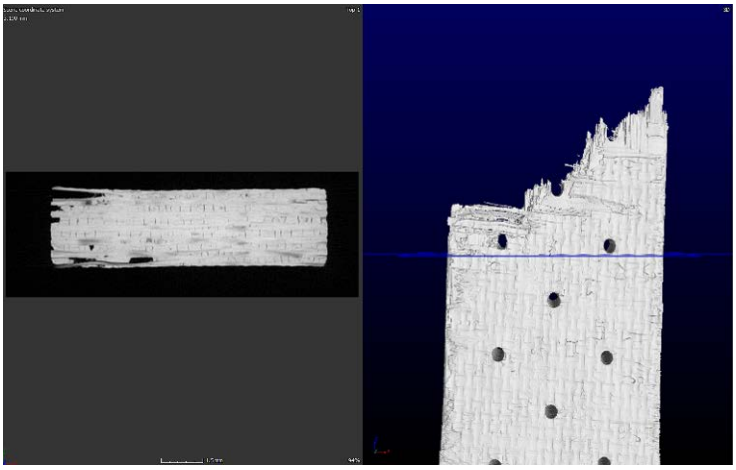

Figure B. 15: Step 3 – 2D (x-y plane) vs 3D location for specimen #7, tested in tension to failure following 100 h creep at 46 MPa at 1200°C in air

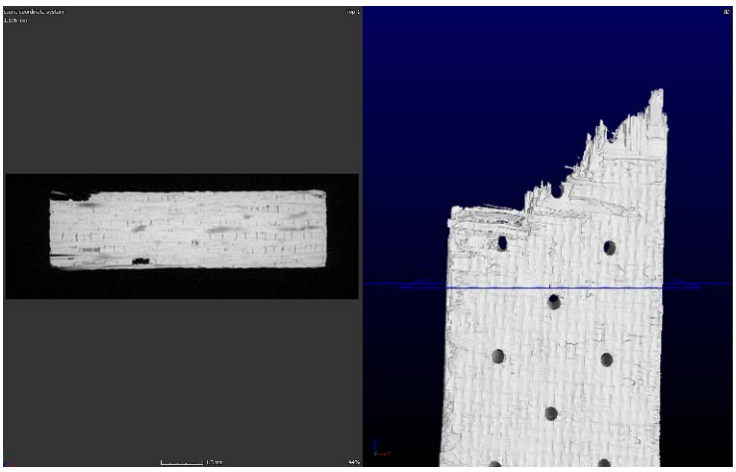

Figure B. 16: Step 4 – 2D (x-y plane) vs 3D location for specimen #7, tested in tension to failure following 100 h creep at 46 MPa at 1200°C in air

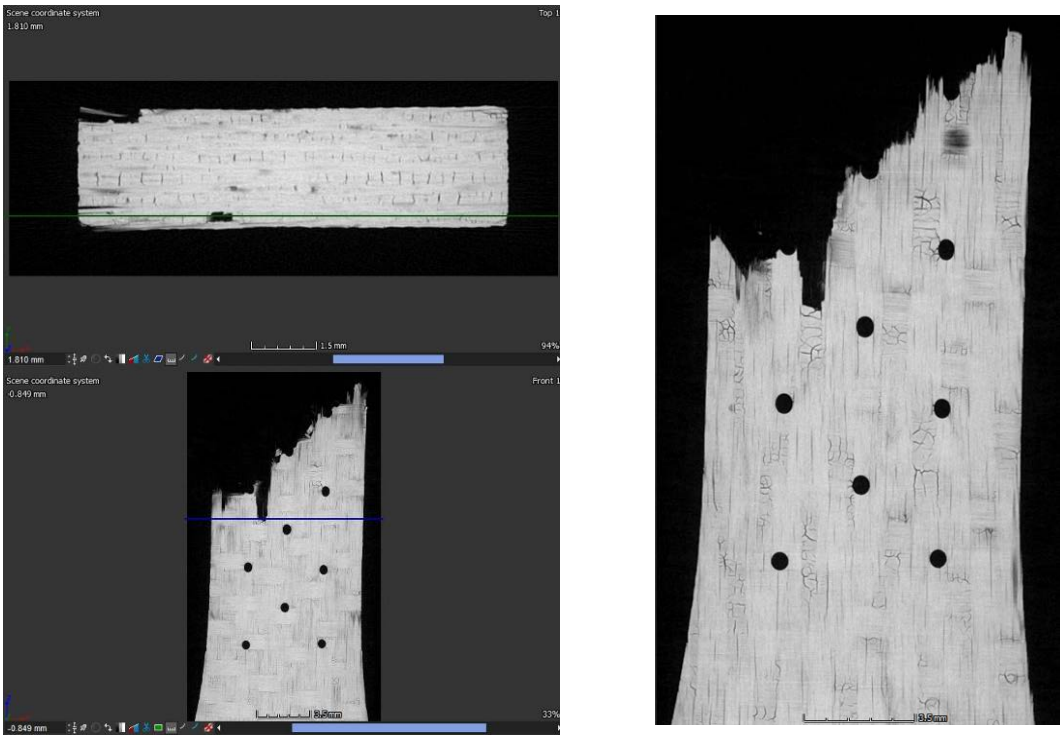

Figure B. 17: 2D (x-z plane) vs 2D (x-y plane) location showing damage zone at Step 4 for specimen #7, tested in tension to failure following 100 h creep at 46 MPa at 1200°C in air

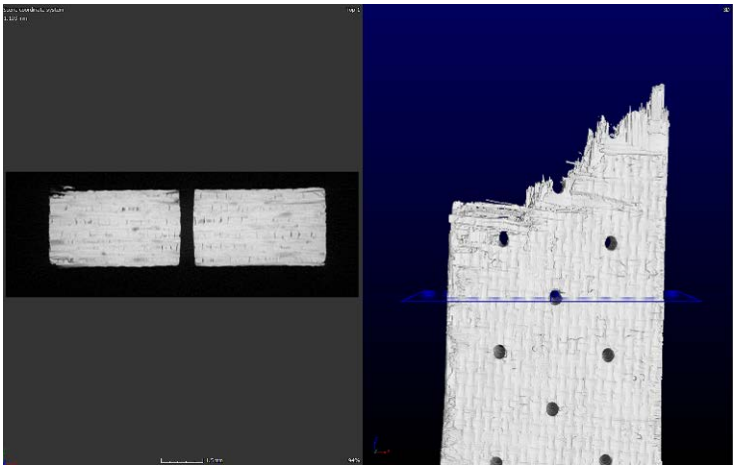

Figure B. 18: Step 5 – 2D (x-y plane) vs 3D location for specimen #7, tested in tension to failure following 100 h creep at 46 MPa at 1200°C in air

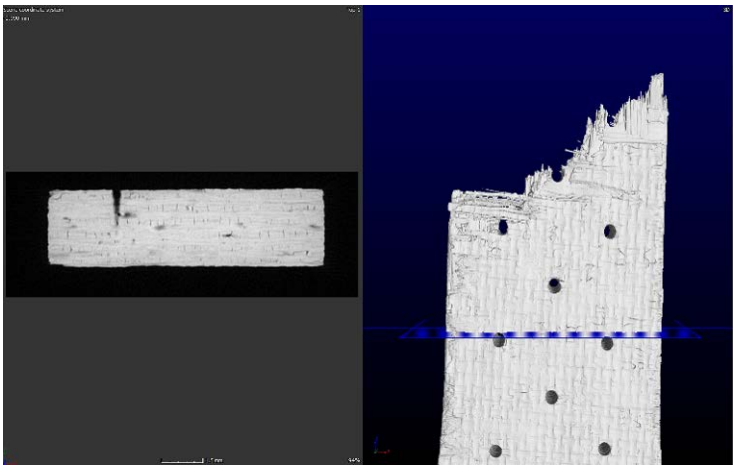

Figure B. 19: Step 6 – 2D (x-y plane) vs 3D location for specimen #7, tested in tension to failure following 100 h creep at 46 MPa at 1200°C in air

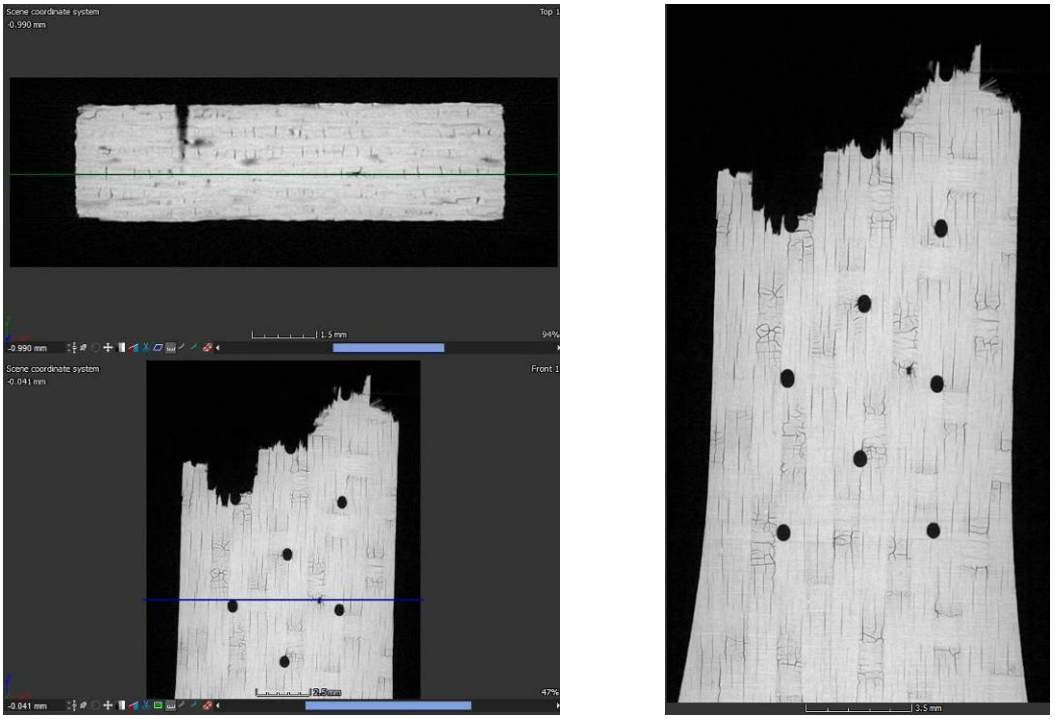

Figure B. 20: 2D (x-z plane) vs 2D (x-y plane) location showing damage zone at Step 6 for specimen #7, tested in tension to failure following 100 h creep at 46 MPa at 1200°C in air

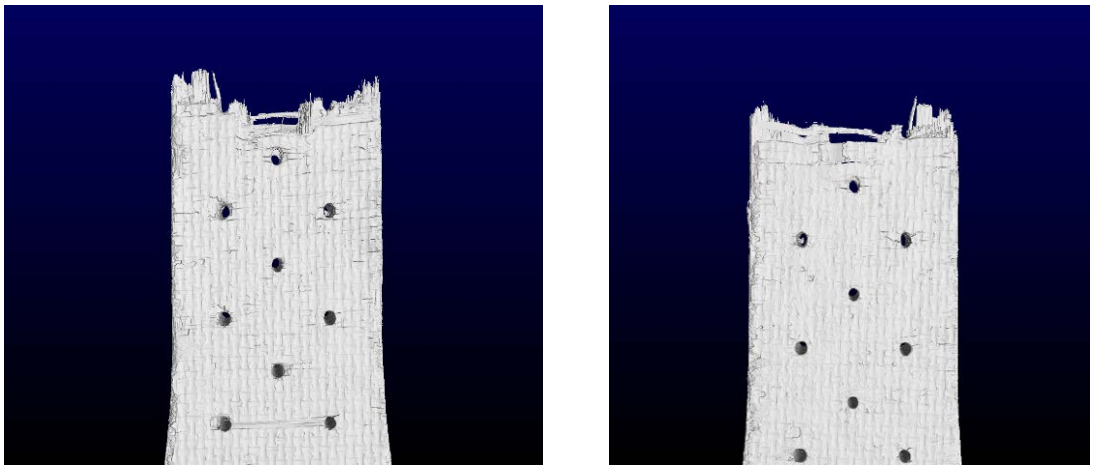

Figure B. 21: 3D image of the bottom fracture surface of specimen #6, tested in creep at 1200°C in air (σ_{cr} = 69 MPa, t_f = 30.95 h)

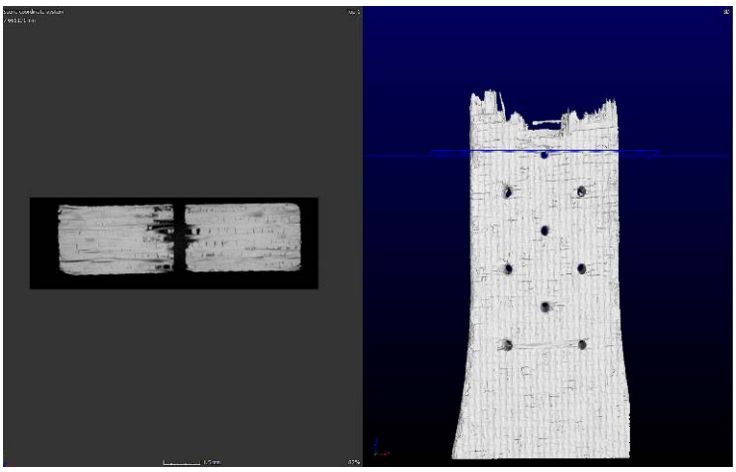

Figure B. 22: Step 1 – 2D (x-y plane) vs 3D location for specimen #6, tested in creep at 1200°C in air (σ_{cr} = 69 MPa, t_f = 30.95 h)

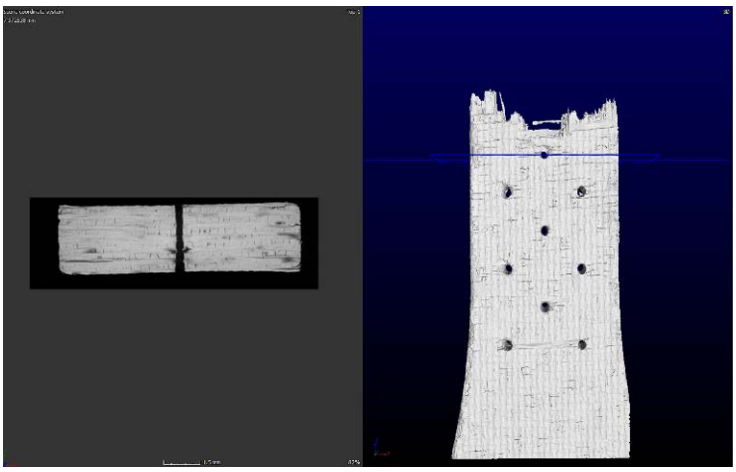

Figure B. 23: Step 2 – 2D (x-y plane) vs 3D location for specimen #6, tested in creep at 1200°C in air (σ_{cr} = 69 MPa, t_f = 30.95 h)

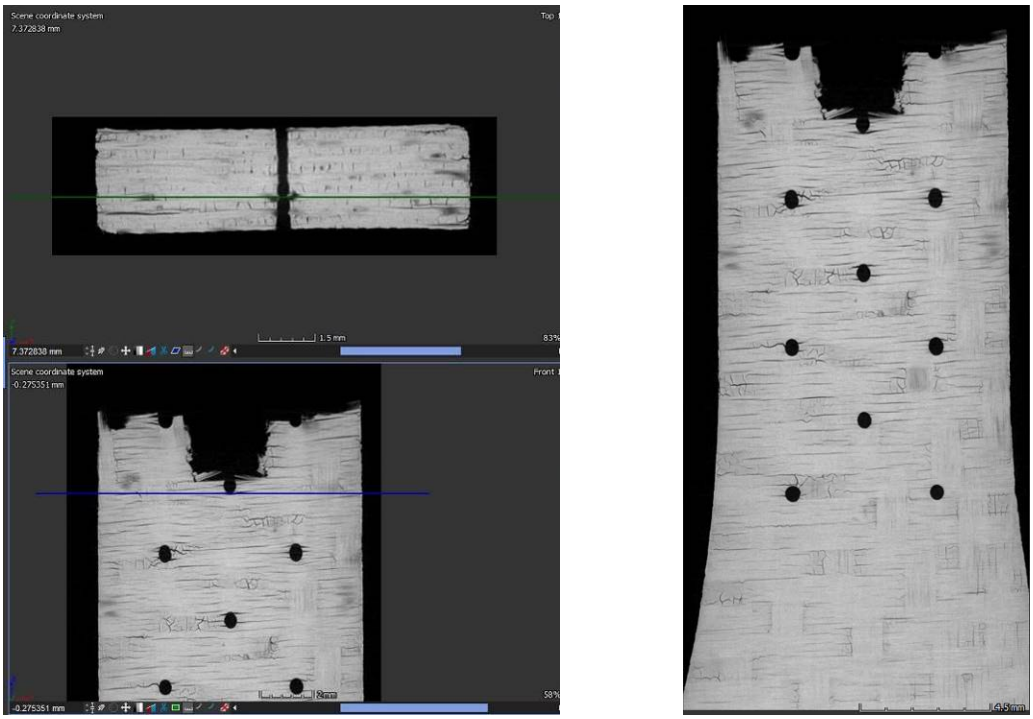

Figure B. 24: 2D (x-z plane) vs 2D (x-y plane) location showing damage zone at Step 2 for specimen #6, tested in creep at 1200°C in air (σ_{cr} = 69 MPa, t_f = 30.95 h)

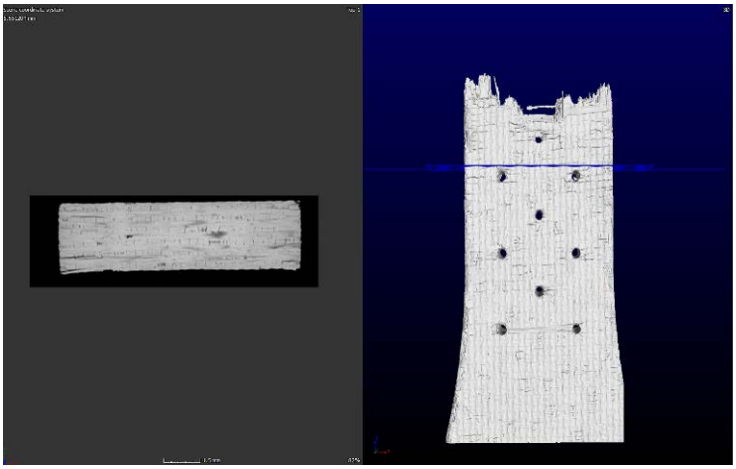

Figure B. 25: Step 3 – 2D (x-y plane) vs 3D location for specimen #6, tested in creep at 1200°C in air (σ_{cr} = 69 MPa, t_f = 30.95 h)

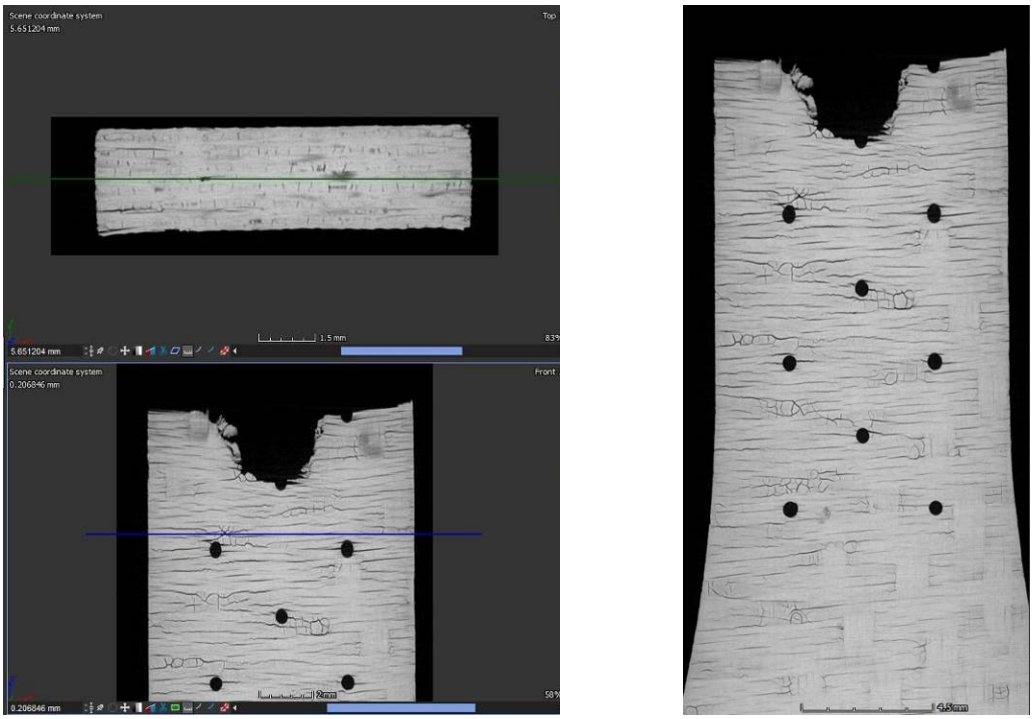

Figure B. 26: 2D (x-z plane) vs 2D (x-y plane) location showing damage zone at Step 3 for specimen #6, tested in creep at 1200°C in air (σ_{cr} = 69 MPa, t_f = 30.95 h)

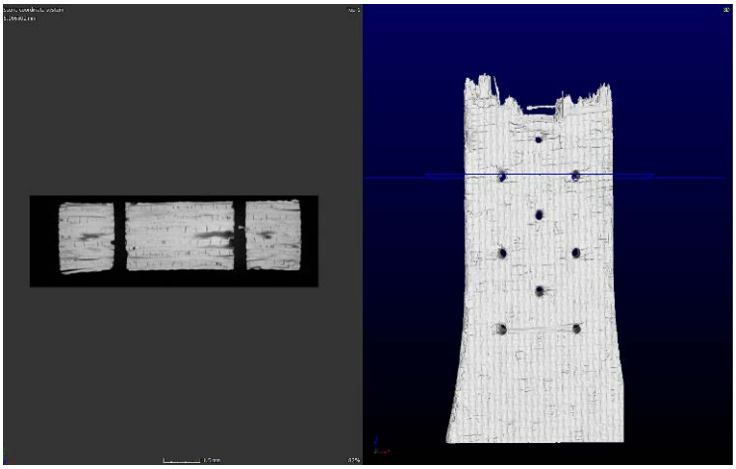

Figure B. 27: Step 4 – 2D (x-y plane) vs 3D location for specimen #6, tested in creep at 1200°C in air (σ_{cr} = 69 MPa, t_f = 30.95 h)

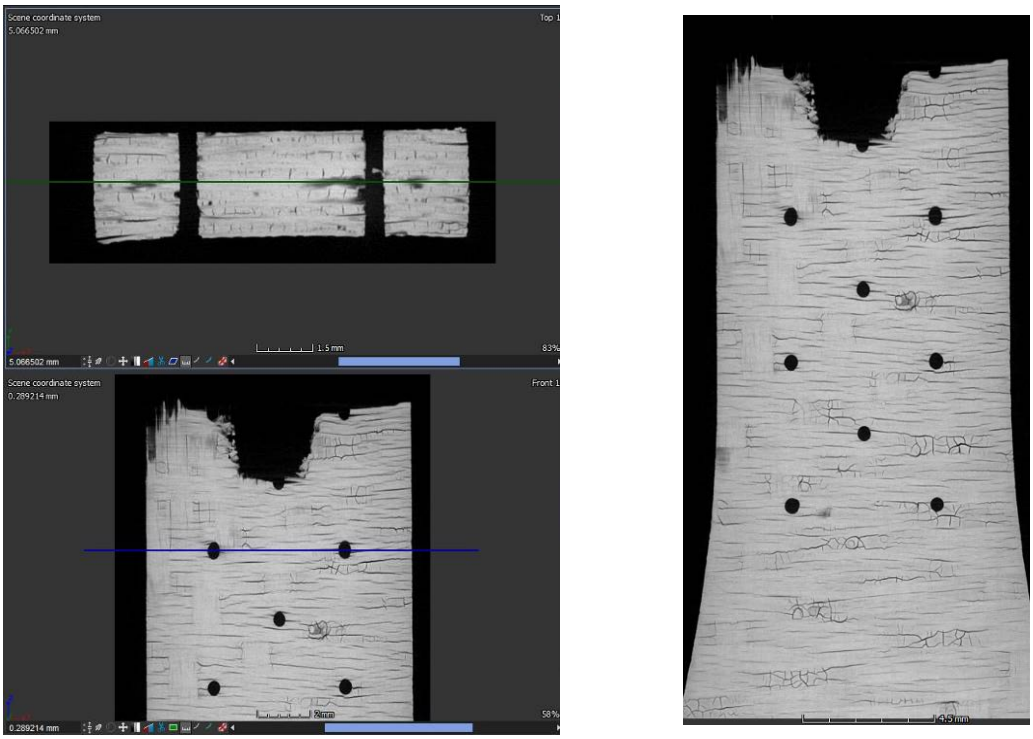

Figure B. 28: 2D (x-z plane) vs 2D (x-y plane) location showing damage zone at Step 4 for specimen #6, tested in creep at 1200°C in air (σ_{cr} = 69 MPa, t_f = 30.95 h)

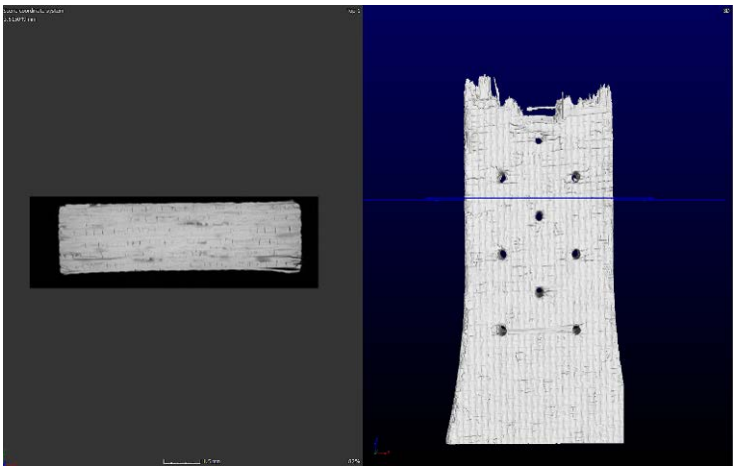

Figure B. 29: Step 5 – 2D (x-y plane) vs 3D location for specimen #6, tested in creep at 1200°C in air (σ_{cr} = 69 MPa, t_f = 30.95 h)

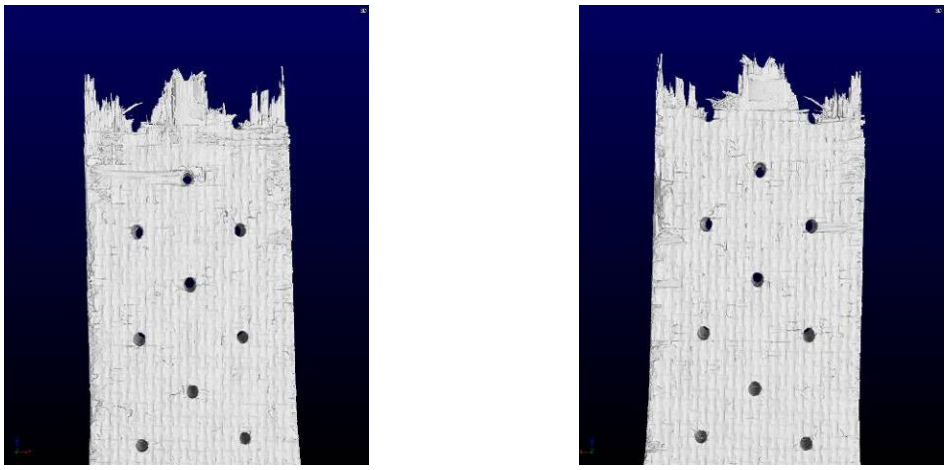

Figure B. 30: 3D image of the top fracture surface of specimen #5, tested in creep at 1200°C in air (σ_{cr} = 94 MPa, t_f = 6.55 h)

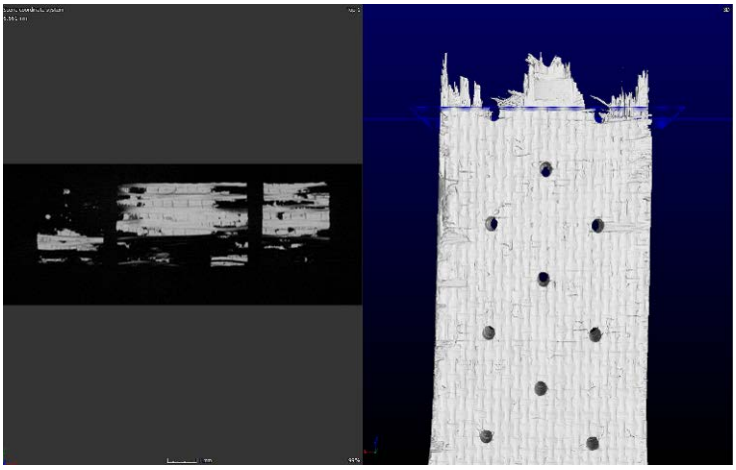

Figure B. 31: Step 1 – 2D (x-y plane) vs 3D location for specimen #5, tested in creep at 1200°C in air (σ_{cr} = 94 MPa, t_f = 6.55 h)

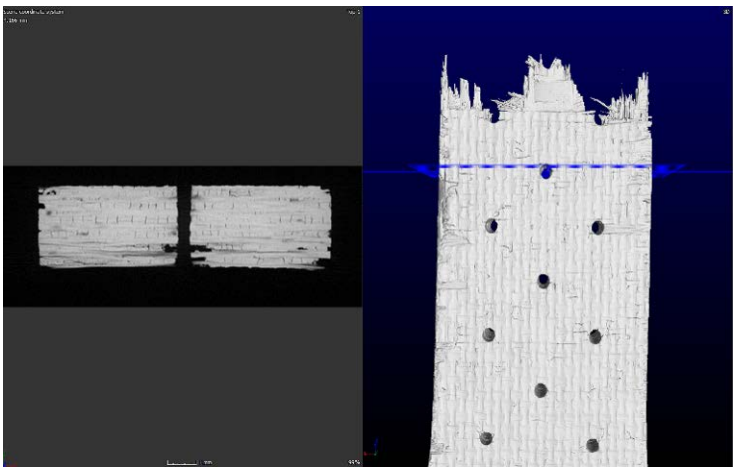

Figure B. 32: Step 2 – 2D (x-y plane) vs 3D location for specimen #5, tested in creep at 1200°C in air (σ_{cr} = 94 MPa, t_f = 6.55 h)

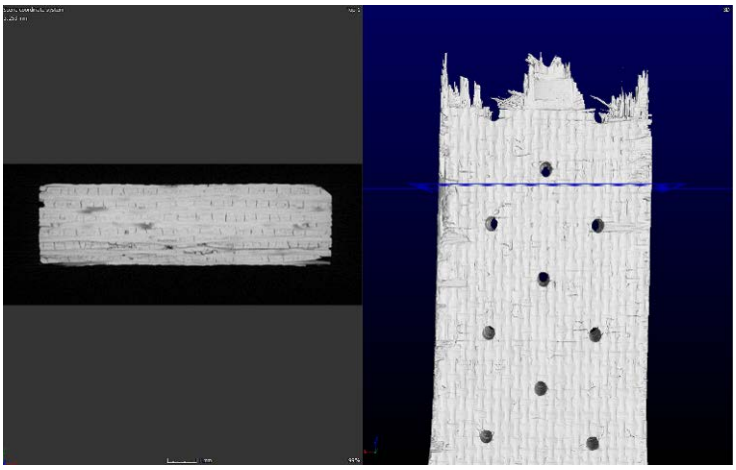

Figure B. 33: Step 3 – 2D (x-y plane) vs 3D location for specimen #5, tested in creep at 1200°C in air (σ_{cr} = 94 MPa, t_f = 6.55 h)

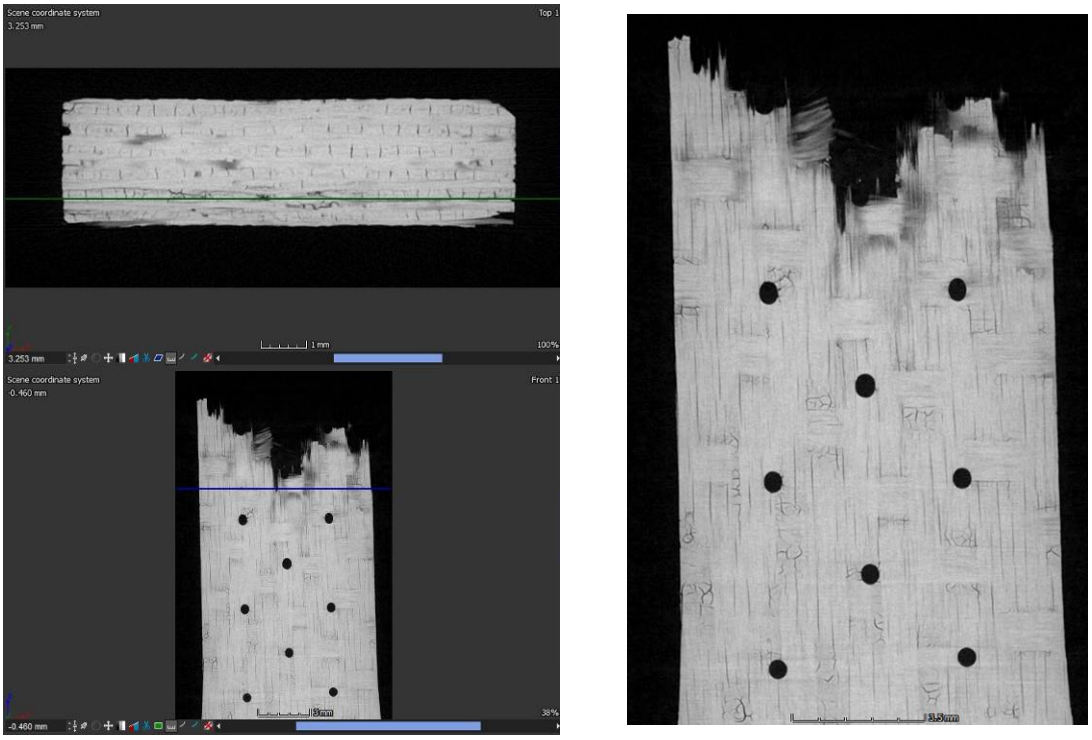

Figure B. 34: 2D (x-z plane) vs 2D (x-y plane) location showing damage zone at Step 3 for specimen #5, tested in creep at 1200°C in air (σ_{cr} = 94 MPa, t_f = 6.55 h)

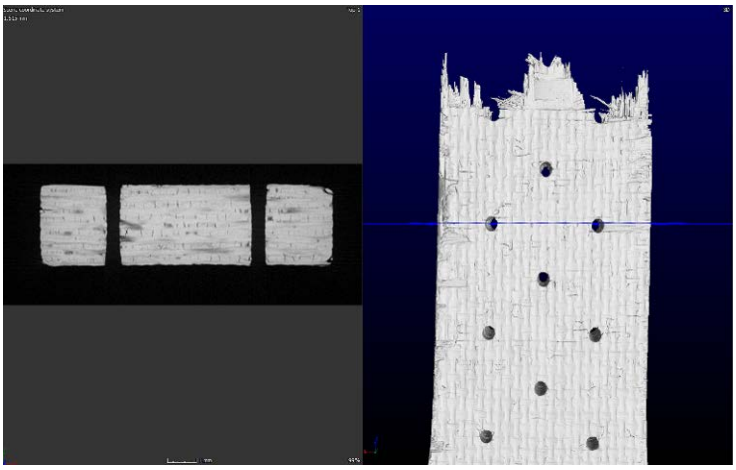

Figure B. 35: Step 4 – 2D (x-y plane) vs 3D location for specimen #5, tested in creep at 1200°C in air (σ_{cr} = 94 MPa, t_f = 6.55 h)

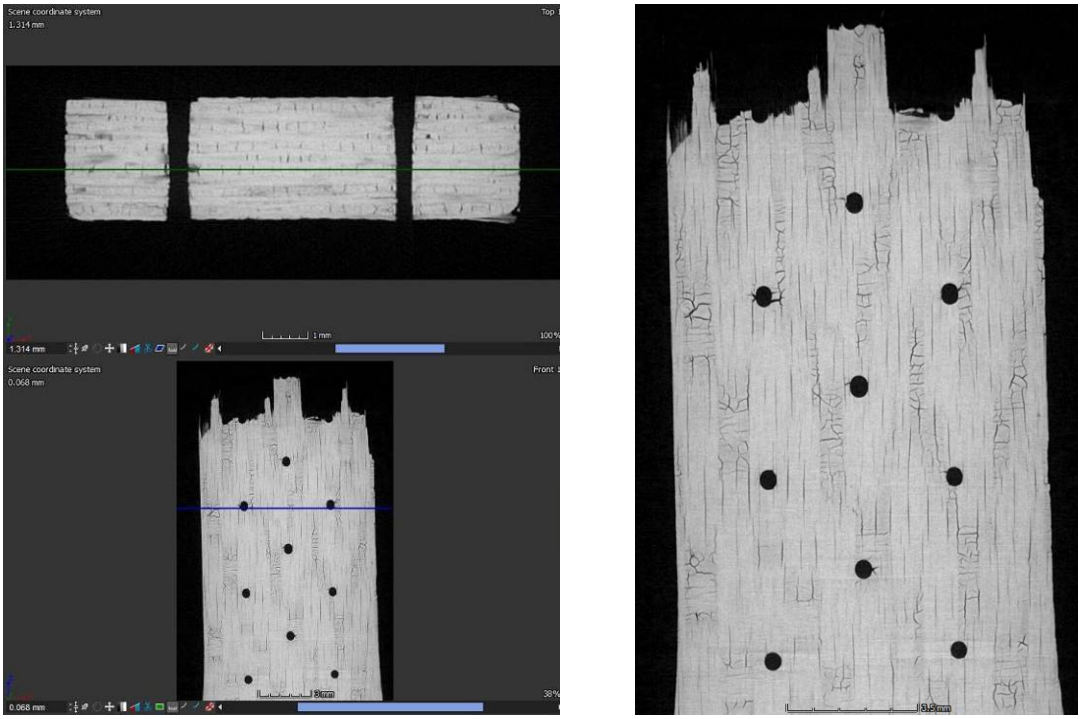

Figure B. 36: 2D (x-z plane) vs 2D (x-y plane) location showing damage zone at Step 4 for specimen #5, tested in creep at 1200°C in air (σ_{cr} = 94 MPa, t_f = 6.55 h)

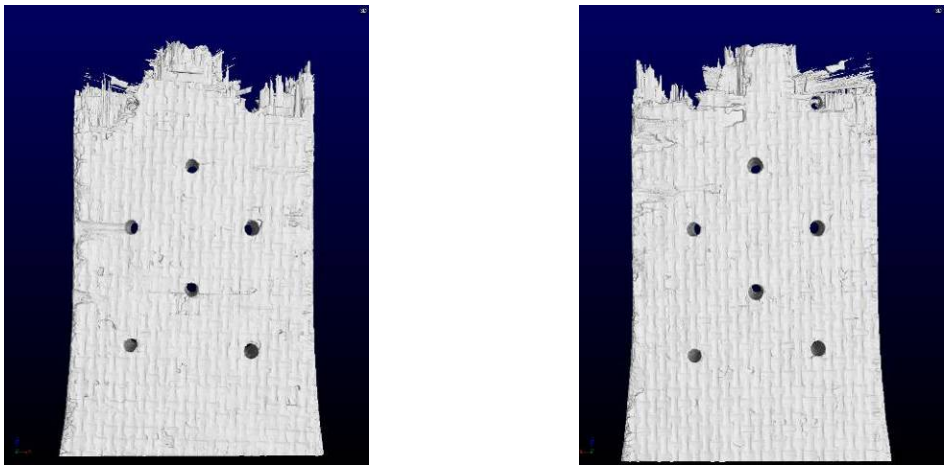

Figure B. 37: 3D image of the top fracture surface of specimen #12, tested in tension to failure following 100 h creep at 46 MPa at 1200°C in steam

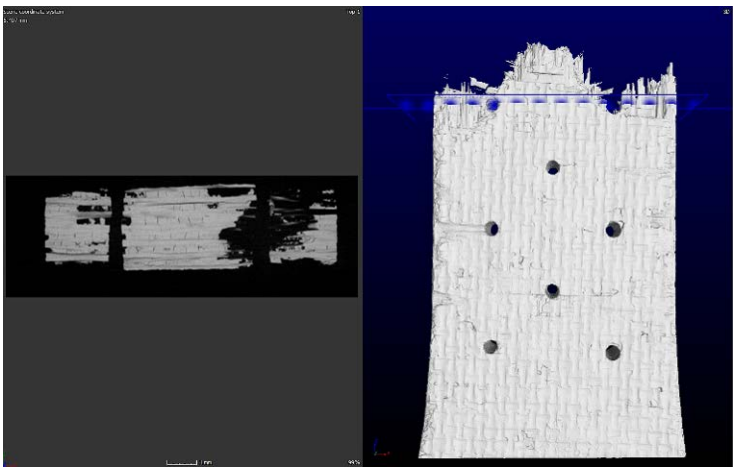

Figure B. 38: Step 1 – 2D (x-y plane) vs 3D location for specimen #12, tested in tension to failure following 100 h creep at 46 MPa at 1200°C in steam

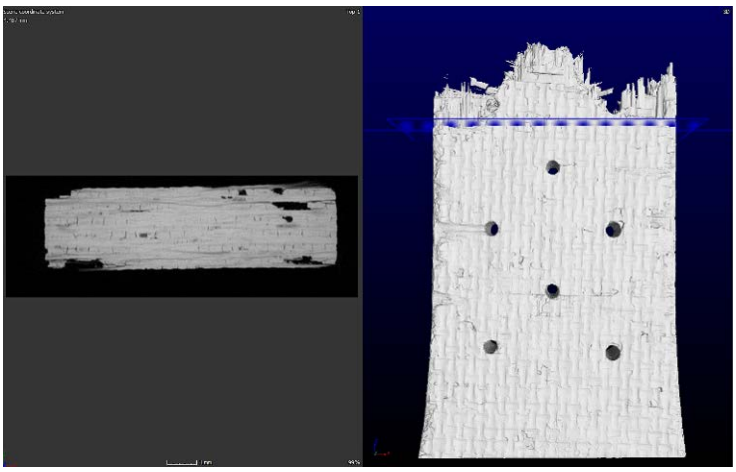

Figure B. 39: Step 2 – 2D (x-y plane) vs 3D location for specimen #12, tested in tension to failure following 100 h creep at 46 MPa at 1200°C in steam

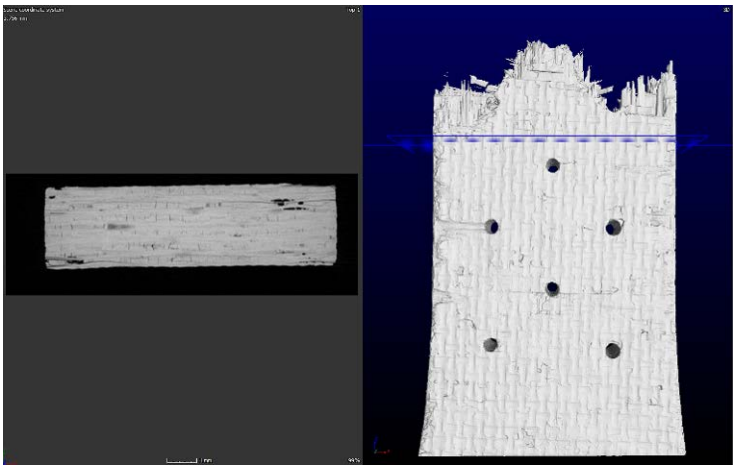

Figure B. 40: Step 3 – 2D (x-y plane) vs 3D location for specimen #12, tested in tension to failure following 100 h creep at 46 MPa at 1200°C in steam

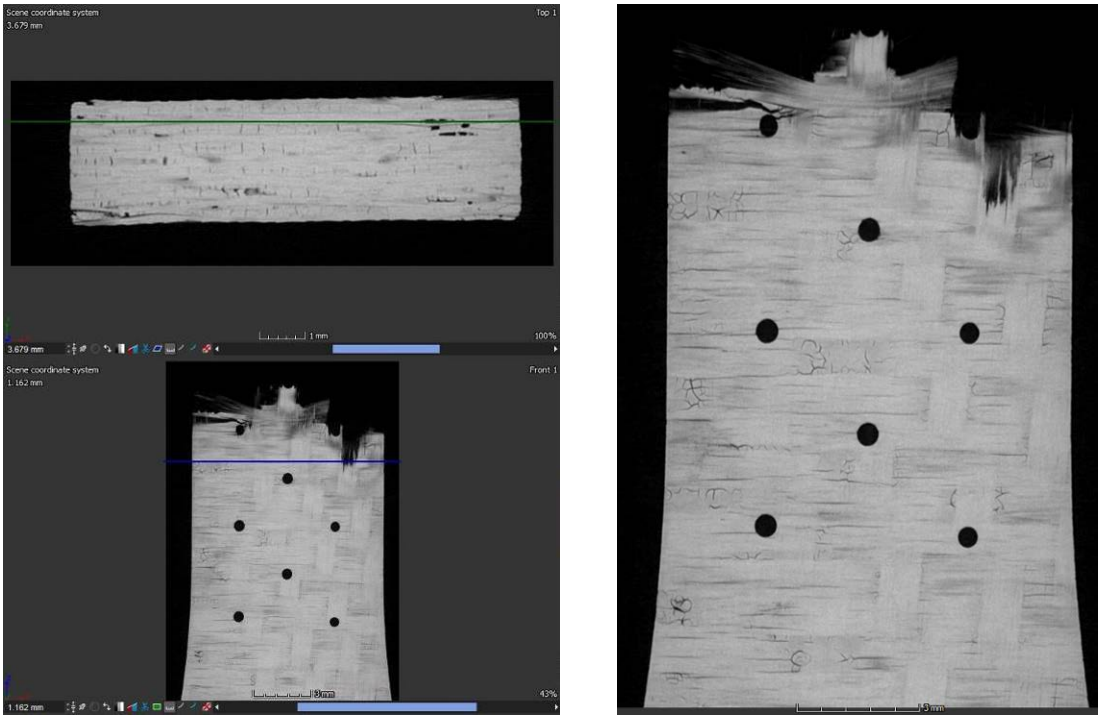

Figure B. 41: 2D (x-z plane) vs 2D (x-y plane) location showing damage zone at Step 3 for specimen #12, tested in tension to failure following 100 h creep at 46 MPa at 1200°C in steam

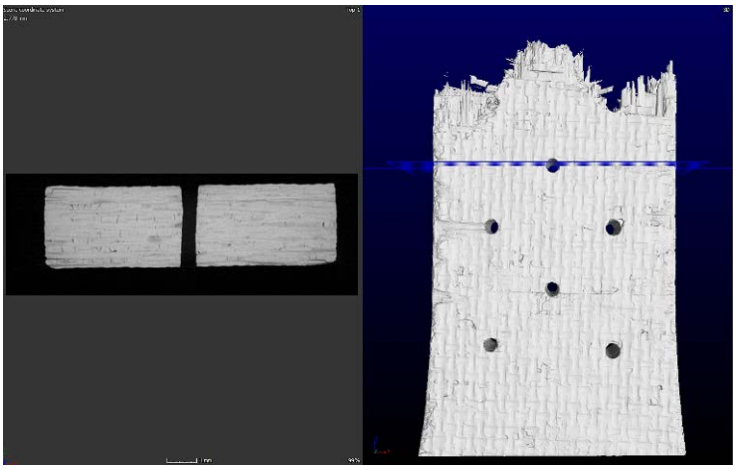

Figure B. 42: Step 4 – 2D (x-y plane) vs 3D location for specimen #12, tested in tension to failure following 100 h creep at 46 MPa at 1200°C in steam

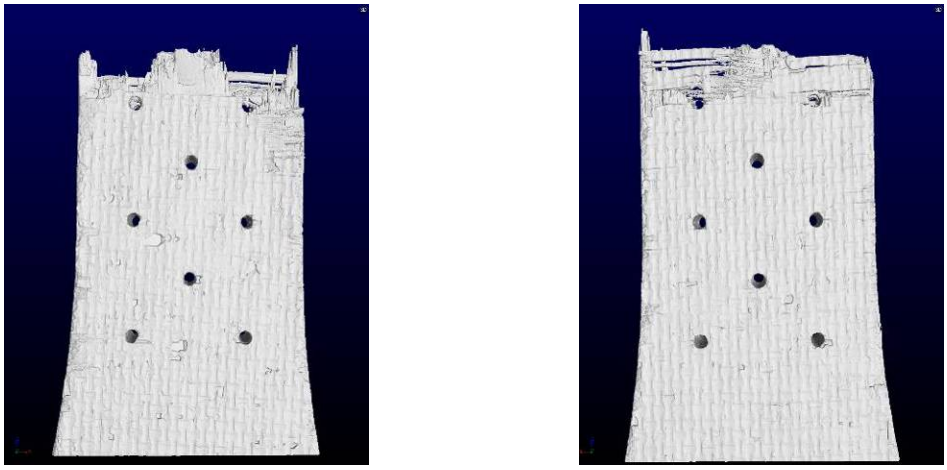

Figure B. 43: 3D image of the top fracture surface of specimen #10, tested in creep at 1200°C in steam (σ_{cr} = 93 MPa, t_f = 6.05 h)

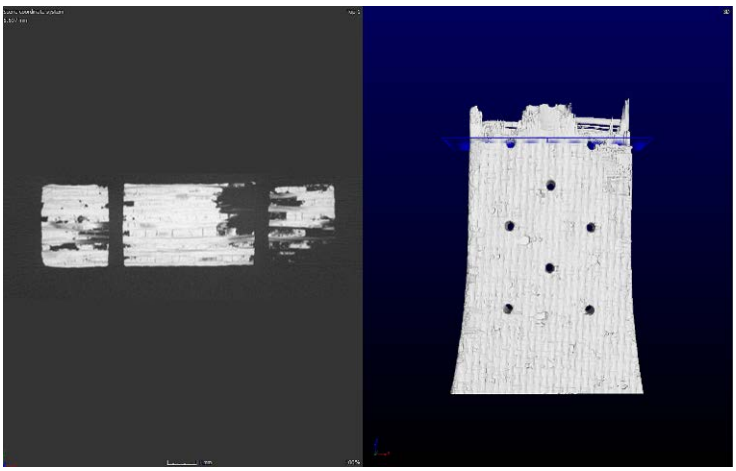

Figure B. 44: Step 1 – 2D (x-y plane) vs 3D location for specimen #10, tested in creep at 1200°C in steam (σ_{cr} = 93 MPa, t_f = 6.05 h)

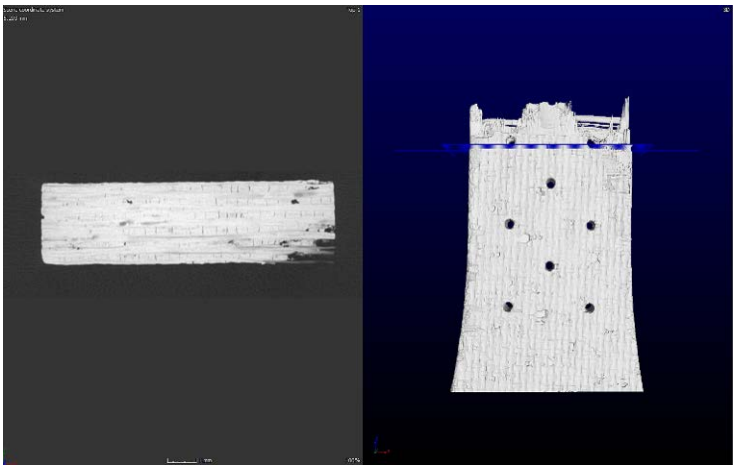

Figure B. 45: Step 2 – 2D (x-y plane) vs 3D location for specimen #10, tested in creep at 1200°C in steam (σ_{cr} = 93 MPa, t_f = 6.05 h)

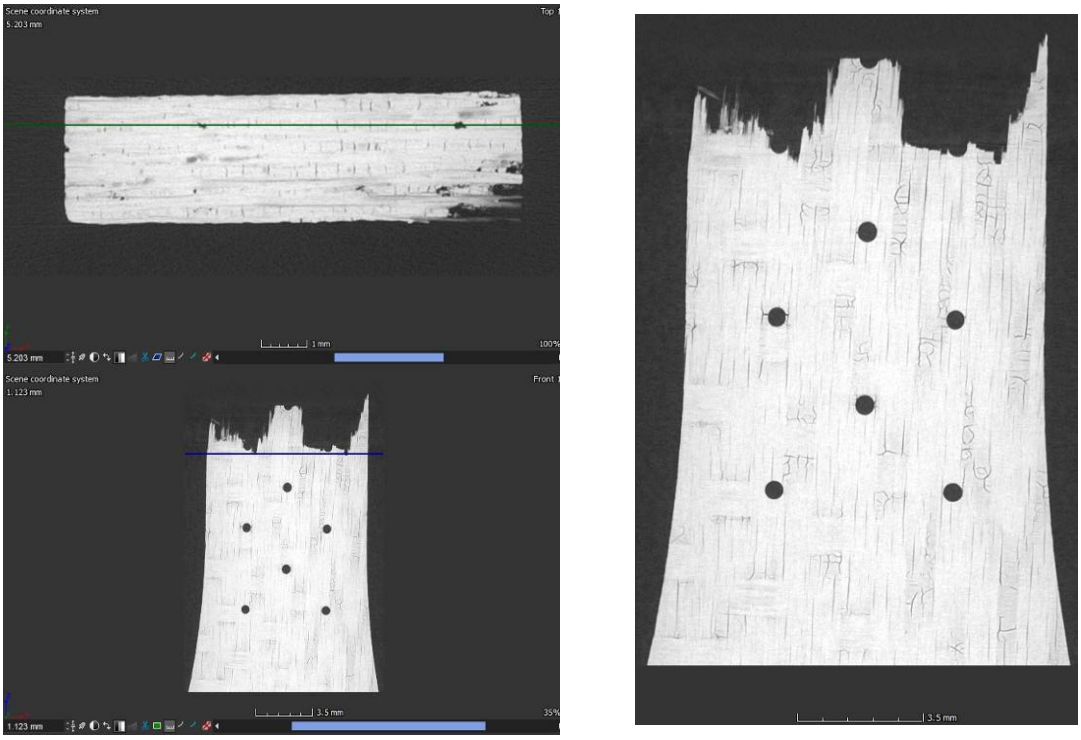

Figure B. 46: 2D (x-z plane) vs 2D (x-y plane) location showing damage zone at Step 2 for specimen #10, tested in creep at 1200°C in steam (σ_{cr} = 93 MPa, t_f = 6.05 h)

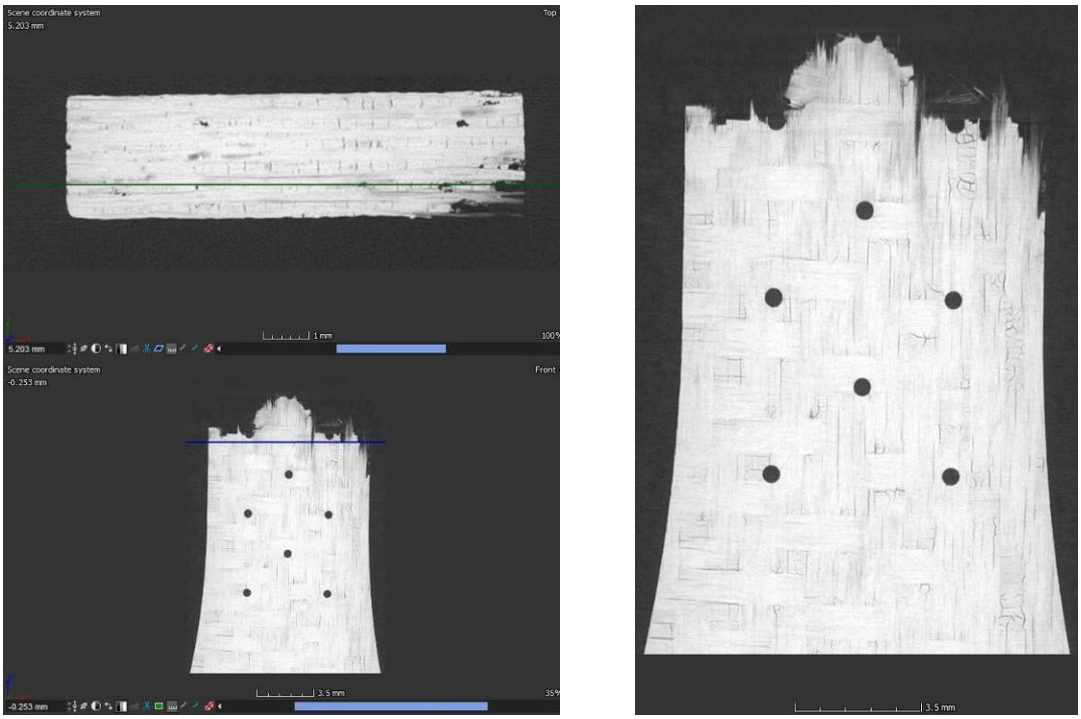

Figure B. 47: 2D (x-z plane) vs 2D (x-y plane) location showing damage zone at Step 2 for specimen #10, tested in creep at 1200°C in steam (σ_{cr} = 93 MPa, t_f = 6.05 h)

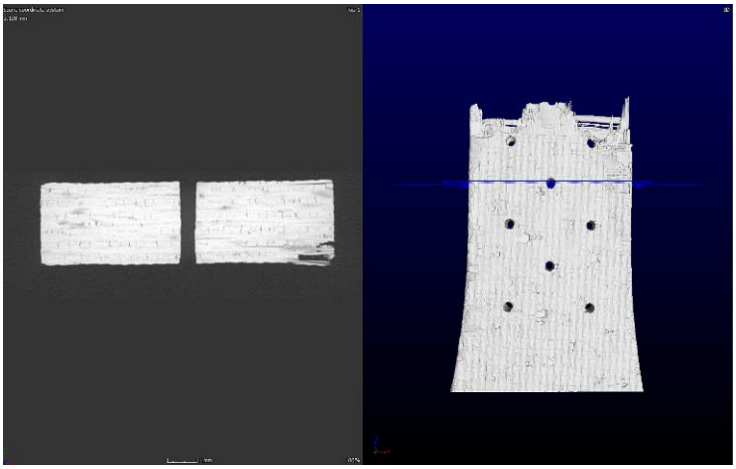

Figure B. 48: Step 3 – 2D (x-y plane) vs 3D location for specimen #10, tested in creep at 1200°C in steam (σ_{cr} = 93 MPa, t_f = 6.05 h)

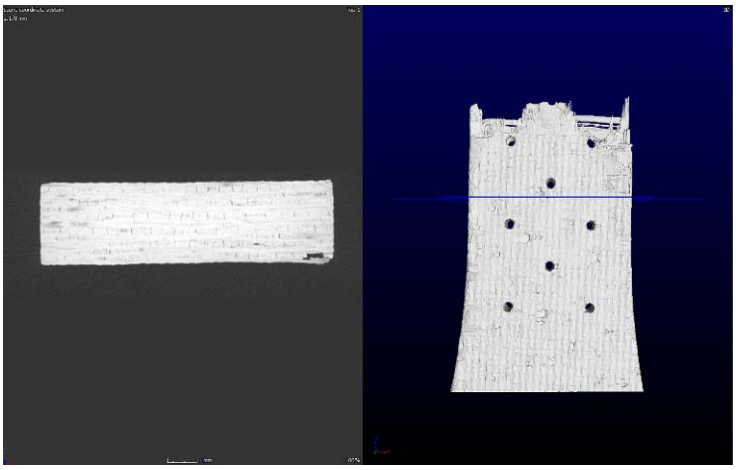

Figure B. 49: Step 4 – 2D (x-y plane) vs 3D location for specimen #10, tested in creep at 1200°C in steam (σ_{cr} = 93 MPa, t_f = 6.05 h)

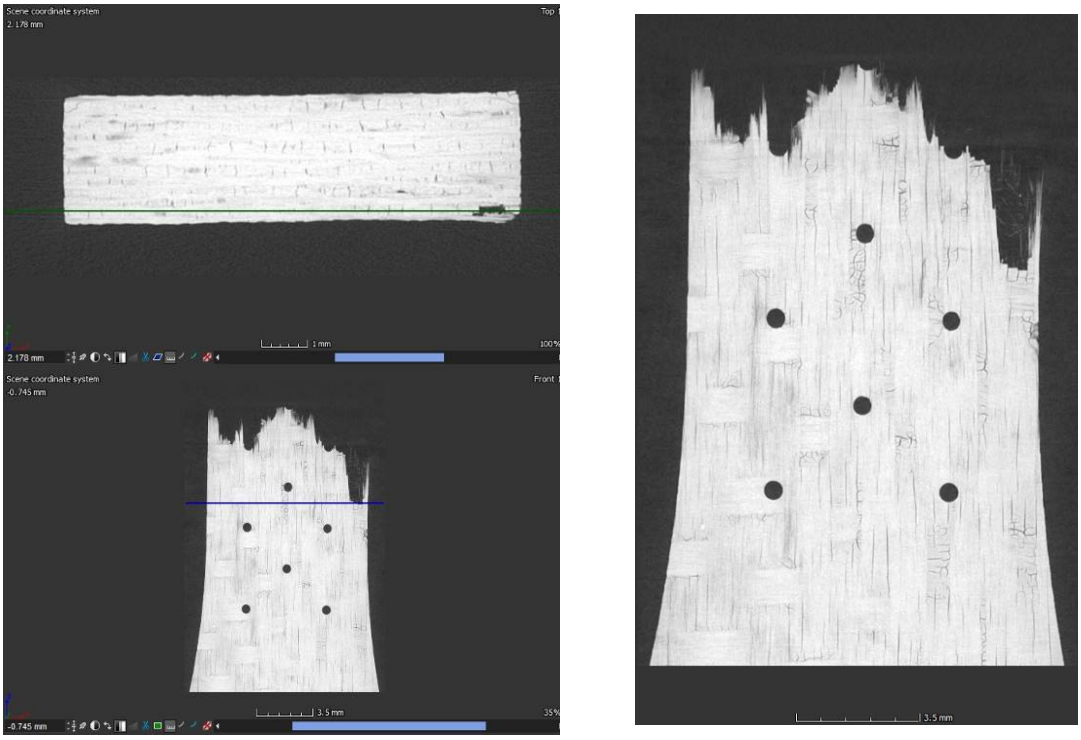

Figure B. 50: 2D (x-z plane) vs 2D (x-y plane) location showing damage zone at Step 4 for specimen #10, tested in creep at 1200°C in steam (σ_{cr} = 93 MPa, t_f = 6.05 h)

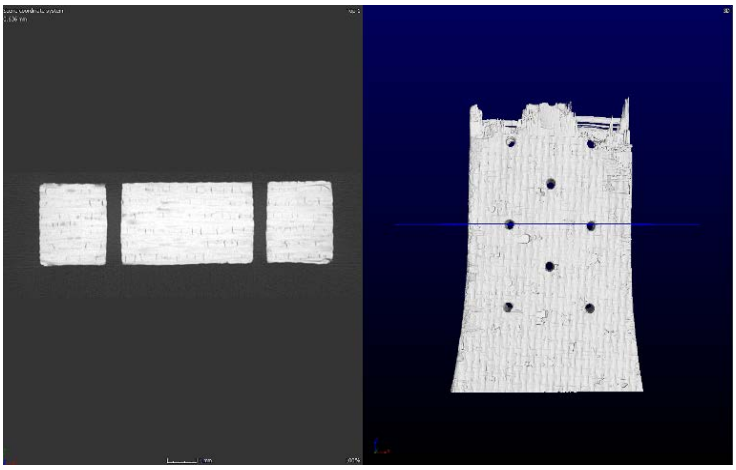

Figure B. 51: Step 5 – 2D (x-y plane) vs 3D location for specimen #10, tested in creep at 1200°C in steam (σ_{cr} = 93 MPa, t_f = 6.05 h)

Appendix C: Quanta FEG Scanning Electron Micrographs

This Appendix consolidates all Quanta FEG micrographs that were taken as part of this effort. Specimen #'s 3, 5, 7, 8 10, 11 and 12 were selected for imaging as a means to characterize any microstructural differences between short and long exposure in air and steam environments. The tension test micrographs are presented first, followed by creep tests in air, then creep tests in steam. The MAIA3 TESCAN micrographs in Appendix D are similarly organized and presented.

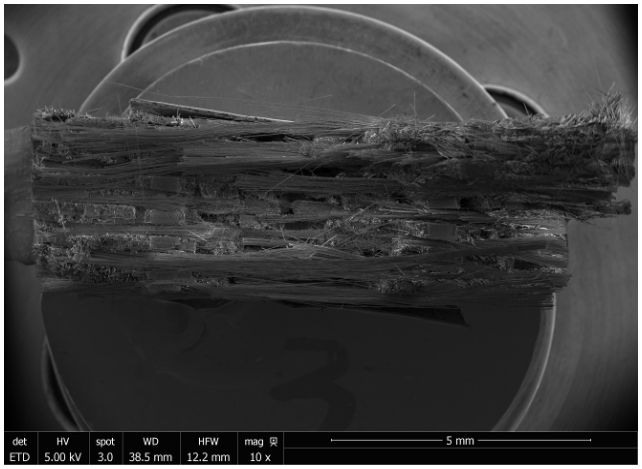

Figure C. 1: Fracture surface of specimen #3, tested in tension to failure at 1200°C in air

Figure C. 2: Fracture surface of specimen #3, tested in tension to failure at 1200°C in air

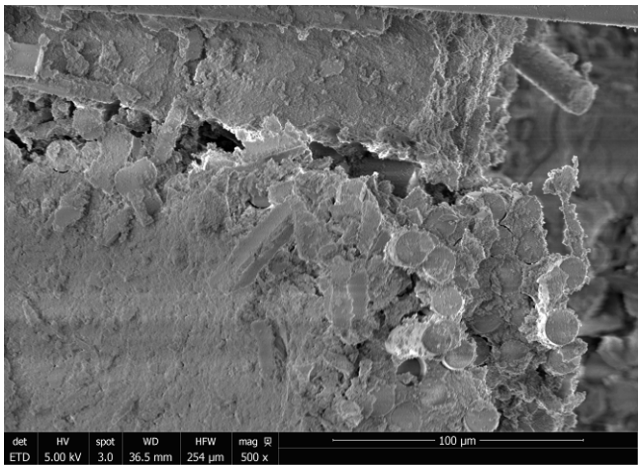

Figure C. 3: Fracture surface of specimen #3, tested in tension to failure at 1200°C in air

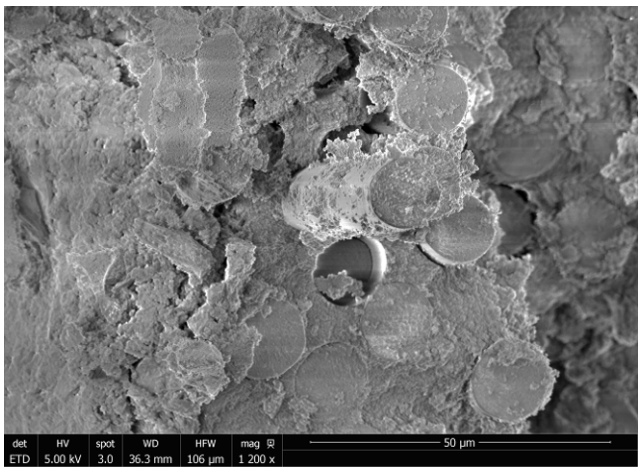

Figure C. 4: Fracture surface of specimen #3, tested in tension to failure at 1200°C in air

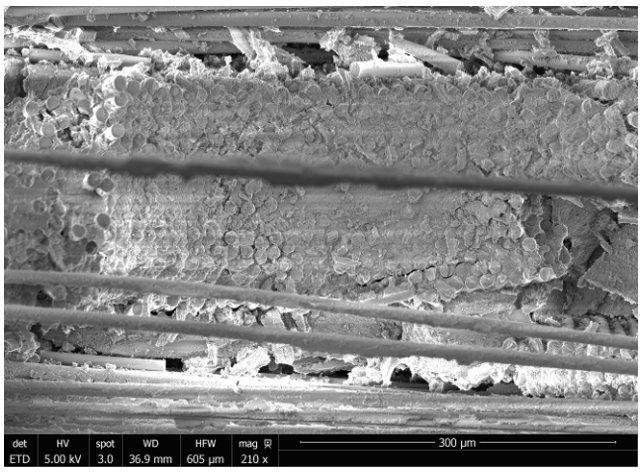

Figure C. 5: Fracture surface of specimen #3, tested in tension to failure at 1200°C in air

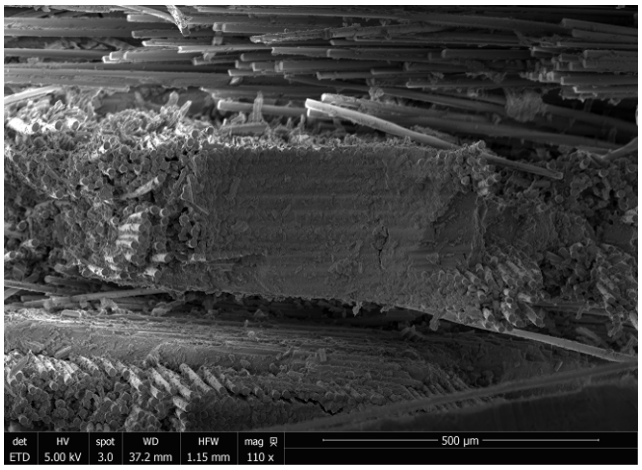

Figure C. 6: Fracture surface of specimen #3, tested in tension to failure at 1200°C in air

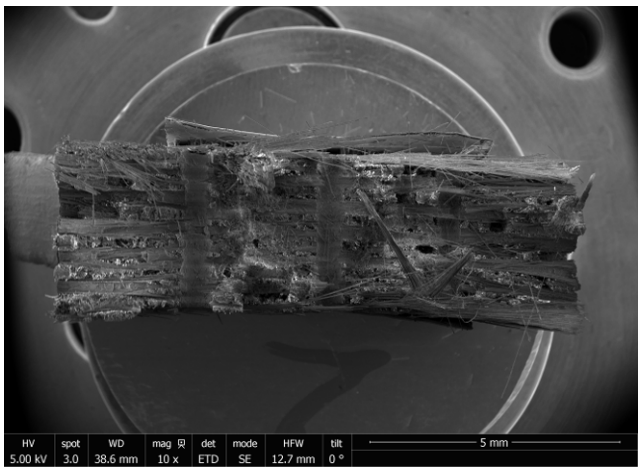

Figure C. 7: Fracture surface of specimen #7, tested in tension to failure following 100 h creep at 46 MPa at 1200°C in air

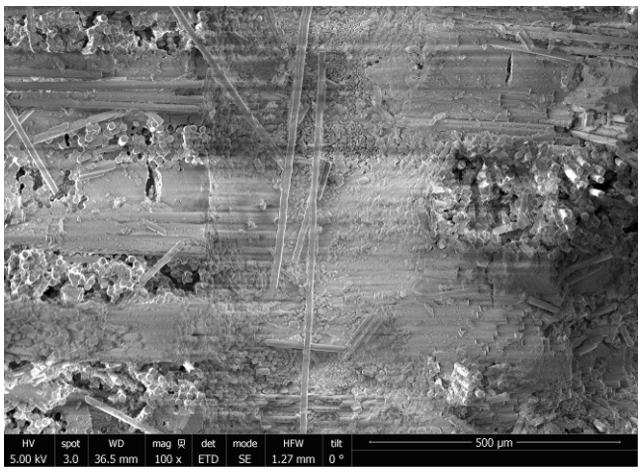

Figure C. 8: Fracture surface of specimen #7, tested in tension to failure following 100 h creep at 46 MPa at 1200°C in air

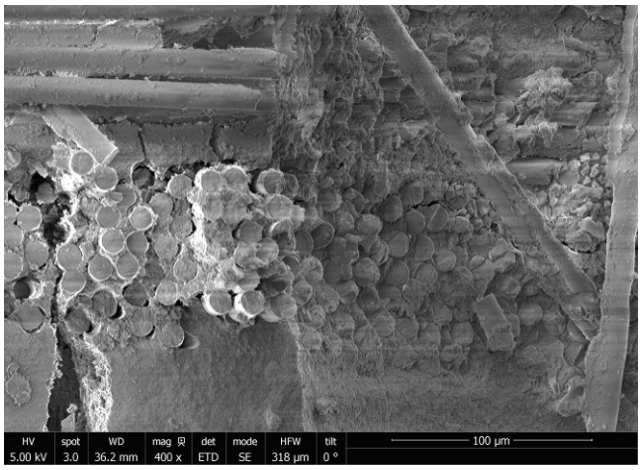

Figure C. 9: Fracture surface of specimen #7, tested in tension to failure following 100 h creep at 46 MPa at 1200°C in air

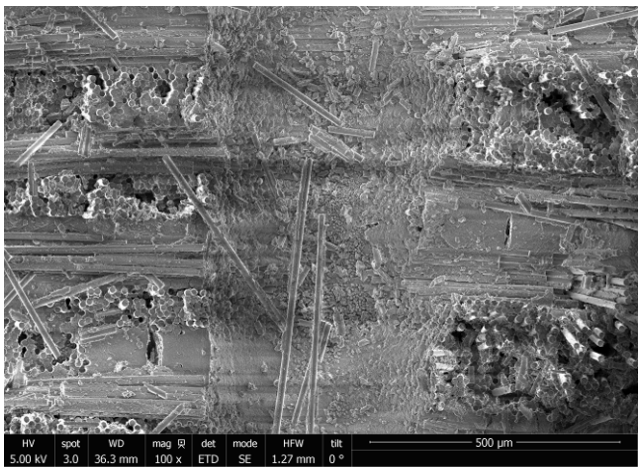

Figure C. 10: Fracture surface of specimen #7, tested in tension to failure following 100 h creep at 46 MPa at 1200°C in air

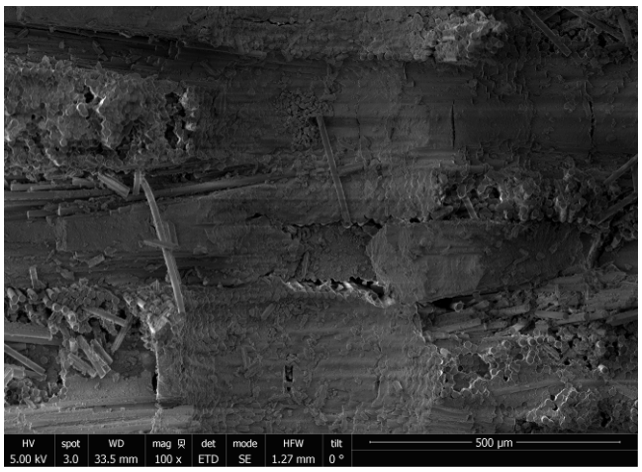

Figure C. 11: Fracture surface of specimen #7, tested in tension to failure following 100 h creep at 46 MPa at 1200°C in air

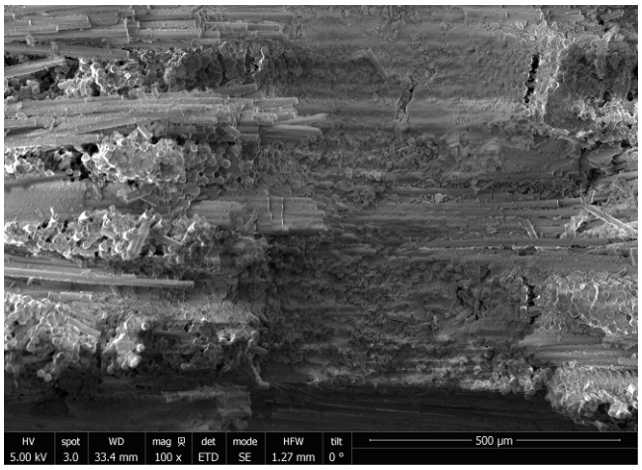

Figure C. 12: Fracture surface of specimen #7, tested in tension to failure following 100 h creep at 46 MPa at 1200°C in air

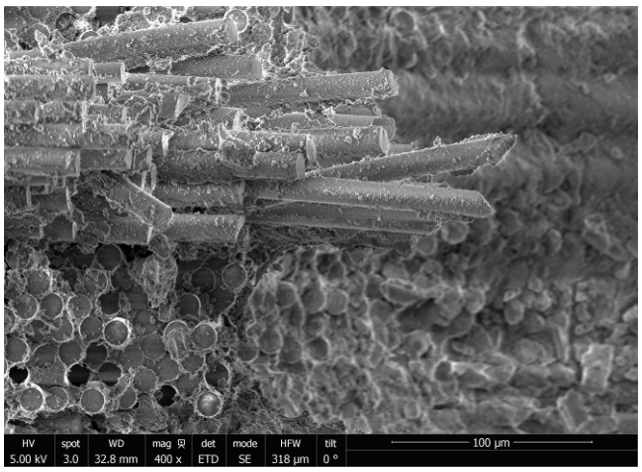

Figure C. 13: Fracture surface of specimen #7, tested in tension to failure following 100 h creep at 46 MPa at 1200°C in air

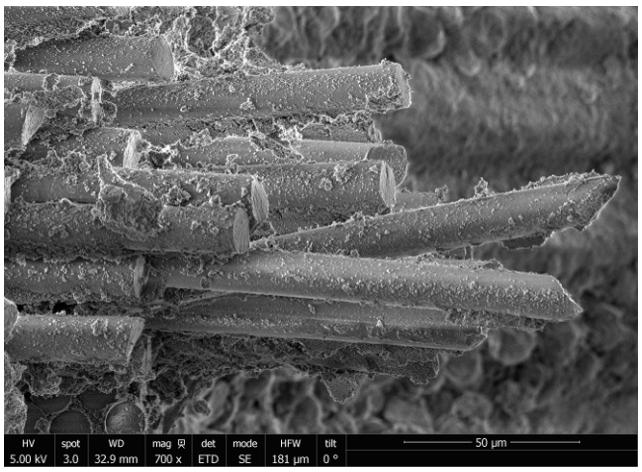

Figure C. 14: Fracture surface of specimen #7, tested in tension to failure following 100 h creep at 46 MPa at 1200°C in air

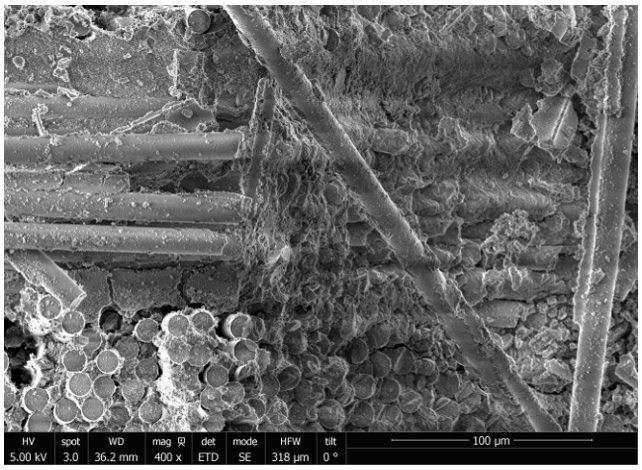

Figure C. 15: Fracture surface of specimen #7, tested in tension to failure following 100 h creep at 46 MPa at 1200°C in air

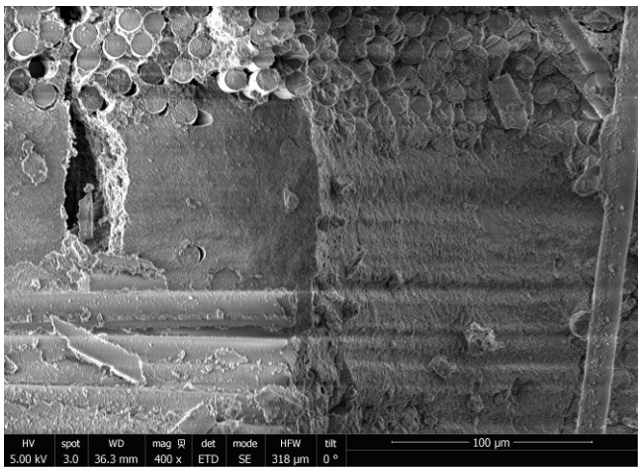

Figure C. 16: Fracture surface of specimen #7, tested in tension to failure following 100 h creep at 46 MPa at 1200°C in air

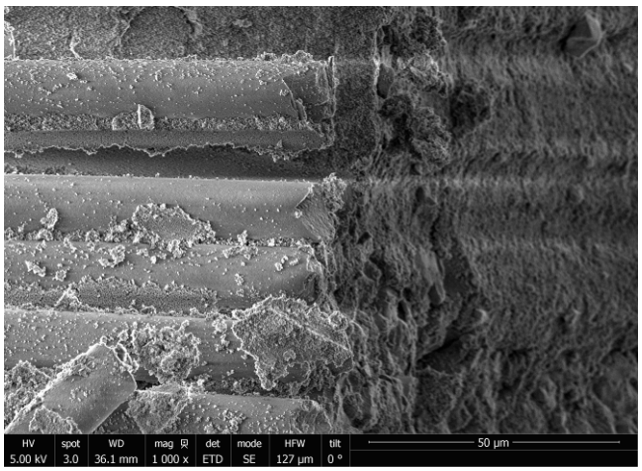

Figure C. 17: Fracture surface of specimen #7, tested in tension to failure following 100 h creep at 46 MPa at 1200°C in air

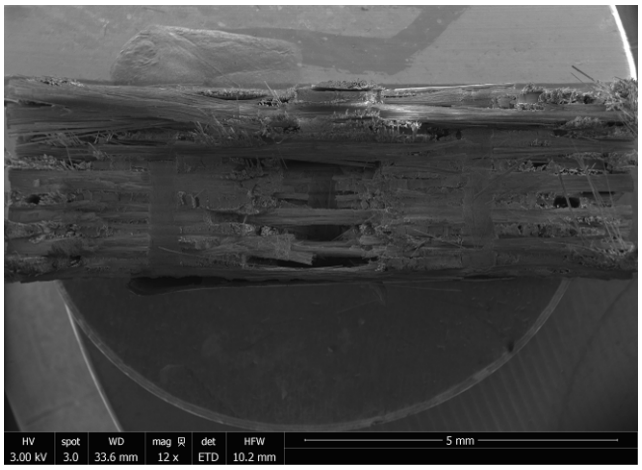

Figure C. 18: Fracture surface of specimen #5, tested in creep at 1200°C in air (σ_{cr} = 94 MPa, t_f = 6.55 h)

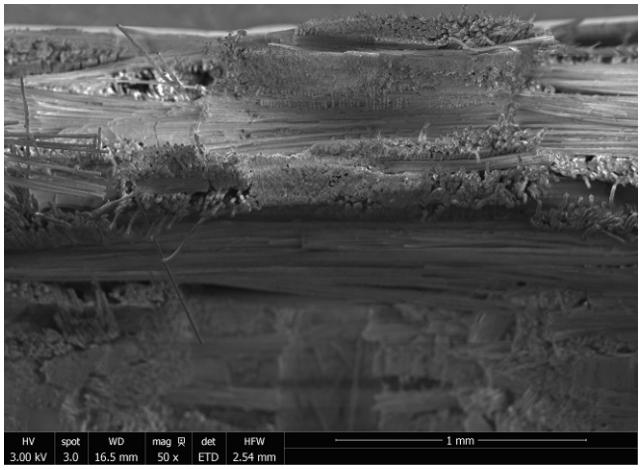

Figure C. 19: Fracture surface of specimen #5, tested in creep at 1200°C in air (σ_{cr} = 94 MPa, t_f = 6.55 h)

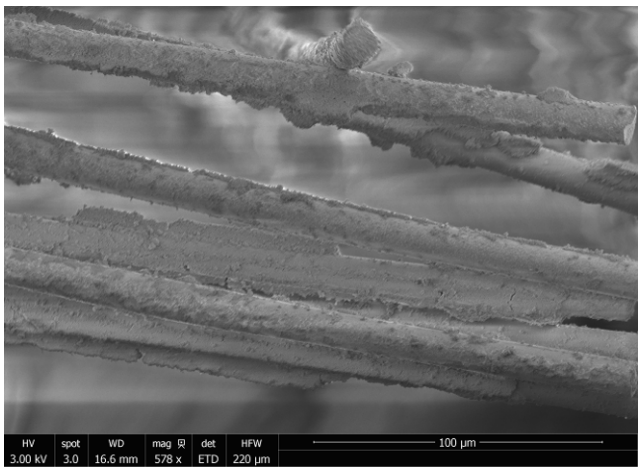

Figure C. 20: Fracture surface of specimen #5, tested in creep at 1200°C in air (σ_{cr} = 94 MPa, t_f = 6.55 h)

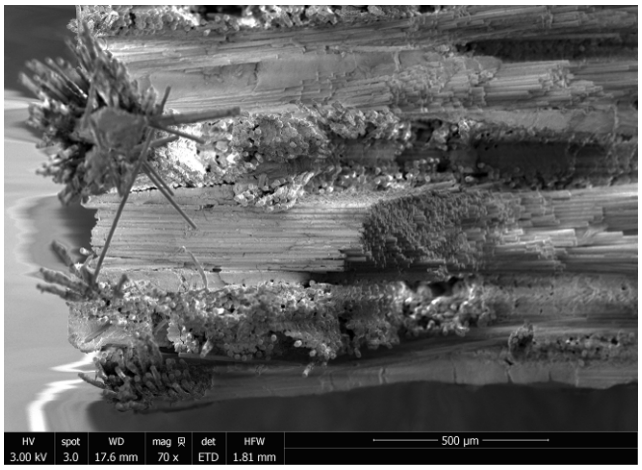

Figure C. 21: Fracture surface of specimen #5, tested in creep at 1200°C in air (σ_{cr} = 94 MPa, t_f = 6.55 h)

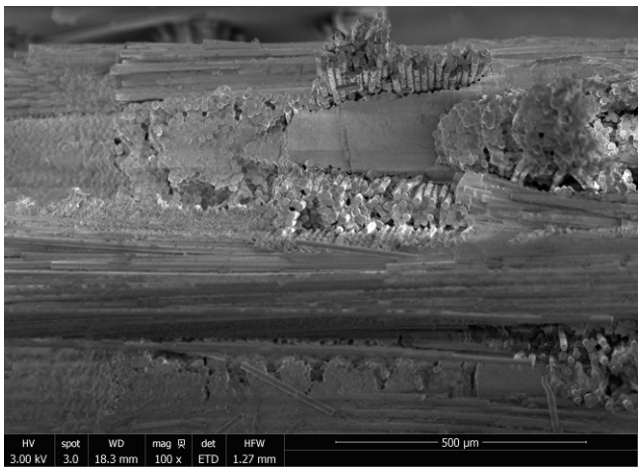

Figure C. 22: Fracture surface of specimen #5, tested in creep at 1200°C in air (σ_{cr} = 94 MPa, t_f = 6.55 h)

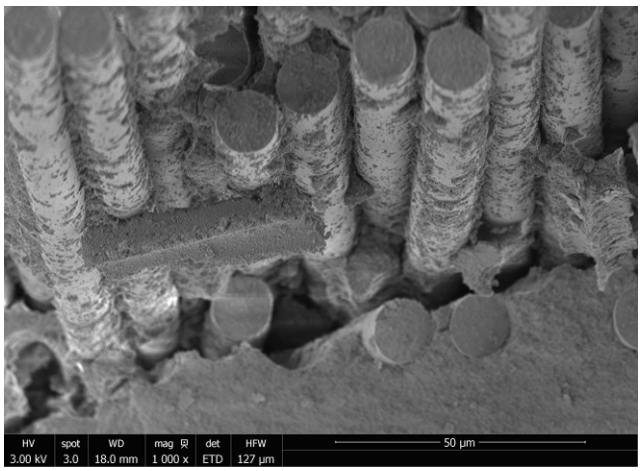

Figure C. 23: Fracture surface of specimen #5, tested in creep at 1200°C in air (σ_{cr} = 94 MPa, t_f = 6.55 h)

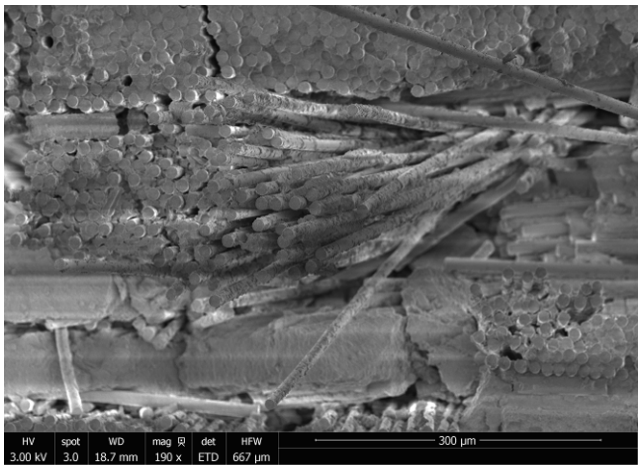

Figure C. 24: Fracture surface of specimen #5, tested in creep at 1200°C in air (σ_{cr} = 94 MPa, t_f = 6.55 h)

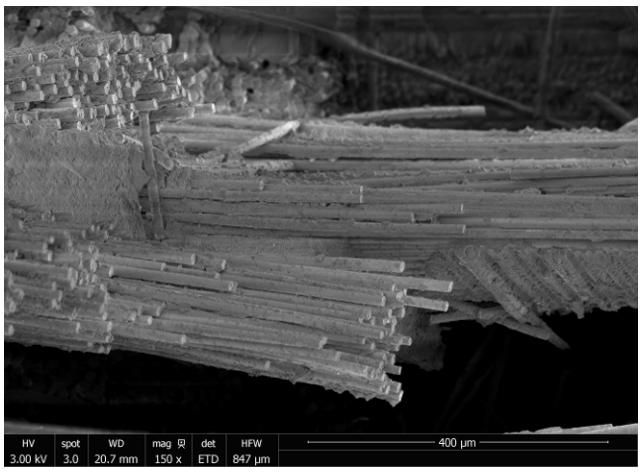

Figure C. 25: Fracture surface of specimen #5, tested in creep at 1200°C in air (σ_{cr} = 94 MPa, t_f = 6.55 h)

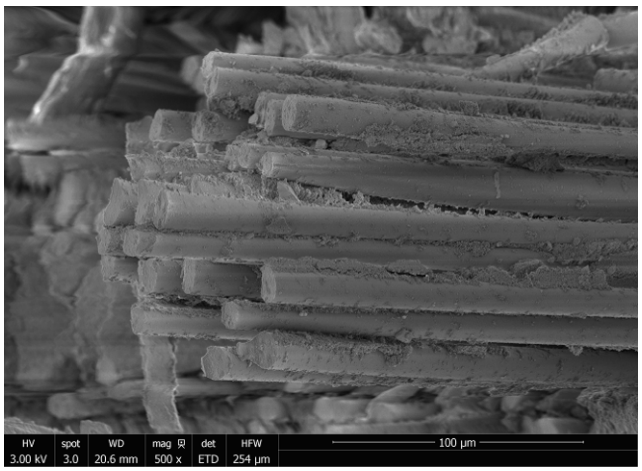

Figure C. 26: Fracture surface of specimen #5, tested in creep at 1200°C in air (σ_{cr} = 94 MPa, t_f = 6.55 h)

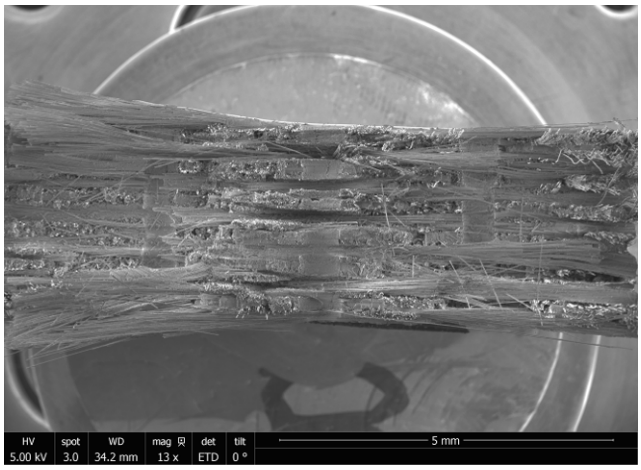

Figure C. 27: Fracture surface of specimen #8, tested in creep at 1200°C in air (σ_{cr} = 150 MPa, t_f = 0.01 h)

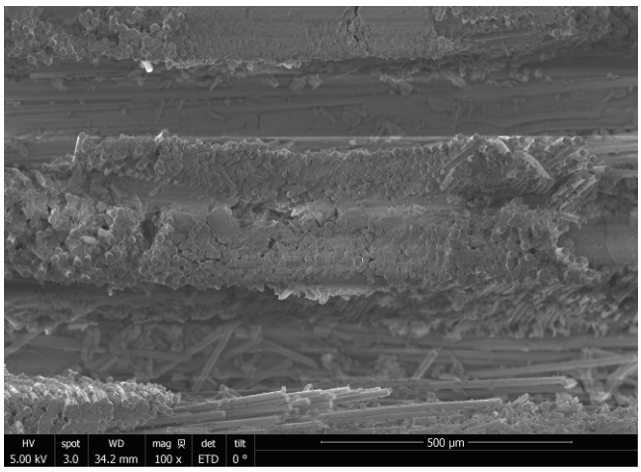

Figure C. 28: Fracture surface of specimen #8, tested in creep at 1200°C in air (σ_{cr} = 150 MPa, t_f = 0.01 h)

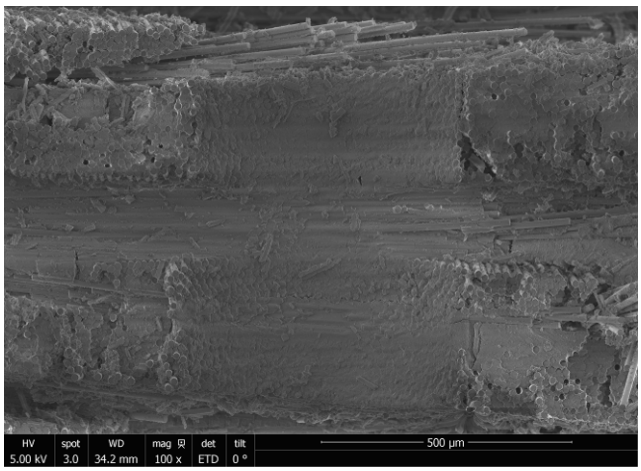

Figure C. 29: Fracture surface of specimen #8, tested in creep at 1200°C in air (σ_{cr} = 150 MPa, t_f = 0.01 h)

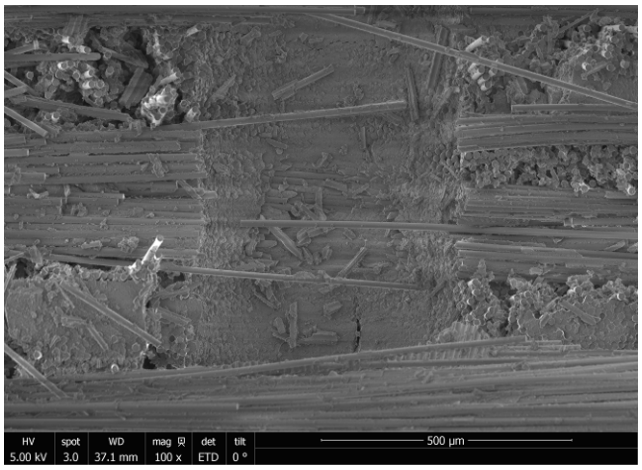

Figure C. 30: Fracture surface of specimen #8, tested in creep at 1200°C in air (σ_{cr} = 150 MPa, t_f = 0.01 h)

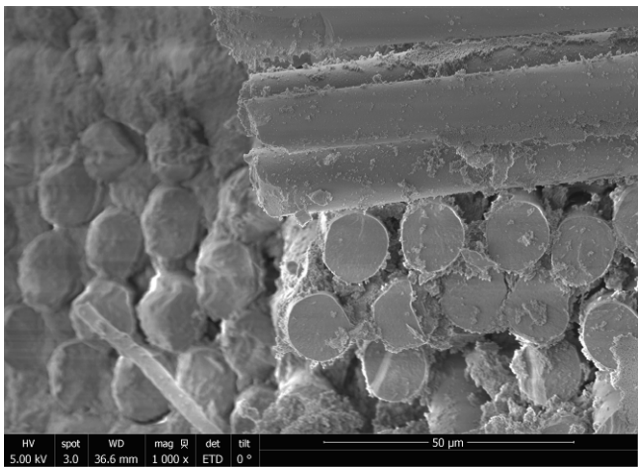

Figure C. 31: Fracture surface of specimen #8, tested in creep at 1200°C in air (σ_{cr} = 150 MPa, t_f = 0.01 h)

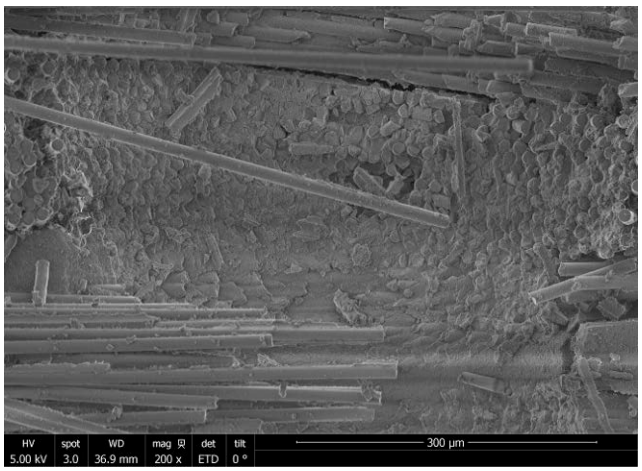

Figure C. 32: Fracture surface of specimen #8, tested in creep at 1200°C in air (σ_{cr} = 150 MPa, t_f = 0.01 h)

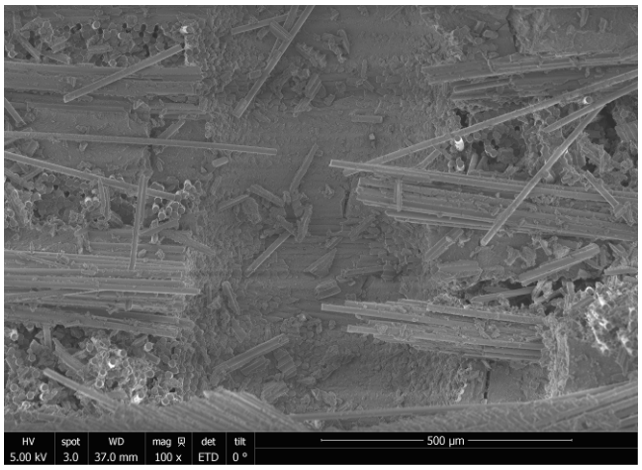

Figure C. 33: Fracture surface of specimen #8, tested in creep at 1200°C in air (σ_{cr} = 150 MPa, t_f = 0.01 h)

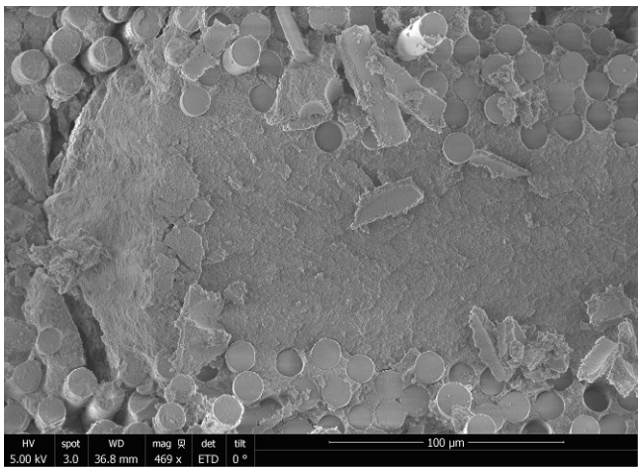

Figure C. 34: Fracture surface of specimen #8, tested in creep at 1200°C in air (σ_{cr} = 150 MPa, t_f = 0.01 h)

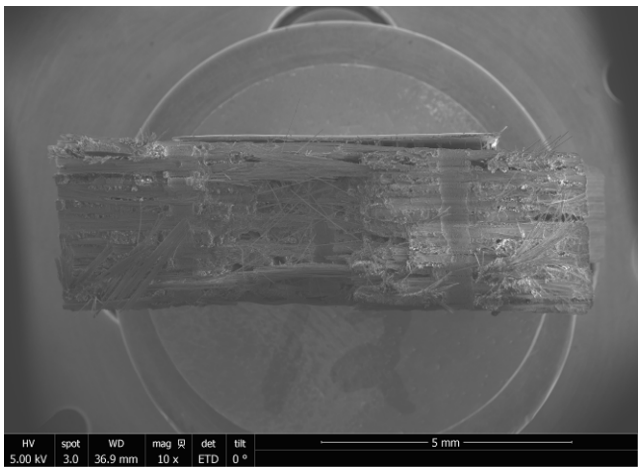

Figure C. 35: Fracture surface of specimen #12, tested in tension to failure following 100 h creep at 46 MPa at 1200°C in steam

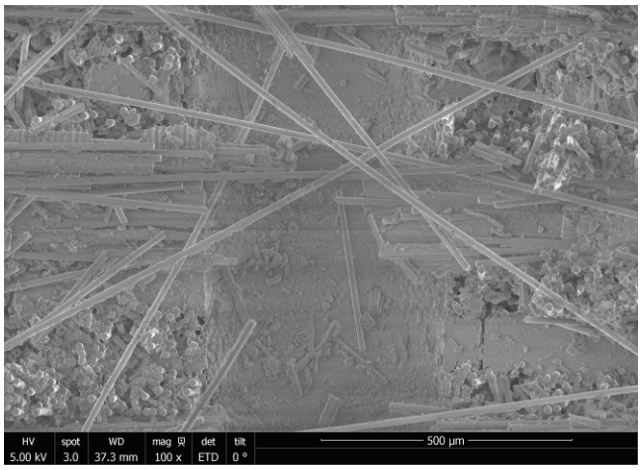

Figure C. 36: Fracture surface of specimen #12, tested in tension to failure following 100 h creep at 46 MPa at 1200°C in steam

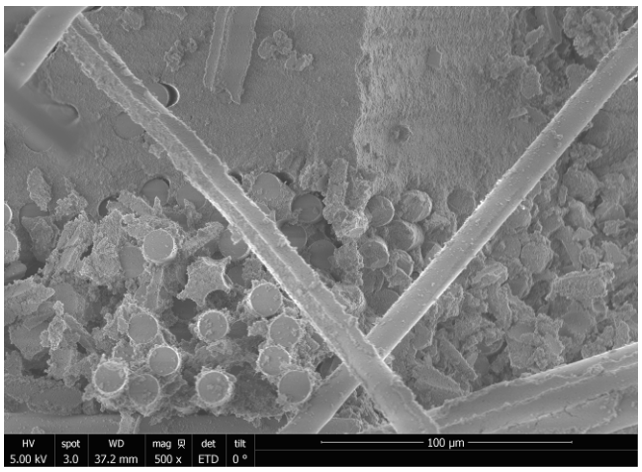

Figure C. 37: Fracture surface of specimen #12, tested in tension to failure following 100 h creep at 46 MPa at 1200°C in steam

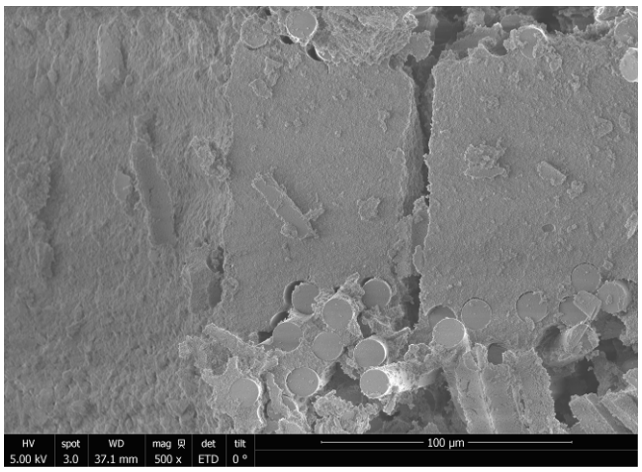

Figure C. 38: Fracture surface of specimen #12, tested in tension to failure following 100 h creep at 46 MPa at 1200°C in steam

Figure C. 39: Fracture surface of specimen #12, tested in tension to failure following 100 h creep at 46 MPa at 1200°C in steam

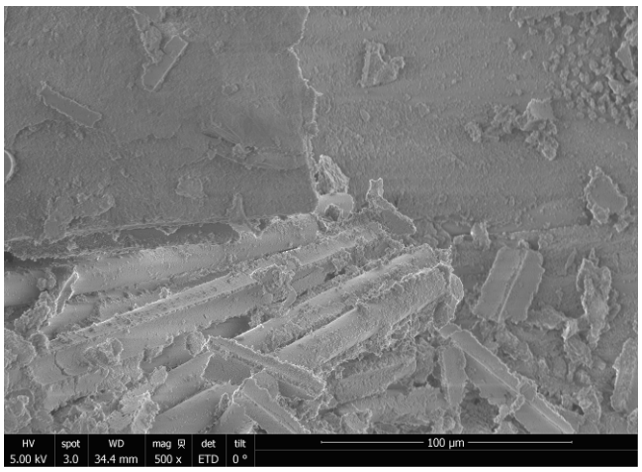

Figure C. 40: Fracture surface of specimen #12, tested in tension to failure following 100 h creep at 46 MPa at 1200°C in steam

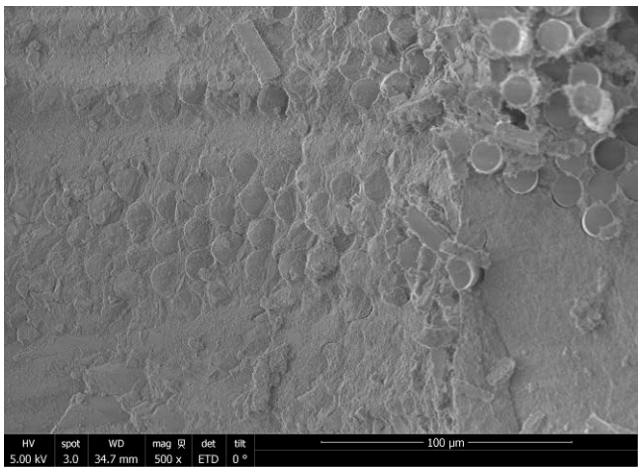

Figure C. 41: Fracture surface of specimen #12, tested in tension to failure following 100 h creep at 46 MPa at 1200°C in steam

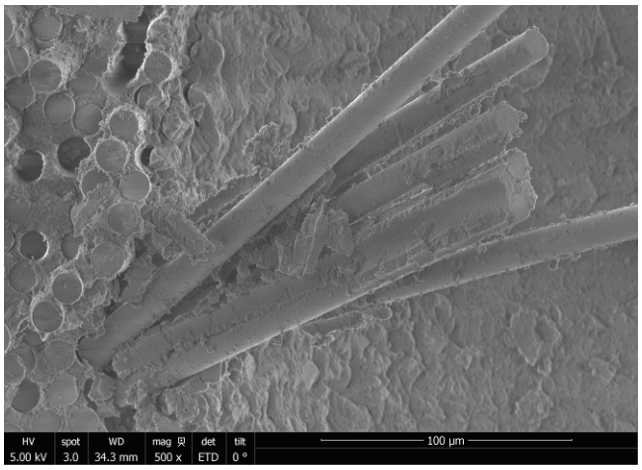

Figure C. 42: Fracture surface of specimen #12, tested in tension to failure following 100 h creep at 46 MPa at 1200°C in steam

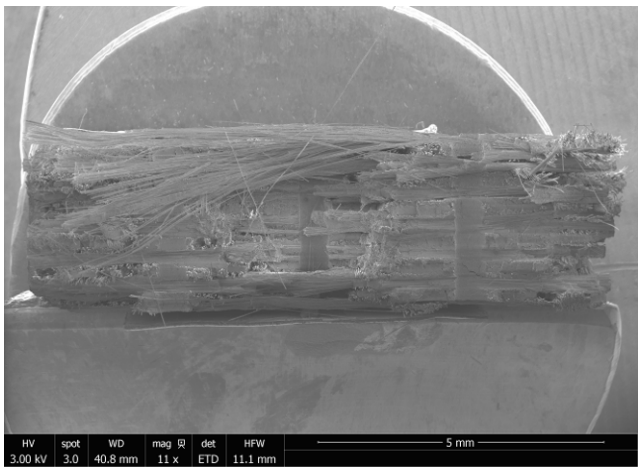

Figure C. 43: Fracture surface of specimen #10, tested in creep at 1200°C in steam (σ_{cr} = 93 MPa, t_f = 6.05 h)

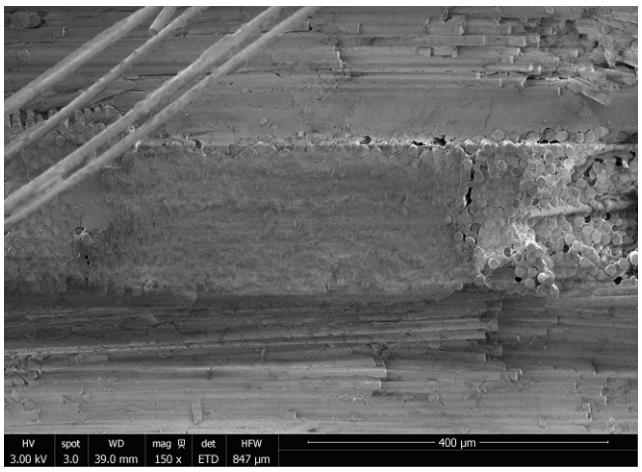

Figure C. 44: Fracture surface of specimen #10, tested in creep at 1200°C in steam (σ_{cr} = 93 MPa, t_f = 6.05 h)

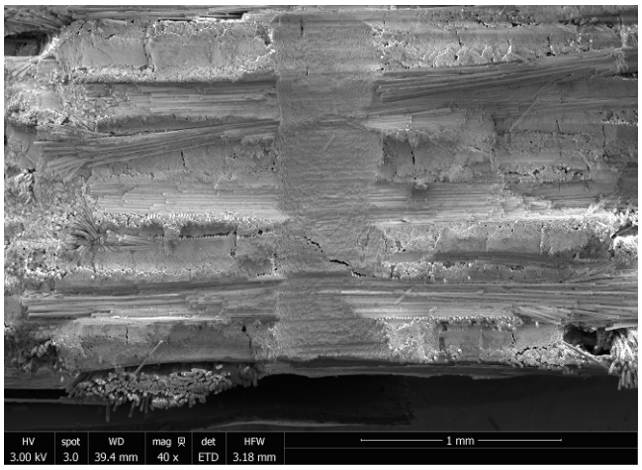

Figure C. 45: Fracture surface of specimen #10, tested in creep at 1200°C in steam (σ_{cr} = 93 MPa, t_f = 6.05 h)

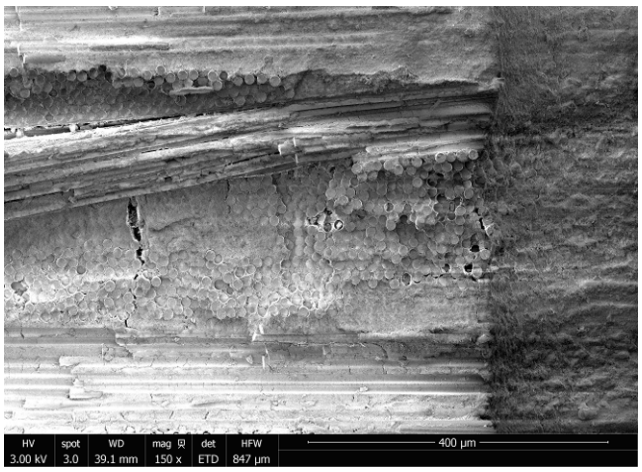

Figure C. 46: Fracture surface of specimen #10, tested in creep at 1200°C in steam (σ_{cr} = 93 MPa, t_f = 6.05 h)

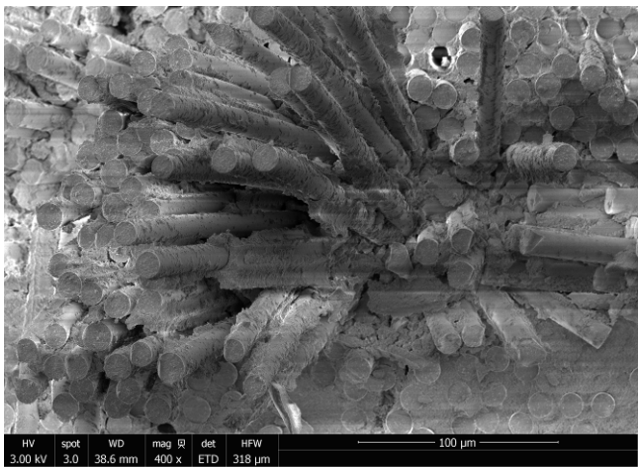

Figure C. 47: Fracture surface of specimen #10, tested in creep at 1200°C in steam (σ_{cr} = 93 MPa, t_f = 6.05 h)

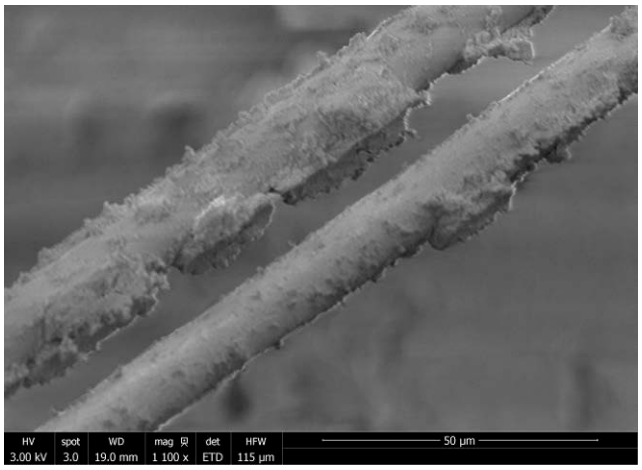

Figure C. 48: Fracture surface of specimen #10, tested in creep at 1200°C in steam (σ_{cr} = 93 MPa, t_f = 6.05 h)

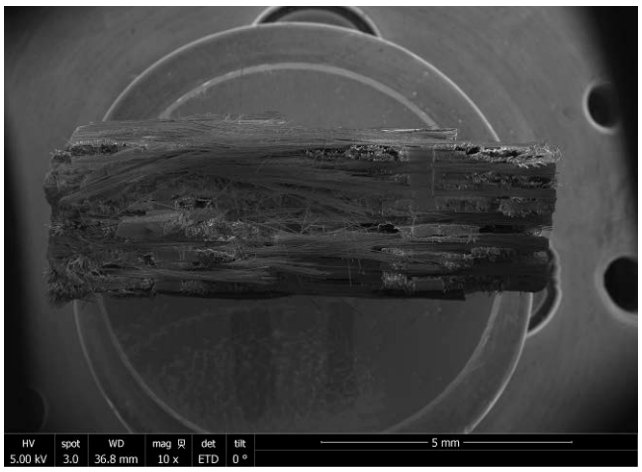

Figure C. 49: Fracture surface of specimen #11, tested in creep at 1200°C in steam (σ_{cr} = 150 MPa, t_f = 0.04 h)

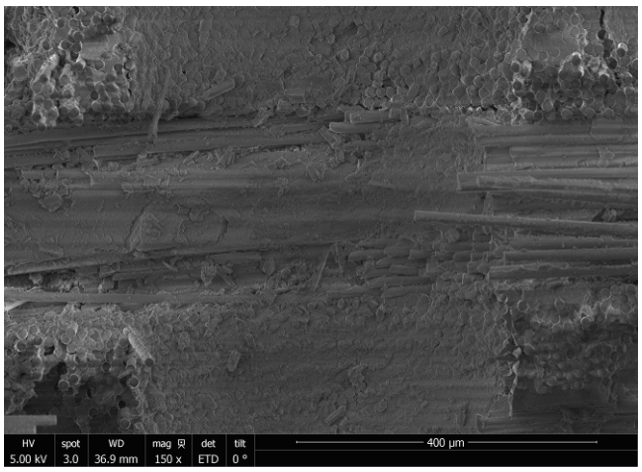

Figure C. 50: Fracture surface of specimen #11, tested in creep at 1200°C in steam (σ_{cr} = 150 MPa, t_f = 0.04 h)

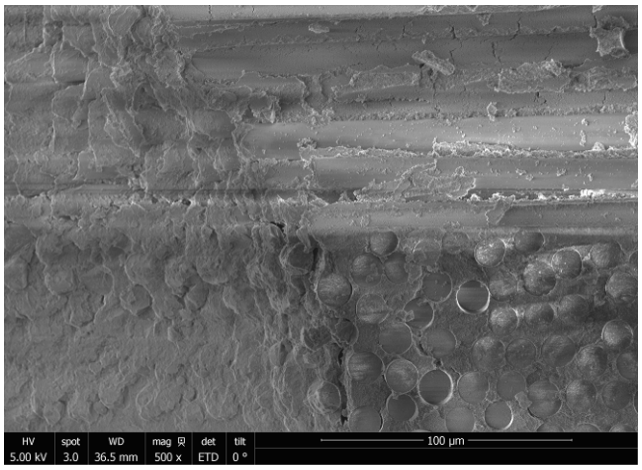

Figure C. 51: Fracture surface of specimen #11, tested in creep at 1200°C in steam (σ_{cr} = 150 MPa, t_f = 0.04 h)

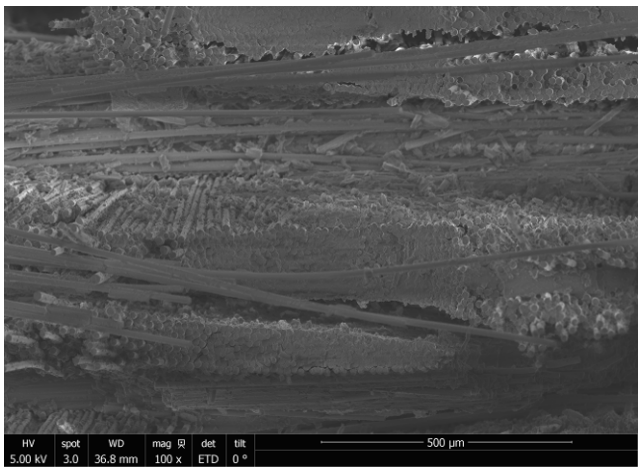

Figure C. 52: Fracture surface of specimen #11, tested in creep at 1200°C in steam (σ_{cr} = 150 MPa, t_f = 0.04 h)

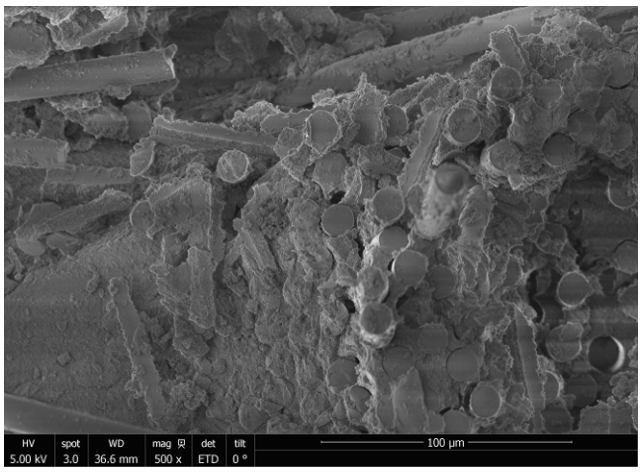

Figure C. 53: Fracture surface of specimen #11, tested in creep at 1200°C in steam (σ_{cr} = 150 MPa, t_f = 0.04 h)

Appendix D: MAIA3 TESCAN Scanning Electron Micrographs

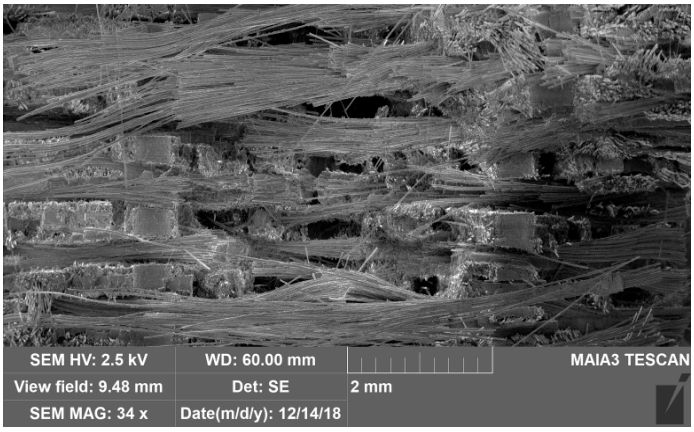

Figure D. 1: Fracture surface of specimen #3, tested in tension to failure at 1200°C in air

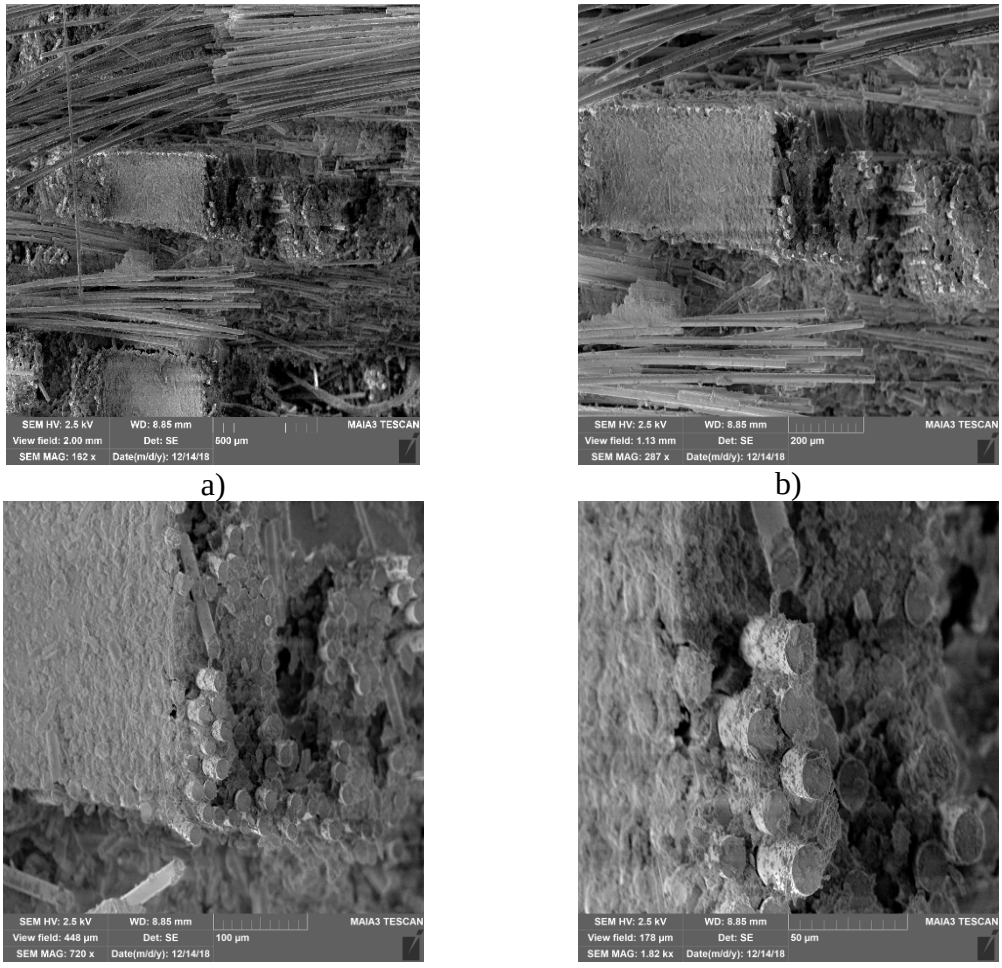

Figure D. 2: Fracture surface of specimen #3 (Area 1), tested in tension to failure at 1200°C in air: (a) 162X, (b) 287X, (c) 720X, (d) 1.82kX

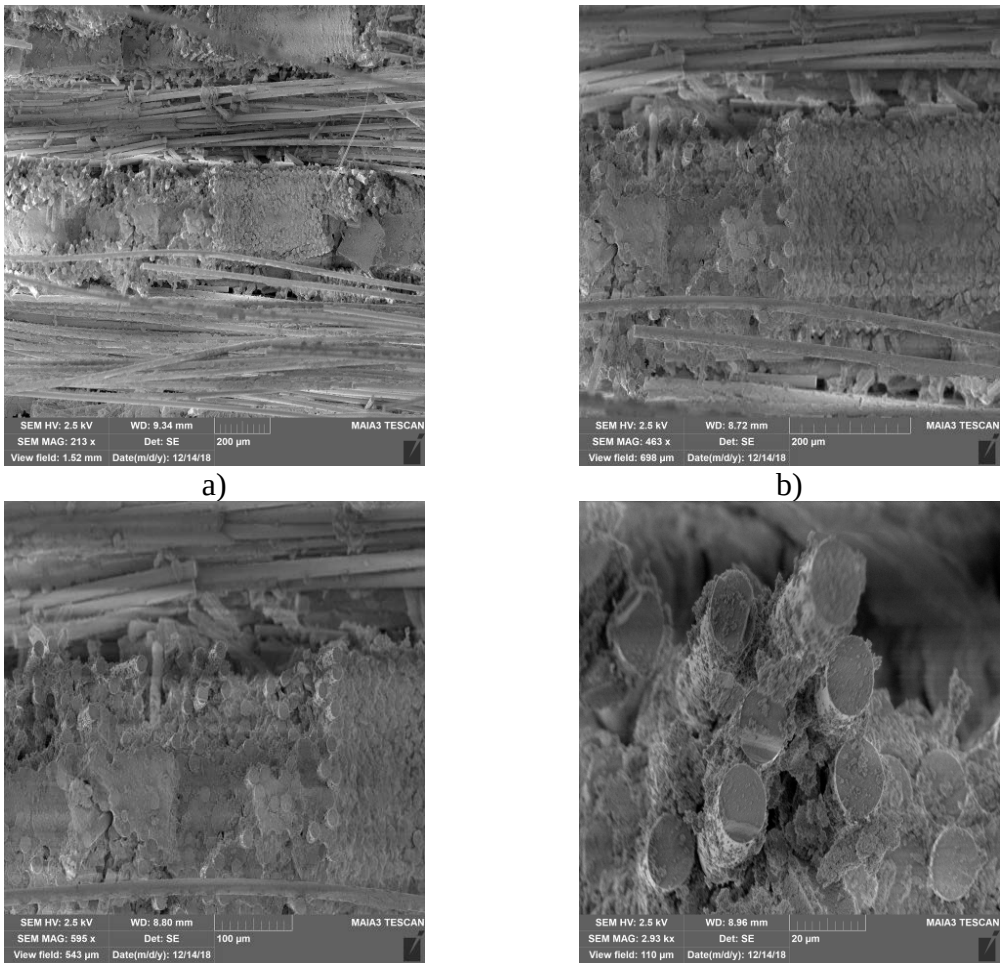

Figure D. 3: Fracture surface of specimen #3 (Area 2), tested in tension to failure at 1200°C in air: (a) 213X, (b) 463X, (c) 595X, (d) 2.93kX

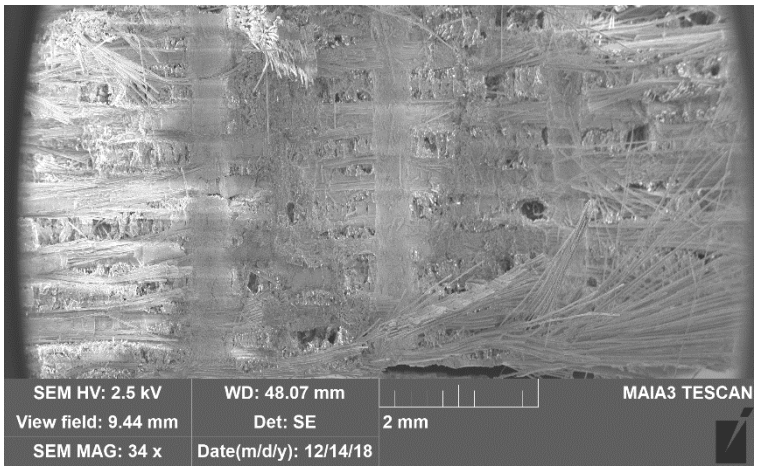

Figure D. 4: Fracture surface of specimen #7, tested in tension to failure following 100 h creep at 46 MPa at 1200°C in air

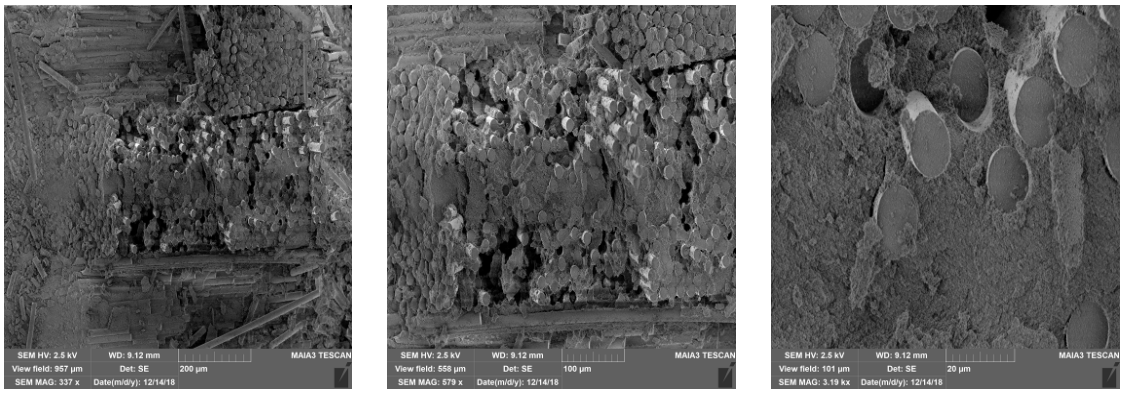

a) b) c)

Figure D. 5: Fracture surface of specimen #7 (Area 1), tested in tension to failure following 100 h creep at 46 MPa at 1200°C in air: (a) 337X, (b) 579X, (c) 3kX

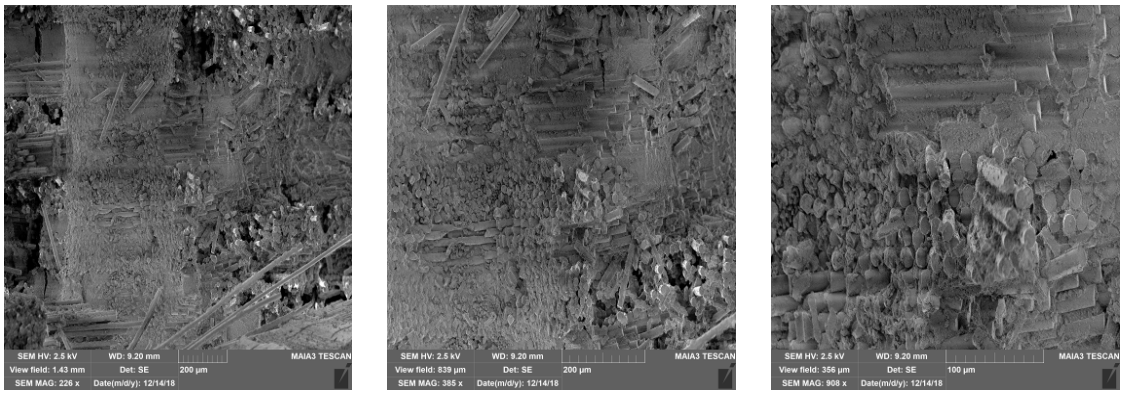

a) b) c)

Figure D. 6: Fracture surface of specimen #7 (Area 2), tested in tension to failure following 100 h creep at 46 MPa at 1200°C in air: (a) 226X, (b) 385X, (c) 908X

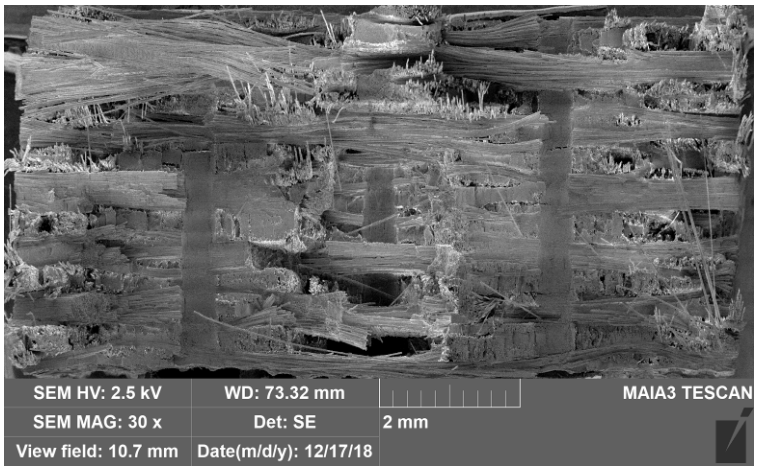

Figure D. 7: Fracture surface of specimen #5, tested in creep at 1200°C in air (σ_{cr} = 94 MPa, t_f = 6.55 h)

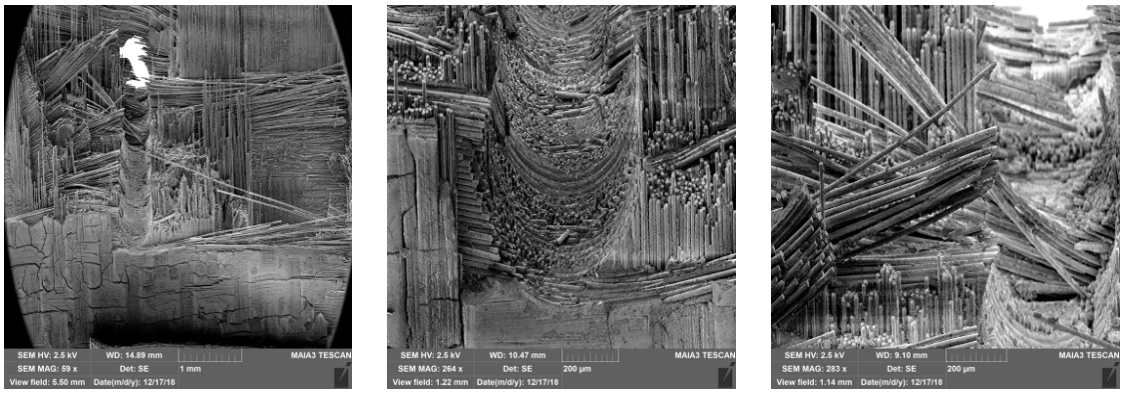

Figure D. 8: Fracture surface of specimen #5 (left hole), tested in creep at 1200°C in air (σ_{cr} = 94 MPa, t_f = 6.55 h)

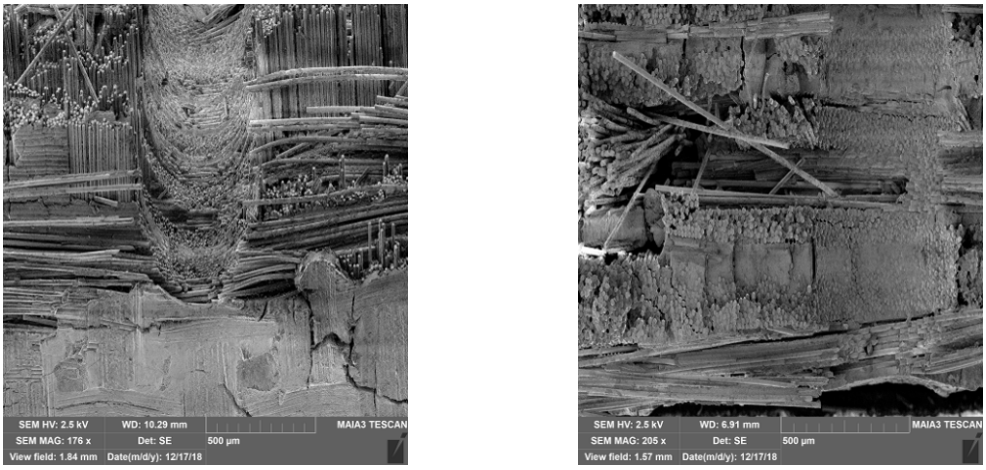

Figure D. 9: Fracture surface of specimen #5 (right hole), tested in creep at 1200°C in air (σ_{cr} = 94 MPa, t_f = 6.55 h)

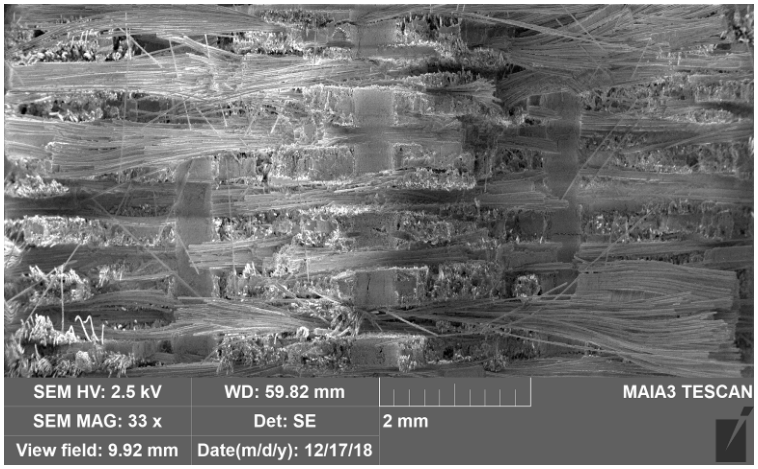

Figure D. 10: Fracture surface of specimen #8, tested in creep at 1200°C in air (σ_{cr} = 150 MPa, t_f = 0.01 h)

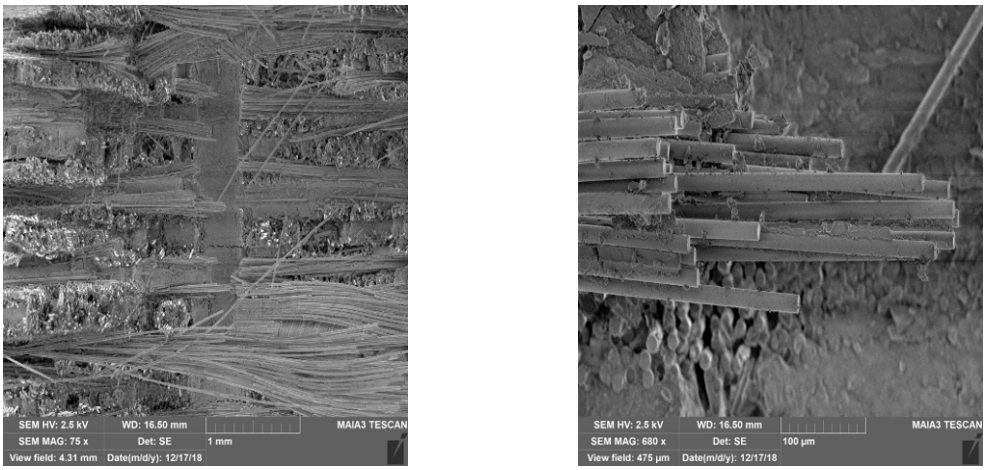

a) b)

Figure D. 11: Fracture surface of specimen #8 (Area 1), tested in creep at 1200°C in air (σ_{cr} = 150 MPa, t_f = 0.01 h): (a) 75X, (b) 680X

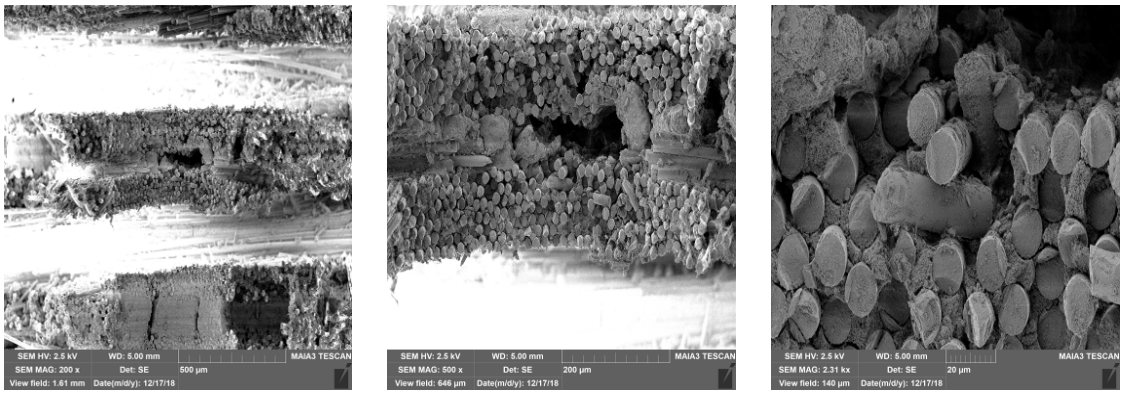

a) b) c)

Figure D. 12: Fracture surface of specimen #8 (Area 2), tested in creep at 1200°C in air (σ_{cr} = 150 MPa, t_f = 0.01 h): (a) 200X, (b) 500X, (c) 2.3kX

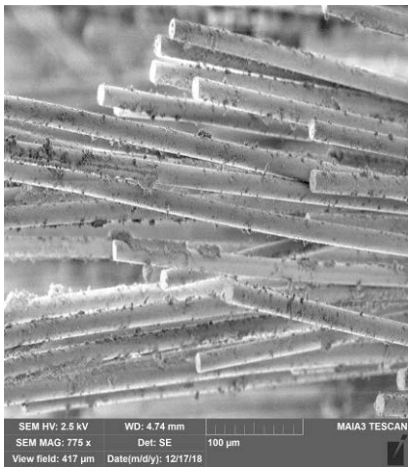

Figure D. 13: Fracture surface of specimen #8, tested in creep at 1200°C in air (σ_{cr} = 150 MPa, t_f = 0.01 h)

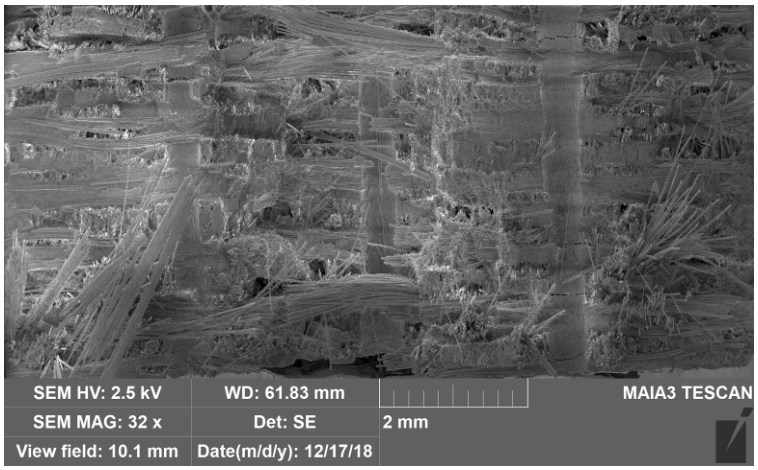

Figure D. 14: Fracture surface of specimen #12, tested in tension to failure following 100 h creep at 46 MPa at 1200°C in steam

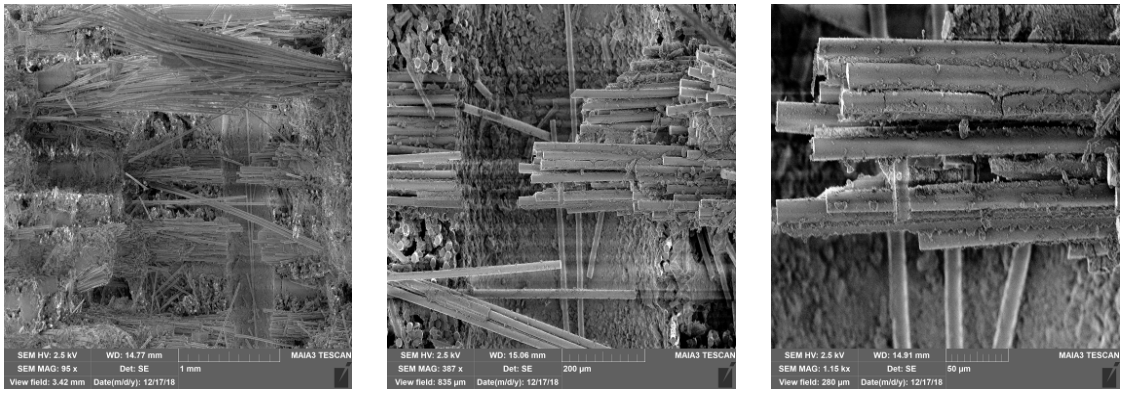

a) b) c)

Figure D. 15: Fracture surface of specimen #12 (Area 1), tested in tension to failure following 100 h creep at 46 MPa at 1200°C in steam: (a) 95X, (b) 387X, (c) 1kX

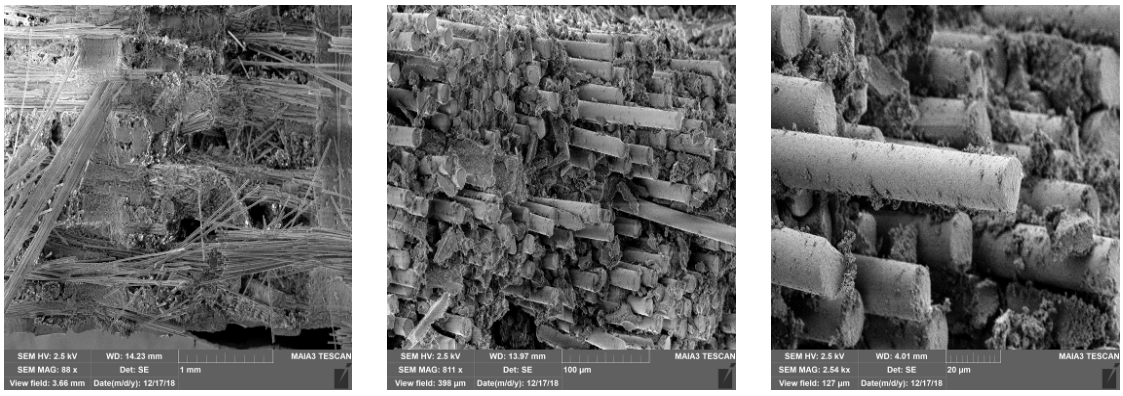

a) b) c)

Figure D. 16: Fracture surface of specimen #12 (Area 2), tested in tension to failure following 100 h creep at 46 MPa at 1200°C in steam: (a) 88X, (b) 811X, (c) 2.5kX

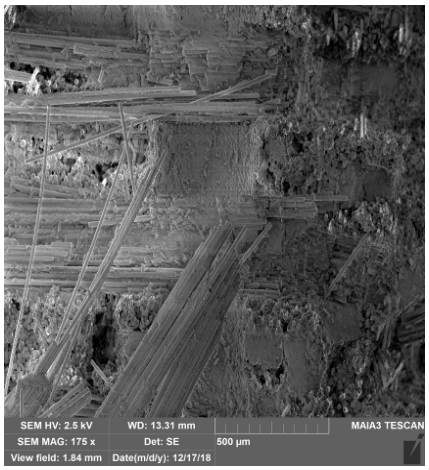

a)

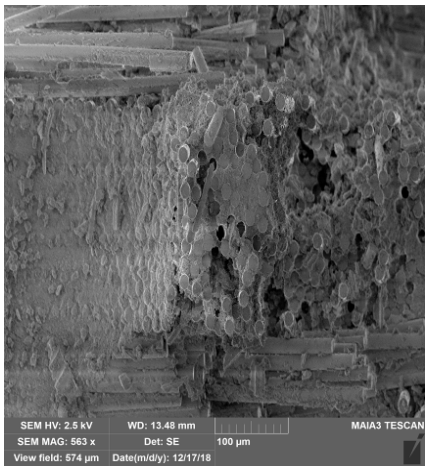

b)

Figure D. 17: Fracture surface of specimen #12 (Area 3), tested in tension to failure following 100 h creep at 46 MPa at 1200°C in steam: (a) 175X, (b) 563X

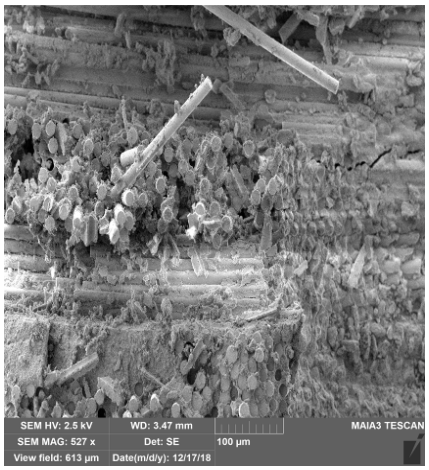

a)

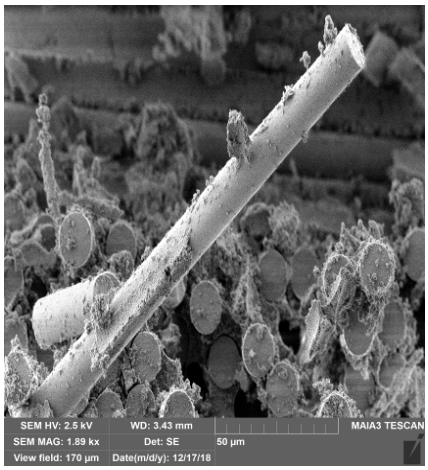

b)

Figure D. 18: Fracture surface of specimen #12 (Area 4), tested in tension to failure following 100 h creep at 46 MPa at 1200°C in steam: (a) 527X, (b) 1.9kX

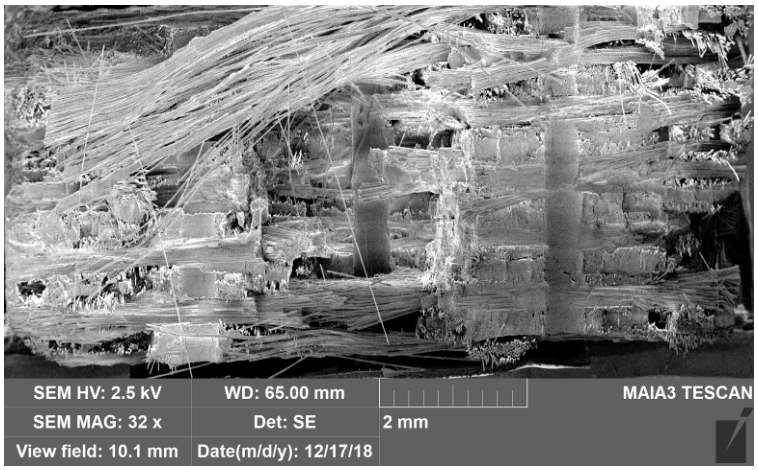

Figure D. 19: Fracture surface of specimen #10, tested in creep at 1200°C in steam (σ_{cr} = 93 MPa, t_f = 6.05 h)

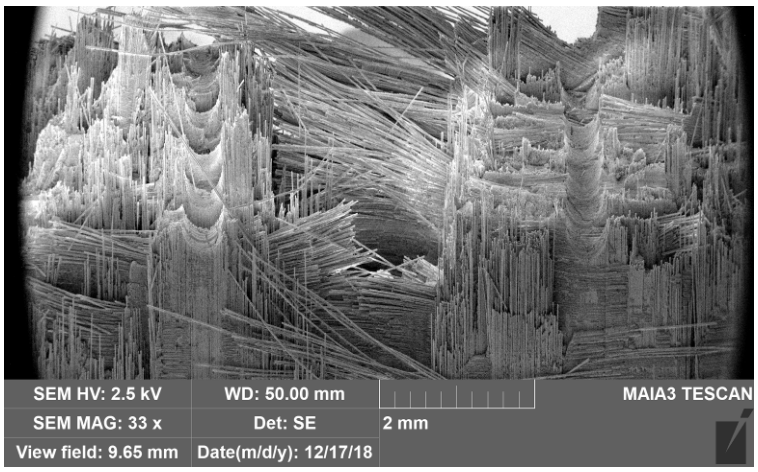

Figure D. 20: Fracture surface of specimen #10 (55° tilt), tested in creep at 1200°C in steam (σ_{cr} = 93 MPa, t_f = 6.05 h)

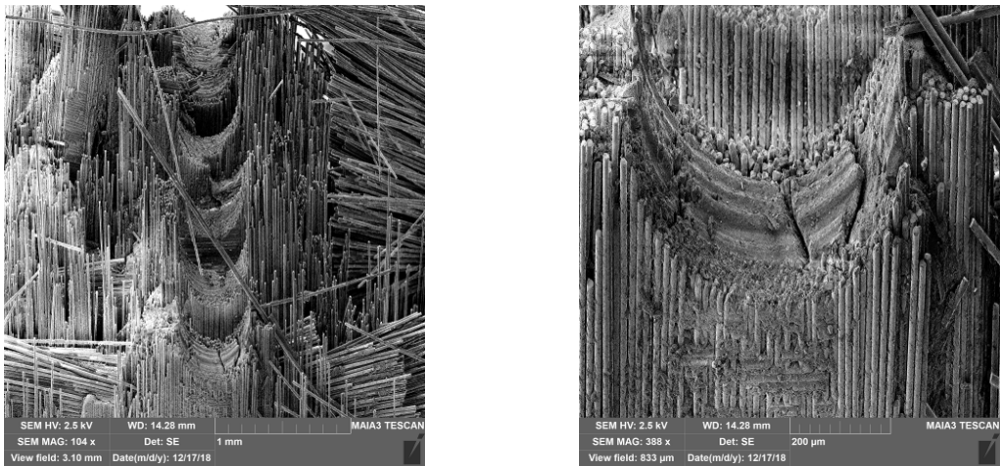

a) b)

Figure D. 21: Fracture surface of specimen #10 (left hole), tested in creep at 1200°C in steam (σ_{cr} = 93 MPa, t_f = 6.05 h): (a) 104X, (b) 388X

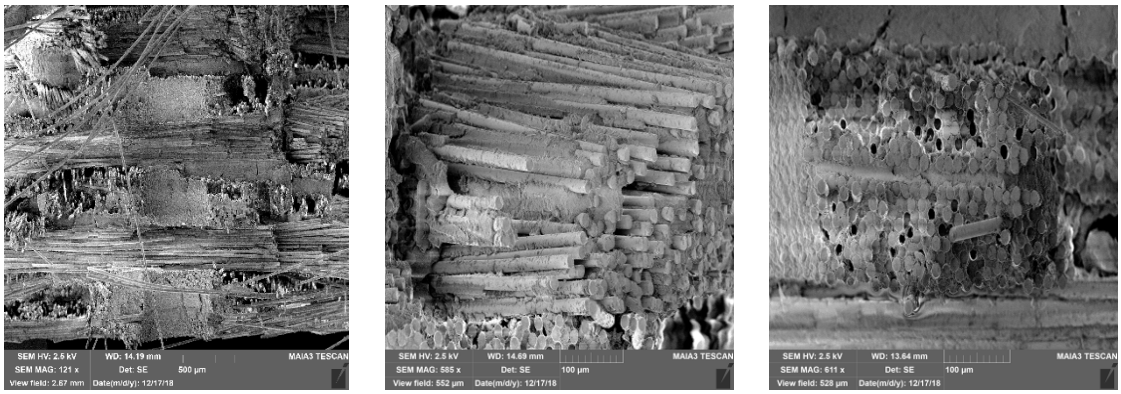

a) b) c)

Figure D. 22: Fracture surface of specimen #10 (left hole, Area 1 & 2), tested in creep at 1200°C in steam (σ_{cr} = 93 MPa, t_f = 6.05 h): (a) 121X, (b) 585X, (c) 611X

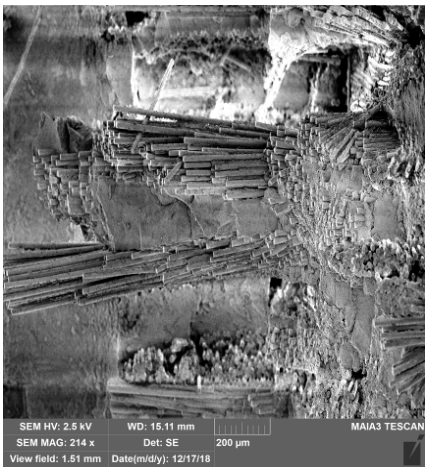

Figure D. 23: Fracture surface of specimen #10 (center hole), tested in creep at 1200°C in steam (σ_{cr} = 93 MPa, t_f = 6.05 h)

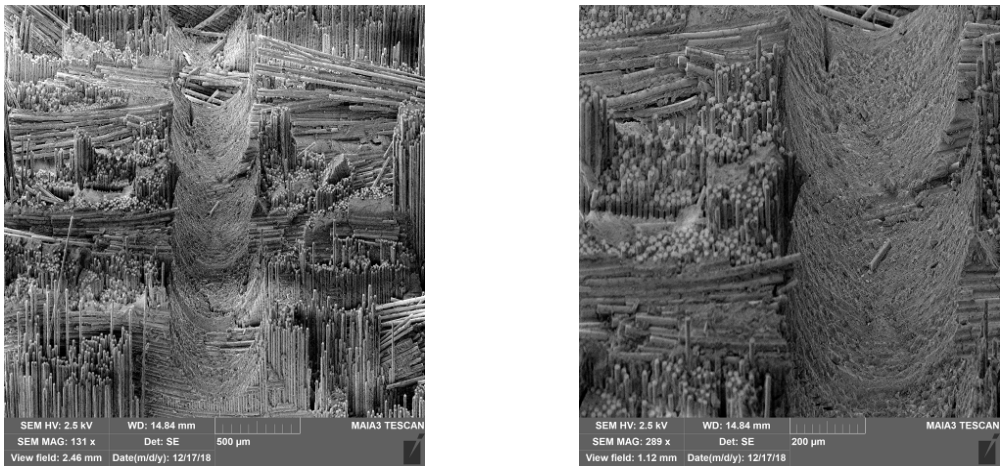

Figure D. 24: Fracture surface of specimen #10 (right hole), tested in creep at 1200°C in steam (σ_{cr} = 93 MPa, t_f = 6.05 h)

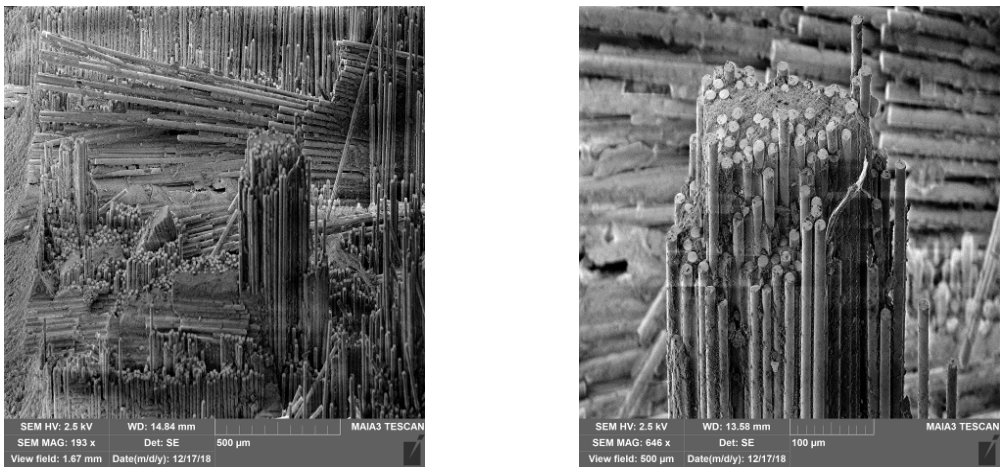

a) b)

Figure D. 25: Fracture surface of specimen #10 (right hole, Area 1), tested in creep at 1200°C in steam (σ_{cr} = 93 MPa, t_f = 6.05 h): (a) 193X, (b) 646X

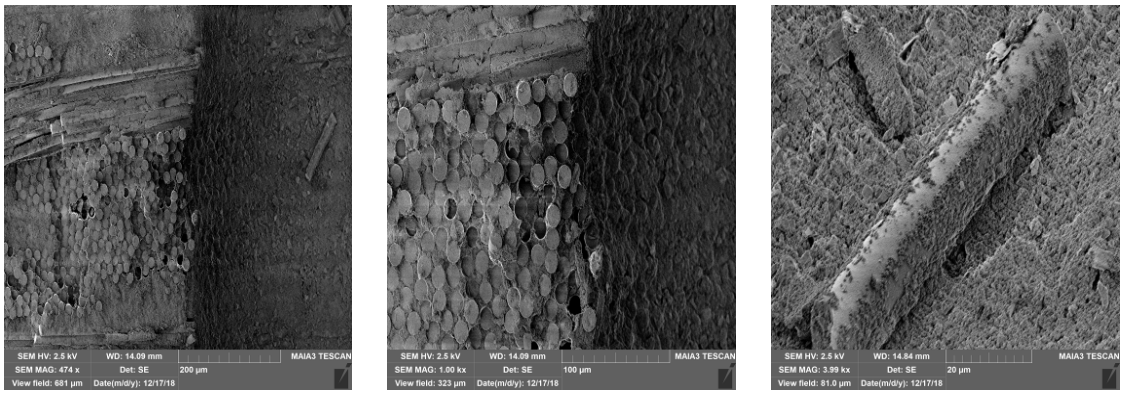

a) b) c)

Figure D. 26: Fracture surface of specimen #10 (right hole, Area 2), tested in creep at 1200°C in steam (σ_{cr} = 93 MPa, t_f = 6.05 h): (a) 474X, (b) 1kX, (c) 4kX

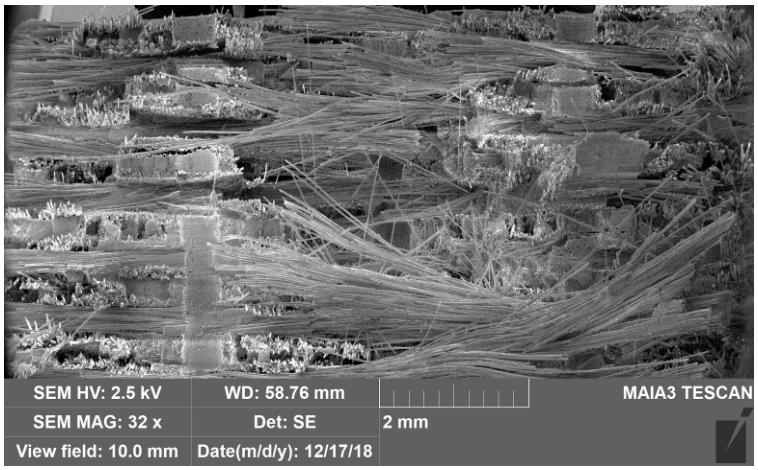

Figure D. 27: Fracture surface of specimen #11, tested in creep at 1200°C in steam (σ_{cr} = 150 MPa, t_f = 0.04 h)

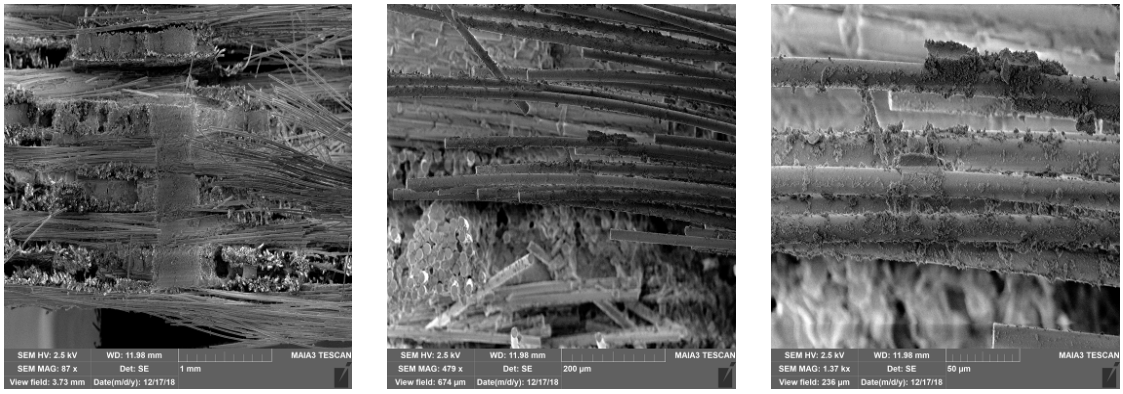

a) b) c)

Figure D. 28: Fracture surface of specimen #11 (Area 1), tested in creep at 1200°C in steam (σ_{cr} = 150 MPa, t_f = 0.04 h): (a) 87X, (b) 479X, (c) 1.4kX

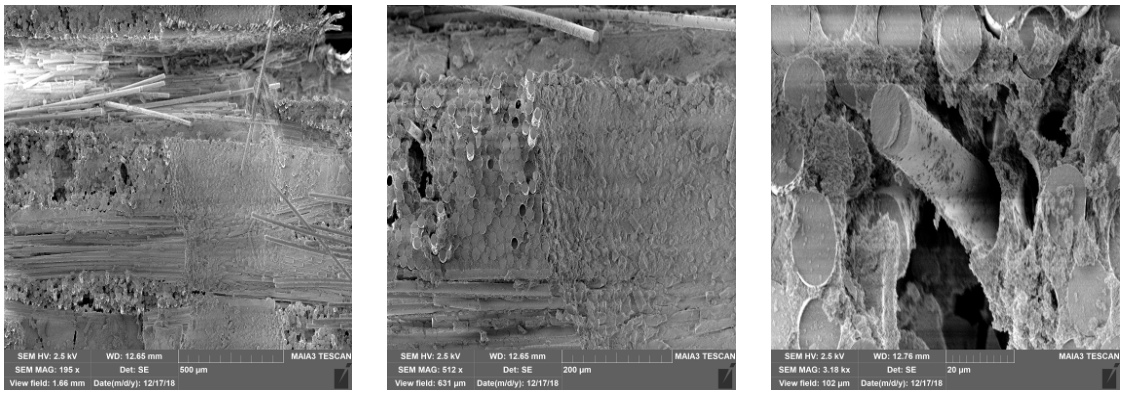

a) b) c)

Figure D. 29: Fracture surface of specimen #11 (Area 2), tested in creep at 1200°C in steam (σ_{cr} = 150 MPa, t_f = 0.04 h): (a) 195X, (b) 512X, (c) 3kX

Bibliography

[1] V. A. Kramb, R. John, and L. P. Zawada, “Notched Fracture Behavior of an Oxide/Oxide Ceramic-Matrix Composite,” *J. Am. Ceram. Soc.*, vol. 82, no. 11, pp. 3087–3096, 1999.

[2] K. K. Chawla, *Ceramic Matrix Composites*. London: Chapman & Hall, 1993.

[3] S. N. Minor, “Creep of Nextel 720A Ceramic Matrix Composite With Laser Drilled Effusion Holes at 1200°C in Air and in Steam,” Wright Patterson Air Force Base, 2018.

[4] M. B. Ruggles-Wrenn, S. N. Minor, C. P. Przybyla, and E. L. Jones, “Creep of a Nextel ™ 720/alumina ceramic composite containing an array of small holes at 1200°C in air and in steam,” *Int. J. Appl. Ceram. Technol.*, 2018.

[5] T. L. Anderson, *Fracture Mechanics: Fundamentals and Applications*, Third. Boca Raton, FL: Taylor & Francis Group, 2005.

[6] F. W. Zok and C. G. Levi, “Mechanical Properties of Porous-Matrix Ceramic Composites,” *Adv. Eng. Mater.*, pp. 15–23, 2001.

[7] F. W. Zok, “Developments in Oxide Fiber Composites,” *J. Am. Ceram. Soc.*, 2006.

[8] K. A. Keller, G. Jefferson, and R. J. Kerans, “Oxide-Oxide Composites,” in *Ceramic Matrix Composites: Materials, Modeling and Technology*, New Jersey: John Wiley & Sons, Inc., 2015, pp. 236–264.

[9] G. T. Siegert, “Effect of Environment on Creep Behavior of an Oxide/Oxide CFCC with ±45° Fiber Orientation,” Wright Patterson Air Force Base, 2006.

[10] M. B. Ruggles-Wrenn, “Environmental Effects on Oxide/Oxide Composites,” in *Ceramic Matrix Composites: Materials, Modeling and Technology*, N. P. Bansal

and J. Lamon, Eds. John Wiley & Sons, Inc., 2015, pp. 295–333.

[11] M. B. Ruggles-Wrenn, S. Mall, C. A. Eber, and L. B. Harlan, “Effects of steam environment on high-temperature mechanical behavior of NextelTM720/alumina (N720/A) continuous fiber ceramic composite,” *Compos. Part A Appl. Sci. Manuf.*, vol. 37, pp. 2029–2040, 2006.

[12] J. M. Mehrman, M. B. Ruggles-Wrenn, and S. S. Baek, “Influence of hold times on the elevated-temperature fatigue behavior of an oxide-oxide ceramic composite in air and in steam environment,” *Compos. Sci. Technol.*, vol. 67, pp. 1425–1438, 2007.

[13] M. B. Ruggles-Wrenn and J. C. Braun, “Effects of steam environment on creep behavior of Nextel^{TM}720/alumina ceramic composite at elevated temperature,” *Mater. Sci. Eng. A*, vol. 497, pp. 101–110, 2008.

[14] M. B. Ruggles-Wrenn, P. Koutsoukos, and S. S. Baek, “Effects of environment on creep behavior of two oxide/oxide ceramic-matrix composites at 1200°C,” *J. Mater. Sci.*, vol. 43, pp. 6734–6746, 2008.

[15] L. P. Zawada, R. S. Hay, S. S. Lee, and J. Staehler, “Characterization and High-Temperature Mechanical Behavior of an Oxide/Oxide Composite,” *J. Am. Ceram. Soc.*, vol. 86, pp. 981–990, 2003.

[16] V. A. Kramb, R. John, and D. A. Stubbs, “A study of the damage progression from notches in an oxide/oxide ceramic-matrix composite using ultrasonic C-scans,” *Compos. Sci. Technol.*, vol. 1, pp. 1561–1570, 2001.

[17] R. John, D. J. Buchanan, and L. P. Zawada, “Creep Deformation and Rupture Behavior of a Notched Oxide/Oxide Nextel 720/AS Composite,” in *Ceramic*

Engineering and Science Proceedings, vol. 21, T. Jessen and E. Ustundag, Eds. 2000, pp. 567–574.

[18] R. John, D. J. Buchanan, and L. P. Zawada, “Notch-Sensitivity of a Woven Oxide/Oxide Ceramic Matrix Composite,” in *Mechanical, Thermal and Environmental Testing and Performance of Ceramic Composites and Components*, 2000, pp. 172–181.

[19] D. J. Buchanan, R. John, and L. P. Zawada, “Notched Fracture Behavior of Oxide/Oxide Nextel 720/AS Composite,” in *Ceramic Engineering and Science Proceedings*, vol. 21, T. Jessen and E. Ustundag, Eds. 2000, pp. 581–588.

[20] S. Mall and M. A. Sullivan, “Creep Rupture and Fatigue Behavior of a Notched Oxide/Oxide Ceramic Matrix Composite at an Elevated Temperature,” *Int. J. Appl. Ceram. Technol.*, vol. 8, no. 2, pp. 251–260, 2011.

[21] D. J. Buchanan, V. A. Kramb, R. John, and L. P. Zawada, “Effect of Small Effusion Holes on Creep Rupture Behavior of Oxide/Oxide Nextel 720/AS Composite,” in *Ceramic Engineering and Science Proceedings*, M. Singh and T. Jessen, Eds. 2001, pp. 659–666.

[22] R. John, D. J. Buchanan, V. A. Kramb, and L. P. Zawada, “Creep Rupture Behavior of Oxide/Oxide Nextel 720/AS and MI SiC/SiC Composites with Effusion Holes,” in *26th Annual Conference on Composites, Advanced Ceramics, Materials, and Structures: A*, 2002, pp. 617–628.

[23] L. B. Harlan, “Creep-Rupture Behavior of an Oxide/Oxide Ceramic Matrix Composite at Elevated Temperatures in Air and Steam Environments,” Wright Patterson Air Force Base, 2005.

[24] J. M. Mehrman, “Effect of Hold Times on Fatigue Behavior of Nextel™ 720/Alumina Ceramic Matrix Composite at 1200°C in Air and in Steam Environment,” Wright Patterson Air Force Base, 2006.

[25] G. Hetrick, “Effects of Frequency and Environment on Fatigue Behavior of an Oxide-Oxide Ceramic Composite at 1200 °C,” Wright Patterson Air Force Base, 2006.

[26] COIC, “Oxide Ceramic Matrix Composites.” [Online]. Available: http://www.coiceramics.com/oxidepg.html.

[27] M. B. Ruggles-Wrenn, A. T. Radzicki, S. S. Baek, and K. A. Keller, “Effect of loading rate on the monotonic tensile behavior and tensile strength of an oxide-oxide ceramic composite at 1200 °C,” *Mater. Sci. Eng. A*, vol. 492, no. 1–2, pp. 88–94, 2008.

REPORT DOCUMENTATION PAGE

Form Approved
OMB No. 074-0188

1. REPORT DATE *(DD-MM-YYYY)*	2. REPORT TYPE	3. DATES COVERED *(From – To)*
21-03-2019	Master's Thesis	Sept 2017 – March 2019

TITLE AND SUBTITLE

Creep of Nextel 720/Alumina Ceramic Matrix Composite with Diamond-Drilled Effusion Holes at 1200°C in Air and in Steam

5a. CONTRACT NUMBER

5b. GRANT NUMBER

5c. PROGRAM ELEMENT NUMBER

6. AUTHOR(S)

Harkins, Megan L., Major, USAF

5d. PROJECT NUMBER

5e. TASK NUMBER

5f. WORK UNIT NUMBER

7. PERFORMING ORGANIZATION NAMES(S) AND ADDRESS(S)
Air Force Institute of Technology
Graduate School of Engineering and Management (AFIT/ENY)
2950 Hobson Way, Building 640
WPAFB OH 45433-8865

8. PERFORMING ORGANIZATION REPORT NUMBER

AFIT-ENY-MS-19-M-218

9. SPONSORING/MONITORING AGENCY NAME(S) AND ADDRESS(ES)

Intentionally left blank

10. SPONSOR/MONITOR'S ACRONYM(S)

11. SPONSOR/MONITOR'S REPORT NUMBER(S)

12. DISTRIBUTION/AVAILABILITY STATEMENT
Distribution Statement A: Approved for Public Release; Distribution Unlimited

13. SUPPLEMENTARY NOTES
This material is declared a work of the U.S. Government and is not subject to copyright protection in the United States.

14. ABSTRACT
This effort evaluated the tensile creep behavior of Nextel™720/alumina with diamond-drilled (DD) effusion holes at 1200°C. Tensile properties at 1200°C in laboratory air were unaffected by the presence of an array of 17 DD holes. Notably, examination of the composite microstructure did not reveal any damage caused by the drilling process. The DD specimens exhibited similar degradation to creep lifetimes as laser-drilled (LD) specimens for creep tests between 46-150 MPa in air, but contrary to unnotched and LD specimens, saw minimal degradation due to steam. These results were attributed to a change in dominant damage mechanism that caused minimum creep rates in air to exceed those in steam.

15. SUBJECT TERMS
Oxide/Oxide Ceramic Matrix Composite, Nextel 720 Fibers, Porous Alumina Matrix, Diamond-Drilled Effusion Holes, Tensile Creep, 1200°C

16. SECURITY CLASSIFICATION OF:			17. LIMITATION OF ABSTRACT	18. NUMBER OF PAGES	19a. NAME OF RESPONSIBLE PERSON
a. REPORT	b. ABSTRACT	c. THIS PAGE			Dr. Marina Ruggles-Wrenn, AFIT/ENY
U	U	U	UU	175	19b. TELEPHONE NUMBER *(Include area code)* (937) 255-3636, x4641 marina.ruggles-wrenn@afit.edu

Standard Form 298 (Rev. 8-98)
Prescribed by ANSI Std. Z39-18